UNIVERSITY OF BIRMINGHAM

A VARIABLE TEMPERATURE SCANNING TUNNELING MICROSCOPY STUDY OF ORGANIZING C_{60} MOLECULES ON NANOSTRUCTURED GOLD SURFACE

by

XIN ZHANG

A thesis submitted to

The University of Birmingham

for the degree of

DOCTOR OF PHILOSOPHY

School of Physics and Astronomy

The University of Birmingham

November 2010

ABSTRACT

The nucleation and growth of C_{60} molecular nanostructures on the Au (111) surface are studied under various conditions using variable temperature UHV STM.

At room temperature, the C_{60}/Au interface exhibits rich features observed in the STM images, for instance the lifting of the reconstruction and the appearance of dim molecules in the close-packed C_{60} overlayer. Furthermore, the structural changes at the interface result in different bonding configurations of the adsorbed C_{60} molecules, of which the strong bonding configuration can retain individual C_{60} molecules on the elbow sites even at room temperature. This further leads to C_{60} island nucleation at unexpected location.

C_{60} molecules deposited at reduced temperatures, 47 K and 180 K, respectively, do not induce atomic rearrangement of the Au (111) surface. The C_{60} molecules are bonded to the intact reconstructed surface. However, the nucleation site and the island growth mode are still determined by the reconstruction pattern of the substrate. By increasing the C_{60} coverage step-by-step and comparing with the growth scenario observed at the two temperatures, the details of the intermolecular and molecule-substrate interactions are revealed.

Temperature dependent processes for the C_{60}/Au (111) system are studied by gradually raising the sample temperature from 47 K to room temperature. Diffusion is activated at ~160 K leading to ripening of the C_{60} molecular structures. At higher

temperatures, when a large number of C_{60} molecules are released from the elbow sites, C_{60} clusters with a magic number of seven are formed. These clusters only diffuse within the FCC regions of the surface with their diffusing direction confined by the reconstruction ridges (the discommensuration lines, the DLs). The ripening process is also studied at room temperature over a long timescale. A combination of Ostwald ripening and Smoluchowski ripening process is observed.

ACKNOWLEDGEMENTS

My sincere gratitude goes to my supervisor Dr. Quanmin Guo, without whom the work presented in this thesis would be impossible. Dr. Guo is my mentor. It was he who introduced me to the methodologies of rigorous scientific research, both theoretical and experimental. I am indebted to him for his insights, guidance and encouragement throughout my PhD program. His knowledge and intellectual acumen sheds lights on problems and difficulties emerged during my research work. I owe my broadened vision of my field of study and improved ability in English academic writing to his patience, meticulousness and unselfish contributions to my papers. His kindness, consideration and hospitality also helped me to accommodate to life in the UK.

I would like to express my appreciation to Prof. Richard. E. Palmer, Dr. Ziyou Li and Dr. Wolfgang Theis for illuminating and thought-provoking discussions. I would also like to thank Dr. Feng Yin and Dr. Neil Kilpatrick, whose acute observations and generous and succinct direction facilitated my apprenticeship with the UHV system and STM.

Discussions with Dr Hao Zheng, Dr. Lin Tang and Tianluo Pan throughout the doctoral program, both on and off academic topics, are highly valued and appreciated. I recognize all the members who now work or used to work in the NPRL for advice, collaboration and friendship.

Special thanks must go to my parents and my family, who selflessly supported and encouraged me. To them I owe much more than this thesis.

At last, I want to mention my girlfriend Meng, who is also pursuing an academic career. During my four years' study in the UK, we were separated by ten thousand miles for most of the time, but the love and inspiration that we share bind us together. The understanding and solicitude I receive from her are the treasure of my life. I am so happy to have her as my soulmate from the beginning of my career and I hope to be with her all the way through.

Contents

CHAPTER 1
INTRODUCTION

Self-assembly of molecules on metal surfaces has attracted a significant level of scientific interest during the past decade for its potential in the realization of molecular electronic devices [1]. In order to design and fabricate molecular structures with desired functions, controlling of the motion and aggregation of the molecules on the substrate is required. A number of studies demonstrate that the intermolecular interaction and the molecule-substrate interaction play important roles in guiding the diffusion, nucleation and assembly of the molecules on metal surfaces, thus determine the final configuration of the molecular structure [2-5]. Furthermore, these interactions also present a great influence on the electronic and dynamical properties of these molecular structures [6-9]. Fully understanding of and the ability of fine tuning the intermolecular interaction and the molecule-substrate interaction are therefore the prerequisites of fabricating functional molecular devices. Using pre-patterned surfaces as the template is an ideal way to tune these interactions and guide the growth of the molecular structure. For this purpose, surface patterns created by lithography-based techniques are widely used. Besides, the naturally formed periodical pattern of reconstructed surfaces is also a kind of easy-to-obtain template for directing the self-assembly of molecules with nanometer-accuracy [10, 11]. Moreover, the capacity of atomic manipulation of the scanning tunneling microscope (STM) offers us another method to create surface patterns. The situation of the

intermolecular and molecule-substrate interactions on patterned surfaces is rather complicated due to the variety of atomic structures, therefore, numerous studies involving various substrates and molecules have been devoted to reveal the basic rules that determine how the molecular structures assemble on patterned surfaces.

Among all the metals, gold is known as the only FCC crystal with a reconstructed (111) surface. The (22 × √3) Au (111) surface presents a herringbone reconstruction pattern and is frequently used as template for the building of molecular structures. On this surface, alternating FCC and HCP stacking regions are separated by corrugation ridges (or called discommensuration lines, DLs). The DLs present a zigzag pattern with long-range order. In addition to its unique atomic structure, novel electronic and catalytic properties also arise from the reconstruction. With such rich characteristics, the Au (111) surface has been employed to support the growth of many kinds of metal atoms and organic molecules under various conditions. For metal deposition, site-specific nucleation always takes place at the elbow sites of the herringbone pattern, comprising ordered arrays of metal islands [12-15]. In the case of organic molecule deposition, the elbow site, FCC region and HCP region of the Au (111) surface usually present different affinities to the landed molecules, therefore, the molecules will preferentially adsorb on certain features of the surface and form periodical structures according to the herringbone pattern. Structural and spectroscopy investigations of the molecular-Au (111) system reveal many interesting properties that can be used in the design of functional nanostructures [3, 4, 7, 9]. However, most of the molecules mentioned above have a two-dimensional structure. These molecules

prefer to adsorb with their planes lie parallel to the substrate. In comparison, the situation of the self-assembly of three-dimensional molecules on the Au (111) surface is more complicated, and of greater scientific interests.

The C_{60} buckminsterfullerene molecule has a typical three-dimensional configuration. Since the discovery in 1985 [16, 17], it has attracted a great deal of research attention, especially after the finding that upon doping with alkali metal atoms, the C_{60} solid will present superconductivity [18-20]. With its 3D configuration and interesting properties, the C_{60} molecule and many C_{60} derivatives have been used as building blocks to construct nanostructures on various surfaces [21]. The deposition of C_{60} molecule on the Au (111) surface has also been studied. It is widely agreed that the C_{60} molecule presents high mobility on the surface and can only be retained in the middle of the terrace at low temperatures [22, 23]. However, regarding whether the adsorbed C_{60} molecules can lift the underlying herringbone reconstruction of the Au (111), there are conflicting observations [24, 25]. Furthermore, some molecules in a close-packed C_{60} layer formed on the Au (111) are found to have lower apparent height than the surrounding molecules. Different explanations towards this phenomenon coexist [25-28]. All these arguments about the above two phenomena indicate that the interface structure of the C_{60}/Au (111) system is very complicated and requires further exploration. Not only the atomic structure but the electronic characteristic of the C_{60}/Au (111) system has been intensively studied [29-31]. However, there is still no conclusive answer to the existence and the amount of the charge transfer from the Au (111) surface to the C_{60} molecule. All the different

opinions towards the configuration and properties of the C_{60} molecular structures on the Au (111) surface indicate that this topic requires further investigation. A comprehensive study and understanding of the C_{60}/Au (111) system may help to address some key issues in nanoscale self-assembly.

In my doctoral research, the growth of C_{60} molecular structure on the Au (111) surface is studied with a variable temperature ultra-high vacuum STM (VT UHV STM). The high stability of the STM and its capacity of carrying out experiment at different temperatures ranging from 47 K to 1200 K make it possible for us to test the C_{60}/Au (111) system via different approaches. For instance, the C_{60} coverage can be increased step by step without losing the original observation area after *in situ* deposition, therefore, the influence of different C_{60} coverages on the local topography can be revealed. Moreover, the sample can be cooled to 47 K, after C_{60} deposition, we can raise the temperature step-by-step with STM imaging preformed at each temperature until reaching room temperature. By doing so, the dynamical behavior of the C_{60} adsorbate can be thereby observed. Furthermore, a kind of zero-gradient stepped surface (so-called gold-fingers) is created on the Au (111) surface by STM manipulation of surface Au atoms. Study of the nucleation and growth of C_{60} structure on this artificially patterned surface can help us to further understand the effects of various molecule-substrate interactions associated with different local atomic structures. With all the above approaches and experiments carried out under other conditions, the self-assembly of C_{60} molecules on the Au (111) surface is systematically studied. I try to give answers to the pre-mentioned arguments based on

my experimental results. Also, some novel phenomena are observed in my research. Possible explanations of these phenomena are given. All these explanations together with those pre-settled conclusions reveal some universal rules lie behind the rich characteristics of the C_{60}/Au (111) system. Knowing these rules may help us to have a deeper insight into the interplay of the intermolecular interaction and the molecule-substrate interaction of typical molecular-metal systems, thus move a step closer towards the realization of functional molecular devices.

Here, I would like to outline the structure of this thesis. In Chapter 2, the background of my research is comprehensively reviewed. The atomic structure of the reconstructed Au (111) surface is introduced first. The atomic structures associated with various features on the surface, for example the compressed surface unit cell, the elbow sites of the DLs, the step edges and the surface defects, are clarified for the convenience of discussion in the following chapters. The electronic characteristic of the surface is also mentioned because it has strong influence on the configuration and properties of the C_{60} molecular structure. Later in Chapter 2, the C_{60} fullerene and the formation of C_{60} molecular structures on various substrates are introduced. Especially, the previous studies devoted to the self-assembly of C_{60} molecules on the Au (111) surface are systematically reviewed. As mentioned above, there are still many uncertain issues about the C_{60}/Au (111) system, which will be addressed in Chapter 2. Based on these introductions, the main direction of my research is established, which focuses on the interaction between the C_{60} molecules and the Au substrate under different temperatures. The interface atomic modification, and the diffusion behavior

of the C_{60} adsorbate arising from the interplay of the intermolecular and molecule-substrate interactions are also included in my study. The results and discussions of my research are presented in Chapters 4-8.

In Chapter 3, the experimental methods of my research are introduced. Firstly, common surface characterization techniques are introduced. The principle, construction and operation of the STM system, which offers us not only the atomic resolution imaging ability but also the ability to manipulate atoms, are introduced in detail. Then, our own STM apparatus is introduced. Other details about my methodology, including the preparation of the sample, the fabrication and cleaning of the STM tip, the C_{60} deposition and the operation of low temperature experiment, are also introduced.

In Chapters 4-8, the results of my research are presented and discussed. The results are organized into different chapters according to the different aspects of the topics. In Chapter 4, the most common situation, the deposition of C_{60} molecules onto Au (111) at room temperature, is introduced. Closed-packed C_{60} islands with three different azimuthal orientations are formed. The lifting of the herringbone reconstruction under the C_{60} layer is found to depend on the local density of elbow sites. At last, the appearance of dim molecules in the C_{60} layer is explained as an electronic effect due to the variety of the atomic structure at the C_{60}/Au (111) interface.

In Chapter 5, the attachment of C_{60} molecules to the monoatomic steps of the Au (111) is introduced. Furthermore, the deposition of C_{60} molecules on the gold-fingers

reveals that the two opposite steps of one gold-finger show different affinities to the C_{60} molecules, which further leads to the different nucleation and island-growth situations on the two sides of each gold-finger. Such site-specific binding property of the gold-fingers roots in the different atomic structure and reconstruction pattern associated with the two steps of the gold-finger. The zero-gradient stepped surface consists of parallel gold-fingers has the potential to serve as a functional template for the fabrication of molecular devices.

The results of depositing C_{60} molecules onto the Au (111) surface at two reduced temperatures, 47 K and 180 K, respectively, are introduced in Chapter 6. At 46 K, C_{60} molecules are preferentially adsorbed on the elbow sites of the herringbone pattern. The further growth of C_{60} islands uses these pre-adsorbed molecules at the elbow sites as nucleation cores. The expansion of the C_{60} islands is confined by the shape of the DLs. Similar deposition carried out at 180 K reveals that the pinched and the bugled elbow sites (the structural difference between these two kinds of elbow site will be introduced in Chapter 2) have different abilities to retain molecules. Furthermore, the growth scenario of C_{60} structure is found to be quite different for the three temperatures, 46 K, 180 K and room temperature, respectively, revealing the effect of the thermal activation on determining the final molecular configuration.

In Chapter 7, the dynamical process, which takes place when the temperature of the C_{60}/Au (111) system is raised from 47 K to room temperature, is introduced. It is found that some C_{60} molecules will stay in the middle of the terrace instead of diffusing away even up to room temperature. Moreover, the site-specific decoration of

the herringbone elbow sites by the C_{60} molecules is observed many times at room temperature. In these two cases, a strong bonding between the C_{60} molecules and the Au (111) surface is expected. Such strong bonding is distinct from the normally formed weak bonding which cannot retain the C_{60} molecules in the middle of the terrace. Structural modification happens at the C_{60}/Au (111) interface is used to explain the high bonding strength. The result of Density functional theory (DFT) calculations performed by our collaborators Y. Wu, L. Wang and H. Cheng from University of Florida supports the conclusion of two bonding configurations with different strengths.

The way that the molecules diffuse and ripen on the surface will determine the final structure of the molecular islands. In Chapter 8, the diffusion and ripening behaviors of C_{60} molecules and clusters are introduced. At different temperatures, the diffusion and ripening processes take place in distinct ways. However, these processes are all greatly influenced by the presence of the underlying herringbone reconstruction. Under certain conditions, the C_{60} molecules are found to comprise clusters with a magic number of seven and diffuse as a whole along the FCC regions defined by two parallel DLs. In a long timescale, both Ostwald ripening and Smoluchowski ripening processes are observed at room temperature. The combination of the two processes induces a slow changing of the C_{60} structure, leading to the formation of a uniform close-packed layer, which represents the equilibrium of the C_{60}/Au (111) system.

Chapter 9 is the conclusion of the whole thesis. Some possible future works are

also suggested.

References

[1] J. V. Barth, G. Costantini, and K. Kern, Nature **437**, 671 (2005).

[2] A. Ulman, Chem. Rev. **96**, 1533 (1996).

[3] T. Yokoyama, S. Yokoyama, T. Kamikado, Y. Okuno, and S. Mashiko, Nature **413**, 619 (2001).

[4] Y. F. Wang, X. Ge, G. Schull, R. Berndt, C. Bornholdt, F. Koehler, and R. Herges, J. Am. Chem. Soc. **130**, 4218 (2008).

[5] I. Fernandez-Torrente, S. Monturet, K. J. Franke, J. Fraxedas, N. Lorente, and J. I. Pascual, Phys. Rev. Lett. **99**, 176103 (2007).

[6] M. Feng, J. Lee, J. Zhao, J. T. Yates, Jr., and H. Petek, J. Am. Chem. Soc. **129**, 12394 (2007).

[7] L. Gao, Q, Liu, Y. Y. Zhang, N. Jiang, *et al*., Phys. Rev. Lett. **101**, 197209 (2008).

[8] N. Jiang, Y. Y. Zhang, Q. Liu, Z. H. Cheng *et al*., Nano Lett. **10**, 1184 (2010).

[9] G. Schull, T. Frederiksen, M. Brandbyge, and R. Berndt, Phys. Rev. Lett. **103**, 206803 (2009).

[10] K. Aït-Mansour, P. Ruffieux, W. Xiao, P. Gröning, R. Fasel, and O. Gröning, Phys. Rev. B **74**, 195418 (2006).

[11] M. Böhringer, K. Morgenstern, W. D. Schneider, *et al.*, Phys. Rev. Lett. **83**, 324 (1999).

[12] D. D. Chambliss, R. J. Wilson, and S. Chiang, Phys. Rev. Lett. **66**, 1721 (1991).

[13] B. Voigtländer, G. Meyer, and N. M. Amer, Phys. Rev. B **44**, 10354 (1991).

[14] J. A. Stroscio, D. T. Pierce, R. A. Dragoset, and P. N. First, J. Vac. Sci. Technol. A **10** 1981 (1992).

[15] S. Helveg, J. V. Lauritsen, E. Lægsgaard, *et al*., Phys. Rev. Lett. **84**, 951 (2000).

[16] H. W. Kroto, J. R. Heath, S. C. O'Bren, R. F. Curl and R. E. Smalley, Nature **318**, 162 (1985).

[17] W. Krätschmer, L. D. Lamb, K. Fostiropoulos and D. R. Huffman, Nature **347**, 354 (1990).

[18] R. M. Fleming, A. P. Ramirez, M. J. Rosseinsky, D. W. Murphy, *et al,*. Nature **352**, 787 (1991).

[19] A. F. Hebard, M. J. Rosseinsky, R. C. Haddon, D. W. Murphy, *et al,*. Nature **350**, 600 (1991).

[20] K. Tanigaki, T. W. Ebbesen, S. Saito, J. Mizuki, J. S. Tsai, Y. Kubo and S. Kuroshima, Nature **352**, 222 (1991).

[21] T. Sakurai, X. D. Wang, Q. K. Xue, Y. Hasegawa, T. Hashizume and H. Shinohara, Prog. Surf. Sci. **51**, 263 (1996).

[22] D. Fujita, T. Yakabe, H. Nejoh, T. Sato, and M. Iwatsuki, Surf. Sci. **366**, 93 (1996).

[23] E. I. Altman and R. J. Colton, Surf. Sci. **279**, 49 (1992).

[24] E. I. Altman and R. J. Colton, J. Vac. Sci. Technol. B **12**, 1906 (1994).

[25] J. K. Gimzewski, S. Modesti, Ch. Gerber, and R. R. Schlittler, Chem. Phys. Lett. **213**, 401 (1993).

[26] E. I. Altman and R. J. Colton, Phys. Rev. B **48**, 18244 (1993).

[27] G. Schull and R. Berndt, Phys. Rev. Lett. **99**, 22105 (2007).

[28] J. A. Gardener, G. A. D. Briggs, and M. R. Castell, Phys. Rev. B **80**, 235434 (2009).

[29] C. T. Tzeng, W. S. Lo, J. Y. Yuh, R. Y. Chu, and K. D. Tsuei, Phys. Rev. B **61**, 2263 (2000).

[30] T. R. Ohno, Y. Chen, S. E. Harvey, G. H. Kroll, and J. H. Weaver, Phys. Rev. B **44**, 13747 (1991).

[31] X. Lu, M. Grobis, K. H. Khoo, S. G. Louie, and M. F. Crommie, Phys. Rev. B **70**, 115418 (2004).

CHAPTER 2
LITERATURE REVIEW

2.1 The Au (111) Surface

2.1.1 Morphology of the Au (111) Surface

Gold is a face-centered cubic (FCC) metal, of which the bulk lattice structure is shown in Fig. 2.1(a). The grey triangle in the lattice represents the (111) plane, which consists of hexagonally close-packed atoms. Low index crystalline axes of a (111) plane are drawn in Fig. 1(b). Being a very unique metal, gold is the only FCC metal that presents a reconstructed (111) surface. The Au (111) surface was first studied using Low-energy electron diffraction (LEED) [1, 2] and Reflection high-energy electron diffraction (RHEED) [3], which suggest a 4.55% uniaxial contraction of the hexagonal top-most layer along one of the three equivalent <110> directions and result in the formation of a rectangular (22 × √3) superlattice unit cell in the surface layer. M. A. van Hove *et al*. [2] proposed a stacking-fault model for this reconstruction, in which the atoms in the top-most layer alternately occupy ABC stacking (FCC-type) sites and ABA stacking (HCP -type) sties. Furthermore, the LEED diffraction pattern is interpreted as the superposition of three domains which are 120° rotational related to each other, corresponding to the three-fold symmetry of the gold lattice. TEM [4, 5] observations on the Au (111) surface find finger-like features with 63 Å periodicity, which is consistent with the length of a (22 × √3) unit cell with a ~4% uniaxial contraction in one of the <110> directions. This experiment

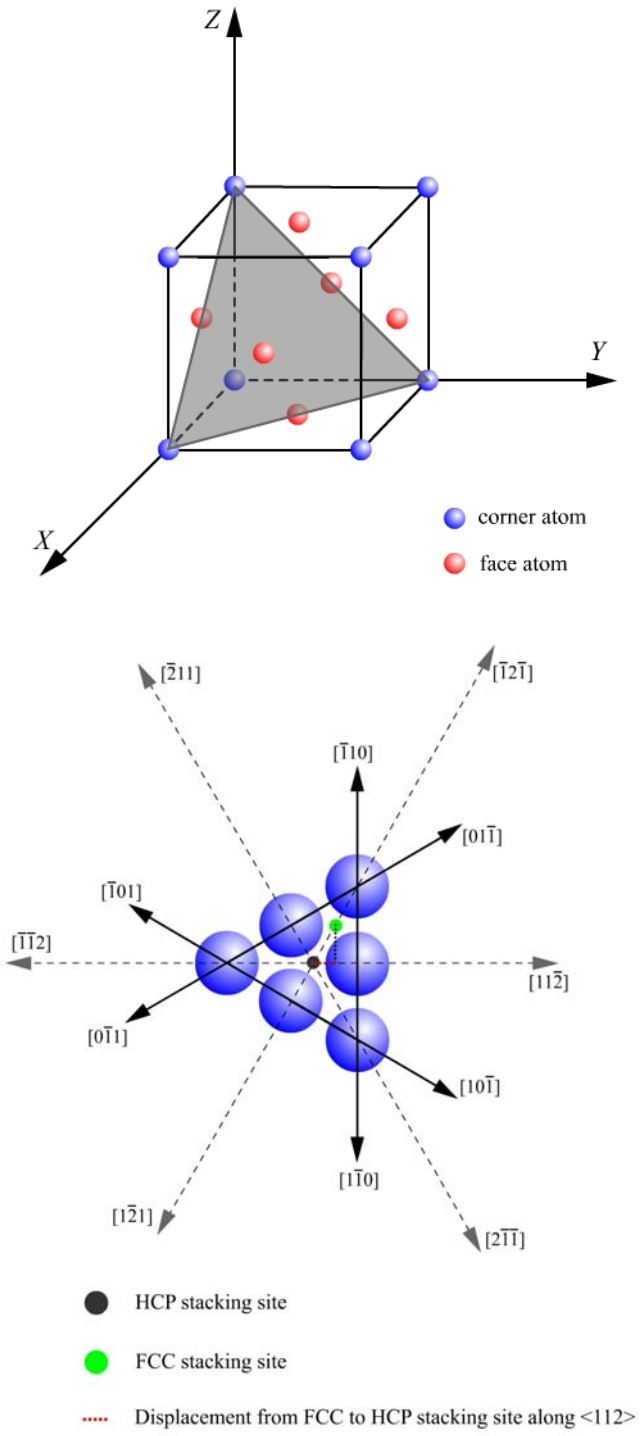

Fig. 2.1 (a): Bulk lattice structure of a FCC metal, the (111) plane is shown by the grey coloured plane. (b): Crystalline axles of (111) plane, green circle and black circles mark the FCC and HCP stacking sites, respectively. The lateral displacement from a FCC site to a HCP site along the [11-2] direction is shown by red dash line. The displacement is equal to $\sqrt{3}/6a$ (a is the atomic constant in the (111) plane).

also supports the domain structure that FCC region and HCP region coexist in the same unit cell.

Besides high resolution TEM [4, 5], Helium atom scattering (HAS) [6] experiments also confirm the 4.55% contraction along the <110> directions and the (22 × √3) superlattice unit cell, with new implications arising from their observation: (1) Due to the splitting of the <112> diffraction spots in the <110> direction, there should be a region of shear on the surface lattice structure. (2) As the HAS diffraction pattern presents threefold symmetry, considering the assumption of three 120° rotational domain structures from LEED work [1, 2], there is no rotational symmetry in each single domain. (3) Besides the contraction along the <110> direction, another ~2% isotropic contraction is found. And this contraction is rooted into at least the second layer because no superlattice structure related to this contraction is shown in the diffraction pattern.

So far, the Au (111) surface, as examined by different experimental methods, shows contraction. As surface atoms have reduced bonding coordination number than bulk atoms, they tend to reduce their atomic spacing. Thus the surface contraction is a natural result. On the other hand, considering the continuity of the bulk atomic lattice, the bulk atoms want to keep the surface atoms in the original FCC hollow sites. The competition between these two potentials determines the final surface atomic structure. The Frenkel-Kontorova model describes the competing interactions rather well [7]. In this model, intralayer interaction within top-most layer is considered as springs connecting nearest neighbor atoms. And the top-most layer sits on a substrate

potential which describes the effects of the bulk. F. C. Frank and H. van der Merwe [8] calculated the ground state of this model, and one of the solutions is a lattice of regularly spaced solitonlike misfit dislocations which separate commensurate regions.

An improved model of the Au (111) surface atomic lattice was given, based on the solitonlike misfit structure. As shown in Fig. 2.2, in a (22 × √3) unit cell, due to the contraction along the <110> direction, 23 atoms occupy 22 bulk lattice positions. There are three commensuration regions in each unit cell separated by two transition (discommensuration) regions. The commensuration regions are marked as C (refer to ABC stacking, FCC-type) and A (ABA stacking, HCP-type). In both of the two kinds of commensuration regions, surface atoms sit in the FCC hollow sites (bulk sites). In the transition regions, surface atoms sit on the bridge sites of second layer atoms and gradually transfer the stacking from ABC (FCC-type) to ABA (HCP-type). A soliton expression is used to describe the shift in the transition region, the lateral shift of an atom is dependent on its position x along the <110> direction [9]:

$$f(x) = (2/\pi)\arctan[\exp(x/\Delta S)]$$

where twice of ΔS is the full width at half maximum (FWHM or so-called half-width) of a soliton centered at the boundary between ABC and ABA stacking regions. In this model, the surface atoms in the transition region are raised vertically to the surface plane, their height H is described by a Gaussian corrugation, which centers at the ABC/ABA stacking boundary and has its half-width equal to the soliton width (see upper part of Fig. 2.2). By fitting this model into their HAS experimental data, U. Harten *et al*. [6] suggested that the half-width ($2\Delta S$) is equal to 11.8 Å. And the height

of transition region atoms is 0.15 Å, which agrees with the difference between atoms sitting in the hollow site and the bridge site under hard-sphere model. At last, a ratio R, equal to 0.7, between the sizes of ABC and ABA region is given to match the model with the He-scattering data. However, this ratio cannot be deduced from the Frenkel-Kontorova model with the sine-Gordon substrate potential as they used. Later, M. El-Batanouny *et al*. [10] introduced a double-sine-Gordon (DSG) substrate potential to the Frenkel-Kontorova model and successfully predicted the different regional sizes, which is consistent with the experimental observation in He-scattering.

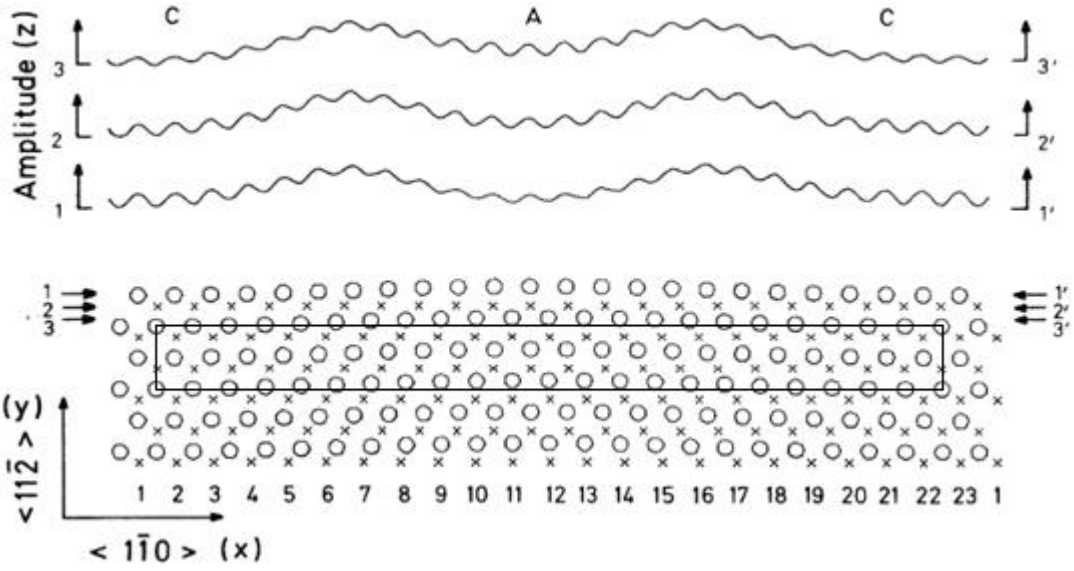

Fig. 2.2 (from [6]): Lower part: atomic structure of the proposed model, circles refer to surface layer atoms and crosses refer to second layer atoms. In commensuration regions (marked C or A for ABC and ABA stacking, respectively), surface atoms occupy hollow sites, and in transition regions (discommensuration), surface atoms take bridge sites. A (22 × √3) unit cell is marked with a rectangle. The displacement of atoms from the longer edge of unit cell is clear. Upper part: profile of corrugation in the *z*-direction for three sections (marked 1, 2 and 3). The amplitude is enhanced for clarity.

They confirmed the height of transition corrugation to be 0.15 Å. And the addition 2% isotropic contraction found in Harten, *et al*.'s model [6] was justified to be uniaxial along the <112> direction. Furthermore, this DSG model mentioned the ABC stacking region is more energetically favored than the ABA stacking as the former is the continuation of the bulk lattice.

Both U. Harten, *et al*. [6] and M. El-Batanouny, *et al*. [10], used a 1-Dimensional Frenkel-Kontorova model in the <110> direction to describe the surface reconstruction. The theoretical model of reconstruction of the Au (111) surface is improved by N. Takeuchi *et al* [11], who introduced a more realistic two-dimensional substrate potential based on their first principle calculation. The calculation reveals that if occupying an HCP site, each surface is only 1 mRy higher in energy than occupying an FCC site. This small difference in energy makes it possible for the coexistence of FCC and HCP stacking on the same surface. For atoms to occupy the bridge site and the top site, the energy is higher than FCC site by 3 mRy and 14 mRy, respectively. A contour plot of the potential energy for different occupation sites is given in Fig. 2.3. From the potential map, the contraction along the <110> direction is energetically favored because of the small difference in energy between FCC, HCP and bridge site. The surface atoms would find it easier to transfer stacking mode from FCC to HCP via bridge and all mediate sites along the <110> direction, which can be regarded as a low-energy "channel", indicated by the red line in Fig. 2.3(a). On the other hand, surface contraction along the <112> direction will not be favorable, because in that case, surface atoms need to occupy high energy top sites (The 2%

contraction in <112> direction found in Harten and El-Batanouny's model roots into several bulk layer [6, 10]). A sketch of the surface atomic arrangement from the 2D Frenkel-Kontorova model is presented in Fig. 2.3(b), which is similar to the model in Fig. 2.2. However, differences still exists. In this improved model, the contraction is rather uniform along the length of a unit cell than concentrated in two transition regions as indicated in the previous model. This point is supported by S. Narasimhan and D. Vanderbilt [12] in their molecular-dynamics simulation on the equilibrium configuration of Au (111) surface's reconstruction, which is performed based on the 2D Frenkel-Kontorova model. They also obtained an equilibrium bonding length for the surface atom, which is 2.7744 Å, as well as a spring constant for the bonds equal to 90 mRy/Å^2.

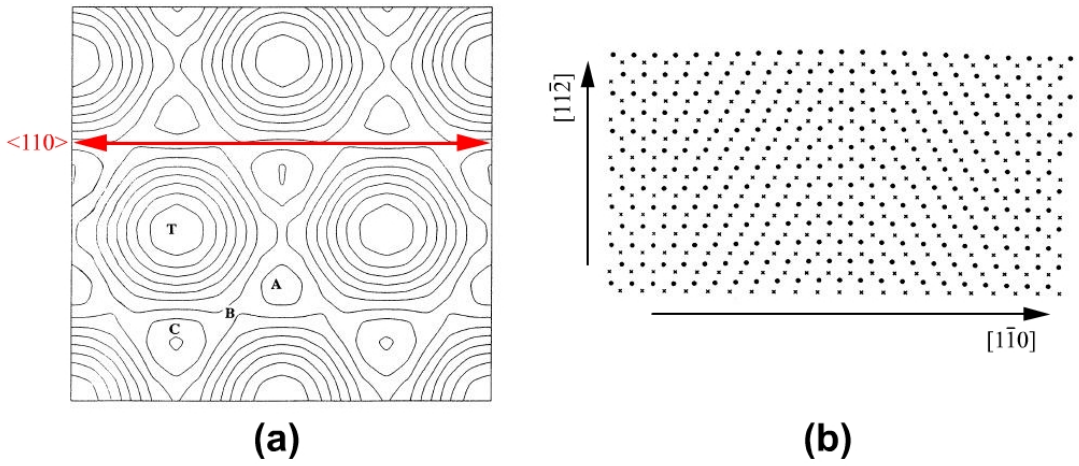

Fig. 2.3 (from [11]) (a): A contour plot of the potential energy for different occupation sites. FCC, HCP, bridge and top site are marked by C, A, B and T, respectively. The red line indicates the low-energy channel along the <110> direction. (b): The atomic arrangement deduced from 2D Frenkel-Kontorova model.

Another detail in the surface atomic lattice needs to be mentioned. Due to the stacking shifts from ABC to ABA, for an atomic row running along the <110> direction, there is a displacement in the <112> direction (perpendicular to the <110>) due to the different positions of FCC and HCP sites, indicated in Fig. 2.1(b), and the displacement should be equal to $\sqrt{3}/6a$ (0.83 Å) according to hard-sphere model (0.83 Å). This displacement can also be identified in lower Fig. 2.2 by the straight edge of unit cell. This feature is directly observed in STM image, see Fig. 2.4.

When STM was introduced to the study of the Au (111) surface, real-space imaging with atomic resolution verify the above model and provide more information about the surface structure [13, 14]. In STM images, the Au (111) surface always presents large terraces separated by monoatomic steps. A single terrace can extend to as wide as hundreds nanometers. On the terraces, regular patterned pair-wise bright stripes running in the <112> direction. These stripes present a period of 63 Å from pair to pair, and within a pair, the two stripes are separated by 22 Å. The period of 63 Å matches perfectly with the length of a ($22 \times \sqrt{3}$) unit cell and the period of the "finger" structure observed by TEM [4, 5], indicating that they are formed by the corrugations in the transition regions in each unit cell. Fig. 2.4 is an atomic resolution image, where each sphere represents a gold atom, and the center to center distance of spheres is distributed within 2.7 to 2.9 Å, this value is consistent with the theoretical simulation result of 2.7744 Å presented above [12]. A ($22 \times \sqrt{3}$) unit cell is marked by a blue rectangle. The assumption of 23 surface atoms being contracted by 4.55% to settle into 22 bulk atom sites is proved by counting the number of atoms in each

period along the [1-10] direction. The lateral displacement of surface atoms perpendicular to the contraction direction is also directly observed. The displacement was measured to be 0.9 Å, equivalent to the $\sqrt{3}/6a$ (0.83 Å) expected from the model in Fig. 2.1(b).

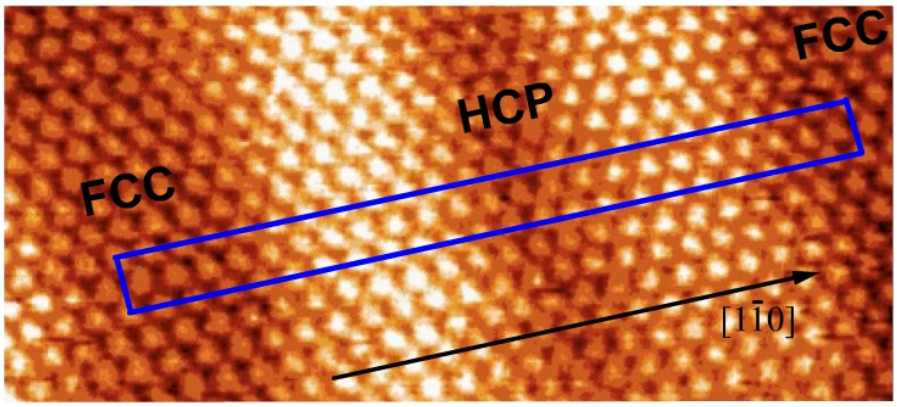

Fig. 2.4: A (22 × √3) unit cell of the Au (111) surface is marked by a blue rectangle. The [1-10] direction of the surface is indicated by the black arrow. The FCC and HCP regions separated by corrugation ridges are also marked.

J. V. Barth et al. measured the spacing between adjacent atoms along the <110> direction in several unit cells and tried to give a statistic information about in which position does the contraction take place [14]. Their result is given in a plot where the atom-atom distance is seen to oscillate as a function of lateral position along the <110> direction, Fig. 2.5. According to this diagram, the atomic lattice shows a trend to shrink in commensuration regions (FCC and HCP) rather than in transition regions. This result is different from either the model suggesting localized contraction in transition regions [6] or the model suggesting uniform contraction [11, 12]. However,

due to the limit of accuracy, the authors did not regard the information in Fig. 2.5 as conclusive. Nevertheless, as measured in my own STM images, distribution of atom-atom spacing is completely random. The corrugation height in the transition is apparently ~0.15 Å in STM images, found in previous studies [13, 14] and from my own STM experiments. Though this value varies a bit according to different scanning conditions, it fits well with the model, in which the atoms occupying the hollow site and the bridge site show a difference in height about 0.15 Å.

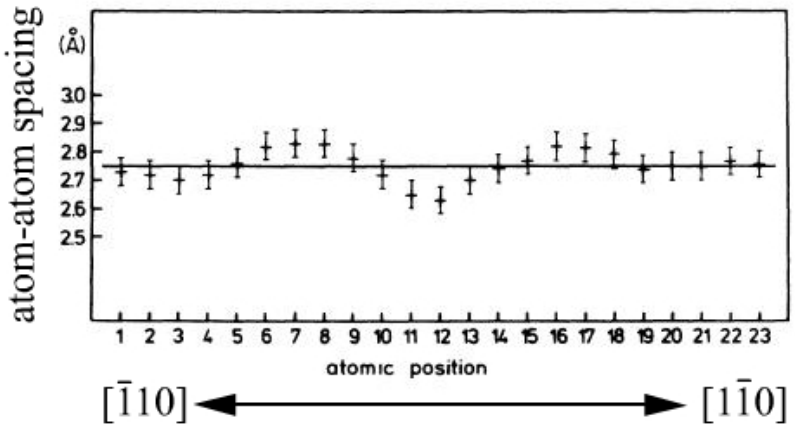

Fig. 2.5 (from [14]): The spacing between adjacent atoms in a row in the <110> direction is plotted as a function of its position in a unit cell. The average spacing is ~2.75 Å as shown by the straight line. The contraction seems to take place at commensuration regions rather than transition regions.

As mentioned above, a regular pattern of pairwise stripes is a distinct character of Au (111) in STM images. These stripes will be called discommensuration lines (DLs) in this thesis, because they are formed by the connection of corrugations at discommensurational transition regions. Thus the DLs run in the <112> direction,

which is perpendicular to the unit cell's contraction direction. Referring to the model raised by He-scattering experiment [6], the region between a DL pair is ABA stacking (HCP region), and the region separate DL pairs is ABC stacking (FCC region). These two have a width of 22 Å and 44 Å, respectively, as measured in STM images. In STM images from a large area of the Au (111) surface, the DLs are found to bend systematically by 120° with a period around 250 Å, see Fig. 2.6(a). The zigzag pattern of DLs is widely known as the "herringbone" pattern of reconstructed Au (111) surface. Because the Au (111) surface consists of three equivalent <110> directions differ by 120° rotationally to each other, the periodic bending of DLs indicates that the Au (111) surface is tessellated by alternating 120°-rotated domains. In each domain, there is a uniaxial contraction along the <110> direction. X-ray diffraction studies on reconstructed Au (111) surface also reveal the same type of alternating equivalent domains [15]. Furthermore, fine details of X-ray diffraction pattern show that at each domain boundaries, there is equal density of kinks, which corresponds to an important atomic structure confirmed by STM observation. We save this point for later discussion.

Fig. 2.6(a) presents a typical topography of reconstructed Au (111) surface. By taking a close observation at the bending sites, rich details of the atomic structure can be found. The pairwise DLs do not bend parallel, instead, every other DL will point out to the adjacent commensuration region, as shown in Fig. 2.7(a). By the structural differences around bending site (or called elbow site), the DLs can be separated into two kinds: the type x DLs have pointed elbows while the type y DLs have rounded

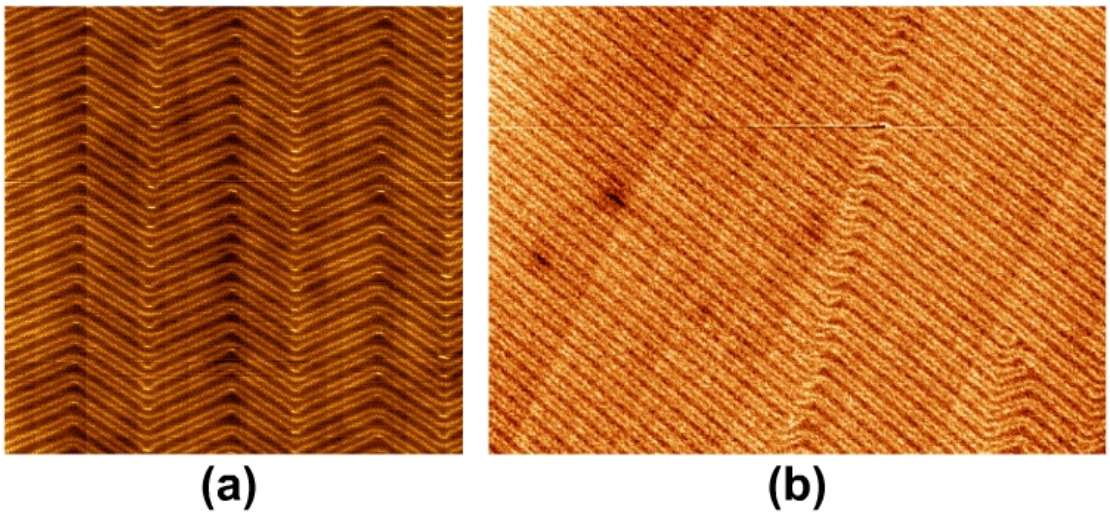

Fig. 2.6 (a): 150 × 150 nm, V = -1.2 V, I = 1.0 nA. The Au (111) surface with regularly bended DLs. (b): 245 × 177 nm, V = -0.9 V, I = 0.03 nA. The Au (111) surface with straight DLs. The density of DL elbow site is very low.

elbows [16]. Besides the different shapes at the elbow site, type x and type y DLs have another structural difference: The DLs can be regarded as a series of dislocation segment including surface bridge-site atoms. Considering in each segment plane, because the surface atoms drift from the hollow sites to bridge sites, there is a Burgers vector pointing perpendicularly to the segment plane. At the left and right sides of an elbow, atoms in type x DLs take the bridge-site with different orientations, as indicated in Fig 2.7(c) by blue bars, thus the Burgers vectors corresponding to these segments will have different pointing directions, indicated by blue arrows. At the same time, atoms in type y DLs always take bridge-sites with the same orientation and the Burgers vectors have the same pointing direction on both side of elbow, indicated by green bars and arrows in Fig. 2.7(c), respectively. Due to this difference, the type y DLs can run smooth from one domain to another and have a rounded shape,

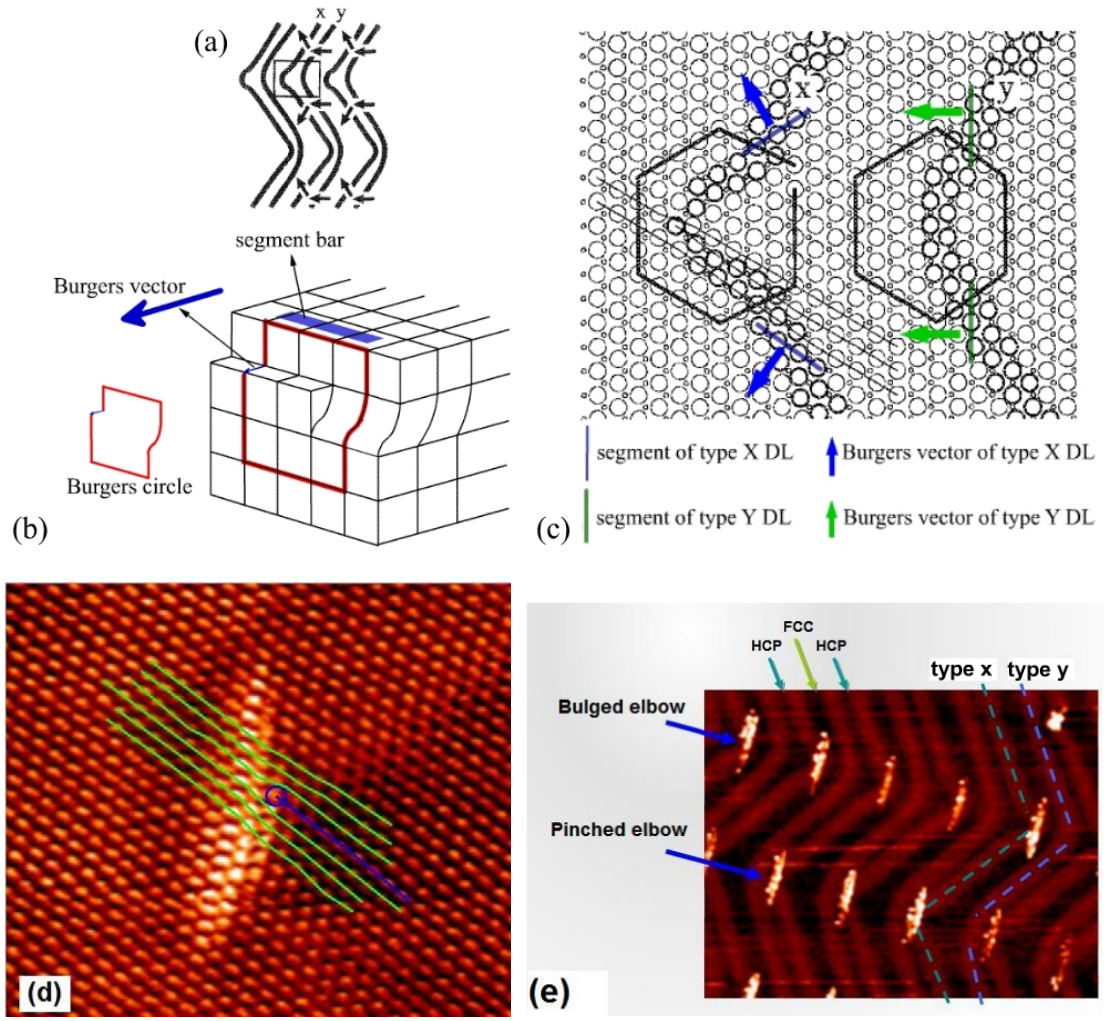

Fig. 2.7 (a): A sketch image of the type x and type y discommensuration lines (DLs). The Burgers vectors of the segments of the DLs are indicated by arrows. (b): A sketch image showing the Burgers vector of a dislocation segment, which is caused by the atomic drift from hollow-site to bridge-site. The blue segment bar is drawn on top of a segment to indicate its orientation. The segment bar is also used in (c). (c): A sketch image of the possible atomic lattice around the elbows, blue bars indicate the different orientations of the segments in type x DLs, while green bars indicate the ones of type y's. We can see type x DLs have their Burgers vector pointing different directions on the left and right of an elbow, in contrast, type y DLs have same Burgers vectors. An extra row of atom is introduced in type x elbows, indicated by the fine lines in (c), while type y elbows do not have such an edge dislocation. (d): An atomic resolution STM image (V = -0.002 V, I = 12 nA) of a type y elbow, by linking the atoms in the same rows, the extra row of atom is clearly seen, which starts at the atom in blue circle. (e): This STM image (V = -0.02 V, I = 12 nA) defines the names of different structures in herringbone pattern.

of which the Burgers circle is closed in Fig. 2.7(c). In contrast, type x DLs have an open Burgers circle because of the meeting of two differently orientating Burgers vectors. The open Burgers circle suggests an extra row of atoms at the type x elbow, which is indicated by the fine lines in Fig. 2.7(c) [17]. Our atomic resolution STM image from the elbow area confirms the existence of the extra row of atoms, Fig. 2.7(d). So, along a domain boundary, there is an extra row of atoms every other DL, this feature is consistent with the equilibrium density of kinks found at each domain boundaries by X-ray experiment introduced above [15].

Looking at Fig. 2.7(d), if all the type x DLs point to FCC (HCP) regions along a domain boundary, then, at the next domain boundary, they would point to HCP (FCC) regions. When a type x DL points to an FCC region, this kind of elbow is named a bulged elbow, otherwise, if it points to an HCP region, it will be called a pinched elbow. In this manner, a herringbone pattern will presents alternating rows of bulged and pinched elbows. These terms will be used in the following sections.

As indicated by the existence of edge dislocations (the extra row of atoms) at domain walls, the formation of domain walls is not energetically favored, because it disrupts the ($22 \times \sqrt{3}$) unit cell. On the other hand, the formation of a long-range ordered structure with herringbone pattern needs a potential that can act at the length scale comparable to its period. These two questions are solved by introducing the long-range elastic interaction to the surface model of Au (111) [12]. The long-range elastic interaction will be introduced by the formation of “elastic-stress domains” on the surface, which requires the surface consisting of different reconstructed phases

and exhibiting an anisotropic stress [18]. The Au (111) surface perfectly fulfills these two conditions. Firstly, the Au (111) surface has three equivalent <110> directions, so it can host three phases of (22 × √3) contraction. Secondly, the contraction in a single domain is uniaxial and can only relieve the tensile stress along the <110> direction. The tensile stress in the orthogonal direction remains, so there is still an overall anisotropic stress on the surface. In this manner, elastic-stress domains will be formed on the Au (111) surface, and the periodically alternating (22 × √3) domains are clearly the consequence. By forming different orientated uniaxial domains on the surface, the anisotropic stress of the surface can be relieved. However, although the formation of periodic domain structure can relieve anisotropic stress and gain elastic relaxation energy, the spontaneous formation of domain boundaries will cost energy to break the (22 × √3) contraction in their neighborhoods, as mentioned above. Therefore, the periodic length of domains (or the frequency of DLs bending) depends on the balance between the elastic relaxation energy and domain wall energy. Narasimhan and Vanderbilt [12] calculated the equilibrium periodic length using the 2D Frenkel-Kontorova model and gave a range from 140 Å to 980 Å. This range is consistent with observations from different research groups. Most experimentally reported periodic lengths are between 120 Å to 250 Å [13, 14, 16 and 17]. However, larger periodic lengths are possible, as shown in Fig. 2.6(b). The periodic length is believed to depend on the local elastic stress environment.

As a conclusion, the Au (111) surface presents a complex herringbone pattern, which is the result of a (22 × √3) reconstruction as well as a long-range periodicity

due to the surface strain domains.

2.1.2 Steps on the Au (111) Surface and Vicinal Au (111) Surfaces

On Au (111), herringbone reconstruction is formed to relieve the surface strain. So the presence of monoatomic steps across Au (111) terraces will obviously influence the local strain and bring changes to the reconstruction pattern. Thus the change of local atomic structure as a consequence of the interaction between steps and reconstruction is an interesting and important part of the Au (111) morphology.

Two kinds of close-packed monoatomic step can be identified on Au (111) surface by the different kinds of microfacet they formed. The one descending along the [-211] azimuth (or the equivalent [11-2] or [1-21] azimuths) presents a {111} microfacet, and this kind of step may be called B step in the discussions of the following sections. Otherwise, if the step is ascending along the [-211] azimuth, it will present a {100} microfacet, and be called an A step. This difference of microfacet of steps is shown in Fig. 2.8(a), from [19]. Within a hexagonal close-packed island on Au (111) surface, the two adjacent steps with a 120° rotational relation will be one {111} and one {100}. Moreover, the opposite steps of a hexagonal close-packed island will be with different kinds of facet, as one of them is descending while the other ascending along a same azimuth. Besides the structural difference, the two kinds of steps are found to have different step energies [20]. The step energy of {111} facet steps is lower than that of {100} facet steps, which can be easily understood as the atomic density is higher in a {111} facet step.

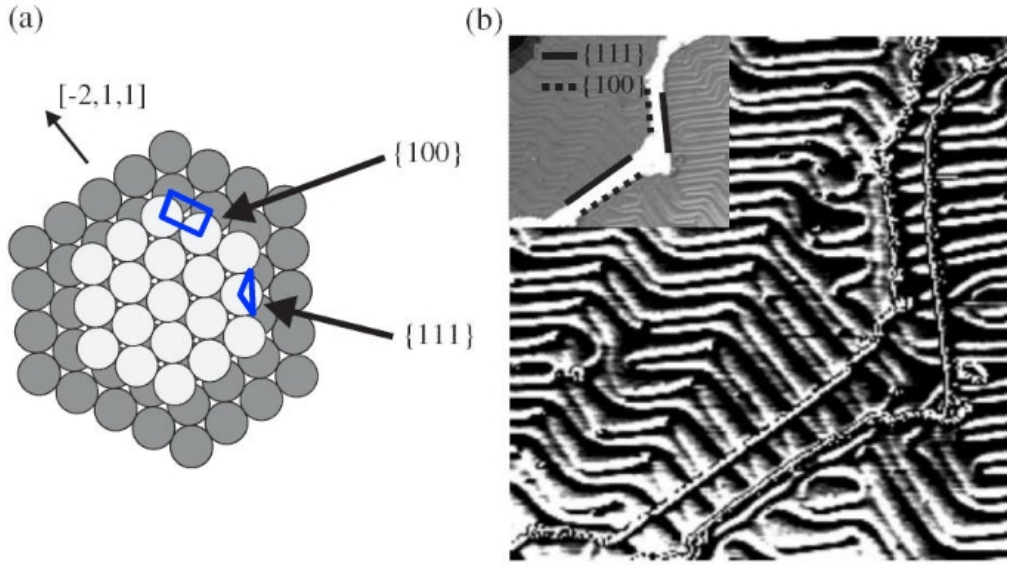

Fig. 2.8 (from [19]) (a): Sketch image of the two kinds of steps on Au (111), one with {100} microfacet and the other one with {111} microfacet. (b): An STM image presenting four terraces, which can be easily identified by different contrasts in the insert. There is a long-narrow plateau lies across the image, the two different kinds of steps are marked by solid line (for {111} type step) and dashed line (for {100} type step). The different interaction with herringbone reconstruction of the two kinds of steps is obvious.

The different structures of the two kinds of steps also influence the herringbone reconstruction in their vicinity. Fig. 2.8(b) presents an STM image of Au (111). A long-narrow plateau runs across a large terrace from the lower-left to the upper-right of the image. As introduced above, the opposite steps of the plateau have different facets. Furthermore, due to the 120° rotation of the plateau, the {111} and {100} type of steps change sides in the two segments of the plateau, as shown in the inset of Fig. 2.8(b). From this image, at a {111} step, the discommensuration lines (DLs) of the herringbone reconstruction can run across from the lower terrace to the upper terrace. However, slightly change of DLs can be observed on the lower terrace near the step.

The FCC stacking regions (wider regions) expand while the HCP stacking regions (narrower regions) shrink. Because the gold layer under the plateau is unreconstructed with FCC stacking, the reconstruction on the lower terrace needs to change to FCC stacking in front of the step, resulting in the expansion of FCC regions. The situation at the {100} step is quite different. The DLs do not run across the step. Instead, the DLs form U-shaped ends to seal FCC regions on the lower terrace of a {100} step. Between these U-shaped ends and the step, there is a DL running parallel to the step. Again, this arrangement of DLs can provide an FCC region to adjoin the FCC layer under the plateau. On the upper terrace of a {100} type step, the DLs remain unchanged until the last row of atoms. Noticeable, due to the stacking fault of the reconstruction, a {100} type step will change to a more energetically favored {111} type step at the HCP segments. After all, these different morphologies of DLs on {111} and {100} type steps are perfectly reversed when the plateau rotates by 120°, consistent with the switch of step types. Similar effects of monoatomic steps on herringbone pattern are observed in the STM images from J. V. Barth, *et al*. [14].

By presenting small misorientation angles with respect to the Au (111) surface, there are a series of vicinal surfaces of Au (111), which consist of periodic succession of monoatomic steps separated by narrow Au (111) terraces. For all the vicinal Au (111) surfaces, with steps parallel to the close-packed <011> direction (or other two equivalent close-pack directions), the misorientation can take place in two opposite azimuths. As shown in Fig. 2.9, for vicinal surfaces descending along [-211], they present {111} microfacet steps. Au (223), Au (577), Au (455), Au (788) and Au (11 12

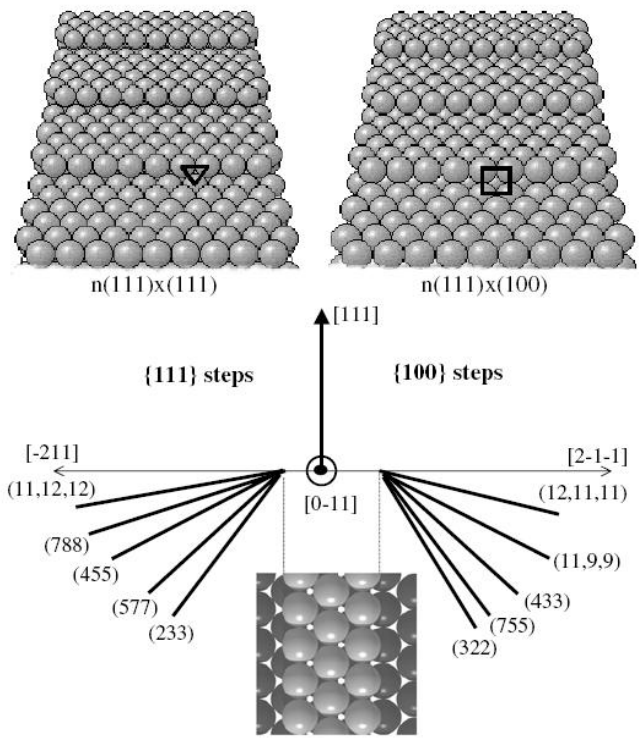

Fig. 2.9 (from [19]): A schematic diagram of vicinal Au (111) surfaces. The ones descending along [-211] have {111} type steps and the ones descending along [2-1-1] have {100} type steps. Different structures of these two kinds of steps are shown above for Au (233) (left) and Au (322) (right), respectively.

	θ (deg)	n	W (nm)
Au(12, 11, 11)	2.38	23	5.7
Au(11, 9, 9)	5.57	10	2.4
Au(433)	8.05	7	1.7
Au(755)	9.45	6	1.4
Au(322)	11.4	5	1.2
	{100}		

	θ (deg)	n	W (nm)
Au(11, 12, 12)	2.27	24	5.83
Au(788)	3.51	16	3.83
Au(455)	5.76	10	2.33
Au(577)	8.47	7	1.58
Au(233)	10.0	6	1.33
	{111}		

Table 2.1 (from [19]): the nominal angles of misorientation θ, number of atomic rows in each terrace n and terrace widths W for vicinal Au (111) surfaces.

12) are in this catagory. Otherwise, for vicinal surfaces descending along [2-1-1], there are Au (322), Au (755), Au (433), Au (11 9 9) and Au (12 11 11), which present {100} microfacets. The misorientation angles θ, number of atomic rows in each

terrace *n* and terrace widths *W* are given in Table 1, from [19].

The interaction between the herringbone reconstruction and the periodic steps of vicinal Au (111) surface is of great interests. For those vicinal surfaces present {111} type steps, take Au (788) for instance, the DLs run perpendicular across the steps, see Fig. 2.10(a). A closer observation in Fig. 2.10(b) reveals that the DLs are slightly rotated to form a V shape. The FCC region near the low edge of a step expands a bit, which is consistent with the situation described above, as it needs to adjoin to the FCC stacking layer underneath the upper terrace of the step.

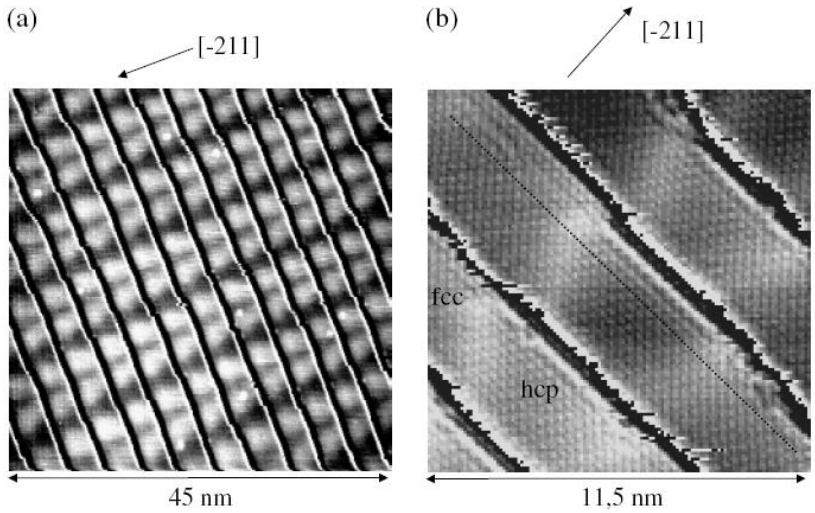

Fig. 2.10 (from [19]): STM images of Au (788) surface, which consists of {111} type steps. (a): On large scale, the DLs run perpendicular through the steps. (b): Atomic resolution image, the DLs are found to perform V-shape, with FCC region expands toward the lower edge of previous step in order to adjoin the FCC stacking layer under the step.

The vicinal Au (111) surfaces with {100} type steps are less stable and tend to facet, resulting in terraces with different widths. As shown in Fig. 2.11, three successions of terraces with different widths are observed for Au (12 11 11). For the

narrow terraces in (a), there is a single DL run parallel with the step in each terrace, which perfectly reduce the step energy by providing an FCC stacking region towards the lower edge of previous step as well as an HCP stacking toward the upper edge of next step, which changes the step into a {111} type. For wider terraces in (b), it presents a typical herringbone pattern of {100} type step. And in another situation in (c), the DLs form an unusual triangular pattern. This pattern together with the formation of super-kinks along the step edge, ensure the largest FCC segment to be provided towards the lower edge of previous step and largest HCP segment towards the upper edge of next step, which are both in order to reduce the step energies by the greatest extent.

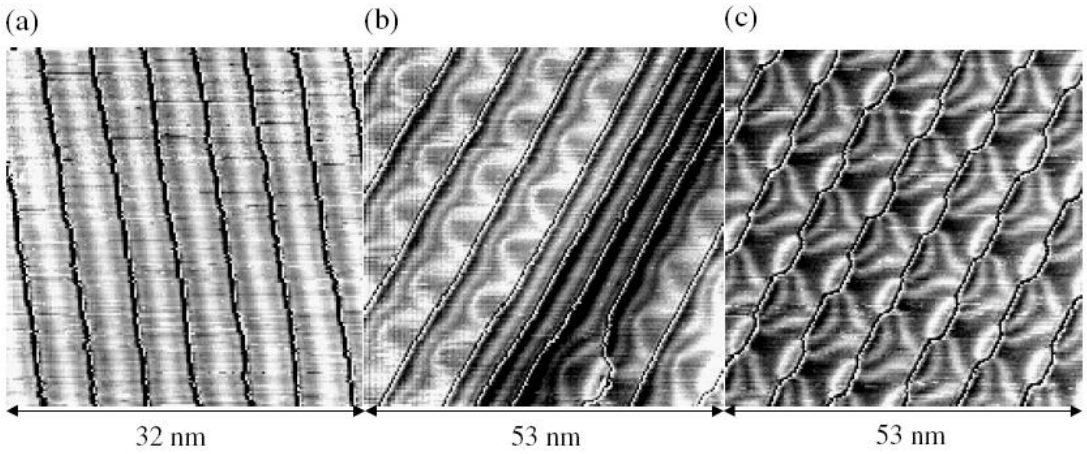

Fig. 2.11 (from [19]): STM images of Au (12 11 11) surface, which consists of {100} type steps. Due to the faceting, this vicinal surface presents terraces with various widths. (a): on terraces with small width, one DL runs parallel with the step. (b): On wider terraces, a typical reconstruction pattern of {100} type steps is seen. The situation of terrace with single parallel DL is also seen in the narrow terraces in this image. (c): Another situation for wide terraces, the DLs form a triangular shape pattern. The steps are also faceted to form kinks. All these structural changes are collaborative and in order to reduce the step energies.

As a conclusion, the monoatomic steps have strong interaction with the herringbone reconstruction. All structural changes follow the principle to reduce step energies.

2.1.3 Electronic Structure of Au (111)

At close-packed noble metal surface, surface electrons behavior as 2D nearly free electron gas and occupy Shockley-type surface states, which are confined in the vicinity of the surface by the vacuum barrier and projected band gap of bulk states. In Kevan and Gaylord's angle resolved photoemission (ARPES) experiment [21], a Shockley-type surface state of Au (111) localized in the *sp*-band gap of projected bulk state is observed, over a board range of photon energy, as marked S_1 in Fig. 2.12. This *sp* surface state has a binding energy of 410 ± 10 meV. Another peak S_2 can be observed at the binding energy of 780 ± 100 meV, where is near the projected *sd*-band gap. However, whether it is an intrinsic surface state is uncertain.

Fig. 2.12(b) presents the energy distribution curves of the *sp* surface state measured at different emission angles, to both the left and right of the surface normal. A parabolic dispersion of the surface state peak in these curves, which is symmetric about the normal, is clearly seen. According to the experimental measurements shown in Fig. 2.12(b), a dispersion relation is given in Fig. 2.12(c), of which also presents a parabolic shape and has its highest binding energy E_0 equal to 408 ± 10 meV at the center of the surface Brillouin zone Γ. The effective mass m_s of derived from these dispersion relations is equal to 0.284 ± 0.003 m_e, of which m_e is the free electron mass.

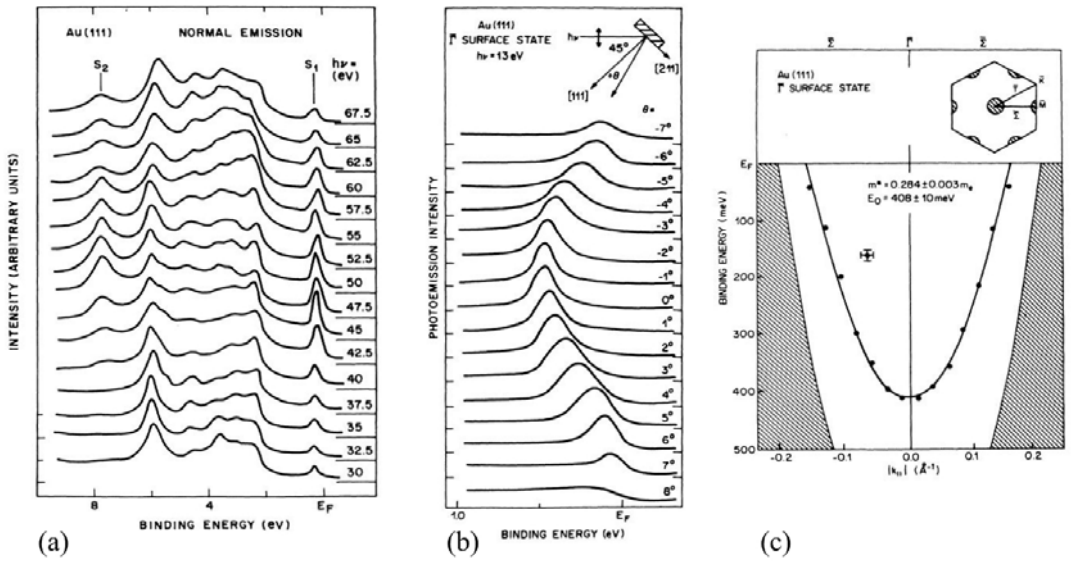

Fig. 2.12 (from [21]) (a): The energy distribution curves taken with different photon energy as a function of binding energy. The peak S_1 corresponds to the *sp* surface state, which locates 0.41 ± 0.01 eV below the Fermi energy. (b): The energy distribution curves of the *sp* surface state taken with different emission angles, the highest binding energy is reached at 0º (0 $Å^{-1}$), and a parabolic shape of the dispersion is obvious. (c): The dispersion relation converted from (b). Surface Brillouin zone is shown up-right.

By knowing E_0 and m_e, the Fermi wave vector k_F for the parabolic surface state dispersion relation is derived to be 0.173 $Å^{-1}$.

S. LaShell *et al*. repeated the ARPES experiment on Au (111) but with an improved angular resolution [22]. Their result is presented in Fig. 2.13. By comparing Fig. 2.13 with Fig. 2.12(b), the binding energy of *sp* surface state at 0º (0 $Å^{-1}$) is consistent at ~410 meV and the surface state peaks show parabolic dispersion relations in both cases. However, as the *k* value increases, the peak splits in to a doublet structure. This split is interpreted as a result of spin-orbit coupling (SOC),

which breaks the spin degeneracy in surface state levels and allows opposite spin to have different energies. The split structure is hidden in previous studies because of poor angular resolution and possibly questionable surface quality.

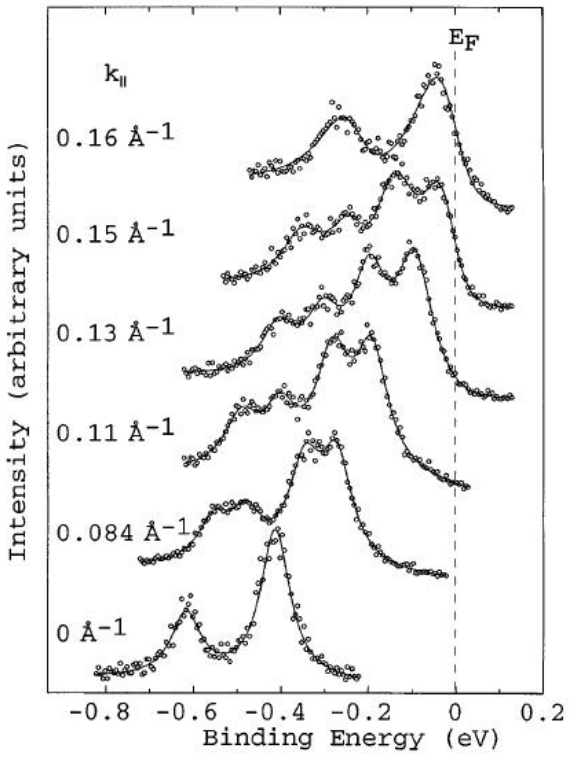

Fig. 2.13 (from [22]): Energy distribution curves taken along the Γ-M line as a function of parallel monenta. At 0 $Å^{-1}$, the peak of *sp* surface state is located at a binding energy ~410 meV (the peak ~200 meV higher is from the Ar satellite). The *sp* surface state peak splits into two as the parallel monenta increases, which is due to spin orbit coupling.

Theoretical calculation also reveals this *sp* surface state. Fig. 2.14 shows the result from N. Takeuchi *et al*. [11]. They simulated the three different situations with Au top layer atoms occupying FCC, HCP and bridge site, respectively. In fact, the results from all the three are quite similar with each other, and the band structure for FCC stacking is shown in Fig. 2.14. In this image, the bulk band structure is projected

for Au (111) surface and shown as grey shade, and the surface state dispersion relation curve is found near the Fermi level, lies in a gap of projected bulk states and marked by A. In the inset of Fig. 2.14, the theoretic result is compared with ARPES experimental results (marked by crosses) from [21]. These two results bear great resemblance with each other, both have symmetric parabolic shape and the highest binding energy of ~410 meV.

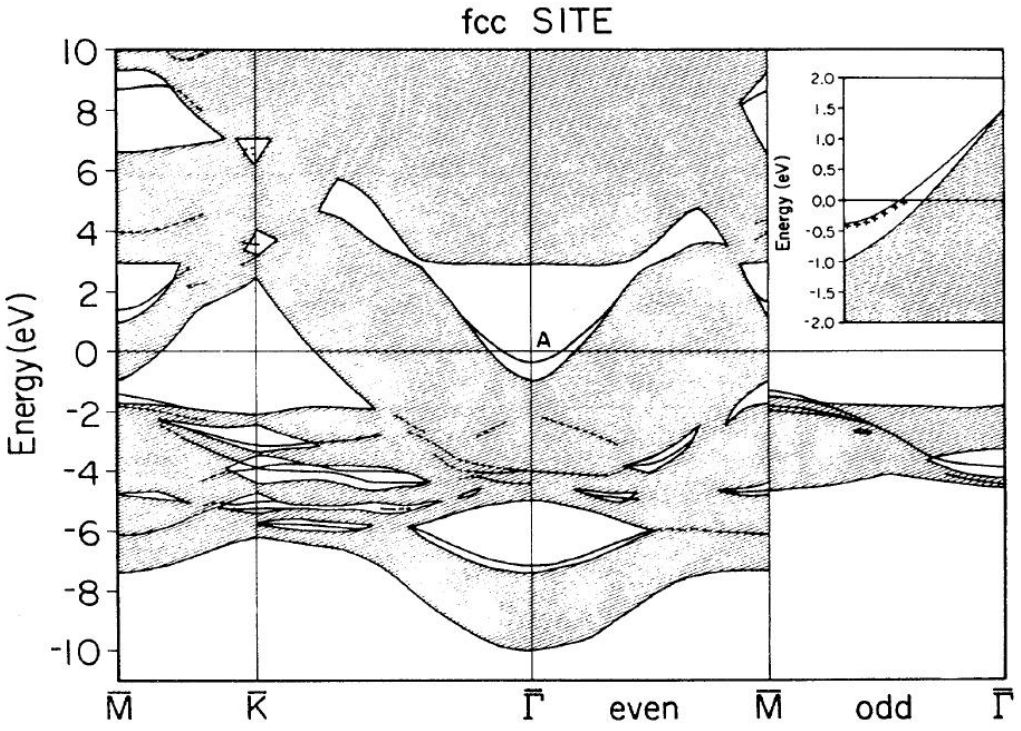

Fig. 2.14 (from [11]): Theoretically simulated band structure of Au (111) surface with FCC stacking first layer atoms. The sp surface state is marked A in a gap of projected bulk band. The inset is a zoom-in image to show the surface state dispersion curve, compared with the result from ARPES experiment (crosses). The theoretic result is consistent with the experimental result.

When STM was introduced to the investigation of the Au (111) surface, besides giving real space image of the atomic structure, it also provides the information about

the local density of electronic states (LDOS). The conductance (*dI/dV*) recorded in STS mode is proportional to the LDOS of a very localized area under the tip. Such experiment had been done by M. P. Everson *et al*. [23], and their *dI/dV* traces as a function of bias voltage is presented in Fig. 2.15. As shown, there is a peak located at ~400 mV, which corresponds to the *sp* surface state with a binding energy of ~410 meV found in ARPES experiments [21, 22]. The surface structures on the Au (111) surface seen to have effects on the LDOS. The presence of a monoatomic step on Au (111) terrace will change the local barrier potential, and introduce a decrease of LDOS as shown by the dashed line in Fig. 2.15, of which the intensity of *dI/dV* peak near 400 mV is suppressed. The compressed ($22 \times \sqrt{3}$) unit cell also influence the LDOS, as the *dI/dV* map taken with bias voltage of -300 mV displays bright-dark stripes feature, Fig. 4(b). By comparing it with topographic image of the same area, they found that the FCC stacking regions have lower LDOS than the HCP regions, which cause the contrast difference in the *dI/dV* map. General, the effect on LDOS from the reconstruction of Au (111) is found to be much smaller than that from the monoatomic steps.

In order to explain the decrease of LDOS at step edges, a first-principle calculation was performed to simulate the conductance versus bias voltage traces [24]. The authors developed a model considering the electrons in the Au (111) surface as 2D nearly-free electron gas, which will be scattered at the line potential of a step edge. The reflection coefficient R and transmission coefficient T for electron wave impinging a step are involved in the simulation of *dI/dV* trace. By fitting the

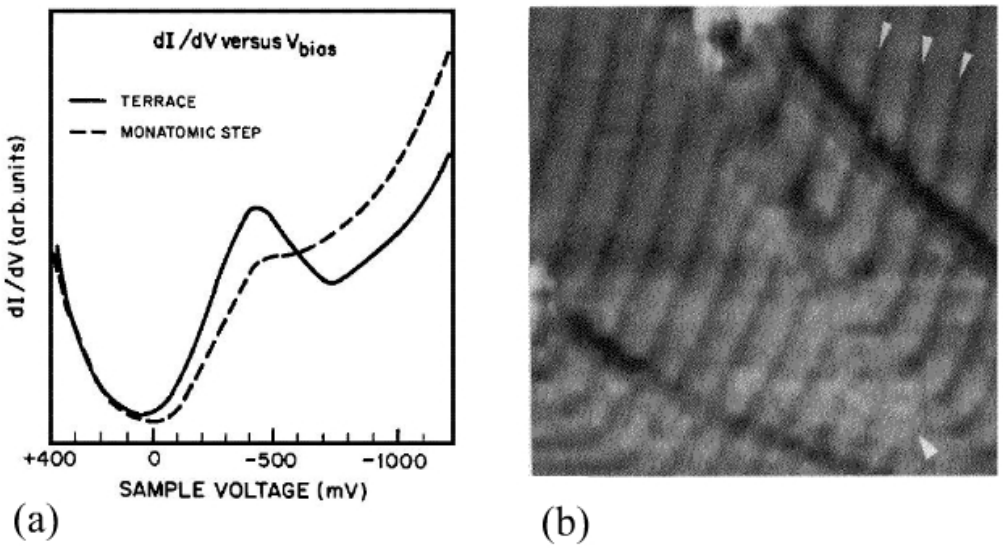

Fig. 2.15 (from [23]) (a): The *dI/dV* as function of bias voltage taken at different STM tip locations. For the LDOS at wide terrace, as shown by the solid line, a peak corresponds to the *sp* surface state is found at ~400 mV. At a monoatomic step, the intensity of this surface state is suppressed, due to a change of surface potential. (b): *dI/dV* map taken with a bias voltage of -300 mV. The FCC regions and HCP regions have different LDOS, show as bright-dark stripes on this *dI/dV* map.

theoretical result into experimental result, they went to the conclusion that a monoatomic step does act as a repulsive barrier for the surface states electrons. However, the reflection coefficient R will not be significant unless within ~10 mV of the bottom of the *sp* surface state band, which is located at ~400 mV below the Fermi level. This theory also predicted an oscillatory behavior of the LDOS as a function of the distance from step edge, as well as a 1D Kronig-Penney band structure that should be observed over a periodic array of steps on the Au (111) surface.

Because the step edge acts as a repulsive barrier and scatters electron waves, the interference between incident and reflected waves will form a standing wave near the steps. Consequently, spatial modulation of LDOS will also take place in the vicinity

of steps. This modulation of LDOS has been observed in STM experiments [25, 26], as shown in Fig. 2.16(b). In this image, each pixel presents the (*dI/dV*)/(*I/V*) values at +1.5 V, which is calculated from the STS spectrum data over the area. The (*dI/dV*)/(*I/V*) image highlights the changes in LDOS. Thus the presence of periodic bright strips along a step edge of Au (111) in the (*dI/dV*)/(*I/V*) image indicates an oscillation of LDOS near the step. By measuring the period *L* (~18 Å) of the oscillation, the wave number of surface state electrons can be deduced using the relation of $k_{//} = \pi/L$. The resultant $k_{//} \approx 0.17$ Å is consistent with the wave number of surface state electrons at Fermi level ($k_F = 0.173$ Å, [21]) found in ARPES experiment. Fig. 2.16(c) shows the (*dI/dV*)/(*I/V*) oscillations measured at different bias voltages. A drift of these traces is very obvious. The LDOS trace with higher energy has an oscillatory structure closer to step edge and has shorter period. This drift is expected because according to the dispersion relation of the *sp* surface state, higher energy level corresponding to larger $k_{//}$, which gives shorter period *L*. Furthermore, from these (*dI/dV*)/(*I/V*) traces, the phase shift can be easily measured. At the step perpendicular to the <112> direction, which presents a {111} facet, there is a phase shift of $-\pi$, implies that as a repulsive barrier, this step has a reflection coefficient of R = 1. On the other hand, for the step perpendicular to the <211> direction, which presents a {001} facet, the phase shift is $-\pi/2$, indicating some transmission of surface state electron wave is permitted through this kind of step. This difference in reflectance between the two kinds of step is probably a resultant of structural difference, as the {001} facet has low atomic density and more open structure.

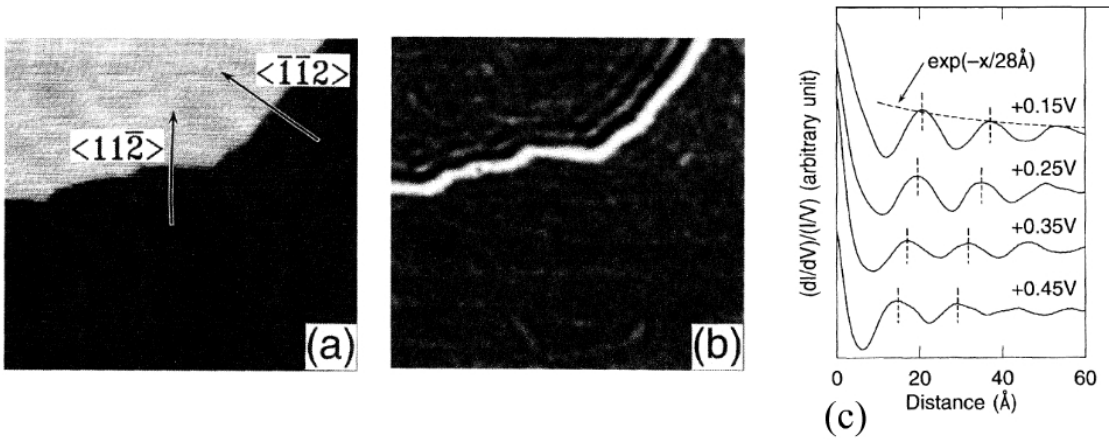

Fig. 2.16 (from [25]) (a): Topographic image of Au (111) surface, a step is seen. The directions are marked for two kinds of steps with different facets. (b): Contrast image of (*dI/dV*)/(*I/V*), taken with sample bias voltage of 0.15 V, shows the same area as (a). Bright area corresponds to higher LDOS. The oscillation of LDOS is clearly seen along the step edge. (c): Plot of (*dI/dV*)/(*I/V*) taken with different sample bias voltages as function of the distance from a <112> step. The drift of oscillation maximums and shortening of period take place while energy increasing.

By reducing the temperature to 30 K, STM experiments can provide more detailed information about the standing wave formed at step edges. The effect of the (22 × √3) reconstruction on the standing wave was first observed by D. Fujita *et al*. [27]. As shown in Fig. 2.17(a), the oscillation amplitudes of the standing wave on the FCC region, HCP region and DLs (soliton walls) are presented. The average amplitudes of the standing wave on HCP region and DLs are roughly equally, around 0.02 nm, while the average amplitude on FCC region is smaller, only around 0.01 nm. This difference in amplitude is attributed to the inhomogeneous distribution of LDOS of the *sp* surface state over the reconstructions. Another interesting phenomenon was observed when the standing wave met an elbow of herringbone pattern, as shown in Fig. 2.17(b). In this image, elbow site is marked by letter *e*, and *s* for soliton wall, *f* for

FCC region and *h* for HCP region. Height plot along A-B and C-D is presented in Fig. 2.17(c), in which the oscillation of standing wave causes periodic maxima and minima. As the direction of C-D is 120º rotated from the A-B's, if the direction of the standing wave from step edge remain unchanged when entering the second domain, the interval of oscillation maxima along C-D is expected to be twice (= 1/cos60º) as it is along A-B. But from Fig. 2.17(c), we can see the period barely changed. This phenomenon indicates an important influence on the interference of surface state electrons from the herringbone reconstruction. The standing wave of LDOS has anisotropic property, and probably propagates quasi-one-dimensionally along the DLs.

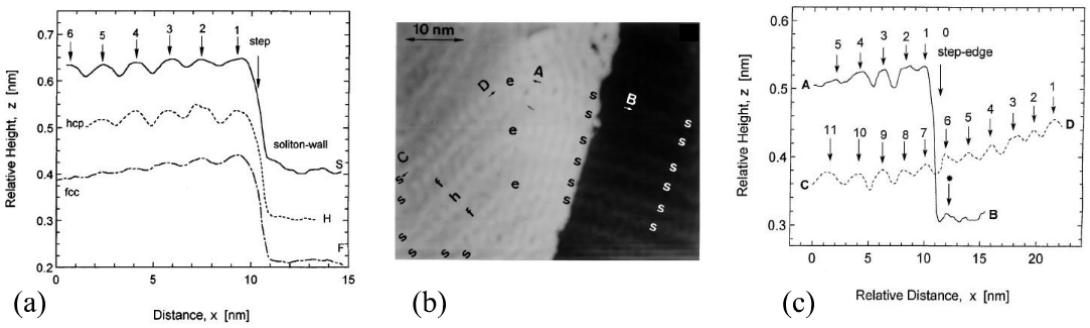

Fig. 2.17 (from [27]) (a): The plot of standing wave oscillation along FCC region, HCP region and DLs (soliton wall), respectively. The amplitudes on the later two are about twice larger as on FCC region, indicating a homogeneous distribution of LDOS of surface state on the reconstruction. (b) An STM image taken at 30 K, V = -2 mV, I = 0.3 nA. Different surface structure is marked as follow: *e* for elbow site, *f* for FCC region, *h* for HCP region and *s* for soliton wall (the DL). The amplitudes of standing wave oscillation are recorded along two soliton walls, A-B and C-D, showing in (c). Though these two soliton walls have a rotational difference of 120º, the periodic length of the oscillation on these two are the same, suggesting a one-dimensionally propagation of the standing wave along the soliton walls.

As mentioned before, the FCC regions have different LDOS of the sp surface state with HCP regions [23]. This feature is further studied by W. Chen *et al*. with low temperature STS at 4 K [28]. They did STS at FCC and HCP regions, respectively. Their results are shown in Fig. 2.18(a). The low band edge of the *sp* surface state is found 0.52 eV below Fermi energy in their experiment, which shows as an abrupt decrease of the *dI/dV* trace. The difference between FCC and HCP region presents as an enhancement of HCP trace at ~-0.48 V where the FCC trace suppressed. This difference results as a peak centered at -0.48 V in the difference image (b). Towards higher energy, at ~-0.43 V, a "crossover" takes place, where the FCC trace rises higher than HCP trace. From the difference in *dI/dV* traces, a tendency can be identified that low energy surface state electrons would like to localize in HCP region, while at energy higher than -0.43 eV, surface state electrons prefer FCC region. An extended square-well Kronig-Penney potential is introduced to explain the experiment findings. Like shown in Fig. 2.18(c), this Kronig-Penney potential has the same period with the reconstruction and presents a low square potential well of 25 meV at every HCP regions. In this case, lower energy surface state electrons will be localized in the potential well in HCP regions. And surface state electrons with higher energy will propagate in "continuum" regime and be slowed down by the barriers over FCC regions, hence the LDOS on FCC region will increase and the *dI/dV* trace will rise above the HCP trace. The origin of this potential difference between FCC and HCP regions is probably the slightly higher concentration of atoms in the HCP region, which is mentioned in Section 2.1.1 (see Fig. 2.5). The different distribution of

surface state LDOS on FCC regions and HCP regions may respond to the difference in adsorption behaviors over these two regions for many adsorbate, which will be introduced in the following sections.

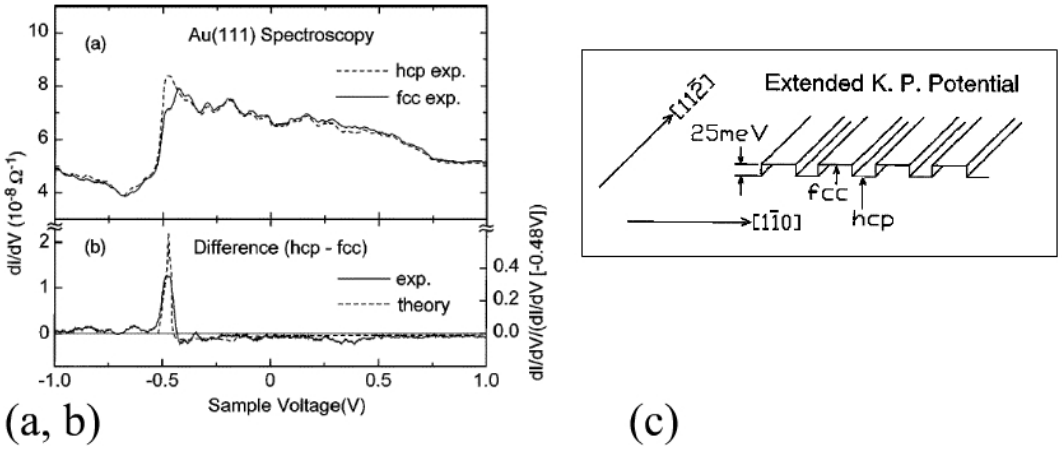

Fig. 2.18 (from [28]) (a): *dI/dV* spectrums taken at FCC (solid line) and HCP (dashed line) regions, respectively. The HCP trace has an enhancement at -0.48 V while FCC trace has a decline. The FCC trace rises above HCP trace at -0.43 V. The relationship between the two traces is clearly seen in the difference image (b). These *dI/dV* traces indicates the different energy distribution of surface state LDOS on the two regions. And periodic Kronig-Penney potential is introduced to model this phenomenon, as shown in (c).

2.2 Adsorption on the Au (111) Surface

2.2.1 Metal Deposition on the Au (111) Surface

As introduced in previous sections, the Au (111) surface presents a structured morphology. A contraction of 4.5% along one of the three equivalent <110> directions leads to a (22 × √3) reconstruction, in which corrugation ridges (the DLs) separate FCC and HCP stacking regions. Moreover, the reconstruction also presents long-range

order by periodically changing the surface domain orientations in order to isotropically relieve the uniaxial tensile stress. Thereupon, the DLs form "herringbone" patterns on terraces with an ordered array of edge dislocations associated with the type x elbows. A surface with such rich structural features as well as long-range periodicity is an ideal template for the growth of various nanostructures. So ever since as the unique surface morphology of Au (111) was revealed, there have been attempts to employ it as template for growth of nanostructures.

Various metal elements have been deposited onto the reconstructed Au (111) surface. At very low coverages, two kinds of nucleation behavior have been observed. The first kind is preferential occupation of the herringbone elbow sites, leading to highly ordered arrays of adislands on gold substrate. Ni [29-32], Co [33, 34], Fe [35, 36], Mo [37, 38], Pt [39], Pd [40, 41] and Ti [42] are examples of metal that adsorb on elbow sites, as shown in Fig. 2.19. These metals nucleate at every elbow sites of the herringbone, or accurately, at every type x elbow site where an edge dislocation exists, as revealed in the inset of Fig. 2.19(b). The subsequently formed metal adislands present polygon shape, and have small size distributions. As all these adislands nucleate at herringbone elbow sites, they are equally spaced between neighbors in the same row, while the distance from row to row is determined by the periodicity of the substrate domains, thus highly ordered arrays are always formed. On the other hand, metals such as Al [43, 44] and Ag [45, 46] do not nucleate at the elbow sites of the Au (111) surface. They form rather irregular structures, as shown in Fig. 2.20. After landing on the surface, Ag or Al atoms diffuse to step edges and nucleate there to

form finger-like structures. At slightly high coverage, Ag and Al adislands will appear on the terraces. The growth of Ag islands is defined by the substrate reconstruction thus the islands have long-narrow shapes and they even bend at the elbow sites. Meanwhile, the Al islands present irregular dendritic shapes. At last, different from the two catalogs above, Au atoms deposited on Au (111) is a unique situation, at very low coverages, small Au islands form on the terraces. However, at slight higher

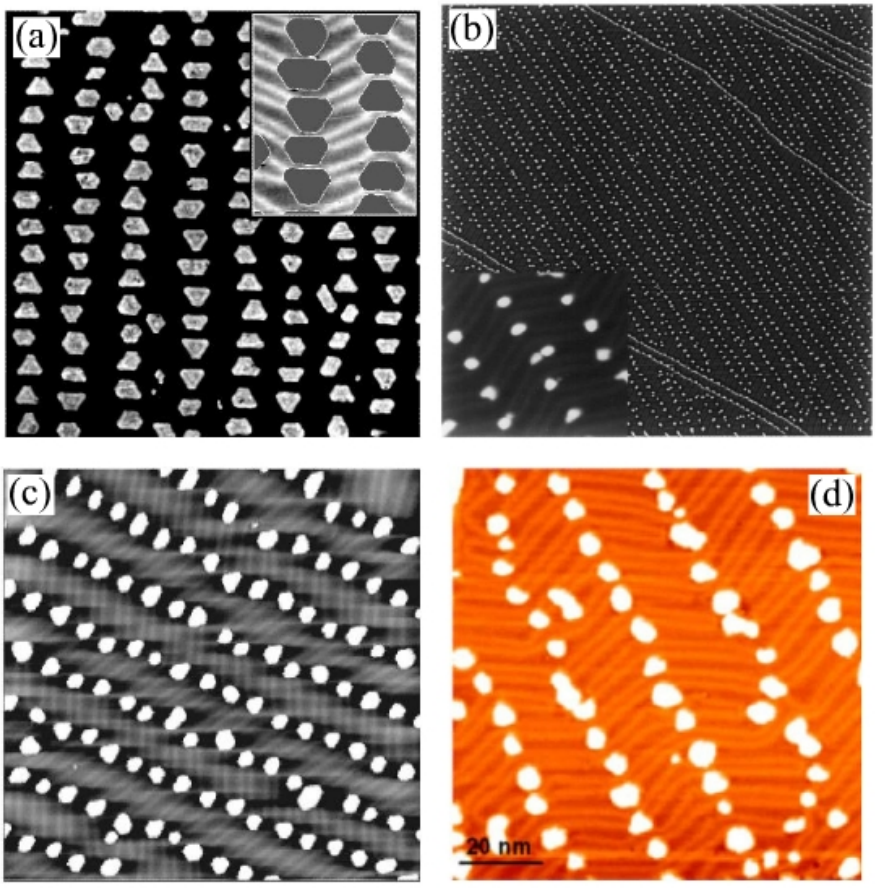

Fig. 2.19: Metal atoms aggregate at the elbow sites of herringbone reconstructed Au (111) surface and form highly ordered arrays of adislands. Each array consists of islands, which are equally spaced and are of similar sizes. (a) (from [32]): 0.25 ML of Ni deposited at 300 K, 99 × 90 nm. (b) (from [37]): ~0.05 ML of Mo deposited at 307K, 400 × 400 nm. (c) (from [34]): 0.26 ML of Co deposited at 300 K, 100 × 100nm. (d) (from [41]): 0.14 ML of Pd deposited at 300 K, 90 × 90 nm.

coverages as shown in Fig. 2.20(d), the Au adislands present some preferential alignment along substrate domain walls [30, 47], similar to the cases of Ni, Co, Fe *et al*., but not every elbow site is occupied and the size distribution of the Au island is much more random. The variety in nucleation location for different metal adatoms shown above indicates a complication adsorption mechanism, which is expected for the feature-rich Au (111) surface.

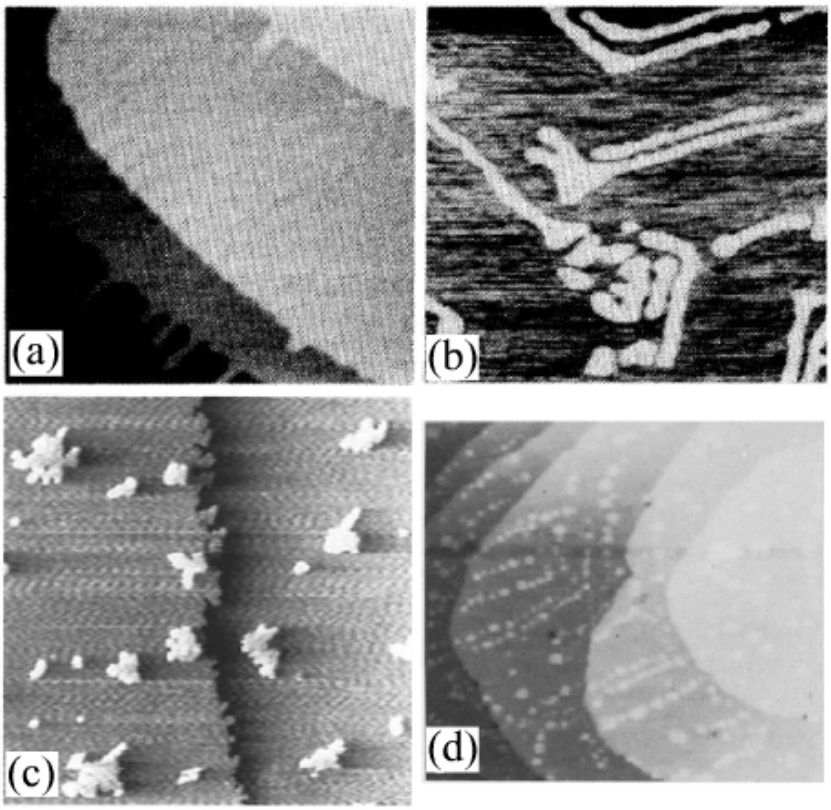

Fig. 2.20 (a) (from [45]): 115 × 115 nm, 0.1 ML of Ag deposited at RT, Ag atoms diffuse to step edges of the substrate and form finger-like structures there. (b) (also from [45]): 115 × 115 nm, at higher coverage of 0.25 ML, Ag islands nucleates on terraces. The growth of these Ag islands is obviously defined by the herringbone pattern, and follows the bends at the elbows. (c) (from [44]): 240 × 240 nm, 0.1 ML of Al deposited at 260 K, Al atoms nucleate at Au step edges, and they also form dendritic islands randomly distribute on terraces. (d) (from [47]):115 × 115 nm, 0.1 ML of Au on Au (111), alignment of Au islands of variable sizes.

J. A. Meyer *et al*. [31] explained the two different kinds of nucleation behavior by introducing a two step nucleation process for metals that exhibit preferential nucleation at the elbow site. In the proposed process, the first atom landing on the surface will exchange place with a surface layer Au atom, and then, the substitutional adatom will act as the nucleation center which traps incoming adatoms to form islands on top of it. The substitution had been directly observed in atomic resolution STM images at very low coverage [31]. In this case, the preferential nucleation at the elbow site is actually preferential atomic place exchange at such site, which can be easily understood because the elbow site is highly strained and due to the edge dislocation, there is an Au atom with reduced coordination that can be substituted more easily. To allow the atomic substitution taking place, this process must be energetically favored, which means the metal elements that can substitute Au atom from its lattice site must have higher surface free energy and higher heat of sublimation than Au. From Table 2.2 we can see that Ni, Co and Fe have higher surface free energy and heat of sublimation than Au and these three elements do preferentially nucleate at the elbow

Element	Surface free energy (eV)	Heat of sublimation (eV)
Ag	0.50	2.95
Al	0.56	3.39
Cu	0.69	3.51
Au	0.72	3.79
Ni	0.90	4.45
Co	0.94	4.40
Fe	0.96	4.32

Table 2.2 (from [31]): The surface free energy and heat of sublimation for different elements.

site. On the other hand, with lower surface free energy and heat of sublimation, Ag, Al and Cu do not show such substitution. Thus the place exchange explanation is well supported by experimental findings.

Besides the specific nucleation site, the herringbone reconstruction of the Au (111) surface also influences the further growth of metal adislands [36]. As shown in Fig. 2.21(a) and (b), the shape of Fe adislands at bulged elbows is different from that at pinched elbows at coverage of 0.18 ML. At bulged elbows, island growth is

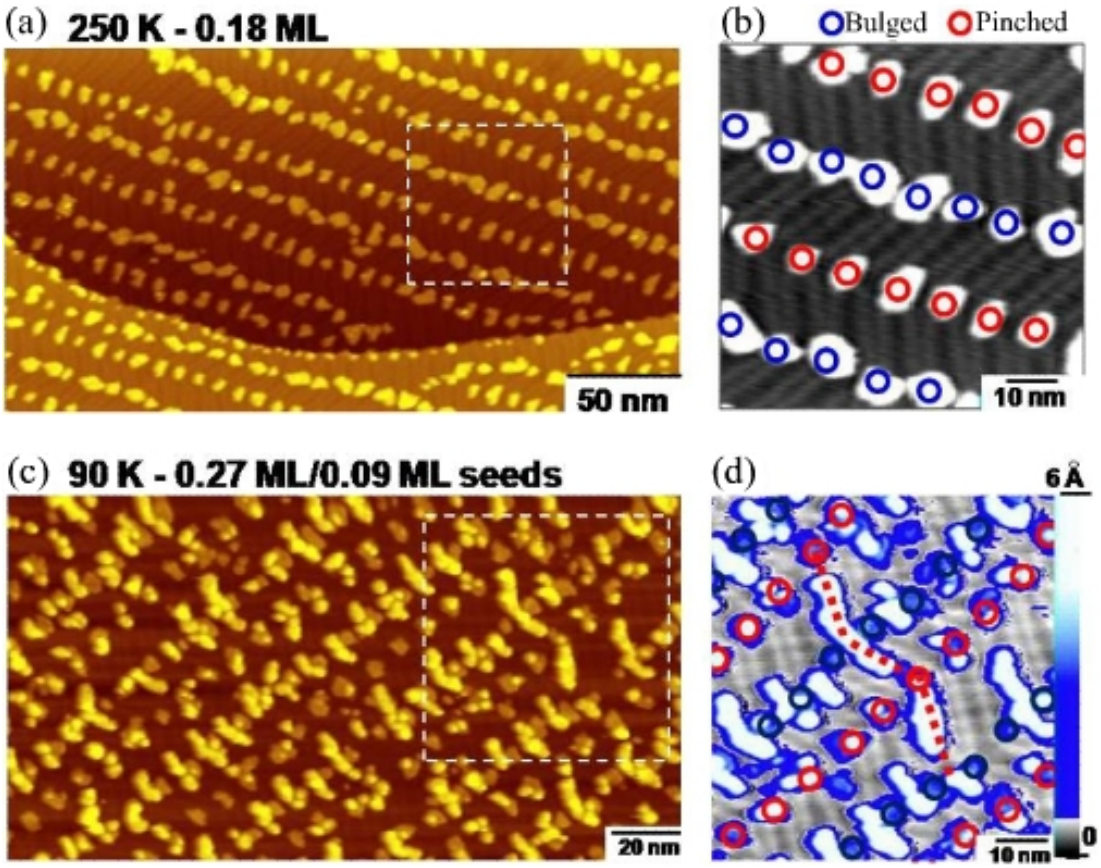

Fig. 2.21 (from [36]) (a): 0.18 ML of Fe grown at 250 K, (b): A zoomed-in image, in which the different island shapes at bulged and pinched elbow are obvious. The two kinds of elbow are marked by blue circles (for bulged elbows) and red circles (for pinched elbows), respectively. (c): 0.09 ML of seeds is deposited at 250 K, following by deposition at 90 K to 0.27 ML. (d): Later coming Fe atoms prefer to adsorb on FCC stacking regions, and form zigzag islands.

restricted in the region defined by two neighboring DLs and the island presents a long-narrow shape. Meanwhile, islands at pinched elbows are not defined by substrate structure and grow isotropically. Furthermore, in a two step growth process, in which 0.09 ML of Fe is firstly deposited at 250 K at elbow sites to serve as seeds, then, the sample is cooled down to 90 K and further Fe atoms are deposited to reach a coverage of 0.27 ML. The resulting morphology is presented in Fig. 2.21(c) and (d). As can be seen, the later coming Fe atoms form islands preferentially in FCC regions, and give a zigzag shape due to the bending of FCC stacking regions at domain boundaries. Thus we can see the adlayer structure depends on the specific elbow type of Au substrate as well as its atomic stacking type. This is a unique property of Au (111) when used as template for growing nanostructure, and we will discuss its influences on the corrugations of organic molecular later, in particular sub-monolayer of fullerene.

2.2.2 Organic Molecule Deposition on the Au (111) Surface

As introduced in the previous section, when Ni, Co, Fe, Mo, Pt, Pd and Ti [29-42] atoms are deposited onto the Au (111) surface, the unique herringbone reconstruction of the Au (111) is found to guide the nucleation and growth of these atoms and result in highly ordered structures. Besides the metal atoms, many efforts are devoted to research the self-assembly of organic molecules on the Au (111) surface [48-53]. Normally, organic molecules present high mobility on the Au (111) surface at room temperature thus will not stay on the terrace after landing. However, if studied under low temperature, many molecules will present site-specific adsorption over the

reconstructed surface, similar to the situation of the metal atoms listed above.

The elbow sites of the DLs are the most favoured adsorption site for the organic molecules, especially the elbow site of the type x DLs which presents an edge dislocation. As shown in Fig. 2.22, at very low coverages, all the molecules are exclusively adsorbed on the elbow sites. The molecules adsorbed on each elbow site form a highly ordered superlattice, giving a similar topography as shown in Fig. 2.19(a-d). For the metal atoms, the selective adsorption on the elbow site starts with an atomic exchange, in which the first landed atom will exchange place with a surface layer Au atom and then serve as a nucleation core. The adsorption of organic molecules sometimes also involves an arrangement of the surface Au atoms. L. Gao *et al*. found that when (t-Bu)$_4$-ZnPc molecules are deposited onto the Au (111) surface, an extra Au atom at each DL elbow sites will help retaining the molecule there [48].

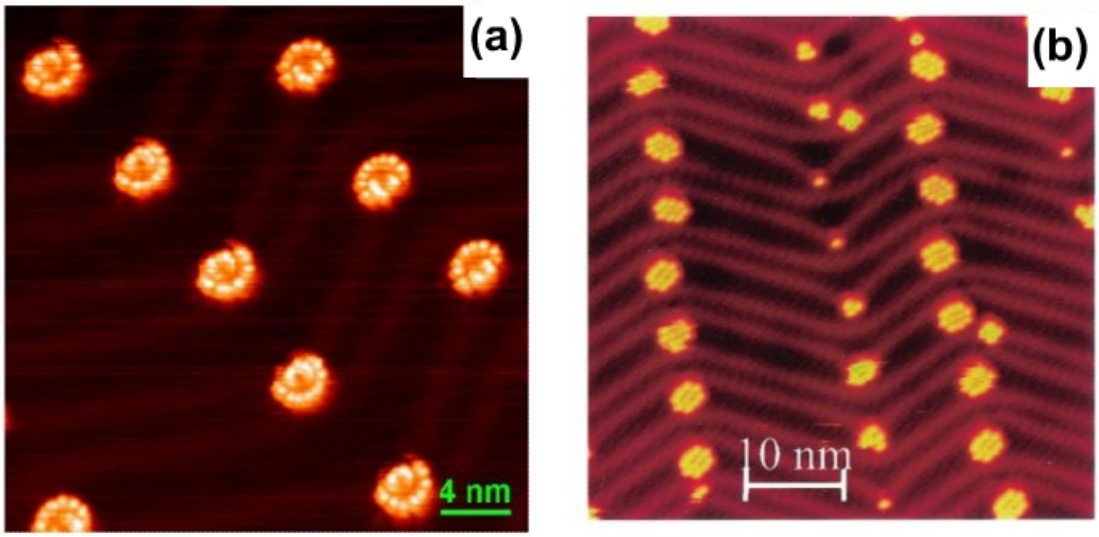

Fig. 2.22: Different kinds of organic molecules are adsorbed on the elbow sites of the DLs of the Au (111) surface and form ordered arrays. (a) (from [48]): (t-Bu)$_4$-ZnPc molecules. (b) (from [49]): 1-nitronaphthalene (NN) molecules.

Adsorbed on such an extra Au atom will enhance the bonding strength between the molecule and the substrate thus prevents the lateral diffusion of the molecule over the surface.

With a close examination of the two images in Fig. 2.22, we can find that in Fig. 2.22(a), all the adsorbed molecules are attached to the elbow sites of type x DLs while all the elbow sites of type y DLs are empty. This can be easily understood as there is an edge dislocation associated with each elbow site of type x DLs, which offers a deeper potential well than the defect free type y elbow site. However, in Fig. 2.22(b), all the molecules are found in FCC regions, regardless of whether it has to attach to the elbow site of type x DLs or type y DLs. Such phenomenon indicates a preferential segregation of the molecules to the FCC regions of the Au (111) surface. After landing, the molecules fall on HCP regions of the surface will diffuse to the FCC regions in a short time and do not diffuse back, resulting in a much higher molecular density in the FCC regions than the HCP region, as shown in Fig. 2.22(b). The preference of

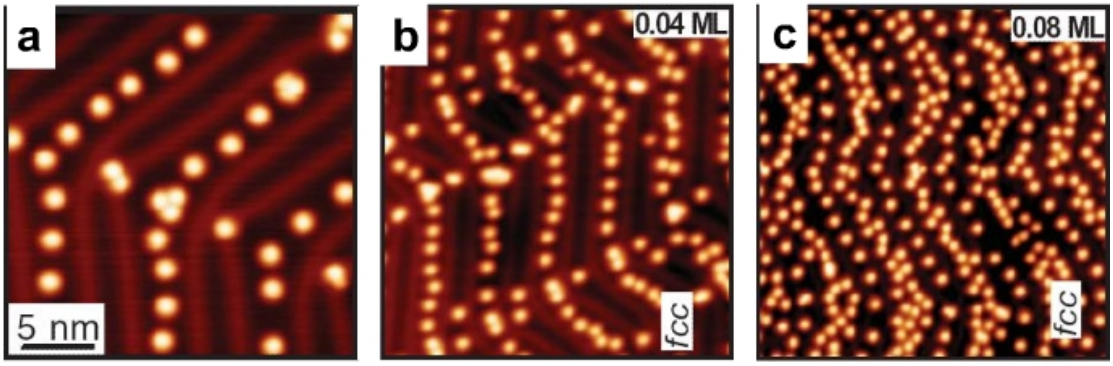

Fig. 2.23 (from [51]): The adsorption of single tetrathiafulvalene (TTF) molecules on the Au (111) surface. (a) and (b): At coverage of 0.04 ML, molecules occupy the elbow sites of the DLs and the FCC regions. (c): At higher coverage of 0.08 ML, the second rows of molecules appear in each FCC region. Meanwhile, the molecules start to occupy the HCP regions of the surface.

adsorbing on the FCC regions of the Au (111) surface is a common feature presented by many kinds of organic molecules. Fig. 2.23 gives another example of the preferential segregation.

The images in Fig. 2.23 (a) and (b) were taken at the same molecular coverage of 0.04 ML. From these two images, all the elbow sites are found to be occupied. Furthermore, some molecules locate in the FCC regions of the Au (111) surface and form 1-dimensional arrays along the trend of the DLs. At the same time, all the HCP regions are free of adsorbed molecules, indicating that it is less favoured than the FCC regions by the adsorption of molecules. Fig. 2.23(c) is taken over a similar terrace as (b) but with a higher molecular coverage of 0.08 ML. At this coverage, more molecules settle down in the FCC regions and the HCP regions are populated with single rows of molecules. Therefore, it is reasonable to conclude that the elbow site of the herringbone reconstruction is the most favoured adsorption site for the deposited molecules, followed by the FCC region of the surface, then is the HCP region and the corrugated ridge (the DL) is the least favoured. This conclusion is proved by the experiment of M. Böhringer *et al*., who found that by depositing small amount of 1-nitronaphthalene (NN) molecules onto the Au (111) surface at room temperature and slowly cooling down, the self-assembled molecular cluster firstly appears at the elbow site at 65 K. When the temperature is further reduced to 50 K, molecular cluster appears in the FCC regions. The molecule will not occupy the HCP regions and the corrugated ridges until 10 K. This result also reveals that the bonding strength between the adsorbed molecules and the substrate is different over the different

structures of the herringbone reconstruction.

Besides the site-specific adsorption, the herringbone pattern of the Au (111) surface also influences the further growth of molecular structures. By confining the growth within the regions defined by the DLs, the herringbone reconstruction always leads to some zigzag molecular structure copy its periodicity and long-range order, as shown in Fig. 2.23(a). In another case, after occupying each elbow sites, if the further landing molecules choose to link up the existing molecules at the elbow sites, parallel molecular chains will be formed, as shown in Fig. 2.24. These molecular chains are straight and can be over 100 nm in length.

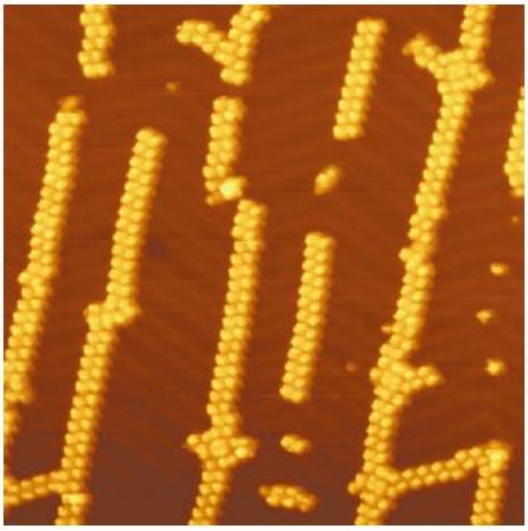

Fig. 2.24 (from [52]): trans-BCTBPP molecular chains extended across the elbow sites of the herringbone reconstruction of the Au (111) surface.

The DLs of the Au (111) surface do not only confine the growth of molecular structures but also confine the diffusion of the molecules on the surface. Once landed on the surface, the molecules prefer to diffuse along the FCC region or the HCP

region defined by the DLs rather than diffuse across the DLs. The images in Fig. 2.25 perfectly illustrate this situation. Fig. 2.25(a) is taken at 5 K, the 0.1 ML of iron phthalocyanine (FePc) molecules deposited on the Au (111) surface presents a similar topography as the ones shown in Fig. 2.23(a) (b), in which all the elbow sites and the FCC regions are occupied by adsorbed molecules. When the temperature is raised to 77 K, the lateral diffusion and rotational motion of the molecules are activated, giving a smooth, uniform high feature in the STM image, as shown in Fig. 2.25(b). However, such feature can only be found on the FCC and HCP regions of the surface. There is no molecule diffuses to the DLs, therefore, the DLs apparent darker in the image because its height (0.06 nm) is lower than a diffusion molecule (~0.02 nm). From this experiment, we can see that the diffusion direction of the molecules is well defined by the DLs, therefore, the DLs serve as "railway" to guide the diffusion of the molecules.

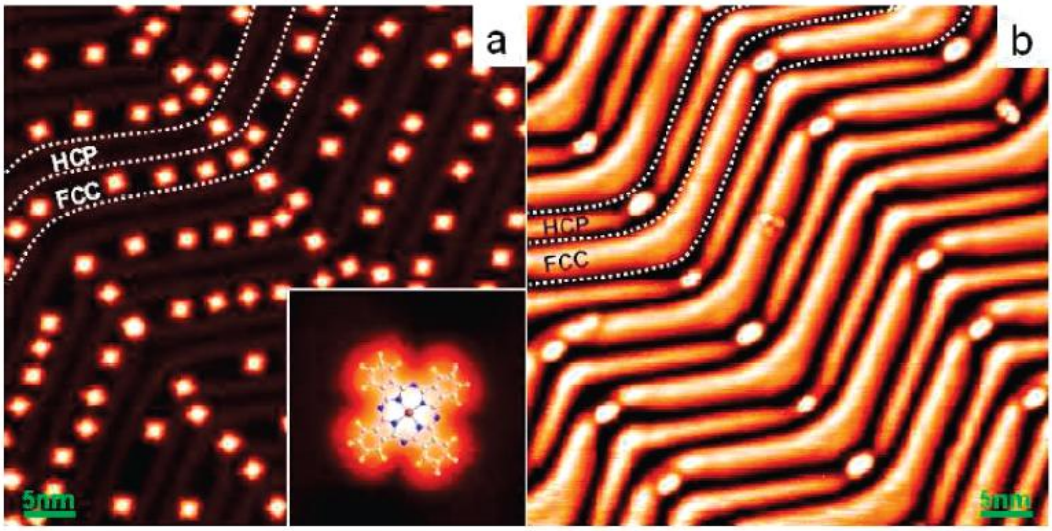

Fig. 2.25 (from [53]) (a): FePc molecules frozen on the Au (111) surface at 5 K. (b): At 77 K, the molecular diffusion is activated. Moving molecules give a smooth and uniform feature over the regions that they can reach. The DLs are free of diffusing molecules and apparent darker. The insert is the schematic image of a FePc molecule.

At last, the reconstruction of the Au (111) surface is recently found to be able to tune the rotational motion of the adsorbed molecule [48]. When a (t-Bu)$_4$-ZnPc molecule is adsorbed on the FCC or HCP regions of the surface, it gives a flower-like feature due to the free rotation of the molecule, as shown in Fig. 2.26(a). If the molecule is adsorbed on an elbow site of the DLs, it gives a feature looks like a folding-fan, as shown in Fig. 2.26(b). The different appearance indicates that when adsorbed on the elbow site, the rotation of the molecule is confined in a range of ~180º by the presence of the underlying DLs. The controlling of the rotational motion of the molecule by choosing the adsorption site on the substrate indicates a new way to design and construct molecular devices.

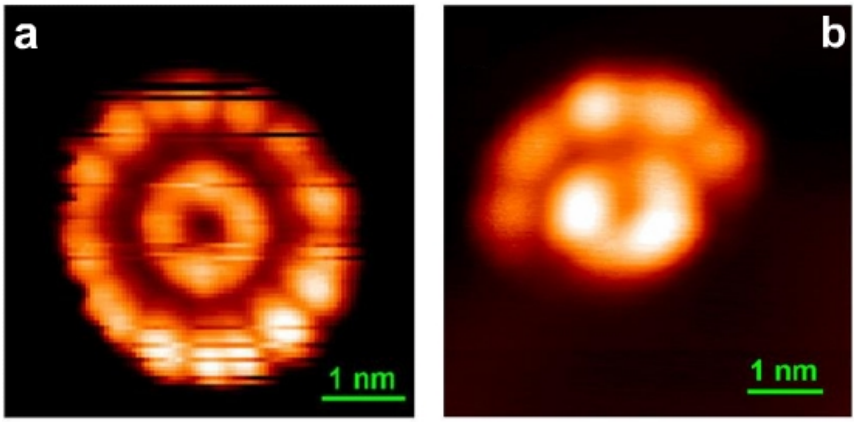

Fig. 2.26 (from [48]) (a): A (t-Bu)$_4$-ZnPc molecule adsorbed on the FCC region of the Au (111) surface. The flower-like appearance of it indicates that the molecule is rotating 360º. (b): A molecule adsorbed on the elbow site of the DLs. The rotation of this molecules is confine in a range of ~180º because of the presence of the underlying DLs. The molecule gives a folding-fan feature due to the reduced rotational freedom.

As a conclusion, the self-assembly of organic molecules on the reconstructed Au

(111) surface is greatly influenced by the different features of the substrate. By carefully choosing the type of the molecules and the growth condition, the Au (111) surface can be employed as a ideal template for the fabrication of desired molecular nanostructure.

2.3 C_{60} Buckminsterfullerene

2.3.1 The C_{60} Molecule

C_{60} buckminsterfullerene, first discovered by H. W. Kroto *et al*. in 1985 [54], followed by the subsequent discoveries of other members of the fullerene family, represents the third kind of carbon, after diamond and graphite. The fullerene family consists of any molecule composed entirely of carbon, and can be classified into two sub-catalogs, which are buckyballs with a shape of a sphere or ellipsoid and carbon nanotubes with a cylindrical shape. C_{60} buckminsterfullerene is a kind of buckyballs which has sixty carbon atoms forming a "spherical" cage. The spherical cage actually adopts a truncated icosahedron configuration, consists of twenty hexagons and twelve pentagons. This structure is a microcosmic resemblance of geodesic dome, of which the concept is generalized by architect Richard Buckminster Fuller and the name buckminsterfullerene was given to C_{60} to honor him. The suffix "ene" in its name indicates that each carbon atom in this kind of molecule is covalently bonded to three others, considering the four sp3-hybrid orbitals of each carbon atom, some double bonds will be formed between two carbon atoms in C_{60} molecule. These double bonds

are shared between two adjacent hexagons in the cage (called 6:6 bond), while single bonds are shared by a hexagon and a neighboring pentagon (6:5 bond). Pentagons in a C_{60} cage never share a edge with another pentagon. The lengths of 6:6 bond and 6:5 bond are found to be 1.401 Å and 1.485 Å, respectively [55]. Fig. 2.27 presents the atomic structure of a C_{60} molecule. It is clearly seen from this schematic diagram that every carbon atom in a C_{60} molecule is in equally coordination, being shared by two hexagons (six-atoms ring) and one pentagon (five-atoms ring), and forming two single bonds and one double bond with three neighboring atoms. The nucleus to nucleus diameter of a C_{60} molecule is 7 Å, while the van der Waals diameter is about 1 nm.

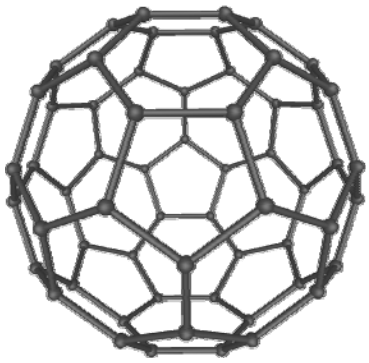

Fig. 2.27: Structure of C_{60} buckminsterfullerene. (Image from wikipedia.org)

In 1990, W. Krätschmer *et al* [56] found a method to produce and isolate C_{60} molecules in macroscopic amount and this has made the research of its properties possible. Since then, this new carbon molecule has been drawing great attention of scientists in almost every research fields. Its unique properties and potential applications in physics, chemistry, biology, material science and electronics are widely explored, especially in nanoscience and technology.

2.3.2 Solid C_{60}

Solid C_{60} are called fullerite. It is a black powder with small crystalline pieces. Under TEM observation, the C_{60} clusters are in shapes of platelets, rods and stars, all with hexagonal symmetry [56]. Single-crystal X-ray diffraction study [57] revealed that at room temperature, the C_{60} crystal adopts a face-centered-cubic (FCC) structure, with $a_0 = 14.17 \pm 0.01$ Å. The crystal presents a high degree of orientational disorder which is caused by the free rotation of molecules at room temperature. When decreasing the temperature, at 249 K, a phase-transition from FCC structure to simple-cubic (SC) structure occurs. And the orientational order develops simultaneously. Neutron scattering studies gave further details of this phase-transition [58]. In Fig. 2.28, the temperature evolution of C_{60} crystal's lattice constant is presented, generally, as the temperature decreases, the lattice constant shrinks along a smooth trace except at two phase-transition points. The first is at 260 K, where the FCC-to-SC phase-transition is indicated by a sudden drop in the curve. At this temperature, a coexistence of FCC and SC phases is observed. The second phase-transition takes place at 90 K, where a cusp of the curve is identified. In the regime from 260 K to 90 K, the C_{60} molecules are found to shuffle between equivalent orientations. At 90 K, the thermal energies become smaller than the rotational barriers and the rotational disorder of C_{60} molecules is frozen. At 5 K, the C_{60} molecules are found to be frozen with a high degree of orientational order that can optimize the intermolecular interaction. With this orientational order, every two neighboring molecules facing each other with one's electron-rich double C-C bond (6:6 bond) positioned parallel (~179.6°) to the other

one's electron-deficient pentagonal face. And for any C_{60} molecule, the interactions with its twelve nearest-neighbor molecules are optimized by adopting this double bond-facing-pentagon structure [58, 59].

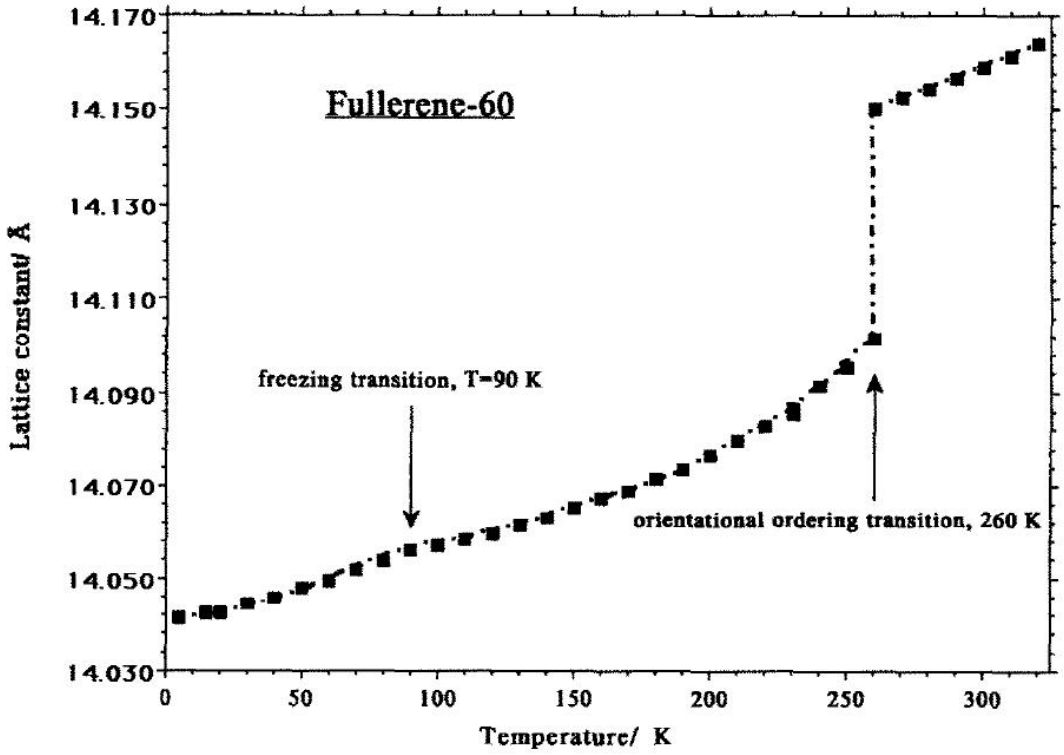

Fig. 2.28 (from [58]): The lattice constant of C_{60} crystal as a function of temperature. The FCC-sc phase transition happens at 260 K, indicated by a sudden drop of the curve. The freezing transition happens at 90 K, indicated by a cusp of the curve.

Besides the geometric structure of solid C_{60}, the electronic structure of the solid has attracted even more research interests, especially after the alkali-doped C_{60} are found to be superconducting with a high transition temperature (T_c = 33 K for $RbCs_2C_{60}$) [60, 61, 62]. Undoped C_{60} solid is a kind of molecular crystal and is a band insulator, of which the band structure was investigated by soft x-ray photoemission

and inverse photoemission [63]. The result is shown in Fig. 2.29. In the upper panel, the peaks representing HOMO and LUMO are labeled 1 on each side of E_F and the HOMO-LUMO gap is 3.7 eV. The lower panel of Fig. 2.29 shows the core emission, in which the C 1*s* main line emission is located at 285.0 eV, with a very narrow width that is close to the instrument limit. The narrow width of C 1*s* main line suggests that the all the carbon sites are spectroscopically equivalent in the solid C_{60}.

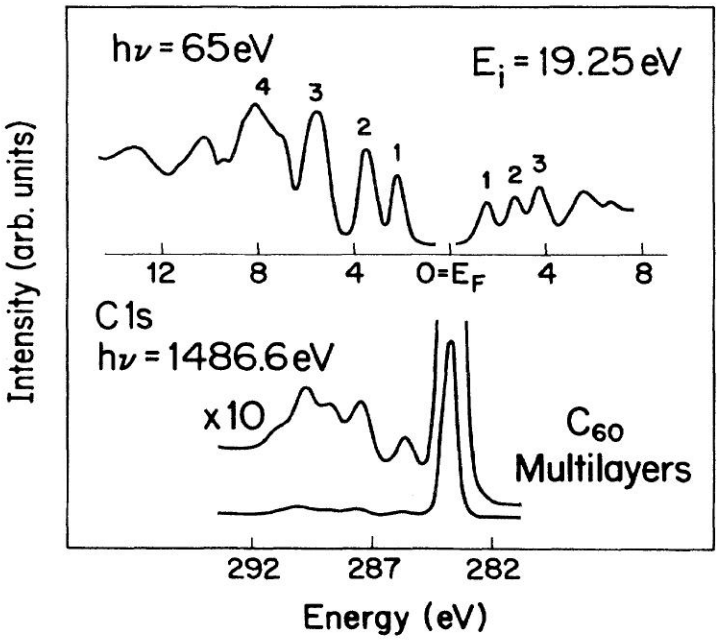

Fig. 2.29 (from [63]) Upper panel: The result of photoemission and inverse photoemission of solid C_{60}, the HOMO-LUMO gap is 3.7 eV. Lower panel: The C 1*s* main line emission of solid C_{60}, of which the peak is located at 285.0 eV and with very narrow width.

With a detail study of the band structure around the Fermi level, some subbands are depicted in Fig. 2.30 (from [64]). The bands at about -0.5 eV are the h_u bands which derived from HOMO and are occupied in C_{60} solid. The bands around 1.5 eV

are the t_{1u} bands which derived from LUMO. The t_{1u} bands are empty in solid C_{60}. However, they are easy to accept electrons from doped alkali metal atoms, and will play a key role when charge transfer happens for C_{60} molecules. The t_{1u} band can take six electrons at most, a half filled t_{1u} band, e.g. found in A_3C_{60} (A = K, Rb), lead to metal-like property, while in the situation of fully occupied, like for A_6C_{60}, it becomes band insulator again.

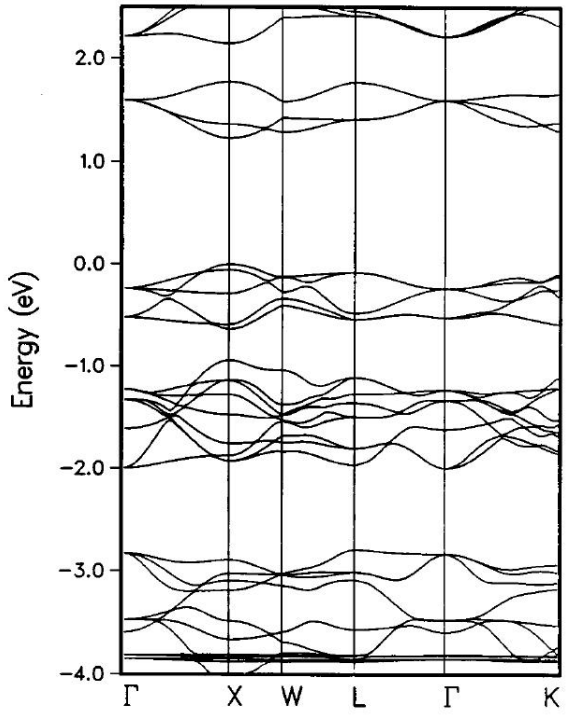

Fig. 2.30 (from [64]): Band structure around the Fermi level for C_{60} solid, the t_{1u} band which plays a key role in charge transfer is located ~ 1.5 eV.

In an alkali-doped C_{60} solid, the alkali metal atoms are located in the tetrahedral and octahedral sites between C_{60} molecules. There is another situation that the doped atoms are encapsulated inside the C_{60} cage. This kind of C_{60} variation is called

"Endohedral fullerene". If there are metal atoms that be encapsulated, e.g. Sc, Y, La, Ca, Sr and Ba, they are called endohedral metallofullerenes and written as $Sc@C_{60}$. The metal atom inside the cage will stay close to the shell due to the interaction with carbon atoms. Charge transfer is also expected, same as alkali-doped C_{60} solid. Depends on the different amounts of charge transfer, the endohedral metallofullerenes exhibit properties of metal, semiconductor or isolator, respectively. Beside metal atoms, some other atoms can also be encapsulated in a C_{60} cage such as He, Ar, Ne, N and Xe. These atoms are much more chemically inert, and will stay in the center of the C_{60} cage. Notable, the discovery of $Sc_3N@C_{80}$ proved that small molecules can also be included inside a fullerene cage [65].

2.4 Deposition of C_{60} Fullerene on Metal Surfaces

In this section, I will review the growth process of C_{60} fullerenes adsorbed on variety metal surfaces and the properties of the formed C_{60} thin films. Because my research is focused on the C_{60} submonolayer grown on the Au (111) surface, the review of C_{60} deposition on other substrates is brief while the previous works on the C_{60}/Au (111) system will be introduced in detail in Section 2.5.

As mentioned above, doping alkali metal into solid C_{60} can cause a charge transfer from metal atoms to the LUMO t_{1u} band of C_{60} molecules and the superconductivity of a alkali-doped C_{60} solid strongly depends on the amount of charge transfer. Similar charge transfer can also take place when C_{60} molecules are

deposited on to a variety of metal surfaces. Photoemission study [63] of multilayer C_{60} films grown on different metal substrates (Au, Ag, Mg, Cr and Bi) reveals that despite the ~1.5 eV variation in the work function of these metals, the HOMO derived peaks are uniformly located 2.2 – 2.3 eV below E_F, indicating that the energy level of the C_{60} film align with the Fermi level of substrate instead of the vacuum level. Such alignment suggests charge redistribution and dipole formation at the metal-C_{60} interface, probably a charge transfer from substrate to the first layer C_{60} molecules. This charge transfer would induce hybridization between C_{60} molecule's LUMO and substrate metal states which is revealed in inverse photoemission energy distribution curve as a shift of the LUMO derived peaks towards Fermi level for monolayer C_{60}, compared with multilayer. The LUMO of multilayer C_{60} remains in the same energy level as solid C_{60} because the first layer C_{60} molecule is not modified very much by the small charge transfer thus the subsequent layer are bond with first layer mostly by van der Waals interaction. S. Modesti *et al.* [66] later confirmed by electronic excitation study that the transferred charges are injected into the six-fold degeneration t_{1u} band of C_{60} molecules, giving quite similar spectrum with the alkali-doped C_{60}. Depending on metal substrate, 1~6 electrons can be transferred to each first layer C_{60} molecule, comparable to the situations of AC_{60}, A_3C_{60} or A_6C_{60} (A = K, Rb, Ca).

Research by S. Modesti *et al.* [66] also reveals that the electronic excitation spectrum for ordered C_{60} thick layers (5 MLs) grown on a metal surface is semiconductor-like while for monolayer, it is metal-like. Such a metallic characteristic makes the C_{60}-monolayer/metal a ideal system for STM investigations. According to

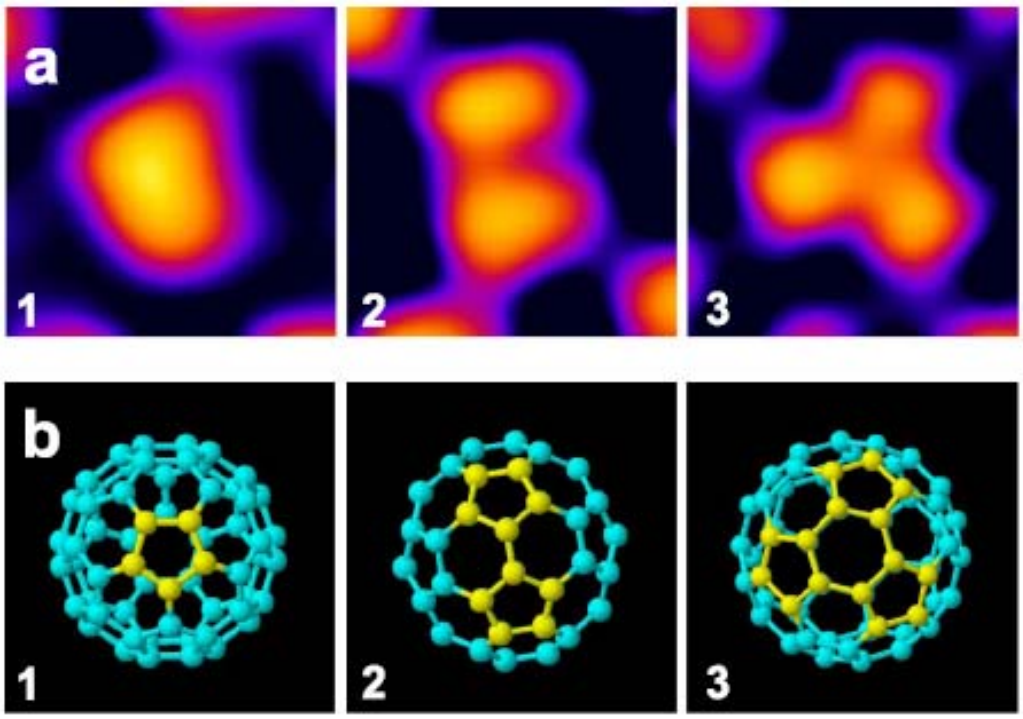

Fig. 2.31 (from [69]) (a): STM images of C_{60} molecules adsorb on Au (111) surface with different geometries: (a1) adsorb with a pentagonal ring facing the substrate, giving a one-fold symmetry image; (a2) adsorb with a carbon atom facing down, giving a two-fold symmetry image; (a3) adsorb with a hexagonal ring facing down, giving a three-fold symmetry image. (b): Corresponding models for the three adsorption geometries, the pentagonal rings are marked in yellow as they are highlighted in STM images.

STM theory, the tunneling current mainly travels through the electronic states near the Fermi level, thus the states in HOMO and LUMO will greatly contribute to the STM imaging. In a C_{60} molecule, the states associated with the LUMO are localized in the single bonds (sp^2 bonds), which form the pentagonal rings in the cage [67, 68]. Therefore, in empty state STM imaging, the pentagonal rings are highlighted, giving a doughnut-like feature, see Fig. 2.31. The different geometries of C_{60} molecule adsorbed on surface thus can be decided by identifying the intramolecular structures, for example: 1) when a C_{60} molecule adsorbs with its hexagonal ring facing the

substrate, another hexagonal ring will face up and three pentagonal rings can be seen in the STM image, so the C_{60} molecule will present a shape of three-fold symmetry, as in Fig. 2.31(a3). 2) if the C_{60} molecule adsorbs with a pentagonal ring facing the substrate, then a one-fold symmetry will be observed in the STM image, as in Fig. 2.31(a1). 3) a two-fold symmetry shape will be seen if the C_{60} molecule adsorbs with a carbon atom facing down, Fig. 2.31(a2).

2.4.1 C_{60} on Cu (111)

Cu (111) is an ideal surface for C_{60} layer growth, due to the small lattice mismatch between the nearest neighboring distance in bulk C_{60} (10 Å) and four times of Cu (111) surface nearest atomic distance (10.2 Å). C_{60} molecule presents high mobility when deposited onto the Cu (111) surface at room temperature. Initial nucleation only happens at Cu step edges, and close-packed C_{60} islands will grow from the step edge towards the flat terrace when the step is saturated. As expected, the close-packed C_{60} layer presents a 4 × 4 superlattice on Cu (111) surface. STM images show that the individual C_{60} molecules in a close-packed monolayer presents a three-leaf clover shape, Fig. 2.32(a), such a three-fold symmetry indicates that the C_{60} molecule is adsorbed with a hexagonal ring facing the Cu surface. Also, the revealing of intramolecular structure indicates that the C_{60} molecules are frozen from rotating at room temperature. Considering the free rotation of molecules in bulk C_{60} at room temperature, a strong bonding with the Cu substrate that prevent the C_{60} molecule from rotating can be expected. The bonding formed between C_{60} molecules and the

Cu surface has been confirmed by STS experiment and DFT calculations [70], in which a pronounced splitting of the HOMO and LUMO levels is revealed, as a symbol of chemisorption. During bond formation, the amount of charge transfer from the Cu substrate to the C_{60} layer is around 1 electron per C_{60} molecule [67] (or 1.6 electron per C_{60} molecule, according to [71]) and the LUMO of the C_{60} is partially occupied. DFT calculations show that 92% of the transferred charge is localized on the hexagonal ring of the C_{60} molecule nearest to the substrate [70]. In this manner, the charge transfer between the Cu substrate and the first layer C_{60} will not affect the bonding of the second or higher layer C_{60}, therefore the second layer C_{60} molecules are bonded to the first layer via relatively weak van der Waals interaction like in bulk

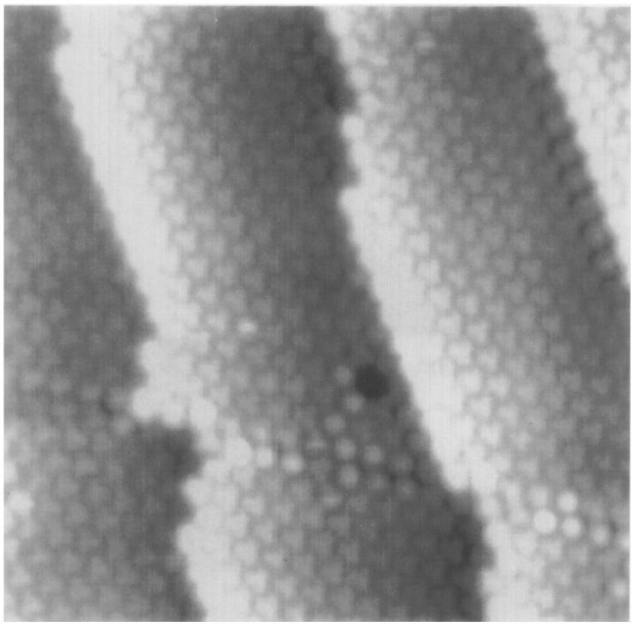

Fig. 2.32 (from [68]): 30 × 38 nm, the close-packed C_{60} monolayer on Cu (111) surface at RT, presenting 4 × 4 superlattice. C_{60} molecules present three-fold symmetry intramolecular structure, indicating that the C_{60} molecules are frozen from rotating. The orientation of C_{60} molecules is also quite uniform.

C_{60}. Because of the different bonding type, the first layer presents much higher desorptions temperature (~700 K) than multilayers (~500 K), and this is a universal situation for C_{60} adlayer grown on all metal substrates. Therefore, this characteristic is commonly employed to produce highly ordered C_{60} monolayer on metal surfaces, in such a process, multilayer of C_{60} is deposited first, followed by annealing to desorb higher layers so only the first layer is left.

2.4.2 C_{60} on Ag (111)

The initial nucleation and growth process of C_{60} on Ag (111) is similar to that on Cu (111), close-packed islands nucleate at step edges and grow to cover the terraces. The Ag (111) 1 × 1 surface has a lattice constant of 2.89 Å, so the most lattice-matched overlayer structure is (2√3 × 2√3)R30º, in which the close-pack direction of the C_{60} layer is parallel to the <112> direction of the Ag (111) surface. In this overlayer structure, every C_{60} molecule has the same adsorption site (a-top) and the C_{60} lattice constant (10.01 Å) is close to the nearest intermolecular distance in the bulk state C_{60} (10.04 Å), Fig. 2.33(a) [72]. Besides the (2√3 × 2√3)R30º structure, several C_{60} overlayer structures with different orientations have been discovered in STM images. For example, C_{60} overlayers with their close-packed directions being 11-14º offset from the <110> direction of the Ag (111) surface are found in the so-called "hex-α" phase. There are also C_{60} overlayers with their close-packed directions being 46-49º offset from the <110> direction of the Ag (111) surface in the so-called "hex-β" phase [73, 68]. In Fig. 2.33(a), domains of C_{60} overlayers with different orientations can be

seen in the same STM image, separated by clear domain boundaries. As depicted in Fig. 2.33(b), C_{60} molecules in the hex-α phase (same to the hex-β phase) occupy different adsorption sites (a-top, hollow and bridge sites), makes these structures less energetically favored than the $(2\sqrt{3} \times 2\sqrt{3})R30^{o}$ phase, therefore, by annealing to 600 K, all the hex-α or hex-β C_{60} layers will transform to the most stable $(2\sqrt{3} \times 2\sqrt{3})R30^{o}$ structure [68].

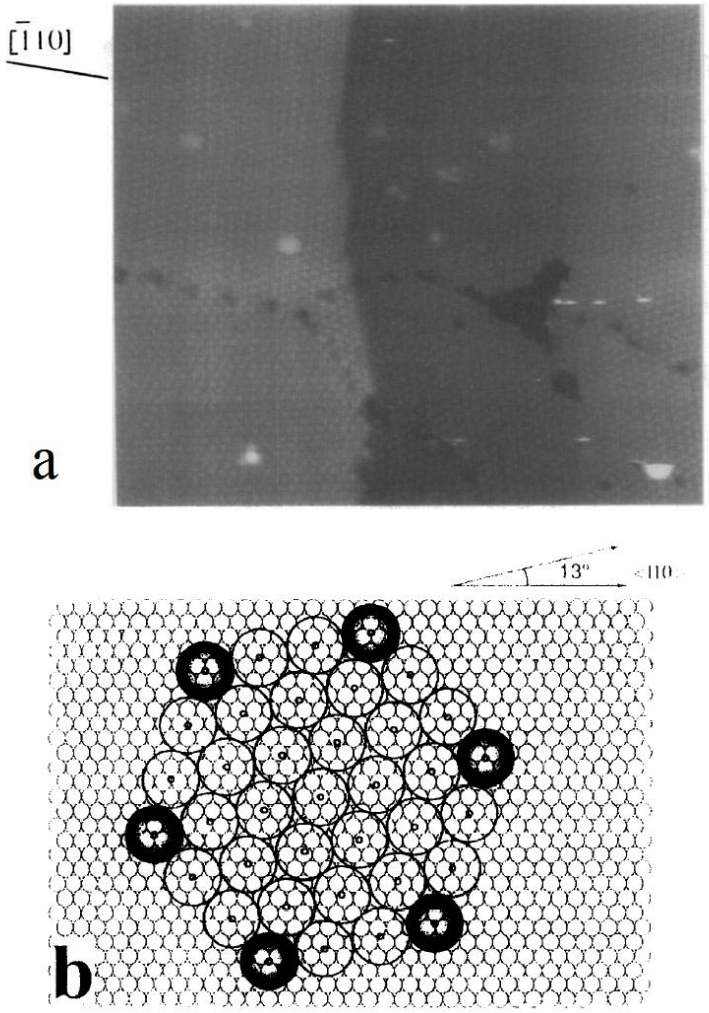

Fig. 2.33 (from [68]) (a): C_{60} monolayer on the Ag (111) surface with different domains. The domain on upper image is in the $(2\sqrt{3} \times 2\sqrt{3})R30^{o}$ phase, the domain at lower-left is in the hex-α phase and the domain in lower-right is in the hex-β phase. (b): A schematic diagram of a C_{60} monolayer has its close-packed direction rotated 13° from the <110> direction of the Ag (111) surface. The C_{60} molecules can be seen occupying different adsorption sites.

Another phenomenon has been observed after a brief annealing of the C_{60} monolayer on Ag (111) at 600 K. Before annealing, the molecules in the $(2\sqrt{3} \times 2\sqrt{3})R30^{\circ}$ C_{60} monolayer show uniform brightness in the STM image because they are all in equivalent adsorption sites. After annealing, the $(2\sqrt{3} \times 2\sqrt{3})R30^{\circ}$ C_{60} monolayer is found to consist of mixed bright and dim molecules, as shown in Fig. 2.34(a). The dim molecules are randomly distributed in the monolayer and take approximately 38% of the total molecular population. Furthermore, the C_{60} molecules are found to be able to switch between bright and dim in sequential STM images. Similar height contrast between molecules within a single layer is also found in annealed C_{60} monolayers on other metal surfaces such as Cu (111) [74], Ni (110) [75], Pt (111) [76] and Au (111) [77]. In order to explain this phenomenon, adsorption induced reconstruction of the substrate is introduced. On Ag (111) surface, using LEED and DFT calculations, H. I. Li *et al.* [78] have found that annealing the C_{60} monolayer will induce a displacement of the silver atom right beneath the molecule and form a nanopit to accommodate the admolecule. C_{60} molecules sitting in such nanopits will have a hexagonal ring facing the substrate and have their mirror plane parallel to the Ag surface's mirror plane, as shown in Fig. 2.34(b). In this configuration, C_{60} molecules are fixed in two orientations, being rotational 180º to each other. XPD observation has confirmed the mixture of orientations at room temperature [79]. Such an orientational difference will lead to a difference in the arrangement of the three STM-sensitive pentagonal rings around the very top hexagonal ring in C_{60} molecules, and cause the brightness contrast in C_{60} monolayer. In contrast, before annealing, the

C_{60} molecules adsorb on intact surface and may rotate freely to give the uniform brightness.

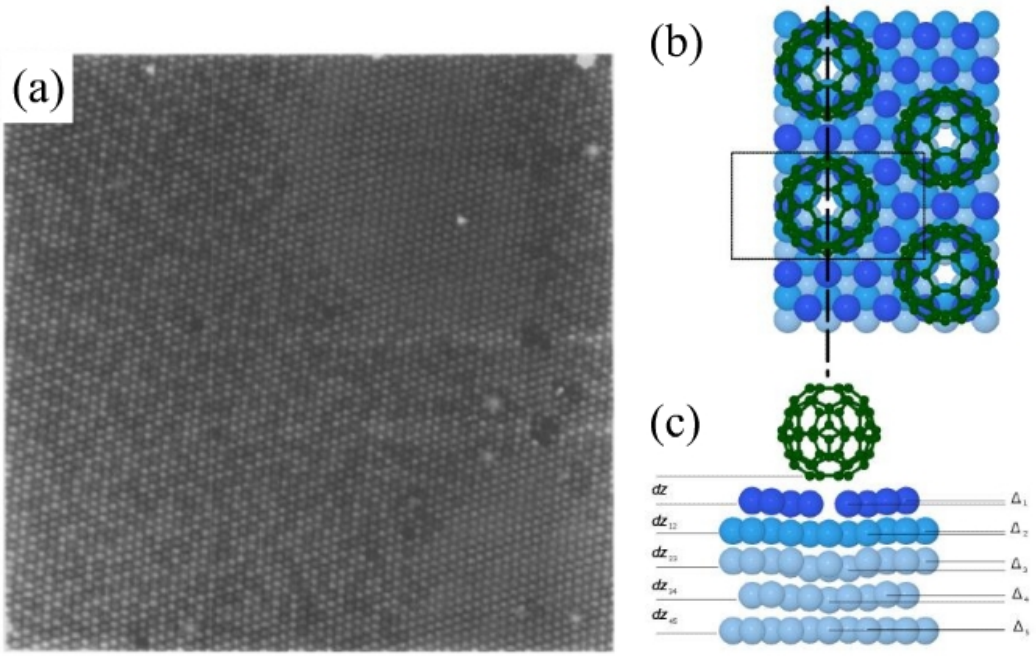

Fig. 2.34 (a) (from [68]): A C_{60} monolayer after annealing, the monolayer consists randomly mixed bright and dim molecules. (b) and (c) (from [78]): A schematic diagram of C_{60} molecules sit on nanopits. The C_{60} molecules have one hexagonal ring facing the substrate and the mirror plane parallel to the substrate's mirror plane, as indicated by the dash line. Two orientations of the molecule coexist, one is shown in the image and the other is rotated by 180º. The three pentagonal rings that can be seen from above in each molecule are arranged in the form of either Δ or a reversed Δ for the two orientations, respectively, giving different apparent heights in the STM image.

2.5 Deposition of C_{60} Fullerene on the Au (111) Surface

2.5.1 Different Configurations

As introduced in detail in Section 2.1, the Au (111) surface is interesting for its unique

reconstruction, of which the discommensuration lines (DLs) form a herringbone pattern. The elbow sites of DLs are found to be the nucleation sites for metal adatoms and organic molecules at room temperature and low temperatures, respectively. Therefore, as expected, the elbow sites of type x DLs were found to be able to trap C_{60} molecules at 30 K [80]. However, at room temperature, similar to the situations with the Cu (111) and Ag (111) surfaces, C_{60} molecules show high mobility on the Au (111) surface. For a low coverage of 0.02 ML, the C_{60} molecules deposited onto Au (111) are found to exclusively adsorb at step edges [72]. When the coverage increases to 0.04 ML, short molecular chains consist of 3~4 C_{60} molecules start to appear at step edges. These molecular chains are formed by the preferential adsorption of C_{60} molecules to the FCC sections of a step, and are separated by empty HCP sections, as shown in Fig. 2.35(a). From this image, one can notice that the steps do not act as diffusing barriers for the C_{60} molecules, because if it does, the step around the large

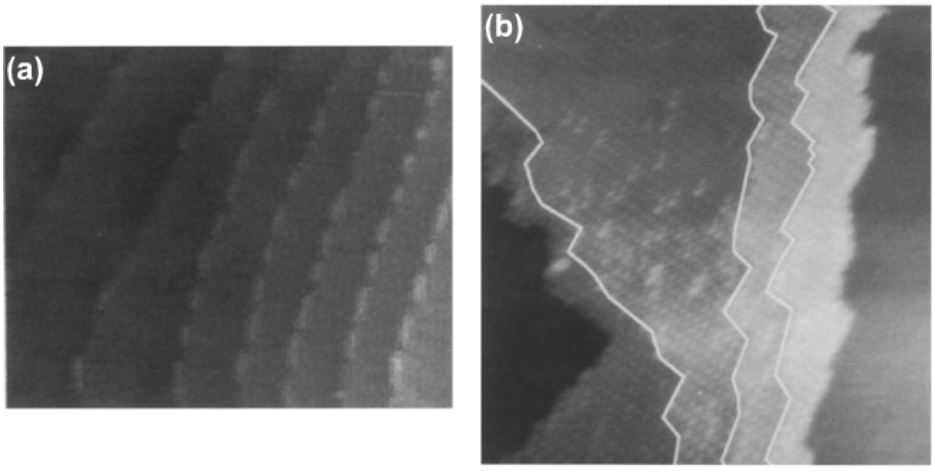

Fig. 2.35 (from [72]) (a): 70 × 58 nm, coverage = 0.04 ML, C_{60} molecules form molecular chains at step edges, all the steps present similar densities of molecules. (b): 35 × 35 nm, coverage = 0.35 ML, close-packed C_{60} layers grow out from step edges on both upper and lower terraces.

terrace should present higher density of molecules than the steps next to narrow terraces, however, the opposite is observed. When the coverage keeps increasing, later landed C_{60} molecules will attach to the molecular chains and grow out from the step edges, simultaneously, the empty HCP sections of step edges start to be occupied. At higher coverage, close-packed C_{60} layers are formed on both the upper and lower terraces linked by a step, as shown in Fig. 2.35(b).

When a close-packed C_{60} monolayer is formed on Au (111), the underlying reconstruction of the gold surface can be lifted by the admolecules thus the C_{60} monolayer is adsorbed on a 1 × 1 Au (111) surface. However, the interaction between C_{60} molecules and the gold substrate is much more complicated in reality, which will be discussed in detail later. Here, for the discussion of different C_{60} monolayer structures, we assume that the substrate is a 1 × 1 surface for simplicity. Four monolayer structures with different azimuthal orientations have been identified so far. The first is 38 × 38 or "in-phase" structure, in which the close-packing direction of the C_{60} molecules is parallel to the close-packing direction of the gold atoms, so this structure will be referred to as R0º for simplicity in the rest of this thesis. In a R0º monolayer, the nearest intermolecular distance is 1.0 nm while the lattice constant of the Au (111) surface is 0.288 nm, thus the C_{60} monolayer cannot form a commensuration structure on this substrate. Instead, the adsorption sites of C_{60} molecules in a R0º monolayer periodically shift from three-fold hollow site to bridge site and to a-top site. Such periodicity leads to a unit cell with the size of 38 × 38 gold atoms or 11 × 11 C_{60} molecules, as shown in Fig. 2.36(a). The second kind of

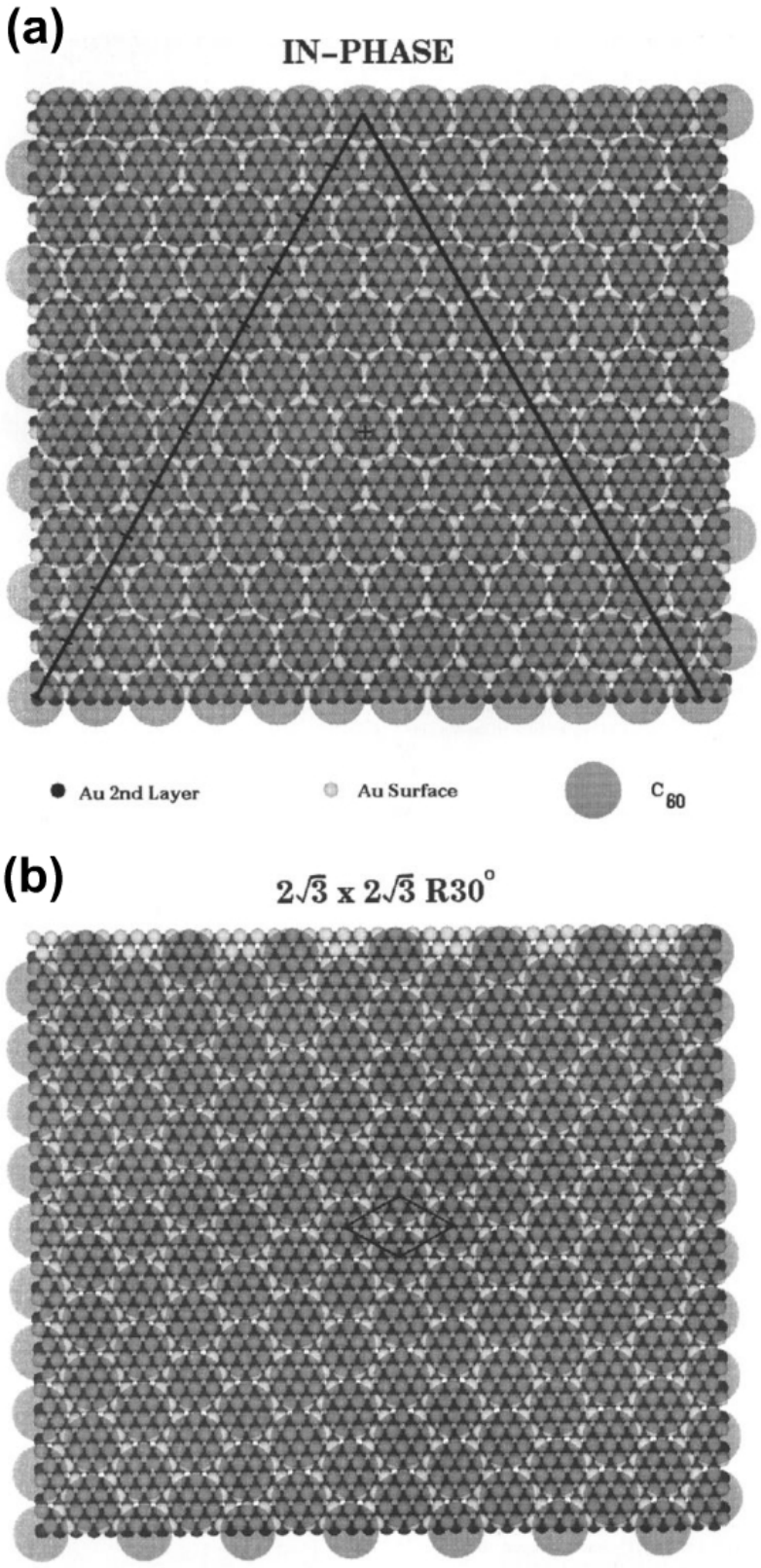

Fig. 2.36 (from [72]) (a): Model of R0º monolayer, the triangle indicates half of a 38 × 38 unit cell. (b): Model of R30º monolayer, a 2√3 × 2√3 unit cell is marked. Every C_{60} molecule occupies identical a-top adsorption site in this structure.

monolayer structure is (2√3 × 2√3)R30º (called R30º structure for simplicity in this thesis), which is similar to that formed on the Ag (111) surface. As the name suggests, for a R30º structure, the close-packing direction of C_{60} molecules is 30º rotated from the close-packing direction of the gold atoms. Because 2√3 times of Au (111) lattice constant (0.988 nm) is almost the same as the preferred intermolecular distance for C_{60} (1.0 nm), the R30º structure is a commensurate structure and every C_{60} molecule occupies identical a-top adsorption site. Thus this structure is more energetically favoured than the R0º structure. A model of the R30º structure is shown in Fig. 2.36(b). Both the R0º and R30º monolayer structures are found using STM by E. I. Altman and R. J. Colton, together with the models suggested [72].

The third kind of monolayer structure is C_{60} R14º, of which the close-packing direction of the C_{60} monolayer is 14º from the <110> direction of the gold surface. The STM observations of this structure have recently been reported independently by our group and R. Berndt, respectively [81, 69]. A model for the R14º structure is given in Fig. 2.37(a). In this model, similar to the situation in R0º monolayer, C_{60} molecules periodically occupy a-top, bridge, hollow sites or any adsorption sites in between them. However, the period is seven C_{60} molecules in the R14º monolayer instead of eleven in the R0º. The fourth kind of monolayer structure, R34º, is suggested in J. Gardener's recent report [77]. In this structure, the period for C_{60} molecules to occupy identical adsorption site further shrinks to three, as shown in Fig. 2.37(b) and Fig. 2.46(c).

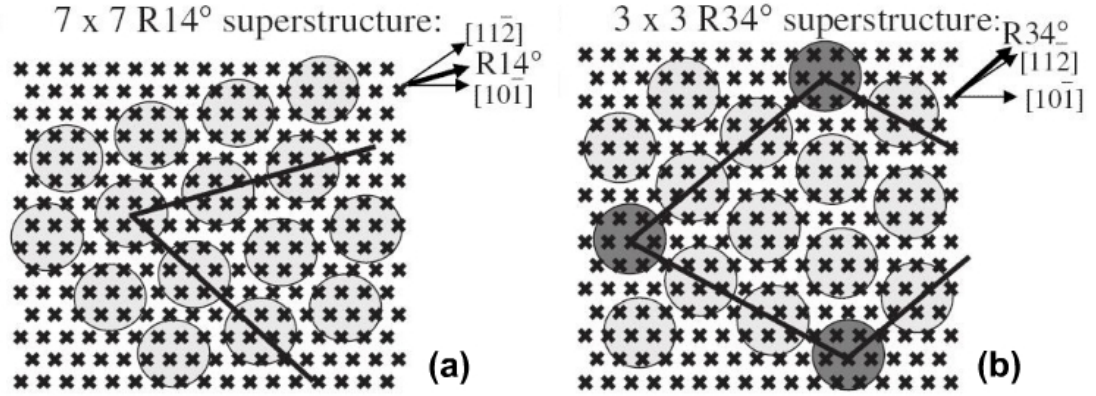

Fig. 2.37 (from [77]): Models of R14º (a) and R34º (b) monolayers. The close-packing direction of each is indicated by thick arrow while the crystallization index of the Au substrate is indicated by thin arrow. Both the two are incommensurate structures. The adsorption site of the C_{60} molecules repeats in a period of seven molecules in R14º and three molecules in R34º.

For the above four monolayer structures, R0º, R30º and R14º have been observed in x-ray diffraction and LEED experiments, respectively [82, 71]. The LEED study also tested the thermostability of C_{60} monolayer adsorbed on the Au (111) surface. At room temperature, multilayers of C_{60} with R0º and R14º structures are observed. By annealing to 473 K, the intensity of the spots representing the R0º structure decreases relative to the R14º structure, indicating that the R14º structure is more stable than the R0º. Moreover, the spot representing the R30º structure appears simultaneously. After annealing to 623 K, only the first C_{60} layer remains and the intensity of LEED spots representing the R30º structure increases at the cost of the other two, indicating that the R0º and R14º structures transform to the more energetically favoured R30º structure upon annealing. The LEED spots for R0º and R14º structures completely disappear after annealing to 693 K. The desorption of the first C_{60} layer happens at 753 K. These thermostability testing results are consistent with the findings from E. I.

Altman's STM study [72], in which the multilayer C_{60} and the monolayer are found to have been desorbed after annealing to 573 K and 773 K, respectively. The ~130 K difference in the desorption temperatures for the first and the multilayers of C_{60} indicates that the interaction between the first C_{60} layer and the gold substrate is not simply through van der Waals force, which is the binding force within C_{60} multilayers. In order to achieve a full understanding of the bonding properties between the C_{60} monolayer and the Au (111) surface, the electronic structure of C_{60} molecule adsorbed on Au (111) is studied by photoemission and STS [63, 71, 83, 84]

2.5.2 Electronic Structure of C_{60} on Au (111)

Photoemission [71] and inversed photoemission [63] spectra are presented in Fig. 2.38(a) and (b), respectively. In Fig. 2.38(a), the energy distribution curve (EDC) of the photoemission spectrum on clean Au (111) surface is shown at the bottom, of which the peak S_1 at ~ -0.3 eV represents the *sp* surface state locating in the projected bulk state band gap and the peak S_2 at ~ -7.7 eV represents the *sd* surface state. The peaks in between S_1 and S_2 are Au *d* band derived, as introduced in Section 2.1.3. The EDC of a 3 ML C_{60} film adsorbed on Au (111) surface presents evident bulk C_{60} characteristics: the peaks marked 1 and 2 are the HOMO and HOMO-1, respectively. For the EDC of C_{60} monolayer, the C_{60} features are much less discernible due to the overlap and hybridization between the C_{60} molecular orbitals and the substrate valence band. However, the peak standing for the HOMO can still be identified at ~ -1.7 eV, which shifts towards the Fermi level from its location in multilayer C_{60}.

Another notable feature is a small peak emerged at ~ -0.1 eV (marked by L), which disappears in the spectrum of multilayer C_{60}. In the inversed photoemission spectra, as shown in Fig. 2.38(b), the peaks representing the LUMO, LUMO+1 and LUMO+2 are clearly seen in the EDC of a 2 ML C_{60} film, however, similar to the situation of photoemission, the peaks for C_{60} monolayer are not so well defined. Even though, a shift toward the Fermi level of the LUMO, LUMO+1 and LUMO+2 peaks can be identified. From the photoemission and inversed photoemission spectra, the

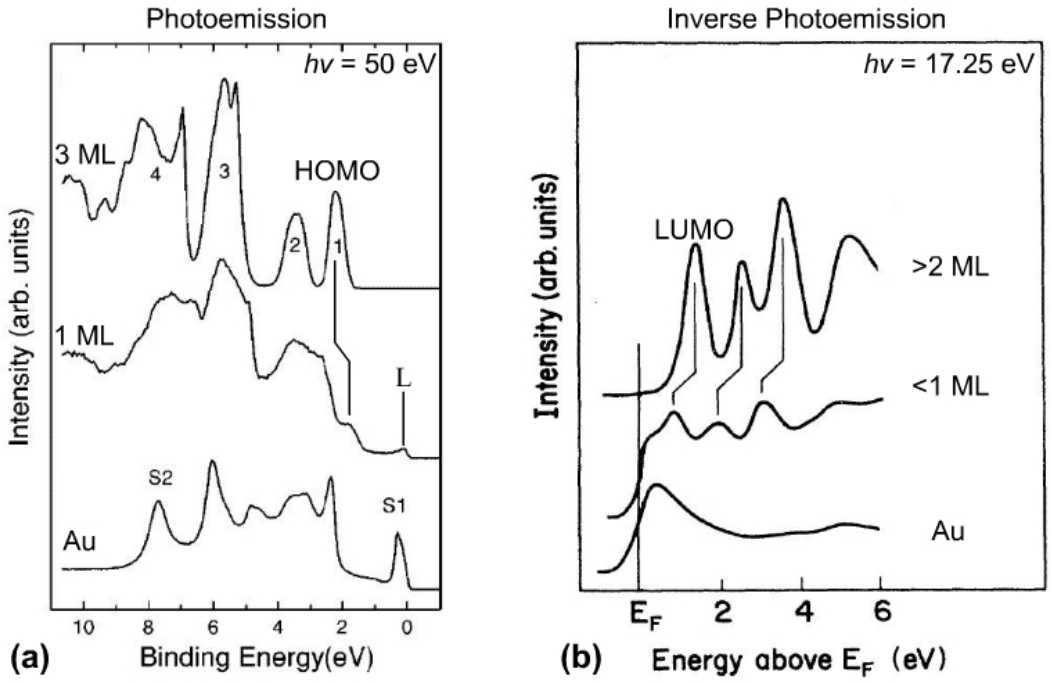

Fig. 2.38 (a) (from [71]): Photoemission spectra of a clean Au (111) surface, monolayer C_{60} adsorbed on Au (111) and 3 ML of C_{60}, respectively. The S_1 and S_2 peaks for clean Au represent the *sp* and *sd* surface states, respectively. The HOMO peak of C_{60} molecule shifts from ~ -2.1 eV for 3 ML to ~ -1.7 eV for monolayer. A small peak near the Fermi level can be seen in the EDC of monolayer, marked by L. (b) (from [63]): Inverse photoemission spectra. The LUMO peak shifts towards the Fermi level at monolayer thickness compared with 2 ML. The shrink of HOMO-LUMO gap for the first C_{60} layer indicating charge transferred from the gold substrate to the C_{60} molecules.

HOMO-LUMO gap for thick C_{60} layer (more than 1 ML) is found to be ~3.7 eV, which is similar to the value of solid C_{60}. And for C_{60} monolayer, the HOMO-LUMO gap shrinks to ~2.7 eV. Such a change in the HOMO-LUMO gap indicates strong interaction between the first C_{60} layer and the Au (111) surface and charge transfer from the metal surface to C_{60} molecules. Similar shifts of the HOMO and LUMO towards the Fermi level for the monolayer are also observed in the scanning tunneling spectroscopy (STS) spectrum in E. I. Altman and R. J. Colton's research [85].

Core-level photoemission is also performed, and the results are shown in Fig. 2.39 for both a thick C_{60} layer and a monolayer. Comparing with the EDC of the thick layer, the peak representing the C 1*s* core-level emission of the C_{60} monolayer is much broadened and shifts towards lower binding energy, moreover, the shape of the peak is asymmetric towards higher energy. All these broadening, shift and asymmetry characteristics of the C 1*s* core-level peak are observed independently by C. T. Tzeng and by T. R. Ohno, and they suggest that the first C_{60} layer becomes metallic due to the charge transfer from metal states to the LUMO of C_{60} molecule [63, 71].

In T. R. Ohno's report [63], the authors propose a resonance formed by the hybridization of the C_{60} molecule's LUMO and the substrate's metal states. This resonance locates above the Fermi level but has a tail extends across the Fermi level. The small peak at -0.1 eV observed in C. T. Tzeng's valence band photoemission (marked L) is much like an evidence for this LUMO-derived resonance. A detailed study of the –0.1 eV peak has been carried out. Photoemission of a C_{60} monolayer with various photon energies reveals that the -0.1 eV peak reaches its highest intensity

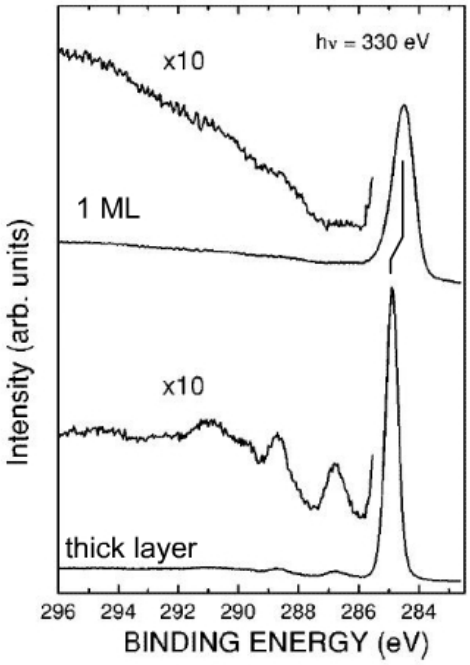

Fig. 2.39 (from [71]): C 1*s* core-level photoemission of C_{60} monolayer and thick layer. The C 1*s* core-level peak for monolayer is broadened, asymmetric and shifted toward lower binding energy compared with that for the thick layer.

at 44 eV, which is the same as the HOMO peak, as shown in Fig. 2.40(a). This feature suggests that the -0.1 eV peak has an angular momentum $l = 5$. The molecular orbitals with an angular momentum l equal to five are the two π-derived orbitals, HOMO and LUMO. As it has the same angular momentum and the same resonant frequency as the HOMO, the -0.1 eV peak should be resulted from a LUMO-derived resonance. After confirming the -0.1 eV peak representing a LUMO-derived resonance, angle-resolved photoemission is used to check its dispersion characteristics. The result is shown in Fig. 2.40(b), only the EDCs taken near the normal-emission direction present the -0.1 eV peak, and the peaks has a tail extending to ~ -0.6 eV. By subtracting all the EDCs with the background spectrum, the tail of the -0.1 eV peak

can be clearly revealed and it is found to move towards higher energy for larger polar angles, which indicates an upward dispersion. In this case, the -0.1 eV peak can be estimated to have a similar upward dispersion, which makes it intersect across the Fermi level and disappear from the photoemission spectrum when the polar angle increases. With such a dispersion, the LUMO-derived resonance that producing the -0.1 eV peak can be confirmed to locate above the Fermi level with a tail extending intersecting the Fermi level. Moreover, the -0.1 eV peak is found to have large intensity for an annealed monolayer than a monolayer without annealing. As

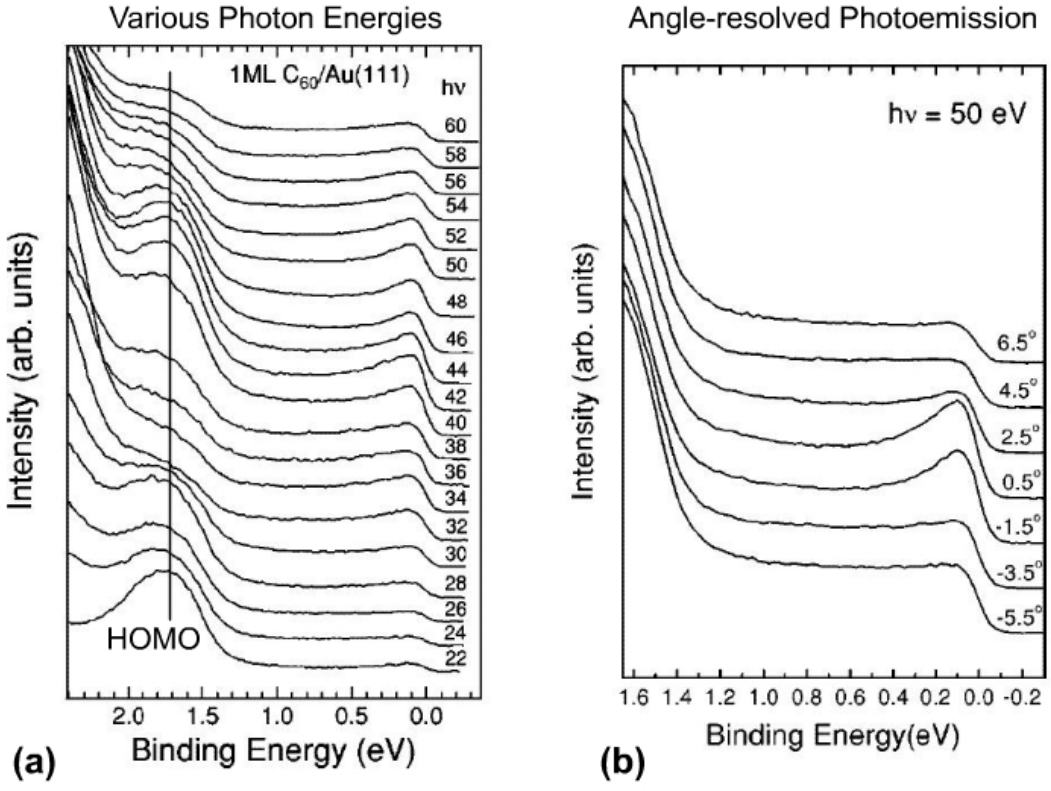

Fig. 2.40 (from [71]) (a): Photoemission with various photon energies. The -0.1 eV peak reaches its highest intensity at the same energy as the HOMO peak. (b): Angle-resolved photoemission. The -0.1 eV peak only appears near normal emission angle and has a tail extending to -0.6 eV. The tail is found to present an upwards dispersion and the -0.1 eV peak is much possible the same.

introduced before, annealing will transfer the R0º or the R14º C_{60} structure to the more energetically favoured R30º structure, which is commensurate with the substrate. Therefore, the special configuration of C_{60} monolayer should also influence the electronic structure.

With the results from above photoemission experiments, a picture can be drawn for the C_{60}/Au (111) interaction. Charges transfer from substrate metal states to one of the LUMO t_{1u} bands of C_{60} molecules, which is similar to the situations of alkali metal doped solid C_{60} or C_{60} molecules adsorbed on other metal surfaces. This charge transfer shrinks the HOMO-LUMO gap of C_{60} molecule as well as produces a LUMO-derived resonance locating right above the Fermi level. The resonance has an upwards dispersion and has its low energy end below the Fermi level at -0.1 eV. Because of the Fermi level resonance, the first C_{60} monolayer is metallic. Moreover, the charge transfer between the Au (111) surface and C_{60} monolayer is calculated to be 0.8 electrons per molecule, with an uncertainty of ± 0.2 electrons. However, a charge transfer of this amount, cannot influence the electronic structure of higher C_{60} layers but only the first, thus photoemission spectra from C_{60} films thicker than 1 ML have similar features to bulk solid C_{60}. Therefore, the first C_{60} monolayer is chemically bonded with the substrate with charge transfer while higher layer are bonded with van der Waals interaction just like in solid C_{60}. This conclusion is consistent with the difference in thermostability of the first C_{60} monolayer and that of the multilayers.

The resonance found intersecting the Fermi level is consistent with the results of

near-edge X-ray adsorption fine structure (NEXAFS) spectra of C_{60} submonolayer adsorbed on the vicinal Au (887) and the Au (111) surfaces [84], which suggest a gap state inside the HOMO-LUMO gap. The Au (887) vicinal surface consists of periodic Au (111) terraces (width ~3.9 nm) separated by monoatomic steps, and C_{60} molecules will form an ordered mesh of close-packed rectangularly shaped islands on it at 0.5 ML coverage. The authors claimed that on both the Au (887) and the Au (111) substrate, NEXAFS spectrum reveals a new feature in the HOMO-LUMO gap, locating at the low energy side of the LUMO peak, as shown in Fig. 2.41(a). This feature is explained as a gap state, of which the possible band structure is sketched in Fig. 2.41(b). The gap state featured in the spectrum is attenuated when the coverage increases to monolayer, and it completely disappears for thick C_{60} film. Therefore, the

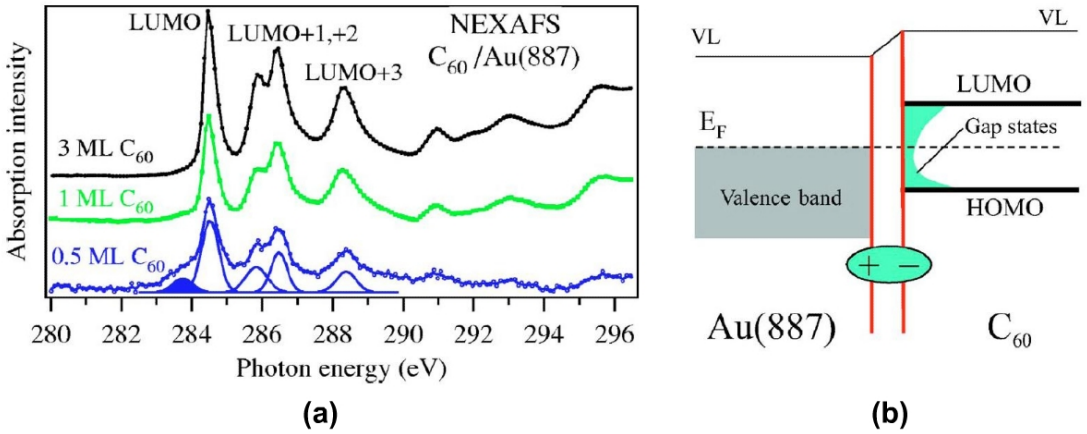

Fig. 2.41 (from [84]) (a): NEXAFS spectrum for C_{60} layers adsorbed on the Au (887) surface. The filled Gaussian curve indicates the gap states inside the HOMO-LUMO gap for submonolayer coverage. For Au (111) as the substrate, the same gap states are observed at similar coverage, but the spectrum is not shown in the report. (b): A schematic diagram of the band structure includes the gap states for the system. The charge transfer from the substrate to the C_{60} monolayer leads an interfacial dipole.

gap state is related to the C_{60} molecules with reduced lateral coordination, for example isolated molecules or molecules at island edges, such molecules may act as defect to induce a continuum of states in the band gap.

The coexistence of LUMO-derived resonance near the Fermi level and the LUMO peak observed at ~1.0 eV suggests a split of the LUMO. This split can be understood as the LUMO are partially occupied, only one of the LUMO t_{1u} bands has accepted charges from the substrate and produced gap resonance, which is also the situation in alkali metal doped solid C_{60}. A LUMO splitting is directly observed in the STS of C_{60} molecules adsorbed on Ag (100) surface, as shown in Fig. 2.42(b), the LUMO splits to $LUMO_{\alpha}$ and $LUMO_{\beta}$ [83]. The $LUMO_{\alpha}$ locates intersecting the Fermi level like what is expected for the gap state, while the $LUMO_{\beta}$ is well above the Fermi level. The STS data of C_{60} molecules adsorbed on Au (111) surface is shown in Fig. 2.42(a), however, no splitting of the LUMO can be found. The locations of the LUMO, LUMO+1 and HOMO peaks in STS spectrum are exactly the same as that revealed by photoemission and inversed photoemission, which gives a HOMO-LUMO gap of ~2.7 eV. For not revealing the gap states in STS, F. Schiller gave a possible explanation in his paper [84] that the *dI/dV* signal in STS is proportional to the DOS at the tip position, which is ~1 nm above the sample. The charge transfer only fills the LUMOs localized near the C_{60}-Au interface, thus the gap states produced by these LUMOs are also localized near the interface and spatially decays into the vacuum. At the tip height, the contribution of these states to the signal may be too weak to be identified. Another notable aspect is that the STS data, NEXAFS spectrum and

photoemission spectrum are obtained on the Au (111) surface with isolated C_{60} molecules, 0.5 ML of C_{60} and a complete monolayer, respectively. The difference in the coverage leads to different lateral coordination of C_{60} molecules and may influence the electronic structure, as revealed in the NEXAFS experiment.

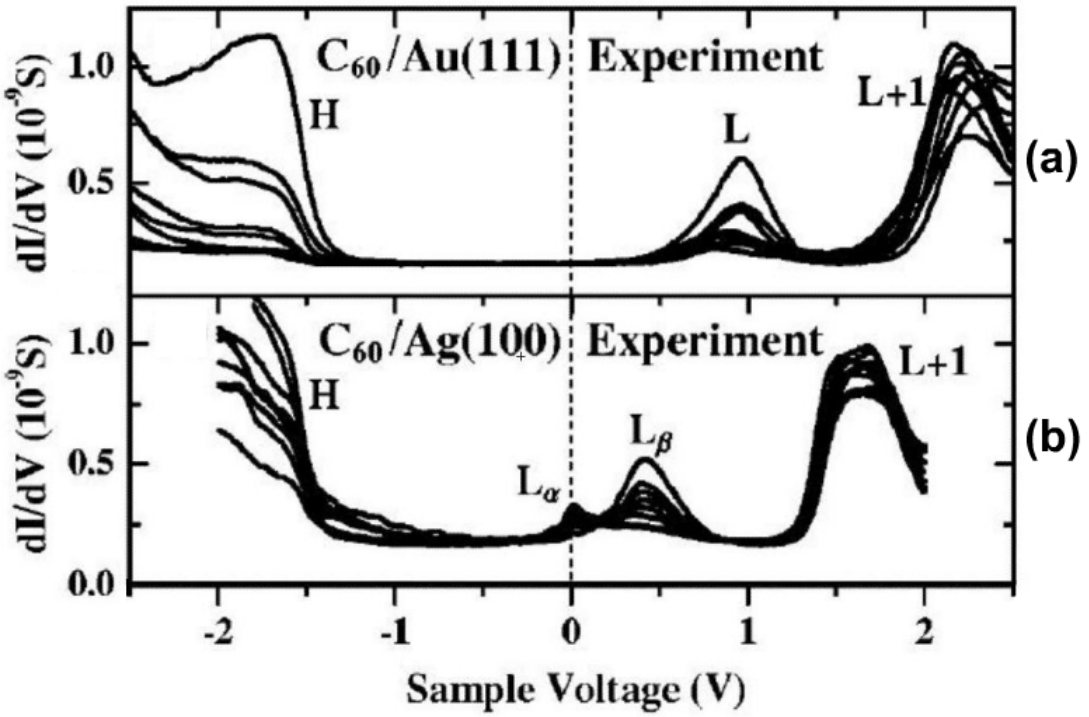

Fig. 2.42 (from [83]): The STS spectrum of C_{60}/Au (111) (a) and C_{60}/Ag (100) (b), respectively. The LUMO of C_{60} molecule on Ag (100) surface splits into $LUMO_{\alpha}$ and $LUMO_{\beta}$, of which the $LUMO_{\alpha}$ locates across the Fermi level, as a representing of the gap states. Such split of the LUMO is not observed in the spectrum of C_{60}/Au (111).

The STS map is used to find out the distribution of local density of states (LDOS) in different molecular orbitals over a C_{60} molecule [83]. The STS maps shown in Fig. 2.43 are obtained with sample positive bias voltages of 2.2 V, 1.0 V and sample negative -1.7 V, which equals to the binding energies of the LUMO+1, LUMO and

HOMO, respectively. From Fig. 2.43, for C_{60} molecule adsorbed on the Au (111) surface, the LUMO+1 is found to reach its highest LDOS at the pentagonal rings, which present themselves as bright rings in the image. The LDOS distribution of the LUMO is an inversion of the LUMO+1's, pentagonal rings are darks under this bias voltage. For the HOMO, its LDOS is quite dislocalized, distributed over the whole molecular cage.

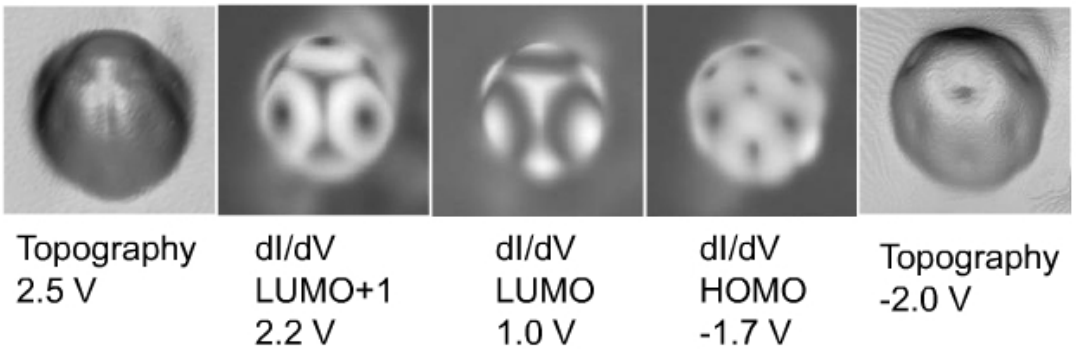

Fig. 2.43 (from [83]): The STS map taken over C_{60} molecule adsorbed on Au (111) surface, revealing the distribution of LDOS of different molecular orbitals (the LUMO+1, LUMO and HOMO, respectively). Two topographic images taken at different bias voltages are shown as a reference.

To investigate the charge transfer between the C_{60} molecule and the Au (111) surface, theoretical simulation is also performed [83]. The results is shown in Fig. 2.44, the situation of C_{60} molecule adsorbed on the Ag (100) surface is also presented for reference. In these images, blue color indicates an increase in electronic density while red color indicates a reduction of it. For the C_{60}/Au (111) interface, the redistribution of electrons is localized near the interface, which is consistent with the

above explanation of the different observations of the gap states by photoemission and STS. Compared with the situation of C_{60}/Ag (100), the charge redistribution of C_{60}/Au (111) interface is more like a charge-neutral polarization rather than charge transfer. DFT calculations suggest a charge transfer of 0.2 electrons per C_{60} molecule on Ag (100) but a negligible amount of charge transfer on Au (111). This result is inconsistent with experimental observation.

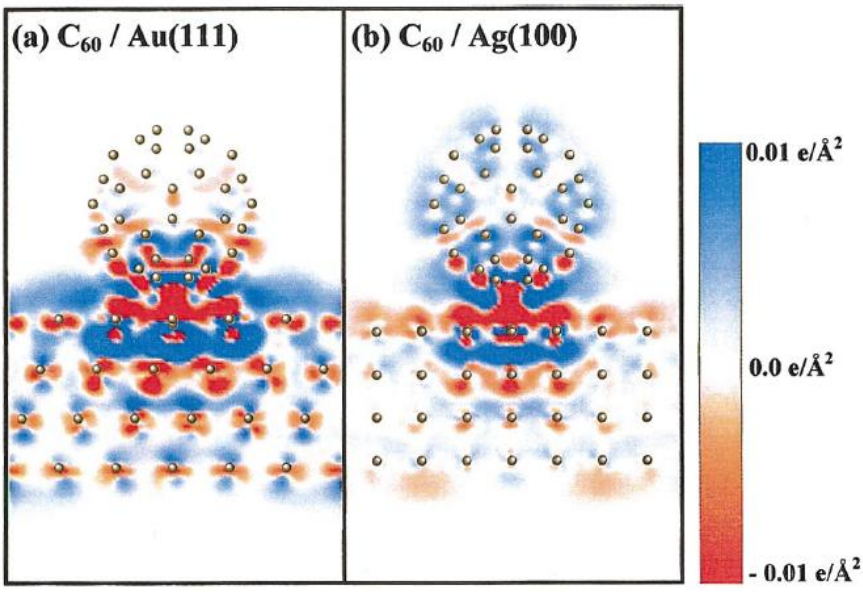

Fig. 2.44 (from [83]): Theoretical simulation of the electronic redistribution of C_{60}/Au (111) interface and C_{60}/Ag (100) interface. Blue and red colors indicate the increase and decrease of electronic density, respectively. The charge transfer on Ag (100) is more evident while on Au (111) the electronic redistribution is more like an interface polarization.

With all the above studies of the electronic structure of C_{60} molecule adsorbed on the Au (111) surface, chemisorption with strong bonding of the first C_{60} layer on the substrate should be expected. However, for the amount of charge transfer from the metal surface to the C_{60} molecule and the existence of gap states, the answers from

different techniques do not match well. The coverage and special molecular configurations seem to influence the electronic structure too. In this case, there is still room for further research of the C_{60}/Au (111) interaction.

2.5.3 C_{60} Induced Surface Modification

As mentioned above, C_{60} molecules can lift the underlying herringbone reconstruction, and adsorb on a 1 × 1 Au (111) surface. This is the most frequently observed situation, as shown in Fig. 2.45(a) [86]. In the image, a R30º C_{60} monolayer is seen, and the height of the molecules in the monolayer is uniform, indicating that the monolayer is sitting on an atomic flat substrate. The C_{60} monolayer also influences the reconstruction around the island, the discommensuration line (DL) at the edge of the C_{60} island deviates from its natural contour and forms a close loop to enclose the island. The region next to the C_{60} island is HCP-stacking, as marked in Fig. 2.45(a), thus the region underneath the island should be FCC-stacking, which is consistent with a bulk terminated 1 × 1 Au (111) surface. Moreover, in the regions that the growth front of the C_{60} island is parallel to the DLs, the island edge is straight and uniform, as shown by the right part of the island in Fig. 2.45(a). On the other hand, if the growth front is perpendicular to the DLs, the island will present a zigzag edge, as shown by the left part of the island in Fig. 2.45(a). Such phenomenon indicates that the DLs act as a growth barrier for the C_{60} island.

Though the C_{60} monolayer lifts the underlying herringbone reconstruction in most cases, occasionally, reconstruction of the Au substrate can be revealed in STM

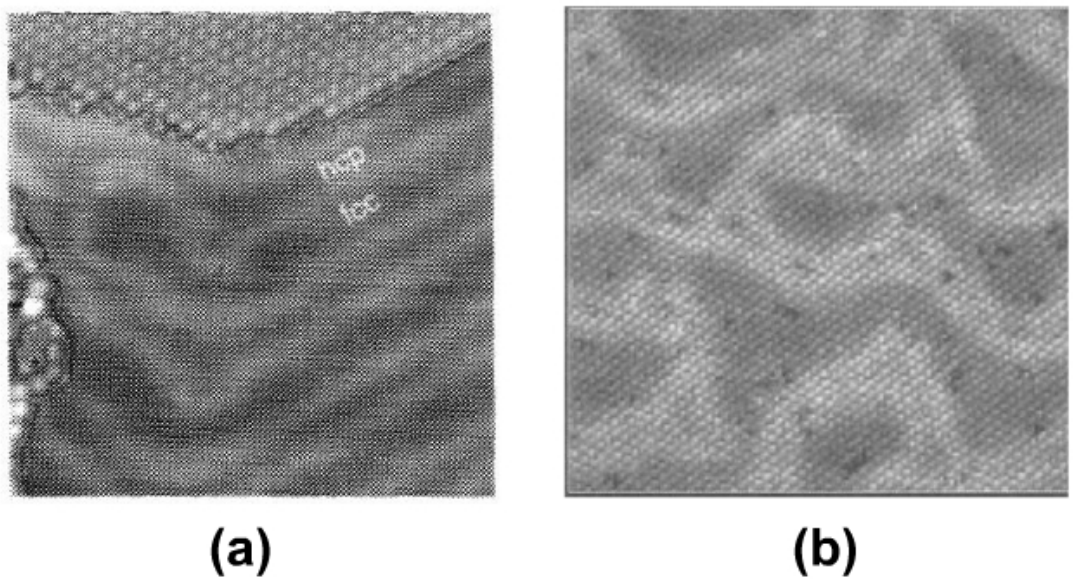

Fig. 2.45 (a) (from [86]): 20 × 20 nm, a R30º C_{60} island adsorbs on Au (111) surface, at the upper part of the image. The HCP and FCC regions are marked. (b) (from [87]): 50 × 50 nm, ridged lines in C_{60} monolayer reveals the remaining substrate reconstruction, the periodicity of reconstruction is enlarged from 6.3 nm to 9~12 nm.

images as a corrugation of the C_{60} monolayer. E. I. Altman and R. J. Colton [86] reported to observe six pairs of ridged lines in a large C_{60} island, which are resulted from a remaining substrate reconstruction. However, these ridged lines are not periodically ordered as the DLs on the clean Au (111) surface, pairs of ridged lines are missing, leads to large FCC regions between the existing pairs of ridged lines and small HCP regions sealed within a pair. Therefore, the corrugation of C_{60} monolayer looks like resulting from an uncompleted relief process of the substrate reconstruction. J. K. Gimzewski prepared a C_{60} monolayer on the Au (111) surface in a different method. They deposited multilayers of C_{60} first, and after annealing to 700 K, all C_{60} molecules desorbed except the first layer [87]. On this C_{60} monolayer, ridged pattern consists of molecules ~1 Å higher than other molecules can be observed all over the

surface, on both R0º domains and R30º domains. As shown in Fig. 2.45(b), this ridged pattern is evidently resulted from a remaining herringbone reconstruction of the substrate. But the periodicity of the reconstruction is enlarged from ~ 6.3 nm for the clean Au (111) surface to 9~12 nm under the C_{60} monolayer. (The authors concluded that the adsorption of C_{60} molecules can only partially relieve the surface strain of the Au surface, leading to an enlargement of the reconstruction unit cell but not a completely relief of it). The observation of remaining reconstruction under C_{60} monolayer is also reported recently by J. A. Gardener *et al*. [77].

The lift of the reconstruction by the adsorption of C_{60} molecules can be easily understood as the energy difference between reconstructed and unreconstructed Au (111) surfaces is small, ~0.1 eV per surface atom, while a typical chemical adsorption energy is also in the magnitude of 0.1 eV per substrate atom. Because the C_{60} molecule tends to form strong chemical bond with the Au (111) surface, the relief of substrate's surface strain and the lift of the reconstruction should be expected. However, the remaining substrate reconstruction depends on the variation in the growth condition of the C_{60} monolayer. To lift the reconstruction, the Au atoms in the HCP regions need to laterally shift to FCC sites and the extra atoms at the elbow sties of type *x* DLs need to be accommodated. These atomic motions of the relaxation process require certain time to be completed. Typically, a reconstruction requires about 3 minutes to respond to an environment change, and the movement of atoms for relocating may last over 15 minutes [88]. In J. K. Gimzewski's research, the deposition rate is very high, therefore, the surface are fully covered before the

completely lift of the reconstruction, once the monolayer is formed, the strong bonding between the C_{60} molecules and Au surface restricts the long-range rearrangement of surface atoms, thus left a reconstruction with enlarged periodicity. In the situation of slow deposition rate, the Au surface atoms have enough time to rearrange before they are covered, thus remaining reconstruction will be very rare.

Besides the ridged lines due to remaining substrate reconstruction, there is a more frequently observed feature on the C_{60} monolayer, the dim molecules, which appear lower than surrounding molecules. This feature is similar to the dim molecules observed in the C_{60} monolayer on the Ag (111) surface but the situation on the Au (111) surface is much more complicated. According to the density and distribution of the dim molecules inside a C_{60} monolayer, five kinds of structures have been identified. The first is C_{60} monolayer without any dim molecules, this kind of structure is often observed for the R30º monolayer at room temperature. The second kind is a uniform height C_{60} monolayer decorated with a small number of dim molecules, and the distribution of the dim molecules is random. This kind of structure has been observed on both the R0º and the R30º monolayers at room temperature. The third kind of structure is observed only on R30º monolayer, which presents high density of randomly distributed dim molecules, as shown in Fig. 2.46(a). Therefore, this kind of structure is named “disordered” structure. A disordered monolayer is seen at room temperature only occasionally but becomes overwhelming after annealing to 673 K [77]. Because the R0º monolayer is found to transfer to the R30º upon annealing, the large abundance of disordered domains observed after annealing are

possibly emerged from either an uniform height R30º monolayer or an orientation-transferred R0º monolayer. The dim molecules are also found on the two newly reported structures, the R14º and the R34º monolayers. Moreover, the distributions of the dim molecules in these two kinds of monolayers present long-range orders, of which clusters comprising 1~3 dim molecules arrange themselves into a hexagonal superlattice over the whole monolayer, as shown in Fig. 2.46(b) and (c). Therefore, this kind of monolayer is named “quasiperiodic” structure. However, the periodicities of the R14º and R34º quasiperiodic monolayers are different. In the R14º monolayer, a dim molecular cluster appears about every 7 molecules along each close-packing direction of the molecules, resulting in a 7 × 7 unit cell for the superlattice. On the other hand, the periodicity for the R34º monolayer is about 3 molecules, resulting in a 3 × 3 unit cell. Notably, the periodicity of the appearance of a dim molecule on the R14º and R34º monolayers is consistent with the periodicity of the molecule to occupy identical adsorption site in these two kinds of monolayers, 7 and 3 molecules, respectively, indicating a possible relationship between a special adsorption site and the origin of the dim molecule.

On either disordered or quasiperiodic monolayer, the C_{60} molecules are found to switch from bright to dim or vice versa. The switch on disordered monolayer is completely random, can happen to any molecules, while on quasiperiodic monolayer, the switch can only happen to the molecule inside a dim cluster or its neighboring molecules, which means that the dim molecule can only appear at a location defined by the superlattice. The switch of molecules has been proved not a tip-induced

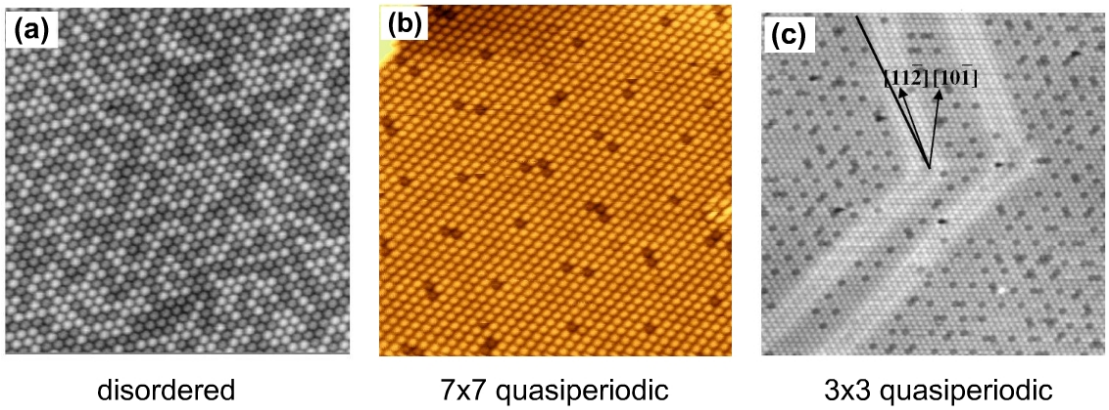

Fig. 2.46 (a) (from [77]): A disordered monolayer with high density of dim molecules. (b) (from my own work): 34 × 34 nm, V = 1.0 V, I = 0.3 nA, a R14º monolayer with 7 × 7 superlattice formed by clusters of dim molecules. (c) (from [77]): A R34º monolayer with 3 × 3 superlattice, two pairs of ridged lines can be seen, indicating some remaining reconstruction of the substrate. With the ridged lines, the crystallization directions of the Au surface can be identified (indicated by the two arrows), the close-packed direction of the C_{60} monolayer (indicated by the solid line) is 4º and 34º to the [11-2] and [10-1] directions of the substrate, respectively.

phenomenon [77], as the total number of molecules that changed their contrast keeps increasing with constant rate when the STM scanning is paused for a certain time. And the switch rate is found to be independent from the scanning parameters. The switch between bright and dim of the molecules is prevented at 77 K, indicating that this is a kinetically driven process.

The dim molecules in the C_{60} monolayer adsorbed on the Au (111) surface have been observed by many researchers, and different theories have been suggested to explain the origin of the height contrast within a monolayer. J. K. Gimzewski *et al*. found the apparent height of dim molecules is ~0.2 nm lower than surround molecules [87]. They proposed that the smaller height is due to gold vacancies under the dim

molecules, which are pre-exist on the Au (111) surface and are stabilized at certain positions by the adsorbed C_{60} molecules. The researchers also estimated a vacancy with the size of 4 gold atoms is required for inducing a height difference of 0.2 nm.

G. Schull *et al*. studied the R14º monolayer at low temperature, 5.7 K [69]. The dim molecules of a 7 × 7 quasiperiodic monolayer are found to be ~0.6 Å lower than surrounding molecules under normal STM scanning parameters of 0.1 nA tunneling current and 1.5 V bias voltage. They suggested that the adsorption of C_{60} monolayer induces a rearrangement of substrate atoms and vacancies are formed under the dim molecules, moreover, they suggested that the vacancy consists of six missing Au atoms.

E. I. Altman *et al*. observed a height difference of 0.09~0.11 nm between bright and dim molecules in a R30º monolayer at room temperature [85]. They did not consider the role of vacancy on the substrate, instead, they testified the electronic structure of the bright and dim molecules by STS, respectively, of which the results are shown in Fig. 2.47. As can be seen, the LUMO of bright molecule is closer to the Fermi level than the LUMO of dim molecule, indicating that the amount of charge transfer from the substrate to the molecule is different for the bright and dim molecules. The difference in electronic structure may be responsible for the apparent height contrast. Because all the molecules in a R30º monolayer occupy identical a-top adsorption sites, the origin of the electronic difference could only be the variety in the molecular orientation, for example, molecule with hexagonal ring facing the substrate should have different bonding configuration with the underneath Au atom to the

molecule with a C-C bond facing the substrate. Therefore, the different bonding states with the substrate lead to the variety of the amount of charge transfer thus cause the difference in the electronic structure and in the apparent height.

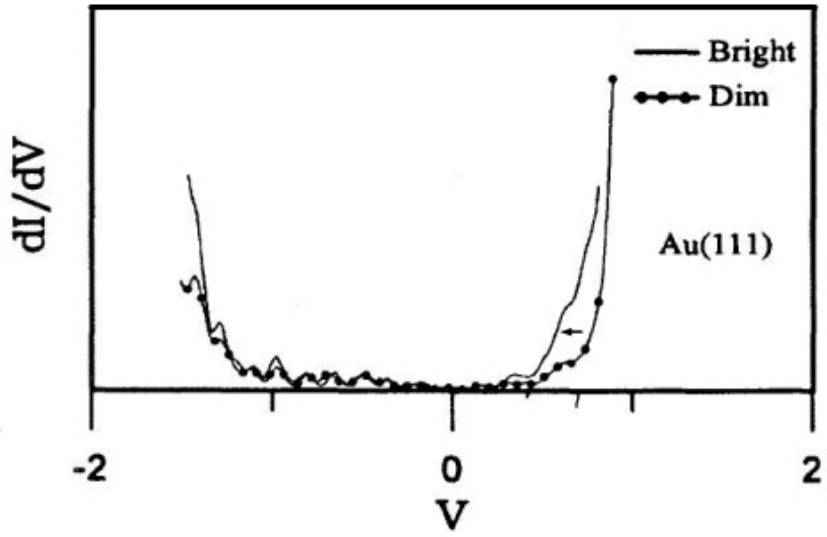

Fig. 2.47 (from [85]): STS spectra of bright and dim molecules in a C_{60} monolayer adsorbed on the Au (111) surface. The unoccupied feature of bright molecule is closer to the Fermi level than the dim molecule's, as indicated by the arrow.

J. A. Gardener *et al*. found that the height contrast between the bright and dim molecules varies from 0.035 nm to 0.12 nm with different bias voltage (in a range of ± 2 V), which confirms the difference in electronic structure, because if the apparent height difference is only due to geometry, it should keep constant under different scanning conditions [77]. However, the origin of the difference in electronic structure cannot be the variety in molecular orientation because the bright and dim molecules are found to have identical orientation within the same monolayer. The authors

suggest that a vacancy or so-called “nanopit” under the dim molecule formed by rearrangement of substrate atoms should be the origin of the difference in electronic structure. By sitting on a nanopit, the coordination with substrate will be enhanced, and more charges will be transferred to the LUMO of the molecule. This is consistent with the fact that the apparent height difference reaches its maximum when the LUMO of the molecule is probed. The model of nanopit can explain why there are fewer dim molecules in the regions of remaining substrate reconstruction, as seen in Fig. 2.46(c), because at these regions, the substrate is not much modified by the adsorption, less nanopit can thus be formed. Furthermore, the appearance of large amount of dim molecules after annealing in disordered monolayer indicates that the formation of nanopit requires overcoming a certain energy barrier, of which the required thermal energy can be offered by the annealing. Moreover, because every molecule in a R30º monolayer occupies identical a-top adsorption site, there is no preferential location for the nanopit formation, which leads to a random distribution of dim molecules in a disordered monolayer. On the other hand, due to the periodicities of the adsorption sites in the R14º and the R34º monolayers, the formation of nanopit may preferentially take place at certain locations that can present a periodicity corresponding to the periodicity of adsorption site, which leads to the observed 7 × 7 and 3 × 3 superlattice formed by dim molecules, respectively. However, the J. A. Gardener’s model does not match with E. I. Altman’s STS result, because by sitting on a nanopit, the charge transfer should be enhanced thus the dim molecule should have the LUMO closer to the Fermi level than the bright molecule,

but the opposite is observed in the STS spectrum. Therefore, the explanation of the origin of the dim molecules requires more consideration.

Another kind of surface modification on the Au surface induced by the adsorption of C_{60} submonolayer is observed on the Au (433) surface [89]. The Au (433) surface consists of Au (111) terraces of 4.0 nm in width separated by a bunch of narrow terraces of 1.4 nm. As shown in Fig. 2.48(a), after deposition of 0.5 ML C_{60} molecules, the wide (111) terraces are empty and all the molecules are adsorbed on the bunches of steps. Because the separation of the steps inside a bunch (1.4 nm) does not match the nearest neighboring molecular distance preferred by C_{60}, the C_{60} molecules adsorbed on a bunch cannot form a close-packed structure. However, by annealing to 500 K, a faceting process will take place resulting in a new

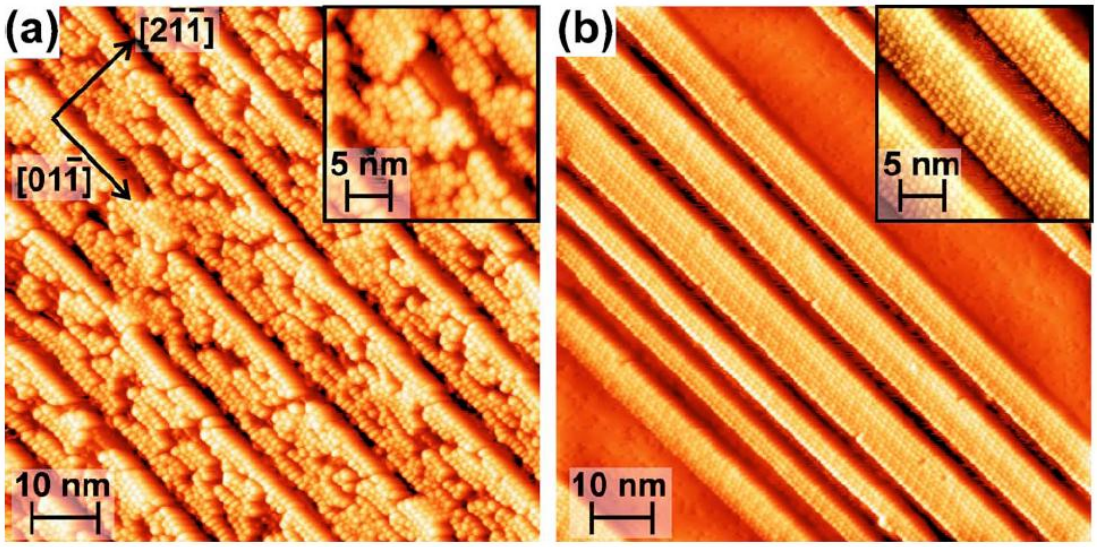

Fig. 2.48 (from [89]) (a): Before annealing, the C_{60} molecules exclusively adsorb on the bunches of steps and form disordered regions. The wide (111) terraces between the bunches are empty. (b): After annealing to 500 K. The steps facet to a new periodicity that allow the molecules adsorbed on them can form close-packed layers. The (111) terraces between the C_{60} bands are widen.

step-separation which is suitable for the C_{60} molecules to form a close-packed layer. As shown in Fig. 2.48(b), the C_{60} molecules adsorbed on a bunch of steps form a close-packed monolayer, separated by wide Au (111) terraces which have larger width than before. This faceting is a thermodynamic process that minimizes the free energy of the system, indicating that the intermolecular interaction between the molecules in a monolayer is part of the system's free energy and the formation of a close-packed layer from a disorder arrangement could minimize the total energy. In order to achieve the minimization of system's energy, a surface modification can be induced by the adsorption of C_{60} molecules.

Surface modification in the forms of lifting reconstruction, nanopit formation and step faceting are all investigated in my research and will be discussed in the following chapters.

2.5.4 The Diffusion of C_{60} Molecules on the Au (111) Surface

As mentioned before, the desorption temperatures of the first C_{60} layer and higher layers are found to be 753 K and 473 K, respectively, by C. T. Tzeng *et al*. [71]. The people also studied the desorption process of the first C_{60} monolayer in detail by carrying out C 1*s* core-level photoemission after annealing to different temperatures. In the spectrum, the normalized intensity of C 1*s* core-level peak represents the amount of C_{60} molecules left on the surface, and these normalized intensities obtained are plotted as a function of annealing temperature in Fig. 2.49. By fitting the curve in Fig. 2.49 into two different desorption models, two desorption energies for C_{60}

molecule on the Au (111) surface can be deduced, 1.87 eV and 1 eV, respectively. The first model is called first-order desorption, in which the intermolecular interaction is not important for a C_{60} molecules and the desorption energy only depends on its interaction with the substrate. In this model, a molecule inside the monolayer can desorb from any location. The second model is half-order desorption, in which the intermolecular interaction is large enough to influence the desorption energy. In this model, the desorption will happen at the rim of an island where the lateral coordination of a molecule is reduced. The experimentally measured desorption energy for C_{60} multilayer on the Au (111) surface is 1.4 eV, because the C_{60} layers higher than the first layer are bonded by van der Waals interaction, the desorption energy for the stronger bonded first layer must be much higher than 1.4 eV, thus excludes the possibility of the half-order desorption. However, if adopt the first-order desorption model, in which the intermolecular interaction is negligible, there is still a problem. The theoretically deduced intermolecular interaction for a C_{60} molecule in the first monolayer is 1.1 eV, which is too larger to be neglected during the desorption of C_{60} molecules. Therefore, the first-order desorption model must to be modified. C. T. Tzeng *et al*. [71] suggested that the C_{60} islands will transform into “gas” phase on the substrate before desorption, thus results in different desorption energy at different coverage. This prediction of the 2-Dimensional gas phase C_{60} is partially proved by S. Guo *et al.* in their STM research of thermal diffusion of C_{60} islands on the Au (111) surface [90].

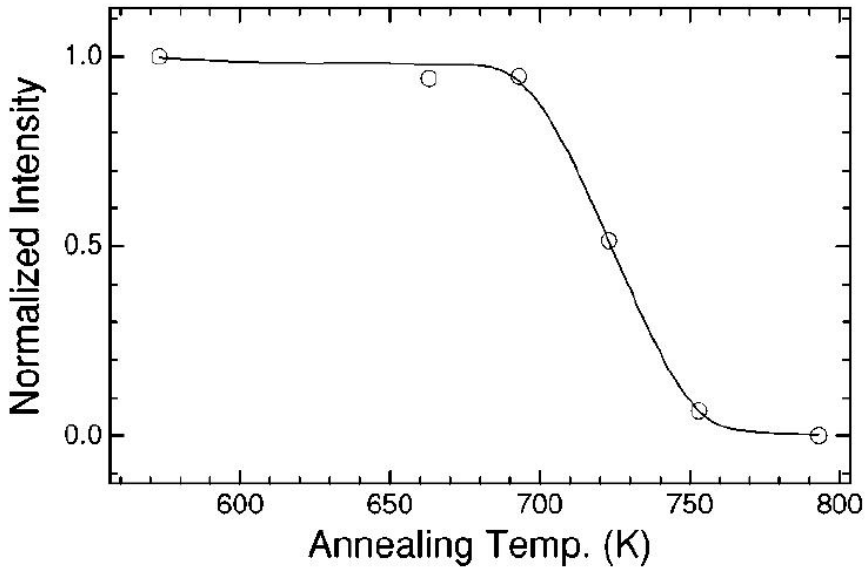

Fig. 2.49 (from [71]): The normalized intensities of C 1*s* core-level photoemission as a function of annealing temperature. The circles are the experimental data and the line is a smoothed interpolation between the circles.

In the research of S. Guo *et al*., a submonolayer of C_{60} molecules is deposited onto the Au (111) surface, and the diffusion behavior of the molecules is investigated using STM under ambient condition. As a function of time, small changes in the shape of the C_{60} island are observed at the edges of the island, indicating that diffusion of molecules is taking place. Furthermore, the molecules are found to diffuse in the form of small clusters, rather than diffusing one by one. About 80% of all diffused molecules are found to do so in the form of clusters and 61% of them form clusters in the size range of 2~15 molecules. Because the molecules diffuse as clusters, a slip diffusing process is suggested, in which a group of molecules at the edge of a C_{60} island lose registry with the substrate, and diffuse across the terrace. Such a molecular cluster diffusing on the surface is consistent with the prediction of 2-Dimensional gas

phase C_{60} mentioned above. During annealing, more molecular clusters can be expected to leave the island and diffuse on the surface in the 2D gas phase before actually leave the surface.

If the C_{60} molecules in a monolayer are isotropically bonded with the substrate and neighboring molecules, there is no reason for them to diffuse in the form of clusters. However, as introduced before, the bonding of C_{60} molecule is anisotropic in a monolayer. The intermolecular interaction varies with different relative orientation between two neighboring molecules, which is indicated in the order-disorder phase transition of bulk C_{60} solid happens at 249 K. And the interaction between the molecule and the substrate is different for R0º monolayer due to different adsorption sites occupied. However, R30º monolayer presents isotropic molecule-substrate interaction because every molecule occupies the identical a-top site. Therefore, the diffusion rate for the R30º monolayer is expected to be lower than the R0º monolayer, which is consistent with the truth that the R30º structure is more stable. With the anisotropic property, an "anchor" model is suggested for the origin of cluster-diffusion. The diffusion always starts from the molecule at the island edge that is weakest bonded, this molecule is called the "anchor". However, because the bonding of molecule is heavily dependent on its environment, after the anchor leaves, the molecules originally adjacent to it may be even weaker bonded than the anchor used to be, thus these molecules are likely to leave the island and diffuse with the anchor as a cluster. Such diffusion behavior of adsorbed C_{60} molecules occurs at submonolayer level is of great interests, as it reveals the characteristics of

substrate-molecule interaction and intermolecular interaction from a different aspect, and the studies of the molecular diffusion can help us to understand the nucleation and growth properties of adsorbate.

2.5.5. Summary

As a result of previous efforts in studying the different properties of the C_{60} monolayer adsorbed on the Au (111) surface using different research methods, a general understanding of the C_{60}/Au (111) system has been achieved. The C_{60} molecules are strongly bonded with the Au atom with charge transfer from the metal states to the LUMO of the molecules. Therefore, due to the strong interaction, the reconstructed Au (111) surface will be modified upon the adsorption, leading to the relief of reconstruction pattern or nanopit formation, and these substrate modifications will consequently influence the morphology and electronic property of the C_{60} monolayer. However, results from different research groups are not always consistent with one another, sometimes they are even contradicting, for example, the arguments about the amount of the charge transfer and the origin of dim molecules. A further investigation on these topics may lead to not only a better understanding of the C_{60}/Au (111) system but also characteristics of the self-assembly process of organic molecules in general. In my PhD research, I attempted to find out at which level the adsorption of C_{60} molecule will modify the substrate under different conditions and how will these changes to the substrate influence the assembly, morphology, bonding and electronic properties of the C_{60} adlayer.

My research is carried out mainly with a variable temperature UHV STM. The UHV environment can ensure the growth of C_{60} monolayer is not disturbed by the presence of contaminations. The STM technique offers us the ability of real space atomic resolution imaging and the contrast in STM image also reveals the electronic states of the sample, which is a crucial aspect in the research of the bonding property of C_{60} molecules. Moreover, the STM has the ability of manipulating the sample. In my research, an artificially created surface is used to testify the interaction between the C_{60} molecules and Au monoatomic steps. Finally, the capacity of carrying out experiments under variable temperatures gives us the opportunity to study the kinetics and thermodynamic characteristics of the growth of the C_{60} monolayer.

Previous STM studies of C_{60} molecules adsorbed on the Au (111) surface introduced above are mainly dealing with a complete monolayer. As photoemission studies revealed, the electronic properties may vary with C_{60} coverage because the chemical bonding situation is different for the isolated molecules or molecules at the edges of islands or molecules in the center of a monolayer. Therefore, my research covers the investigations of a full coverage range from almost isolated molecules to a nearly complete monolayer. Furthermore, at submonolayer coverage, the Au surface can be directly seen, which provides a good reference point for the study of substrate modification upon adsorption. In the following chapters, results of my research addressing several different aspects of the C_{60}/Au (111) system will be introduced. In Chapter 4, room temperature adsorption and growth of C_{60} submonolayer will be introduced, and a detailed discussion addressing the interaction between the molecule

and the DLs together with the formation of nanopit will be presented. In Chapter 5, I will discuss the adsorption of C_{60} molecules on an artificially created zero-gradient stepped surface, and show how C_{60} molecules interact with the DLs and their ability to facet the step edge. In Chapter 6, low temperature growth of C_{60} submonolayer will be introduced, and by comparing the situation with room temperature growth, the roles played by the reconstructed Au (111) surface in the development of a C_{60} submonolayer will be more clearly revealed. In Chapter 7, a novel nucleation process for C_{60} molecule on the herringbone pattern of the Au (111) surface at room temperature will be introduced and explained by comparing it with the low temperature growth situation. At last, in Chapter 8, the diffusion of C_{60} molecules at both room and low temperatures will be discussed in detail.

References

[1] J. Perdereau, J. P. Biberian, and G. E. Rhead, J. Phys. F: Metal Phys. **4**, 798 (1974).

[2] M. A. van Hove, R. J. Koestner, *et al*., Surf. Sci. **103**, 189 (1981).

[3] H. Melle, and E. Menzel, Z. Naturforsh. Teil A **33**, 282 (1978).

[4] J. C. Heyraud, and J. J. Métois, Surf. Sci. **100**, 519 (1980).

[5] Y. Tanishiro, H. Kanamori, K. Takayanagi, *et al.*, Surf. Sci. **101**, 395 (1981).

[6] U. Harten, A. M. Lahee, J. Peter Toennies, and Ch. Wőll, Phys. Rev. Lett. **54**, 2619 (1985).

[7] Y. I. Frenkel, and T. Kontorova, Zh. Eksp. Teor. Fiz. **8**, 1340 (1938).

[8] F. C. Frank, and J. H. van der Merwe, Proc. R. Soc. London **198**, 205 216 (1949).

[9] Per Bak, Rep. Prog. Phys. **45**, 58 (1982).

[10] M. El-Batanouny, S. Burdick, K. M. Martini, and P. Stancioff, Phys. Rev. Lett. **58**, 2762 (1987).

[11] N. Takeuchi, C. T. Chan, and K. M. Ho, Phys. Rev. B **43**, 13899 (1991).

[12] S. Narasimhan, and D. Vanderbilt, Phys. Rev. Lett. **69**, 1564 (1992).

[13] Ch. Wőll, S. Chiang, R. J. Wilson, and P. H. Lippel, Phys. Rev. B **39**, 7988 (1989).

[14] J. V. Barth, H. Brune, G. Ertl, and R. J. Behm, Phys. Rev. B **42**, 9307 (1990).

[15] K. G. Huang, D. Gibbs, D. M. Zehner, A. R. Sandy, and S. G. J. Mochrie, Phys. Rev. Lett. **65**, 3313 (1990).

[16] D. D. Chambliss, R. J. Wilson, and S. Chiang, J. Vac. Sci. Technol. B **9**, 933 (1991).

[17] D. D. Chambliss, R. J. Wilson, and S. Chiang, Phys. Rev. Lett. **66**, 1721 (1991).

[18] O. L. Alerhan, D. Vanderbilt, R. D. Meade, and J. D. Joannopoulos, Phys. Rev. Lett. **61**, 1973 (1988).

[19] S. Rousset, V. Repain, G. Baudot, Y. Garreau, and J. Lecoeur, J. Phys.: Condens. Matter **15**, 3363 (2003).

[20] T. Michely, and G. Comsa, Surf. Sci. **256**, 193 (1997).

[21] S. D. Kevan, and R. H. Gaylord, Phys. Rev. B **36**, 5809 (1987).

[22] S. LaShell, B. A. McDougall, and E. Jensen, Phys. Rev. Lett. **77**, 3419 (1996).

[23] M. P. Everson, R. C. Jaklevic, and W. Shen, J. Vac. Sci. Thechnol. A **8**, 3662 (1990).

[24] L. C. Davis, M. P. Everson, and R. C. Jaklevic, Phys. Rev. B **43**, 3821 (1991).

[25] Y. Hasegawa, and Ph. Avouris, Phys. Rev. Lett. **71**, 1071 (1993).

[26] Ph. Avouris, and I. Lyo, Science **264**, 942 (1994).

[27] D. Fujita, K. Amemiya, T. Yakabe, et al., Phys. Rev. Lett. **78**, 3904 (1997).

[28] W. Chen, V. Madhavan, T. Jamneala, and M. F. Crommie, Phys. Rev. Lett. **80**, 1469 (1998).

[29] D. D. Chambliss, R. J. Wilson, and S. Chiang, Phys. Rev. Lett. **66**, 1721 (1991).

[30] D. D. Chambliss, R. J. Wilson, and S. Chiang, J. Vac. Sci. Technol. B **9**, 933 (1991).

[31] J. A. Meyer, I. D. Baikie, E. Kopatzki, and R. J. Behm, Surf. Sci. **365**, L647 (1996).

[32] W. G. Cullen, and P. N. First, Surf. Sci. **420**, 53 (1999).

[33] B. Voigtländer, G. Meyer, and N. M. Amer, Phys. Rev. B **44**, 10354 (1991).

[34] I. Chado, C. Goyhenex, H. Bulou, and J. P. Bucher, Phys. Rev. B **69**, 085413 (2004).

[35] J. A. Stroscio, D. T. Pierce, R. A. Dragoset, and P. N. First, J. Vac. Sci. Technol. A **10** 1981 (1992).

[36] W. Lin, H. Chang, Y. Hu *et al*., Nanotechnology **21**, 015606 (2010).

[37] S. Helveg, J. V. Lauritsen, E. Lægsgaard *et al*., Phys. Rev. Lett. **84**, 951 (2000).

[38] M. M. Biener, J. Biener, R. Schalek, and C. M. Friend, Surf. Sci. **594**, 221 (2005).

[39] M. Ø. Pedersen, S. Helveg, A. Ruban *et al*., Surf. Sci. **426**, 395 (1999).

[40] A. W. Stephenson, C. J. Baddeley, M. S. Tikhov, and R. M. Lambert, Surf. Sci. **398**, 172 (1998).

[41] C. S. Casari, S. Foglio, F. Siviero *et al*., Phys. Rev. B **79**, 195402 (2009).

[42] J. Biener, E. Farfan-Arribas, M. Biener *et al.*, J. Chem. Phys. **123**, 094705 (2005).

[43] B. Fischer, J. V. Barth, A. Fricke, L. Nedelmann, and K. Kern, Surf. Sci. **389**, 366 (1997).

[44] B. Fischer, H. Brune, J. V. Barth, A. Fricke, and K. Kern, Phys. Rev. Lett. **82**, 1732 (1999).

[45] M. M. Dovek, C. A. Lang, J. Nogami, and C. F. Quate, Phys. Rev. B **40**, 11973 (1989).

[46] D. D. Chambliss, and R. J. Wilson, J. Vac. Sci. Technol. B **9**, 928 (1991).

[47] C. A. Lang, M. M. Dovek, J. Nogami, and C. F. Quate, Surf. Sci. Lett. **224**, 947 (1989).

[48] L. Gao, Q, Liu, Y. Y. Zhang, N. Jiang, *et al*., Phys. Rev. Lett. **101**, 197209 (2008).

[49] M. Böhringer, K. Morgenstern, W. D. Schneider, *et al.*, Phys. Rev. Lett. **83**, 324 (1999).

[50] Y. F. Wang, X. Ge, G. Schull, R. Berndt, C. Bornholdt, F. Koehler, and R. Herges, J. Am. Chem. Soc. **130**, 4218 (2008).

[51] I. Fernandez-Torrente, S. Monturet, K. J. Franke, J. Fraxedas, N. Lorente, and J. I. Pascual, Phys. Rev. Lett. **99**, 176103 (2007).

[52] T. Yokoyama, S. Yokoyama, T. Kamikado, Y. Okuno, and S. Mashiko, Nature **413**, 619 (2001).

[53] N. Jiang, Y. Y. Zhang, Q. Liu, Z. H. Cheng *et al*., Nano Lett. **10**, 1184 (2010).

[54] H. W. Kroto, J. R. Heath, S. C. O'Bren, R. F. Curl, and R. E. Smalley, Nature **318**, 162 (1985).

[55] R. F. Curl and R. E. Smalley, Scientific American **265**, 54 (1991).

[56] W. Krätschmer, L. D. Lamb, K. Fostiropoulos, and D. R. Huffman, Nature **347**, 354 (1990).

[57] P. A. Heiney, J. E. Fischer, A. R. McGhie, W. J. Romanow, *et al*,. Phys. Rev. Lett. **66**, 2911 (1991).

[58] K. Prassides, H. W. Kroto, R. Taylor, *et al*., Carbon **30**, 1277 (1992).

[59] W. I. F. David, R. M. Ibberson, J. C. Matthewman, K. Prassides, *et al,*. Nature **353**, 147 (1991).

[60] R. M. Fleming, A. P. Ramirez, M. J. Rosseinsky, D. W. Murphy, *et al,*. Nature **352**, 787 (1991).

[61] A. F. Hebard, M. J. Rosseinsky, R. C. Haddon, D. W. Murphy, *et al,*. Nature **350**, 600 (1991).

[62] K. Tanigaki, T. W. Ebbesen, S. Saito, J. Mizuki, J. S. Tsai, Y. Kubo, and S. Kuroshima, Nature **352**, 222 (1991).

[63] T. R. Ohno, Y. Chen, S. E. Harvey, G. H. Kroll, and J. H. Weaver, Phys. Rev. B **44**, 13747 (1991).

[64] S. C. Erwin, in *Buckminsterfullerenes*, edited by W. E. Billups and M. A. Ciufolini, VCH, New Tork, p. 217 (1993).

[65] S. Stevenson, G. Rice, T. Glass, K. Harich, *et al,*. Nature **401**, 55 (1999).

[66] S. Modesti, S. Cerasari, and P. Rudolf, Phys. Rev. Lett. **71**, 2469 (1993).

[67] Y. Maruyama, K. Ohno, and Y. Kawazoe, Phys. Rev. B **52**, 2070 (1995).

[68] T. Sakurai, X. D. Wang, Q. K. Xue, Y. Hasegawa, T. Hashizume, and H. Shinohara, Prog. Surf. Sci. **51**, 263 (1996).

[69] G. Schull and R. Berndt, Phys. Rev. Lett. **99**, 22105 (2007).

[70] J. A. Larsson, S. D. Elliott, J. G. Greer, J. Repp, G. Meyer, and R. Allenspach, Phys. Rev. B **77**, 115434 (2008).

[71] C. T. Tzeng, W. S. Lo, J. Y. Yuh, R. Y. Chu, and K. D. Tsuei, Phys. Rev. B **61**, 2263 (2000).

[72] E. I. Altman and R. J. Cotton, Surf. Sci. **279**, 49 (1992).

[73] X. D. Wang, S. Yamazaki, J. L. Li, T. Hashizume, H. Shinohara, and T. Sakurai, Scanning Microscopy **8**,987 (1994).

[74] W. W. Pai, C. L. Hsu, M. C. Lin, K. C. Lin, and T. B. Tang, Phys. Rev. B **69**, 125405 (2004).

[75] P. W. Murray, M. O. Pedersen, E. Laegsgaard, *et al.*, Phys. Rev. B **55**, 9360 (1997).

[76] R. Felici, M. Pedio, F. Borgatti, *et al*., Nature Mater. **4**, 688 (2005).

[77] J. A. Gardener, G. A. D. Briggs, and M. R. Castell, Phys. Rev. B **80**, 235434 (2009).

[78] H. I. Li, K. Pussi, K. J. Hanna, L. L. Wang, *et al*., Phys. Rev. Lett. **103**, 056101 (2009).

[79] A. Tamai, *et al.*, Phys. Rev. B **72**, 085421 (2005).

[80] D. Fujita, T. Yakabe, H. Nejoh, T. Sato, and M. Iwatsuki, Surf. Sci. **366**, 93 (1996).

[81] X. Zhang, F. Yin, R. E. Palmer, and Q. M. Guo, Surf. Sci. **602**, 885 (2008).

[82] A. Fartash, Appl. Phys. Lett. **67**, 3901 (1995).

[83] X. Lu, M. Grobis, K. H. Khoo, S. G. Louie, and M. F. Crommie, Phys. Rev. B **70**, 115418 (2004).

[84] F. Schiller, M. Ruiz-Osés, J. E. Ortega, P. Segovia et al., J. Chem. Phys. **125**, 144719 (2006).

[85] E. I. Altman and R. J. Colton, Phys. Rev. B **48**, 18244 (1993).

[86] E. I. Altman and R. J. Colton, J. Vac. Sci. Technol. B **12**, 1906 (1994).

[87] J. K. Gimzewski, S. Modesti, Ch. Gerber, and R. R. Schlittler, Chem. Phys. Lett. **213**, 401 (1993).

[88] Y. Hasegawa and Ph. Avouris, Science **258**, 1763 (1992).

[89] N. Néel, J. Kröger, and R. Berndt, Appl. Phys. Lett. **88**, 163101 (2006).

[90] S. Guo, D. P. Fogarty, P. M. Nagel, and S. A. Kandel, J. Phys. Chem. B **108**, 14074 (2004).

CHAPTER 3
EXPERIMENTAL TECHNIQUES AND METHODOLOGY

3.1 Surface Characterization

In surface science, a surface can be understood as a transition region between the uniform bulk material and the outside media or vacuum [1]. As a transition region, the physical and chemical properties of the surface are very different to that of bulk materials, resulting from different atomic structure and electronic structure. The properties of surfaces are very important in the research of catalysis, microelectronic devices, solar cells, biosensors, etc, because most of the chemical interactions take place at the surface and those desired functions are realized in the region of the surface. In order to study the surface properties, various surface characterizing techniques are developed.

3.1.1 Surface Analysis Methods

Until now, all the surface characterizing methods, except scanning probe microscopy which will be discussed in details in next section, can be summarized into the beam in and beam out configuration, as shown in Fig. 3.1 [1]. An incident beam impinges the surface and generates out-going (secondary) beams carrying surface information. By detecting the parameters of the secondary beam, such as the number or intensity of secondary particles, the energy distribution curve (EDC), angular distribution,

mass-charge ratio *m*/*e* or spin polarization, different surface properties can be probed. Combining different pairs of incident and secondary beams leads to various surface analysis methods, as listed in Table 3.1, for example, the XPS technique is based on the analysis of emitted electrons excited by incident X-rays.

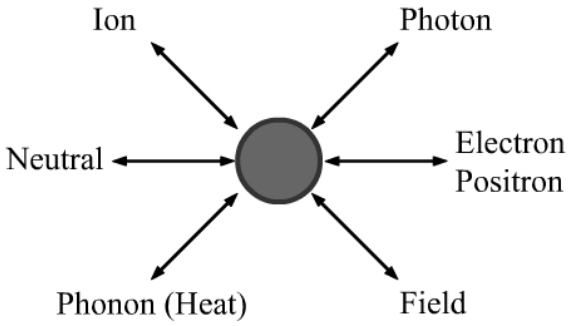

Fig. 3.1 (from [1]): The idea of surface analysis: impinging the surface with a kind of beam, and detect the parameters of secondary beam (can be the same or different kind to incident beam), which carry information of surface.

Incident Particle	Secondary Particle	
	Photon	Electron
Photon	XFS, XRD, IR	XPS, UPS, PES
Electron	APS, IPE, EDX	LEED, RHEED, AES, SEM, TEM, EELS

AES (Auger Electron Spectroscopy)

APS (Appearance Potential Spectroscopy)

EDX (Energy Dispersed X-ray Spectroscopy)

EELS (Electron Energy Loss Spectroscopy)

IPE (Inverse Photoemission)

IR (infrared Spectroscopy)

LEED (Low Energy Electron Diffraction)

PES (Photoelectron Spectroscopy)

RHEED (Reflection High Energy Electron Diffraction)

SEM (Scanning Electron Microscopy)

TEM (Transmission Electron Microscopy)

UPS (Ultra-violet Photoelectron Spectroscopy)

XFS (X-ray Fluorescence Spectroscopy)

XPS (X-ray Photoelectron Spectroscopy)

XRD (X-ray Diffraction)

Table 3.1 (from [1]): Different surface analysis methods are cataloged in this table by the incident and secondary particles employed.

In order to study surface properties, the method used must be surface sensitive, which means that the secondary particles must only carry the information originated from the topmost several atomic layers of the surface. Under this requirement, not all above techniques are suitable for surface analysis, XRD for example, because of the high penetrability of X-rays, the XRD always reflect the structural information of the bulk. Among above listed techniques, AES, LEED, RHEED, EELS, UPS and XPS are the most frequently used methods in surface science research.

AES is commonly used to identify the surface elemental composition, as it detects the Auger electrons, of which the energy only depends on the atomic levels of

the excited atom. Due to the relatively low energy of the Auger electrons, only the electrons excited from the top-most few atomic layers can be detected, hence the AES is surface sensitive.

LEED is the most common method to determine the atomic structure of a surface. Due to the low energy (usually 10~500 eV) of the incident electrons, the penetration depth is only 0.5~1.0 nm, which is just a few atomic layers. The atomic lattice in this region acts as a grating and diffracts the electron wave. By reading the generated diffraction pattern, the atomic structure of the surface can be determined. RHEED employ electron with energy as high as 10~20 keV, however, because in this technique, the electron beam incident onto the surface at a grazing angle of 2º~5º, the electron's momentum projected in the penetration direction is small, thus it can detect the surface information. RHEED is mainly used to monitor the real-time changes of surface structure in thin film growth.

Photoelectron spectroscopy (also known as photoemission spectroscopy), including XPS, UPS and other photoelectron spectroscopy excited by different sources, is based on the photoelectric effect, of which the electrons in a solid can be excited and emitted by incident photons. When the photoelectrons are captured by an energy analyzer, it gives a spectrum (energy distribution curve, the EDC) with a series of photoelectron peaks. The numbers of electrons with different binding energies are revealed by the intensities of the photoelectron peaks located at different energy positions. As the binding energy of the electron is a fingerprint of different elements, the peak positions of the spectrum determine the surface composition, and the peak

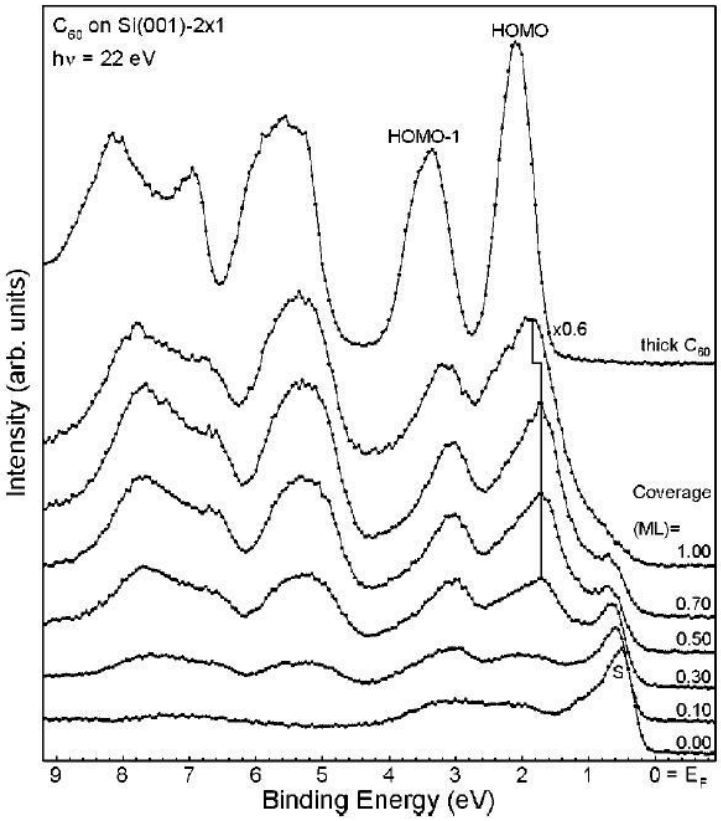

Fig. 3.2 (from [2]): A series of photoemission spectra taken on the Si (001) 2 × 1 surface with different C_{60} coverage. The position, intensity, shape and shift of peaks reveal variety surface information.

intensities can be used to quantitatively analyze the surface composition. Furthermore, chemical environment around a specific element in the surface will affect the peak shape and its binding energy. In this manner, the photoelectron spectrum can also provide information about the chemical bonding in the surface. For example, Fig. 3.2 presents a series of photoemission spectra taken on a Si (001) 2 × 1 surface with different C_{60} coverage [2]. It can be seen that at zero C_{60} coverage, the spectrum shows a well defined peak corresponding to the electron emission from the dangling bond states of the Si surface (the peak is marked S). As the C_{60} coverage increases, the

spectra present more and more C_{60} derived features, at the same time, the peak S for dangling bond state decreases due to the formation of chemical bonds between Si's dangling bond and C_{60} molecules. The spectrum for thick C_{60} layer presents two peaks corresponding to the HOMO and HOMO-1 of C_{60} molecules. Compare to the HOMO peaks in the submonolayer's spectra, there is a shift of the peak position to higher energy, and this shift can be explained as for a thin C_{60} layer, the charge transfer from substrate to the LUMO of C_{60} molecules rises a screening effect for the emission electrons. As demonstrated in this example, the position, intensity, shape and shift of peaks in photoelectron spectrum can provide information about the surface composition and chemical bonding.

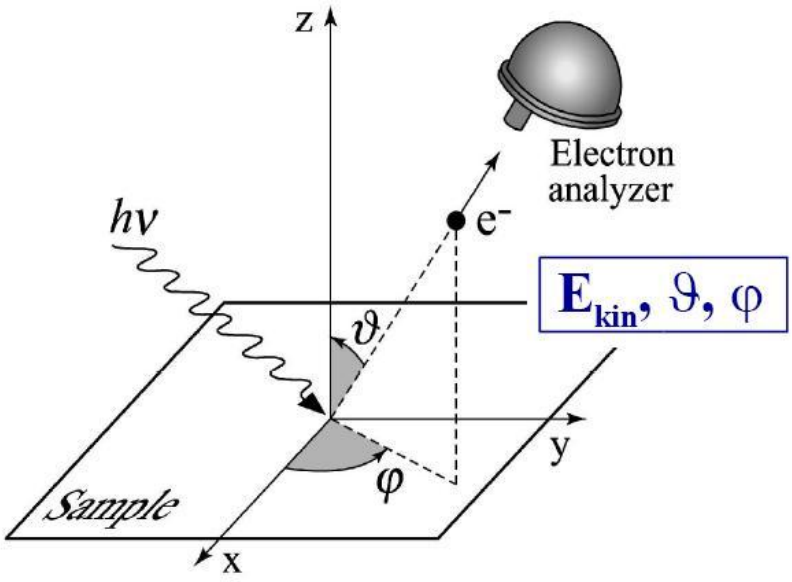

Fig. 3.3 (from [3]): The setup of ARPES, of which the energy analyzer can move to detect the electrons emitted to different angles.

As an addition to photoelectron spectroscopy, there is Angle-resolved

photoemission spectroscopy (ARPES), of which the energy analyzer can move to detect the emitted electrons at different angle θ, as shown in Fig. 3.3. ARPES is momentum sensitive and can provide the dispersion relation of electronic states. For instant, Fig. 2.12(b) from the previous chapter shows a series of photoemission spectra taken from an Au (111) surface at different angles [4]. The peaks in these spectra correspond to the *sp* surface state, and the positions of the peaks are different at each angle, forming a parabolic-shape dispersion relation. As each angle corresponding to a k value in reciprocal space, the dispersion relation of the *sp* surface state can be presented in the form shown in Fig. 2.12(c).

3.1.2 Scanning Tunneling Microscopy

Scanning tunneling microscopy (STM) is a young and powerful technique for surface analysis, introduced by G. Binnig, H. Rohrer and coworkers at the IBM Zürich Research Laboratory in 1981 [5]. It provides real-space atomic resolution imaging of surfaces. Soon after, the STM is appreciated as an epoch-making invention by researcher all over the world and the inventors, G. Binnig and H. Rohrer were awarded the 1986 Nobel Prize in Physics for their contribution. A large family of surface analysis methods named scanning probe microscopy were developed based on the fundamental idea of the STM, including atomic force microscopy (AFM), chemical force microscopy (CFM), electrostatic force microscopy (EFM), Kelvin probe force microscopy (KPFM), magnetic force microscopy (MFM), scanning capacitance microscopy (SCM), etc. However, the most widely used techniques

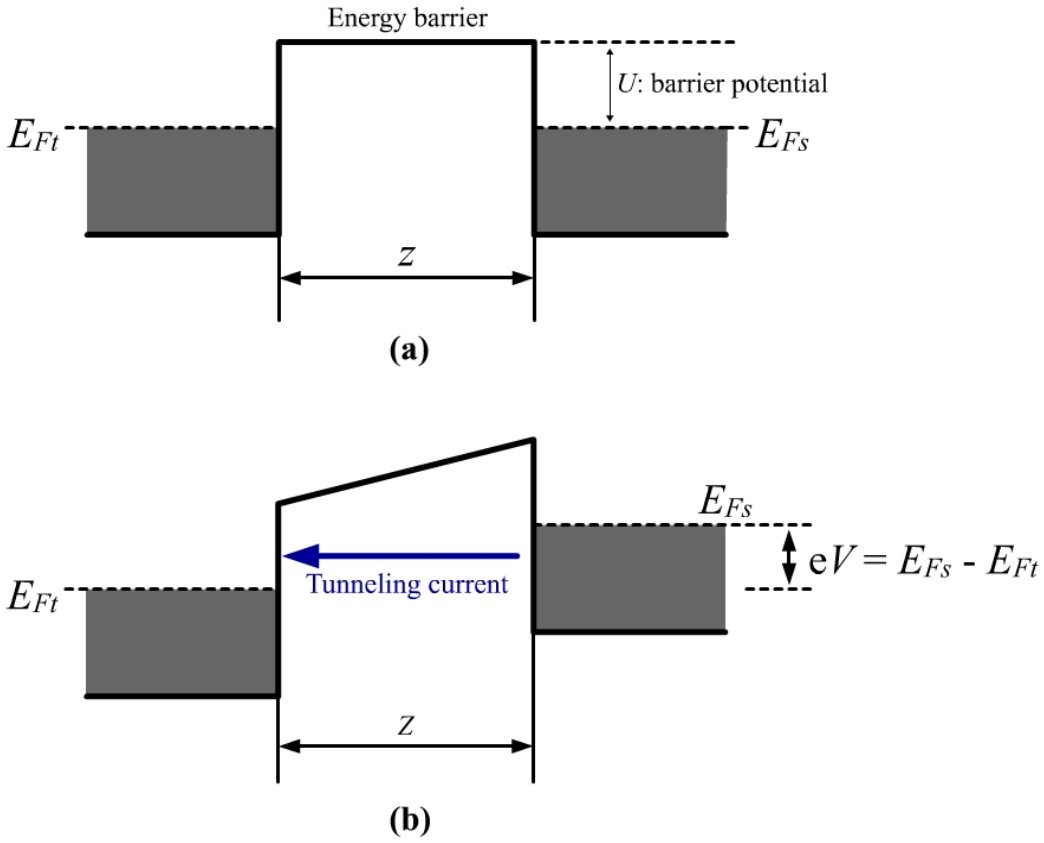

Fig. 3.4: A 1-Dimensional energy model of the tip-barrier-sample junction. The Fermi levels for tip and sample are indicated by dashed lines, the electrons in each side are defined in the grey regions below the Fermi levels. The width of the energy barrier is *z*. (a): Without a bias voltage, the Fermi levels of each side are aligned and there is no tunneling current. (b): When a bias voltage *V* is applied, the Fermi level of the negative biased side will rise by e*V*, and there is a tunneling current flow from the negative side to the positive side. Only the electrons with the energy lies in between the two Fermi levels have the chance to tunnel and form the tunneling current.

among them are the STM and AFM, which provide surface topography (also electronic structure for STM) by detecting the tunneling current or mechanical interaction between a sharp tip and surface, respectively. My research is mainly using STM, and in this section, the general theory, apparatus, operation and variation of STM will be introduced.

For STM, the measurement is done by detecting the tunneling current, which is a quantum mechanics phenomenon named electron tunneling. The concept of electron tunneling can be demonstrated in a 1-Dimensional model sketched in Fig. 3.4. Two electrodes (could be metal or semiconductor) are close to each other and are separated by an energy barrier (could be an insulating layer or just vacuum). Normally, the electrons in each electrode are confined under the Fermi level. Without applying bias voltage, the Fermi levels of the two are equal at equilibrium. When a bias voltage V is applied between the two electrodes, the shape of the energy barrier changes and the Fermi level of the negative side shifts upwards by eV, thus the electrons in the negative electrode intend to travel to the position electrode. According to classical mechanics, the electrons can not travel through the barrier unless their energy is higher than the height of the barrier. However, if the two electrodes are close enough that quantum mechanics becomes applicable, a small number of electrons are allowed to travel through the barrier even if their energy is lower than the barrier height. The Schroedinger's equation inside the barrier has solution in the form of:

$$\Psi(z) = \Psi(0)\, e^{-\kappa z} \qquad (3.1)$$

where

$$\kappa = [2m_e(U - E)]^{1/2}/\hbar \qquad (3.2)$$

where z is the barrier width, m_e is the effective mass of an electron, U is the barrier potential, E is the energy of electron and $\hbar$ is the Planck's constant. The electrons tunneling through the barrier form the tunneling current, so the value of tunneling current is exponentially related to the barrier width z:

$$I \propto e^{-2\kappa z} \qquad (3.3)$$

According to equation (3.3), the tunneling current is very sensitive to the barrier width *z*, a 1 Å difference in barrier width will result in a current difference by an order of 10. STM employs this current-barrier width characteristic to probe the surface structure. In an STM, a sharp tip is brought very close to the sample surface, normally tens of angstroms, the tip, sample and the media between them (could be vacuum, liquid or inert gas depends on the STM working condition) form a junction just like that presented in Fig. 3.4. With such a configuration, the tip-sample distance can be decided by measuring the tunneling current, thus by collecting the distance data at every point on the surface (scanning in a raster manner), a contrast image of the surface topography can be obtained, with one measured point to be one pixel in the image. A typical STM setup is shown in Fig. 3.5:

As shown in Fig. 3.5, the tip is mounted on piezoelectric material which offers the tip a 3-Dimensional movement capacity. Piezoelectric material is such a kind of material that it generates an electric field or electric potential when a mechanical stress is applied, conversely, when a voltage is applied, the piezoelectric material will change in shape. So, by varying the voltage applied to it, the change in its shape can be controlled by the computer, and thus the movement of the tip mounted on it can be controlled. In Fig. 3.5, three piezoelectric material bars are mounted along the *x*, *y*, *z* directions, respectively, indicating the 3D movement ability of the tip driven by the piezoelectric material. In some systems, the piezoelectric material used in STM usually has a shape of a tube, and the movements in the *x*, *y*, *z* directions are all

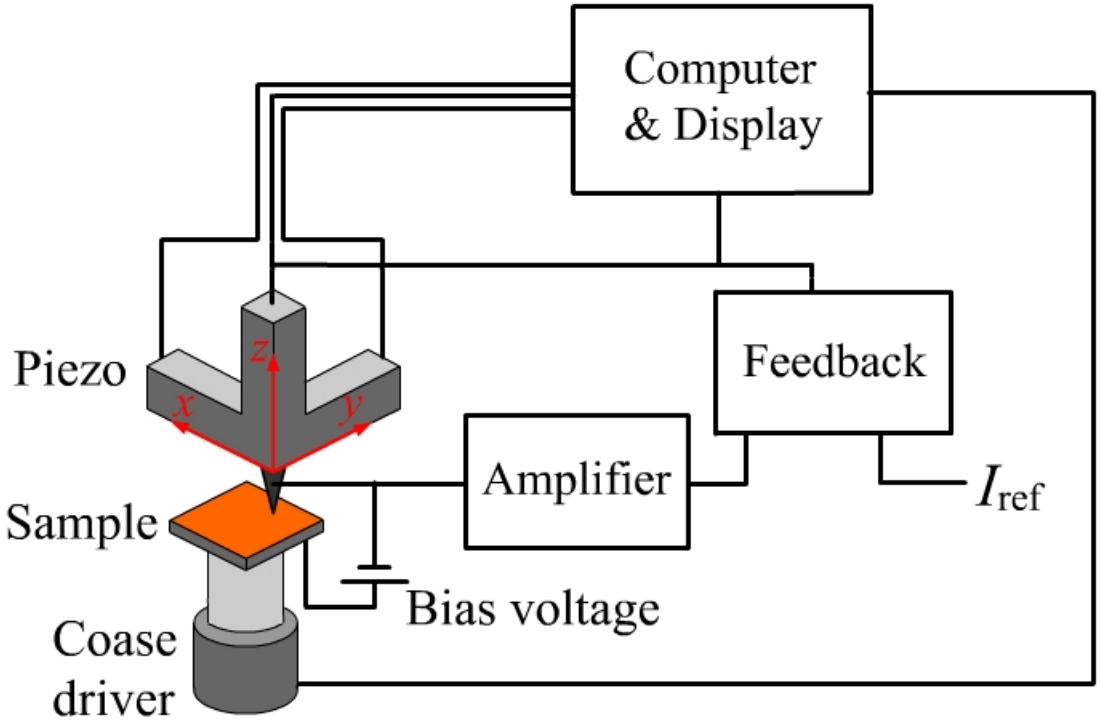

Fig. 3.5: Schematic of a scanning tunneling microscope. The tip is mounted on a piezo-driver, which offers it the capacity of 3D movement. The piezo-driver is mounted on a coarse motion mechanism. The tip height is maintained by a feedback loop while scanning. A computer is used for controlling and display.

achieved by the controlled distortion of a single piezo-tube. Beside the piezo, there is a coarse motion mechanism in STM in order to bring the sample and tip close enough for the piezo-tube to work and also used to select interested sample area on the millimeter scale. The coarse motion mechanism can be manually operated using screw and slide hardware or controlled by an electric stepper motor.

When an STM is operating, the computer controls the piezo to scan the tip over the surface in a raster manner, at points with the same separation on the tip's path, certain signal (tunneling current or tip height) are recorded, together with the position (x, y) of the point. Signals from all the positions form the STM image that to be

displayed. Depending on the different signal types to be recorded, STM has two modes of operation: constant current mode and constant height mode, as shown in Fig. 3.6(a) and (b), respectively. In constant current mode, a feedback circuit is employed to adjust the tip height and maintain the tunneling current at a pre-set value. During the scanning, when the tip meets a surface structure, the variation of tip-sample distance z leads to a change in the tunneling current. By detecting the variation of tunneling current, the feedback electric adjusts the voltage applied on the piezo's z direction, thus change the tip height until the tunneling current goes back to the pre-set value. Then the tip height is recorded for this position. Finally, the heights of tip at all the positions are collected and displayed in an image with its contrasts representing the different heights at each point. On the other hand, for constant height mode, the feedback electric keeps the tip at a fixed height during scanning. The different tunneling current values at each position, which are resulted from the variation in different tip-sample distance z caused by surface corrugation, are recorded. The contrasts in constant height mode STM image represent the relative value of tunneling current from point to point. In this mode, the scanning speed can be very high as it does not require time to adjust the tip height. However, due to the tip height is fixed, it is easy to crash the tip when there is some unexpected high structure on the sample surface. So, it is preferential to use constant current mode to study a surface at first, and for atomically flat regions, fast constant height mode can be used to observe real-time evolution of the surface features.

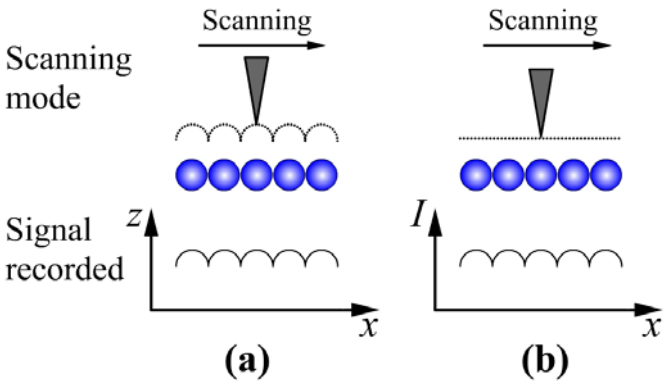

Fig. 3.6: The two working modes of STM. (a): Constant current mode, in which the tip height is adjusted during scanning to maintain a fixed tunneling current value, and the different tip heights at each position are recorded to construct the image. (b): Constant height mode, in which the tip height remains unchanged during scanning, and the different tunneling current values caused by the variation of tip-sample distance z are recorded.

An important thing needs to be noticed is that the contrast in STM image does not only represent the surface geometric corrugation but also the electronic structure of the sample surface and tip. As seen in Fig. 3.4, only the electrons with energy lies in between the two Fermi levels of two electrodes have the chance to travel through the barrier and form the tunneling current. In other words, the availability of electronic states is important, tunneling electrons can only travel from an occupied state of negative side to an unoccupied state of the positive side, so the value of tunneling current does not only related to the distance z, but also depends on the availability of electronic states in the two electrodes. So equation (3.3) can be written in a more realistic form as:

$$I = C\rho_t\rho_s e^{-2\kappa z} \qquad (3.4)$$

Where C is a constant which is linearly related to the bias voltage, ρ_t and ρ_s are the

local density of state (LDOS) of the tip and sample, respectively. So, the tunneling current is related to the convolution of the tip's LDOS and the sample's LDOS. However, when the bias voltage is small, the LDOS of the tip can be regarded as a constant. Thus the STM image can be approximated as a superimposition of the surface's geometric corrugation and electronic structure (the LDOS).

Because the tunneling current is related to the LDOS of the surface, it can be used to probe the electronic structure in a very localized region under the tip. The lateral resolution can reach the magnitude of an angstrom. This method is named scanning tunneling spectroscopy (STS), which was first demonstrated by R. J. Hamers *et al.* in 1986 by probing the surface states of Si (111) 7 × 7 surface [6]. The normal way to perform STS is locating the tip over an interested position on the sample surface. Switch off the feedback circuit and keep the tip at a certain height. Then, vary the bias voltage applied on the tip-sample junction, for example, from - 6 V to + 6 V, and record the variation of the tunneling current as a function of the bias voltage, which is presented in the form of an *I-V* curve. As shown in the Fig. 3.7, if we treat the electronic structure of the tip independent of *V*, the value of the tunneling current at a given voltage is dependent on how many occupied states in the sample are available to give electrons under this bias voltage (when the sample is negatively biased, see Fig. 3.7(a)) or how many unoccupied states in the sample are available to accept electrons (when the sample is positively biased, see Fig. 3.7(b)). The occupied or unoccupied states which contribute to the tunneling current are marked in red or blue, respectively. In this manner, the first differential of the *I-V* curve, *dI/dV* indicates

the distribution of LDOS within the energy range from - eV to + eV (V is the minimum or maximum value of the bias voltage variation). An example of STS data is shown in Fig. 3.8, the thin line is the *I-V* curve and the thick line is the *dI/dV* curve, of which the intensity is proportional to the slope of the *I-V* curve. Along the *dI/dV* curve, the peaks representing the HOMO, HOMO+1 and LUMO of the sample are clearly seen.

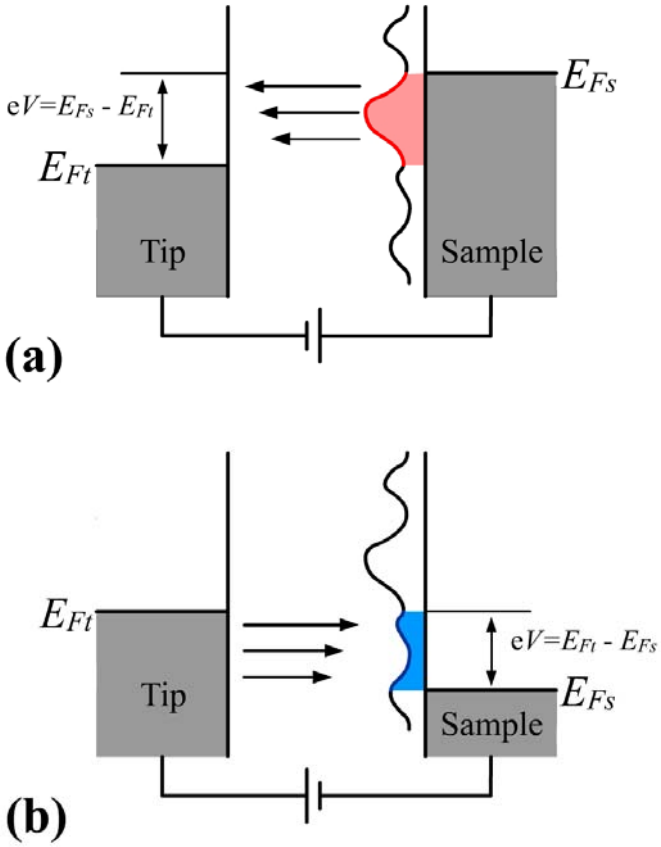

Fig. 3.7: The principle of STS, the tunneling current at certain bias voltage depends on the DOS in the energy window ($eV = E_{F\text{positive}} - E_{F\text{negative}}$, marked by red or blue, respectively), so the differential of the *I-V* curve, the *dI/dV*, represent the DOS at each energy level. (a): The sample is negatively biased, thus the occupied states of the sample in the energy window contribute to the tunneling current. (b): The sample is positively biased, thus the unoccupied states of the sample contribute to the tunneling current.

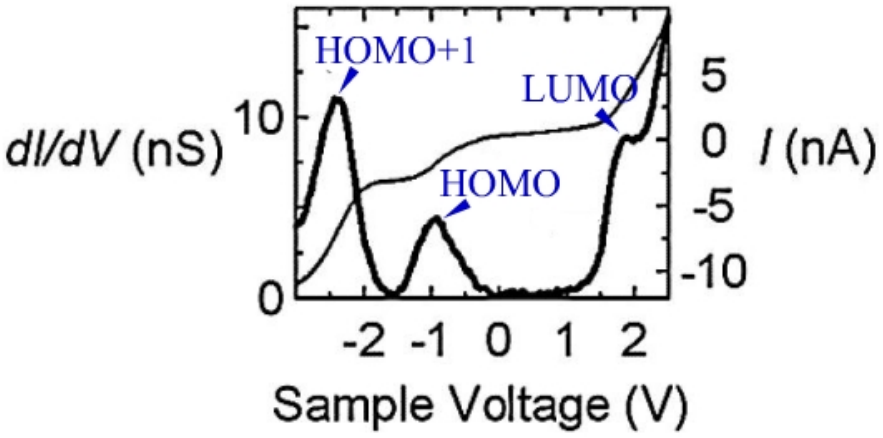

Fig. 3.8 (from [7]): The *I-V* curve (thin line) and *dI/dV* curve (thick line) from an STS taken over a C_{60} molecule on the Cu (111) surface. The *dI/dV* curve represents the intensity of the sample's LDOS. The peaks in the *dI/dV* curve represent the HOMO, HOMO+1 and LUMO states, respectively.

Besides revealing the electronic structure at certain point on the surface, STS can also be used to provide a so-called *dI/dV* map over a surface area, in which the relative density of local electronic states at a certain energy level is presented by color scale in a real-space image. With a *dI/dV* map, the LDOS distribution over a certain surface feature can be directly seen, which is very useful for the investigation of surface electronic behavior, for instance, the chemical reaction at the single molecular level. There are two ways to obtain a *dI/dV* map. The first is to do the bias voltage variation at every point on the surface, and select the LDOS at certain energy level from all the points to construct the image. The second way is to couple a high frequency sinusoidal modulation voltage (an AC voltage) to the constant DC bias voltage applied on the tip-sample junction when perform the constant current mode scanning. The frequency of the AC voltage is higher than the feedback circuit's

response threshold, so the tip scans over the surface in a normal way. However, the oscillation of tunneling current caused by the AC voltage is recorded, and by using a lock-in amplifier, the *dI/dV* at this energy level (set by the DC bias) can be obtained directly. In this way, the *dI/dV* map is obtained simultaneously with the constant current image.

In addition to the ability of providing topographic image and probing electronic structure, the STM can also probe the magnetic structure of the sample surface. However, a specialized spin-polarized STM (SP STM) is required for this job. By using a magnetic tip, the electrons in the sample surface with their spin polarization direction parallel to that of the tip have higher probability to tunnel, resulting in a higher tunneling current. In this way, the magnetic domains with different spin directions can be distinguished by SP STM, and the magnetic resolution can reach atomic level.

Besides being used as a surface analysis method, STM offers the ability to manipulate atoms with high accuracy. Such an ability was first demonstrated by D. M. Eigler and E. K. Schweizer [8]. 35 xenon atoms were moved one by one to form the three letters of IBM on a nickel surface with an STM operated at 4 K. This experiment opened a new era for atomic manipulation. Atomic manipulation is mostly performed at low temperature in order to reduce the thermal diffusion of atoms and minimize the thermal drift, so the atoms can be preciously located. There are three major modes for atomic manipulation with an STM tip. The first is pick-and-drop mode. In this mode, the tip is placed over the atom or molecule to be moved, by

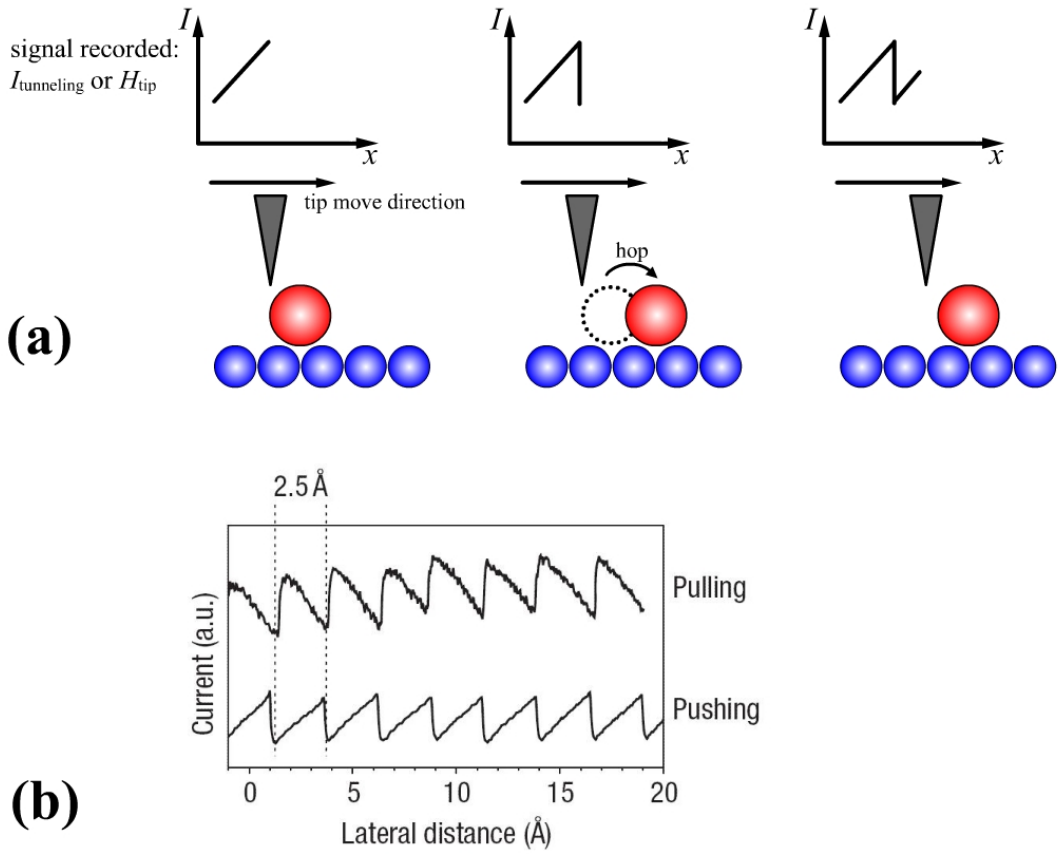

Fig. 3.9 (a): Schematic diagram of pushing an atom over a surface. The signal recorded during the manipulation can be either the tunneling current $I_{tunneling}$ (under constant height mode, as shown in this image) or the tip height H_{tip}. As seen, when the tip approaches the atom, the $I_{tunneling}$ increases, once the lateral force between the tip and the atom becomes larger than the diffusion barrier, the atom will hop to the next adsorption site and results a sudden drop of the $I_{tunneling}$. The process of pulling mode is just conversed. (b) (from [9]): An example of the recorded during pushing and pulling a molecule over a Cu (110) surface, the period of the sawtooth signal is consistent with the atomic period of the Cu (110) surface in [-110] direction, 2.5 Å.

applying a voltage pulse, there is a chance to attach the atom or molecule to the tip. The tip is then moved to the desired location, and another voltage pulse is applied to drop the atom or molecule onto the surface. However, because of the voltage pulse, there is a risk of the surface. The other two modes are the pulling and the pushing

mode, respectively. In these two modes, the atoms being manipulated do not leave the surface, but being pulled or pushed to move laterally by the interaction with the tip. As demonstrated in Fig. 3.9, after identifying an atom to be moved, the tip height is reduced to enhance the interaction with the atom (the height used is normally empirical), then the tip is laterally moved to the destination. The atom will be pulled or pushed to follow the tip to the destination. During the movement, the atom actually hops from one adsorption site to another along the path, and induces a sawtooth-like signal of the tunneling current or tip height under different scanning modes, which can be used to monitor the manipulation process.

My research involves an atomic manipulation process performed with the STM at room temperature to relocate a large number of atoms simultaneously, which will be introduced in detail in the next section.

3.2 Experimental Methods

My PhD research focuses on the STM study of submonolayer C_{60} fullerene growth on the $22 \times \sqrt{3}$ reconstructed Au (111) surface and artificially created surface structures, at both room temperature and low temperatures. The experimental methods are introduced in detail in this section.

3.2.1 Sample Preparation

The Au (111) surface used in my experiment is home-prepared. Highly Oriented

Pyrolytic Graphite (HOPG), cut into a rectangular shape about 10 × 5 mm, is used as the substrate. The HOPG surface is cleaned by exfoliating several layers off with sticky tape before being mounted on the sample holder and placed into an Edward evaporator. Gold wire with 99.99% purity from Goodfellow Cambridge Ltd. is used as the evaporation source, placed in a molybdenum boat in the evaporator. The molybdenum boat is heated by a DC current and the source temperature can be controlled by adjusting the current applied. The gold source is located approximate 7 cm below the HOPG surface and a shutter separates the two.

Then, the evaporator chamber is pumped with turbomolecular pump overnight to reach a pressure of 1×10^{-7} mbar. Before evaporate, the HOPG substrate is heated to 648~658 K to degas and is kept at this temperature during the whole evaporation process. A current of 20~25 A is applied over the molybdenum boat to heat and degas the gold wire. After being degassed for 10 minutes with the shutter closed, the temperature of gold wire is raised until the melting point of gold is reached, normally, a 28 A current is required for this purpose. The shutter is kept closed for another 5 min for the gold vapor to reach a stable evaporation rate, then the shutter is opened and the evaporation begins. A quartz crystal oscillator is used to monitor the growth rate. We intend to obtain sample with wide flat terraces, so, at the beginning, the deposition rate is kept as low as possible in order to reduce the density of nucleation core on the substrate, therefore, a temperature lower than the melting point is used. The deposition rate is kept at 0.1 nm/min for the first 30 minutes. Then, a high current is used and the deposition rate will reach 1 nm/min. In around 5 hours time, the

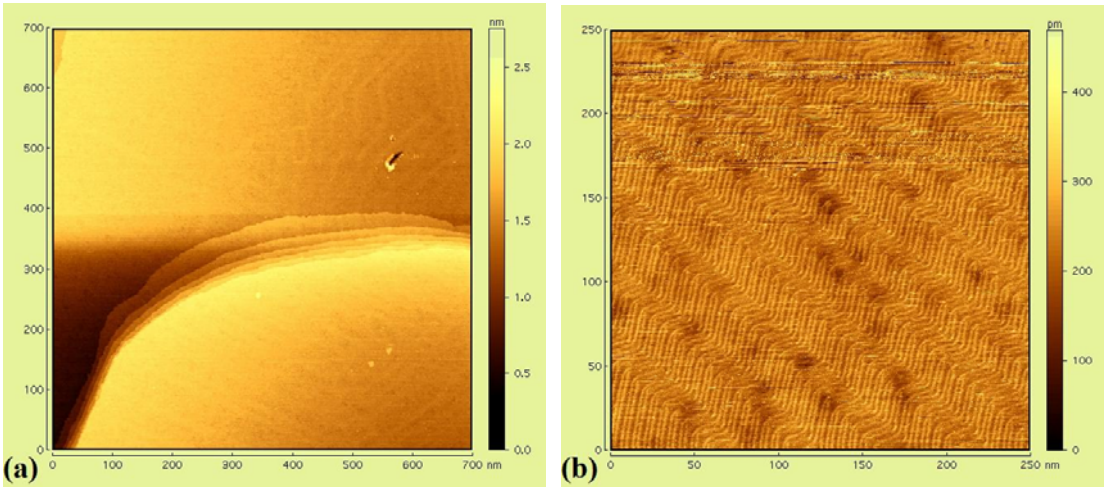

Fig. 3.10 (a): 700 × 700 nm, I = 0.05 nA, V = 0.1 V, Au (111) surface observed by STM in ambient, large atomic flat terraces are presented, of which the width can reach ~1μm. (b): 250 × 250 nm, I = 0.05 nA, V = 0.1 V, Au (111) surface after cycles of ion sputtering and annealing in UHV, herringbone reconstruction is clear seen.

thickness of the gold film will reach about 300 nm and the shutter is closed then. The HOPG substrate is kept at 670 K for another 30 minutes for annealing. During the evaporation, the pressure in the chamber is around ~1 × 10^{-6} mbar.

After cooling to room temperature, the sample is removed from the evaporator and directly observed under an ambient STM. As shown in Fig. 3.10(a), the sample surface presents atomically flat gold terraces separated by monoatomic steps. The width of the terrace can reach as large as 1 μm.

When transferred to the ultra high vacuum (UHV) chamber, the sample is cleaned by several cycles of argon ion sputtering and annealing. In each cycle, the Ar^+ sputtering is performed with 1 keV energy, and the target current density is 10 μA/cm^2, which equals to 6.241×10^{13} ions incident with the surface per square centimeter per second. The annealing is for 30 minutes at 1000 K. After cycles of this sputtering and

annealing, the sample presents a defect-free herringbone reconstructed Au (111) surface in UHV STM imaging, a typical topography is shown in Fig. 3.10(b). The large terrace together with the herringbone reconstruction of the sample surface provides an ideal template for my C_{60} submonolayer growth experiment.

3.2.2 STM Apparatus

My experiment is mainly performed with an Omicron variable temperature STM. The whole system is placed on a floating stage for vibrating isolation. The UHV chamber housing the STM is equipped with titanium sublimation pump (TSP), ion pump, turbomolecular pump with its first stage rotary pump. These pumps maintain a base pressure of 2×10^{-10} mbar in the chamber. Furthermore, there are ion gauge, ion gun and mass spectrometer mounted on the chamber too. The transfer of sample and STM tip into or out of the main UHV chamber is through a load lock chamber which has its own turbomolecular pump, thus the transfer will hardly affect the pressure of the main chamber. A manipulator is mounted in the centre of the UHV chamber, which has the ability of 360º rotating and heating the sample to 1050 K by radiative heating or to 1500 K by direct heating. When initially transferred into the chamber, the sample or tip is placed on the manipulator and annealed to ~470 K to degas. The ion sputtering and annealing cycles are also carried out with the sample on the manipulator. Temporary unused sample and tip can be stored in a carousel sample storage, which has a capacity of resting twelve samples or tips. The transfer of sample or tip inside the chamber is performed by using a wobble stick.

The most important component, the STM stage is shown in Fig. 3.11. On the STM stage, the scanner and the sample stage are mounted on a base plate, which is suspended by four soft springs. The resonance frequency of the spring suspension system is about 2 Hz. In order to adsorb the vibration energy efficiently, an eddy current damping mechanism is employed, for which the base plate is surrounded by a ring of copper plates, and these copper plates come down between permanent magnets as indicated in Fig. 3.11. Such mechanism together with the floating stage provides an excellent vibration-free environment for the STM. A push-pull motion drive (PPM) is used to lock the suspension plate for sample or tip exchange, or unlock it for STM scanning.

This variable temperature STM can do STM imaging in a temperature range from - 44 K to 1500 K. To achieve this capability, separated heating and cooling techniques are used. For cooling, as seen in Fig. 3.11, a Helium flow cryostat is mounted on the base plate, a liquid He flow travels through the cryostat under the control of a gas flow control block can cool down the cryostat to as low as 17 K. There is a resistant heater mounted in the cryostat which is controlled by a Lakeshore temperature controller. By fine tuning the working power of the resistant heater, any temperature between 17 K and room temperature can be achieved at the cryostat. The He flow cryostat is connected to a thermal exchanger which projects through the base plate. At the other end of the thermal exchanger, there is a connector plate cryostat, which is connected via highly flexible copper braids (no shown in Fig. 3.11) to a cooling block mounted on the cooling stage. The cooling block can be moved to cover

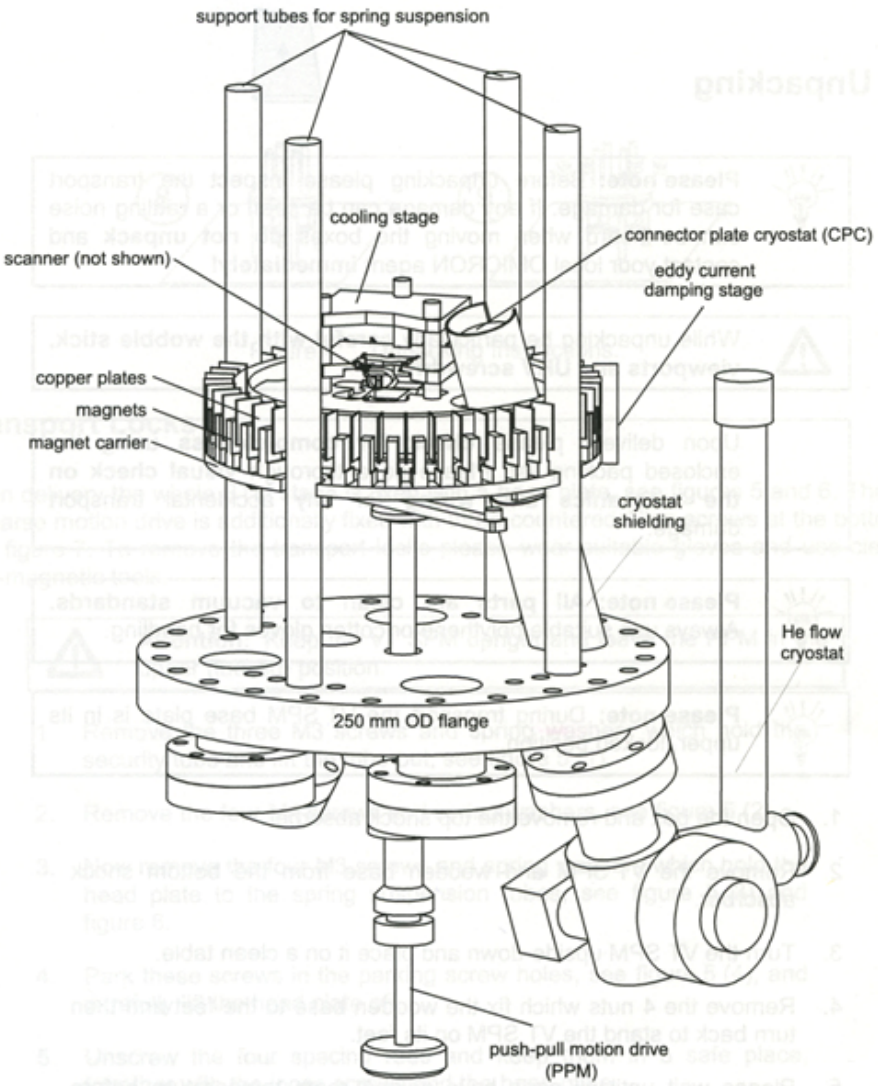

Fig. 3.11: The STM stage (from Omicron's manual). The whole STM system is mounted on a 250 mm flange. The base plate is suspended on four soft springs, a ring of alternating copper plates and magnets are used for vibration damping. Push-pull motion drive (PPM) is used for lock the suspended base plate. He flow cryostat is mounted on the flange, connected to a thermal exchange projecting through the flange and STM base plate, at the other end of the thermal exchange, there is the connected plate cryostat (CPO). The CPO is connected via highly flexible copper braids (not shown in this image) to the cooling block on the cooling stage.

the top of the sample holder (the sample is mounted face down in the sample holder) and thus cooling the sample, see Fig. 3.12(b). The use of highly flexible copper braids

is to minimize vibration during low temperature STM scanning. However, due to the thermal transfer efficiency, the sample temperature is always higher than the temperature of the He flow cryostat. When the He flow cryostat kept at its lowest temperature 5.6 K, the sample temperature can stay stable at 44 K. Both

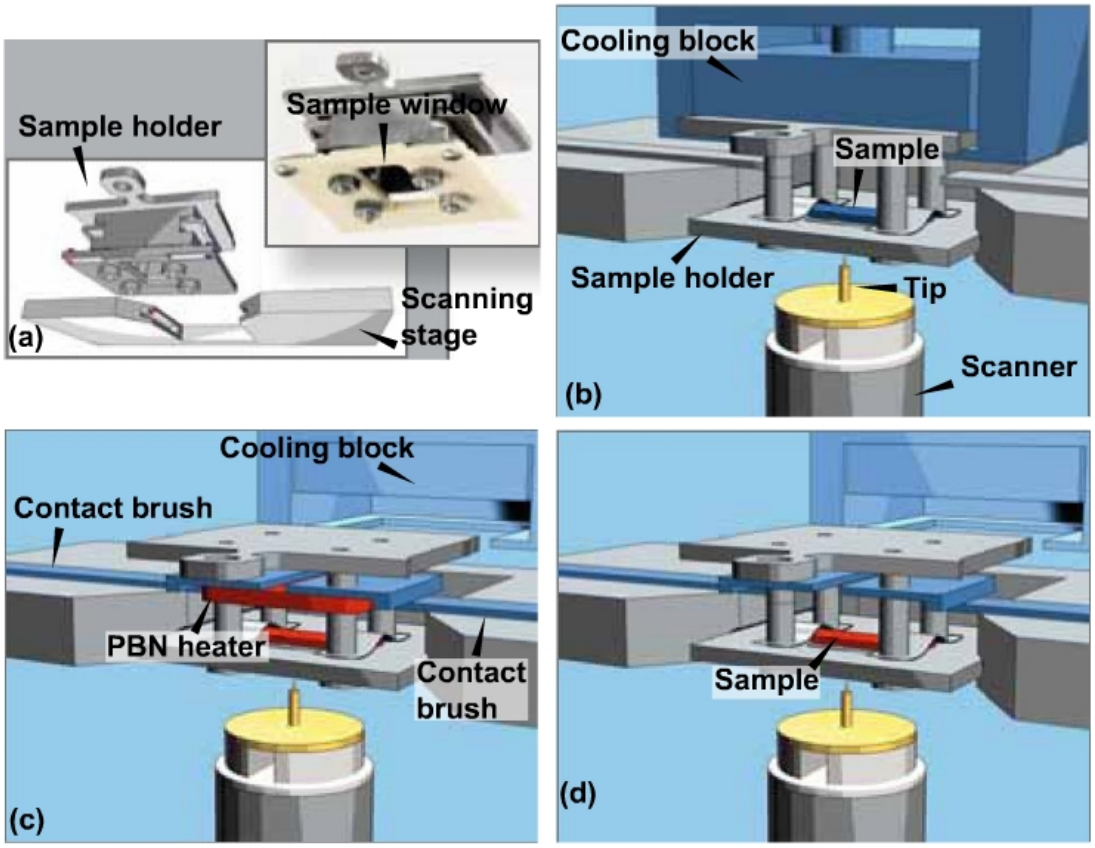

Fig. 3.12 (from Omicron's product introduction) (a): The sample holder, the sample is mounted face down in the sample holder. STM tip approached via the window on the bottom of the sample holder to scan the sample surface. (b): The setup for low temperature experiment, the cooling block is placed over the sample holder to cooling the sample. (c): The setup for radiative heating experiment, cooling block is retracted from the sample holder. The heating current is applied via the contact brushes to the PBN heater in the sample to heat the sample. (d): The setup for directly heating, the current is applied via the contact brushes directly to the sample.

the temperatures of the sample and the He flow cryostat are monitored simultaneously

by the temperature controller with the silicon diodes mounted there, respectively. Liquid nitrogen can also be used as cryogen, but can not reach a temperature as low as using liquid He.

For raising the sample temperature, there are two ways to do so, direct heating and radiative heating. In both case, a DC current is supplied to the sample holder via two contact brushes to the sample holder, as shown in Fig. 3.12(c) (d). For direct heating, the current is applied directly passing the sample. The temperature can reach 1500 K. However, in order to use direct heating, the sample itself must have a large resistance, such as silicon samples. For radiative heating, the current is applied to an embedded solid state (PBN) heating element placed near the sample inside the sample holder. Using this method, the sample temperature can be raised to 923 K.

3.2.3 Tip Preparation

The tip used in my experiment is made from 0.4 mm tungsten wire (99.95% purity) by chemical etching in 10% NaOH solution.

As etched and stored in atmosphere, the tip is covered by oxide and contaminants, which will cause instability of the tunnel junction hence poor quality images. Several methods are used to clean the tip before collecting images. First, when the tip is transferred into the UHV chamber, a 470 K annealing is carried out on the manipulator to remove the oxide layer and adsorbed contaminants. The annealing normally lasts 2~4 hours or as long as the vacuum pressure level falls back to normal. When the tip is used for scanning, if the image quality is poor, a simple way to clean

the tip is to suddenly raise the tunneling current to 8~10 nA and turn it back to normal after scanning for one or two lines. The sudden increase of the tunneling current causes the tip-sample distance to rapidly shrink, sometimes the tip will slightly crash with the surface, which may remove the adsorbate on the tip or rearrange the atoms at the very end of the tip, thus leads to better image quality. However, this method may damage the surface, and if there are C_{60} molecules adsorbed on the surface, such a shrink of tip-sample distance may transfer molecules to the tip. Another more gentle method is also used, in which STS is performed during a constant current scanning. The voltage ramp during the STS may desorb the contaminants attached on the tip. Also, the ramp may reform the shape of the very end of the tip, which leads to better scanning condition. The voltage used for the STS ranges from - 3 V to + 3 V, if this does not improve the image quality, higher voltages is tried, however, the STS voltage will not be raised higher than ± 4 V to avoid possible damage to the surface. Once a tip is proved a good tip for atomic resolution image, it remains good as long as kept in UHV condition.

3.2.4 C_{60} Deposition

The C_{60} molecule used in my research is bought from MER Corp. US. The purity is 99.9%. The C_{60} powder is placed in a home-made Knudsen cell (K-cell). Direct current is used to heat the K-cell and there is a silicon diode attached to the K-cell to monitor the temperature. The K-cell is mounted under the flange of the STM stage, evaporated C_{60} molecular beam travels via an open window on the suspended base

plate to arrive the sample surface. For C_{60} deposition, the K-cell is preheated to 600 K and kept for 5 minutes to degas. At this temperature, no C_{60} molecules will be evaporated. Then, the temperature is raised to 720 K for evaporation. The deposition rate is very low, approximately 0.05 ML/min. The amount of C_{60} molecules received by the sample is controlled by adjusting the evaporation time.

3.2.5 STM Scanning

The STM scanner used in this system is a single tube scanner with a maximum scan range of 12 × 12 μm in the *x*-*y* plane and a *z*-direction travel range of 1.5 μm. The vertical accuracy of the scanner is better than 0.01 nm.

All the images in my research are obtained under constant current mode with tungsten tips. To obtain STM images of reconstructed Au (111) surface, the standard sample bias and tunneling current used are - 1.2 V and 1 nA, respectively. To achieve atomic resolution on a small region on the Au (111) surface, tunneling current larger than 1 nA and a relatively small bias voltage are used, in order to bring the tip closer to the surface and enhance the signal-noise-ratio.

As mentioned above, the C_{60} molecules adsorbed on the Au (111) surface are easily picked up by the scanning tip. Therefore, large tip-sample distance was used to prevent unwanted interaction between the tip and the adsorbed molecules. 0.03 nA is the lowest stable working tunnelling current allowed by this STM and this value is used with a certain bias voltage in order to keep the tip-sample distance large. A negative sample bias of 1.2~1.7 V is found to give the best image with a 0.03 nA

tunneling current. Of course, small adjustment of these parameters is needed from time to time to optimise the image. However, even with caution, some C_{60} molecules inevitably get picked up by the tip when scanning a large area or scanning over some rough area. This usually degrades the performance of the tip. Tip cleaning methods described earlier are used to clean the tip when necessary. To obtain images at low temperatures, similar scanning parameters as that used at room temperature are used.

In situ deposition of C_{60} molecules is involved in my research. During the deposition, the tip must be as far as possible from the surface to avoid the attachment of C_{60} molecules. In order to obtain STM images of the same area before and after the C_{60} deposition, the tip must have the ability to locate the original imaging area on the surface. Fortunately, our STM system is stable enough to achieve this ability. Before deposition, a large image about 4 × 4 μm is recorded with the original investigated area in the centre. Then the tip is retracted in the *z* direction to its limit with the *x*, *y* coordinates unchanged. After the deposition, the tip is approached to the surface again and another 4 × 4 μm image is taken. By comparing the topography in the two large images, the original studied area can be located. The drift is usually less than 1μm.

3.2.5 Gold-finger Fabrication

In my research, the nucleation and growth of submonolayer C_{60} on an artificially created zero-gradient stepped surface (ZGSS) is studied. The ZGSS surface consists of parallel monoatomic gold stripes, which are drawn out from a monoatomic step on Au (111) surface by the STM tip. A typical ZGSS is shown in Fig. 3.13. The parallel

gold stripes are named gold-fingers.

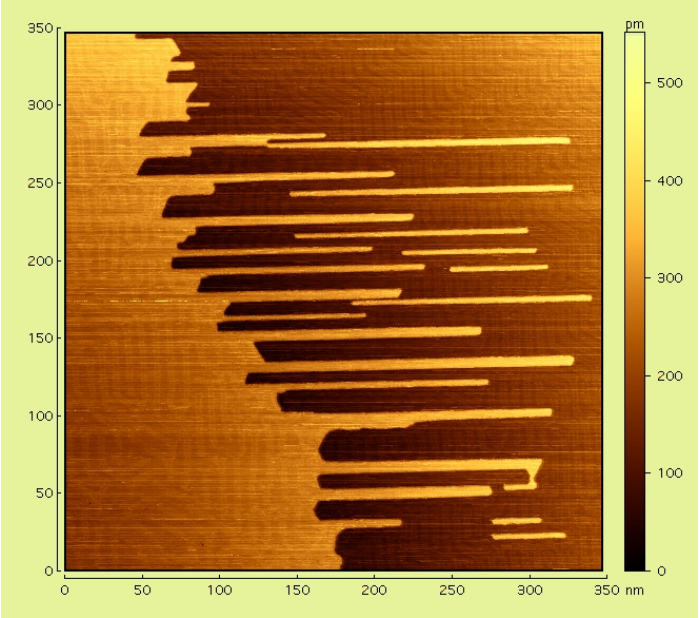

Fig. 3.13: 350 × 350 nm, V = 0.8 V, I = 0.1 nA. A typical zero-gradient stepped surface (ZGSS) consists of gold-fingers.

The fabrication method of gold-finger has been introduced in detail in the previously work of Q. Guo *et al*. [10]. At first, a monoatomic step separating two terraces on the Au (111) surface must be located for the gold-finger fabrication. Gold-finger can only grow in one of the three equivalent directions: [-101], [-110] and [01-1]. These three directions can be easily identified during STM imaging: they are at 30º, 90º and 150º to the direction of the discommensuration lines (DLs) on the upper terrace of the step. If the scanning direction is parallel to one of these three directions during the gold-finger formation, the growth speed is the highest. The gold-finger does not appear at all if the scan direction is perpendicular to one of the three directions. Since the formation of the gold-fingers is driven by a high electric

field beneath the STM tip, a closer tip-sample distance than that used in normal imaging mode is used for the surface modification. A typical value of the bias voltage of 1.8 V is used and the tunneling current is set to 20 nA to start with. If these parameters are insufficient to create the expected gold-fingers, the bias voltage and tunneling current are gradually increased until the appearance of the finger-like structures. Normally, a bias voltage of 1.8~2.2 V and a tunneling current of 30~50 nA can lead to the formation of gold-fingers. However, not every tip can induce the formation of gold-fingers, this is because some tip has large radius of curvature thus the electric field beneath the tip is not so localized as those beneath sharp tips. Blunt tip makes the electric field too weak to extract gold atoms out from the steps.

References

[1] X. M. Ding, X. J. Yang, and X. Wang, in *Surface Physics and Surface Analysis*. Fudan University Press, Shanghai, p1 (2004).

[2] C. P. Chen, T. W. Pi, C. P. Ouyang and J. F. Wen, J. Vac. Sci. Technol. B **23**, 1018 (2005).

[3] A. Damascelli, presentation, from internet.

[4] S. D. Kevan and R. H. Gaylord, Phys. Rev. B **36**, 5809 (1987).

[5] G. Binnig, H. Rohrer, Ch. Gerber and E. Weibel, Phys. Rev. Lett. **49**, 57 (1982).

[6] R. J. Hamers, R. M. Tromp and J. E. Demuth, Phys. Rev. Lett. **56**, 1972 (1986).

[7] G. Schull, T. Frederiksen, M. Brandbyge and R. Berndt, Phys. Rev. Lett. **103**, 206803 (2009).

[8] D. M. Eigler and E. K. Schweizer, Nature **344**, 524 (1990).

[9] L. Grill, K. H. Rieder, F. Moresco, G. Rapenne, S. Stojkovic, X. Bouju and D. Joachim, Nature Nanotech. **2**, 95 (2007)

[10] Q. Guo, F. Yin and R. E. Palmer, Small **1**, 76 (2005).

CHAPTER 4
ROOM TEMPERATURE GROWTH OF C_{60} STRUCTURES

In this chapter, the room temperature growth of C_{60} submonolayer on the Au (111) surface will be introduced. As mentioned in the literature review, the interaction between the C_{60} submonolayer and the substrate is very complicated, leading to lifting of the substrate reconstruction and the appearance of dim molecules in the C_{60} monolayer. This interaction has not been fully understood yet, as observations from different laboratories sometimes point in different directions. Therefore, I am going to present my STM results addressing these topics and try to give a possible explanation for these phenomena in this chapter. Also, the STM observation of the R14º C_{60} monolayer, together with the superlattice formed by an array of dim molecules will be introduced. These points will serve as a foundation for the discussions in the remaining chapters.

4.1 Lifting of the Substrate Reconstruction

The different C_{60} monolayer structures, R0º, R14º and R30º are named after their relative azimuthal angles with an unreconstructed 1 × 1 gold substrate, because the original herringbone reconstruction of the clean Au (111) surface was reported to be lifted upon the adsorption of a C_{60} monolayer [1]. However, this is not always the case. In my research, in some cases the herringbone reconstruction is found to remain intact

under the C_{60} monolayer. As shown in Fig. 4.1(a), at the coverage of ~0.2 ML, two R0º C_{60} islands grow from step edges, indicated by the blue arrows. On these two large islands, pairs of bright lines are seen, which consists of C_{60} molecules that are ~0.3 Å higher than surrounding molecules. The distance between neighboring pairs of bright lines is ~6.3 nm (from center to center), while the separation of the two lines in a pair is ~2.2 nm, such periodicity and separation are the same to those of the discommensuration line (DL) pairs of the Au (111) surface. Moreover, these bright lines arrange themselves into a zigzag pattern with ~120º bends, which is identical to the herringbone pattern of the Au (111) surface. Thus, it is evident that in this particular case, the herringbone reconstruction of the substrate under the C_{60} monolayer remains intact after the adsorption, leading to the corrugation of the C_{60} monolayer which is imaged as bright lines. Furthermore, at the edge of the C_{60} islands, the bright lines are found to match perfectly with surrounding DLs on the bare Au surface, indicating that these DLs propagate from the bare Au region into the C_{60} covered region without being disturbed. Therefore, Fig. 4.1(a) demonstrates that the adsorption of a R0º C_{60} monolayer does not necessarily influence the underlying Au (111) herringbone reconstruction, of which both the periodicity and the contour can remain intact upon the adsorption. This is in contrast to previously observations [1]. As mentioned before, the reconstruction of the Au (111) surface is caused by the surface strain, and the adsorption of C_{60} monolayer can completely or partially relieve the surface strain, therefore, the reconstruction under the C_{60} monolayer will be either completely lifted [1], or partially lifted leading to enlarged periodicity of the DL pairs

and disturbed reconstruction pattern [2, 3]. My results show that the bonding between the C_{60} molecules and the Au (111) surface is not strong enough to influence the surface strain, because both the pattern and the periodicity of the DL pairs under the C_{60} islands remain unchanged.

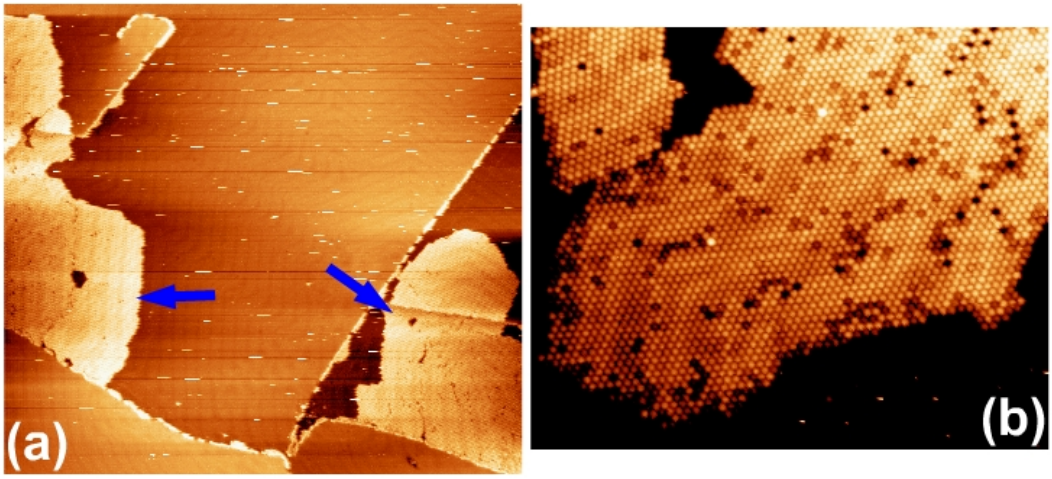

Fig. 4.1 (a): 270 × 250 nm, V = -1.7 V, I = 0.03 nA. Two R0º C_{60} islands are indicated by two blue arrows. On these two islands, pairs of bright lines representing the underlying herringbone reconstruction can be seen. The bright lines on the islands have identical periodicity to the DL pairs on clean Au (111) surface, and these bright lines link continuously with surrounding DLs on bare Au region. Therefore, the substrate reconstruction under the C_{60} monolayer is not disturbed at all upon the adsorption. (b): 63 × 51 nm, V = -1.7 V, I = 0.03 nA. Another example of the herringbone reconstruction remains completely intact under a R0º C_{60} island.

Fig. 4.1(b) shows another example of intact substrate reconstruction upon the adsorption of C_{60} monolayer. The large island in this image is of the R0º structure, on which the corrugation of C_{60} monolayer presents a perfect herringbone pattern, even the difference between the type *x* and type *y* elbows is revealed (pointed and rounded elbows, respectively). The small island on the upper left corner of the image is of the

R30º structure. Two pairs of bright lines can be seen on this R30º island, and the periodicity of the bright line pairs on this island is measured to be ~6.3 nm, which is the same as the value measured on bare Au (111) surface, indicating that despite the R30º monolayer being energetically favoured than the R0º monolayer, the herringbone reconstruction of the Au (111) surface can also be retained under it. Fig. 4.2(a) presents another R30º C_{60} island with underlying substrate reconstruction, but in this case, the reconstruction is partially lifted. The distance from one pair of bright lines to the next pair on this C_{60} island is slightly enlarged to ~7.3 nm, compared with a periodicity of 6.3 nm for the DL pairs on clean Au (111). Moreover, some lines are missing in the reconstruction pattern, leading to the enlargement of some FCC regions, the HCP region is never enlarged and the distance between a pair of DLs remains constant. Such R30º C_{60} island resting on a partially relieved substrate reconstruction is similar to the observation of J. K. Gimzewski *et al* [2]. But in their case, the deposition rate of C_{60} is very high, multilayer of C_{60} is formed in a short time and they subsequently desorbed the multilayers. They concluded that a complete monolayer is formed before the Au surface atoms have enough time to re-organize, which leads to a partially relieved reconstruction. In my case, the deposition rate is very low, ~0.05 ML per minutes. Moreover, only submonolayer is formed in my experiment, so the Au atoms would have enough time and space to relocate, if they want to. However, the reconstruction is retained under the C_{60} submonolayer even under my growth parameters, indicating that the determinative factors for lifting the reconstruction is not the deposition rate or the growth method.

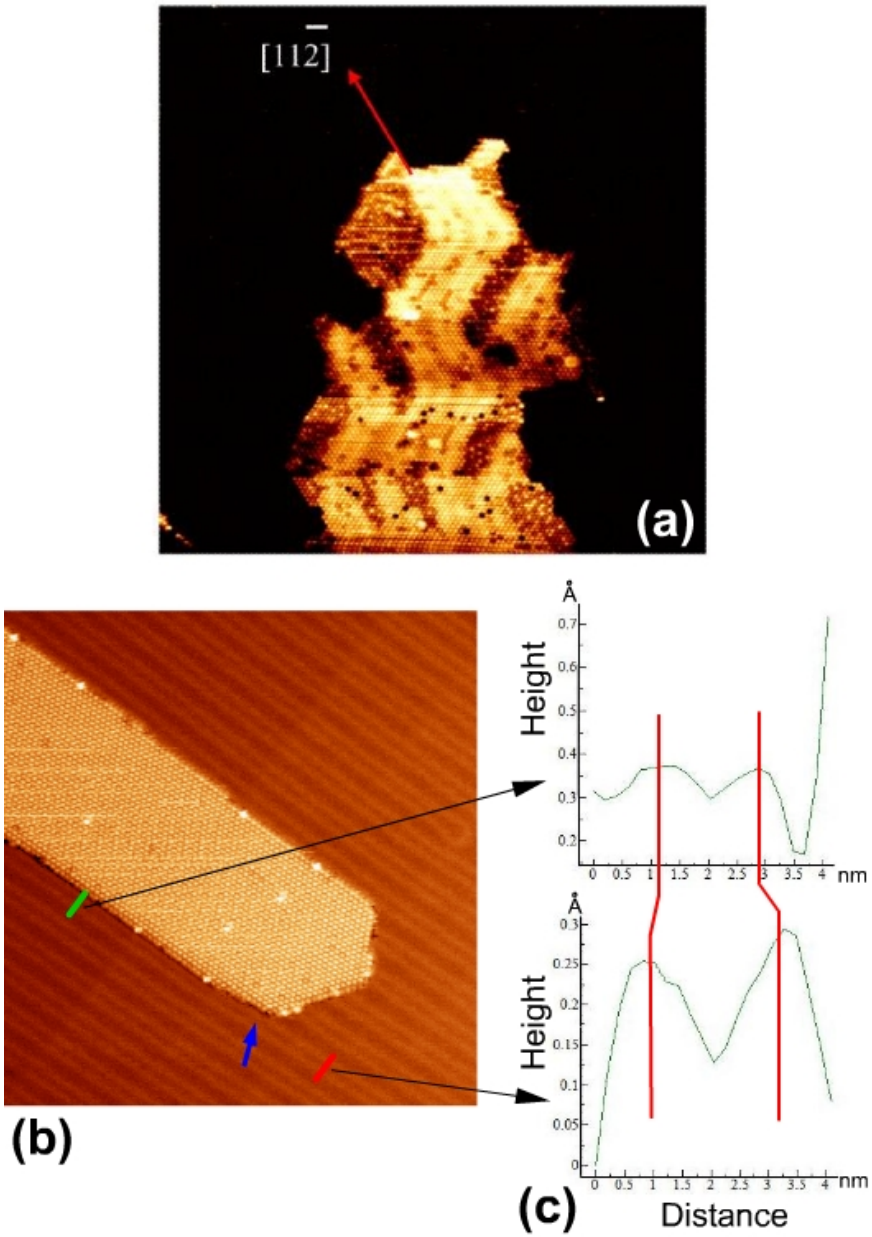

Fig. 4.2 (a): 110 × 110 nm, V = -1.7 V, I = 0.03 nA. A R30º C_{60} island reveals a partially relieved substrate reconstruction underneath. The contrast of this image is adjusted to clearly show the corrugation of the C_{60} island thus the herringbone pattern of surrounding Au surface can not be revealed. The [11-2] direction of the Au (111) surface is indicated, according to the herringbone pattern seen under different contrast. (b): 82 × 85 nm, V = -0.9 V, I = 0.03 nA. A R30º C_{60} island has all molecules in the same height except several bright spots. The surrounding bare Au surface presents uniform straight DLs. The blue arrow indicates a bending of the DL when meets the C_{60} island. (c): The two height profiles along the green and red lines in (b), respectively. The lateral scale bar for the two height profile is exactly the same, thus it is clearly seen that the separation of the DLs in a pair is compressed from ~2.2 nm to ~1.7 nm, indicated by the thin red lines.

With regard to the registration of the R30º C_{60} monolayer with the substrate atomic lattice, when the substrate reconstruction is lifted and the C_{60} molecules sit on a 1 × 1 Au surface, the C_{60} monolayer is commensurate with the Au (111) surface and has an (2√3 × 2√3)R30º unit cell. However, Fig. 4.1(b) and Fig. 4.2(a) show that the Au substrate in some cases is still reconstructed, which means that the molecules in the monolayer can not occupy identical adsorption site, and the C_{60} monolayer is thereby incommensurate with the Au (111) surface. A R30º monolayer being incommensurate with the substrate cannot be described by the (2√3 × 2√3)R30º unit cell. For clarity, the R30º C_{60} monolayer resting on reconstructed substrate will be called R30º-A structure and the R30º monolayer resting on unreconstructed 1 × 1 substrate will be called R30º-B.

R30º-B C_{60} monolayer has been found on the same sample after the same amount of C_{60} deposition with the R30º-A monolayers introduced above, just at different locations. Fig. 4.2(b) presents a typical (2√3 × 2√3)R30º-B C_{60} island, with no evidence of any underlying reconstruction. All the molecules in this island have uniform height except several bright spots. The formation of these bright spots will be introduced in Fig. 4.8. The bare Au surface surrounding the island presents long-straight DLs with no bending inside the imaged area. And the C_{60} island also adopts a long-narrow shape with its two long edges running parallel to the DLs, and both the two long edges fall in the FCC side of two DLs. Moreover, the DL next to one of the C_{60} island's long edge slightly bends in front of the island, indicated by the blue arrow in Fig. 4.2(b). The bending of the DL compresses the width of the adjacent

HCP region from 2.2 nm to 1.7 nm, which is presented in the height profiles shown in Fig. 4.2(c). All these observed features are consistent with the picture that the substrate reconstruction has been completely lifted and the C_{60} island is sitting on a 1 × 1 surface. Therefore, the expansion of the existing C_{60} island in the direction perpendicular to the DLs seems following such steps, if the Au atoms at the growth front of the island occupy HCP sites or incommensurate sites (on the DLs), they need to be laterally relocated to FCC sites, when the transformation is completed, an extra row of C_{60} molecules can attach to the growth front of the island. In this manner, the growth rate of the C_{60} island is controlled by the transformation of the HCP region or DLs into FCC region. This growth process is consistent with the explanation of remaining substrate reconstruction given by J. K. Gimzewski *et al* [2], who claims that if the deposition rate of C_{60} molecules is higher than the transformation rate of HCP region to FCC region, the C_{60} island will cover and retain the not-fully-lifted reconstruction, otherwise, if the deposition rate is low enough, the formed C_{60} monolayer will sit on unreconstructed 1 × 1 surface, which is the case of the R30º-B C_{60} island shown in Fig. 4.2(b). However, this growth process cannot be used to explain the growth of the two R30º-A C_{60} islands described above in Fig. 4.1(b) and Fig. 4.2(a), which reveal that the substrate reconstruction is retained underneath. The R30º-A and R30º-B C_{60} islands observed in my research are formed simultaneously on the same sample, thus the deposition rate is the same for these islands. Therefore, there must be other reasons causing the different situations of the underlying substrate reconstruction.

Comparing the R30º-A C_{60} islands in Fig. 4.1(b) and Fig. 4.2(a) with the R30º-B island in Fig. 4.2(b), the most obvious difference is the arrangement of the DLs of the Au (111) surface. In Fig. 4.1(b) and Fig. 4.2(a), the DLs bend a lot, forming a zigzag pattern, namely the "herringbone", but in Fig. 4.2(b), the DLs run straightly for more than 100 nm without any bending. As introduced in the literature review, the reconstructed Au (111) surface is tessellated by alternating 120°-rotated domains, at the boundary of two adjacent domains, the DLs form a 120°-bended elbow site to connect the two DLs segments on each domains. These domains have an average size of ~25 nm, thus the periodicity for the DLs to bend is also ~25 nm. However, the domain size has a large distribution even for the same sample. As shown here, the domain size can vary from less than 20 nm to more than 100 nm, which leads to a large difference in the density of elbow site from place to place. And we know that, at each elbow site of the type *x* DL, there is an edge dislocation which introduces an extra row of Au atoms. To lift the reconstruction, these edge dislocations must be eliminated and the extra Au atoms must be relocated. Therefore, it is much more difficult to lift the reconstruction of a region with frequently bending DLs, which requires the elimination of edge dislocations and the relocation of a large number of extra substrate atoms. To lift the reconstruction of a region with a large single domain is much easier, which only needs to release the extra atoms in each contracted ($22 \times \sqrt{3}$) unit cell. The subsequently lateral movement of the Au surface atoms from the HCP site and bridge site to the FCC site is energetically favored. This difference in the substrate reconstruction pattern should be the determinative factor for whether the

adsorbed C_{60} molecules can lift the underlying reconstruction or not.

Another interesting phenomenon has been observed in my experiment, which can be called the reformation of the reconstruction. In Fig. 4.3(a), there are two R0º C_{60} islands. By raising the tunneling current from 0.03 nA to 1 nA for several scan lines during the imaging, one C_{60} island is broken by the tip, giving rise to three fragments and many tiny pieces, as shown in Fig. 4.3(b). Both before and after the disruption, there are bright lines on the C_{60} island revealing underlying substrate reconstruction, as shown in Fig. 4.3(c) and (d). Missing lines and enlarged separation of these bright lines indicate that the substrate reconstruction is partially lifted. Fig. 4.3(e) presents a height profile along the green line marked on the C_{60} island in Fig. 4.3(c). In this height profile, four main peaks are clearly seen, representing the four bright bands on the island. Each main peak has two sub-peaks, indicating that each bright band is actually a pair of bright lines. This is consistent with the structure of the DLs, which consists of a pair of ridge lines. From the height profile, the center-to-center distances of these bright bands are measured, giving results of 13.5 nm, 18.0 nm and 10.0 nm, respectively, which means that the separation between the DL pairs of the substrate reconstruction is enlarged from its origin value of 6.3 nm to above new values, driven by the relief of the surface strain. Then, as shown in Fig. 4.3(f), the region used to be covered by the C_{60} monolayer is exposed after the disruption, the DLs in this region can thus be directly seen. A rearrangement of the surface Au atoms at this region must have taken place, because the periodicity of the DL pairs has changed back from those enlarged values to the original value of 6.3 nm.

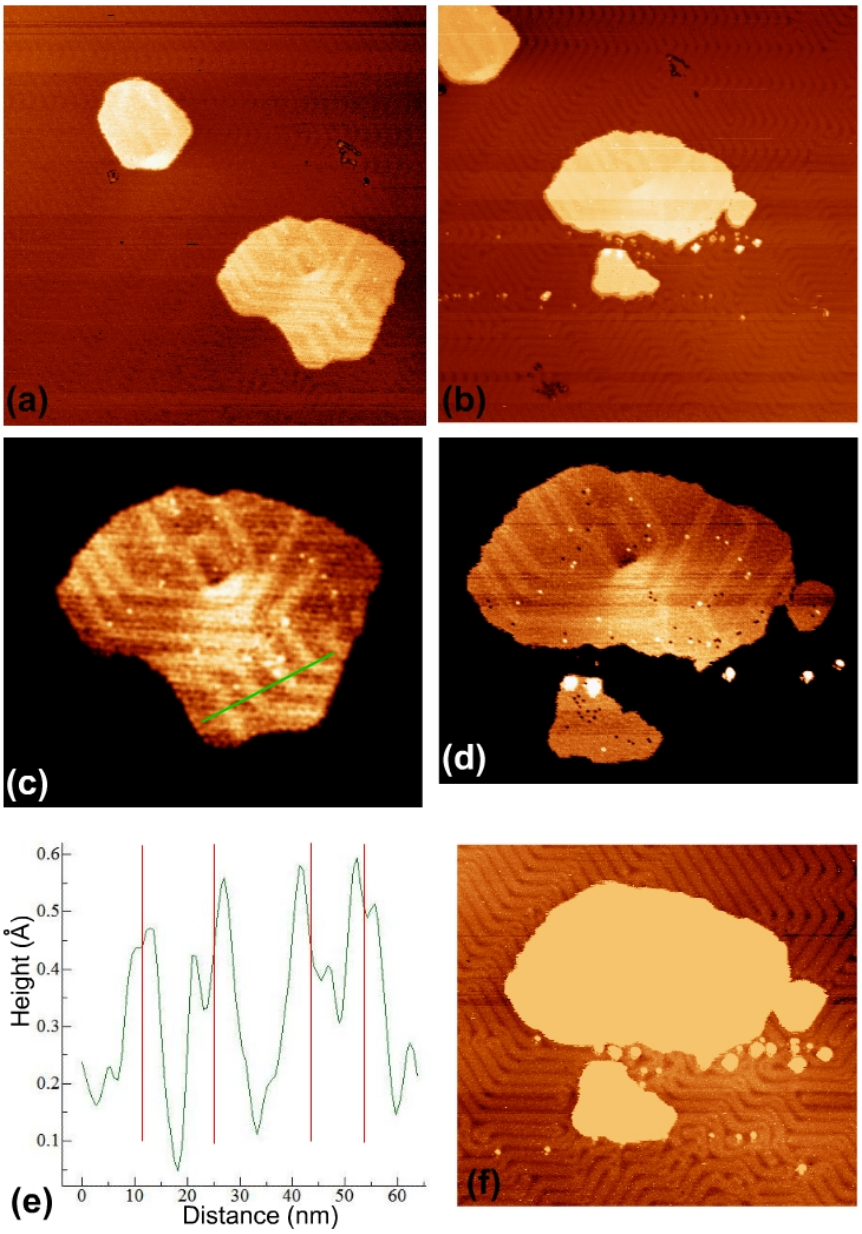

Fig. 4.3 (a): 308 × 308 nm, V = -1.7 V, I = 0.04 nA. Two R0º C_{60} islands adsorb on the Au (111) surface. (b): 308 × 308 nm, V = -1.7 V, I = 0.04 nA. By raising the tunneling current to 1 nA for several scan lines during the imaging, one C_{60} island is broken. (c) and (d): Zoomed-in images of (a) and (b), respectively. The bright lines on the C_{60} island represent the underlying substrate reconstruction, which is partially relieved, resulting in missing lines and enlarged line-to-line separation. (e): the height profile along the green line in (c). By measuring the distances between the peaks, the separations of the DL pairs of the substrate reconstruction can be found out. The red lines are drawn to help finding the centers of each peak, peak-to-peak distance is measured between these red lines. (f): An image shows the DLs on the region used to be covered by the C_{60} molecules.

Such a reformation to the regular DL pattern requires extra Au atoms to be injected to this region, because the higher density of DLs corresponds to higher contraction of surface atoms. The injected Au atoms may come from the newly covered regions, from where the Au atoms are released due to a relief of the substrate reconstruction.

Up to now, we have discussed the interaction between the adsorbed C_{60} submonolayer and the reconstruction of the Au (111) surface. It is found that whether the C_{60} island can lift the underlying reconstruction or to what level it can relieve the reconstruction depends on the density of DLs elbow site at the specific region. A high density of elbow site will make the reconstruction difficult to be lifted, thus the adsorption of C_{60} mainly leads to missing lines and enlarged periodicity of the DL pairs, which is a symbol of partially relieved surface strain. On the other hand, at regions consisting of a large single domain, the reconstruction is much easier to be lifted, thus the C_{60} molecules will sit on a 1 × 1 Au (111) surface. The reformation of the substrate reconstruction is also shown. When the covered C_{60} monolayer is removed, the underlying Au atoms will rearrange and the lifted or partially lifted reconstruction will restore its original state on the clean Au (111) surface.

4.2 R14º C_{60} Monolayer

In addition to the R0º and R30º C_{60} monolayers, R14º C_{60} monolayer is also observed in my experiment. This structure has been predicted by x-ray diffraction and LEED experiment, respectively [4, 5], but no STM observation has been reported until recent times [6, 7]. As seen in Fig. 4.4, there is a monoatomic step running across the image

from top to bottom and C_{60} islands grow from this step, on both its upper and lower terraces. Four C_{60} islands can be seen, marked A, B, C and D, respectively. On the bare Au (111) surface, the herringbone pattern can be seen, of which the DLs are running along the [11-2] direction of the substrate. By confirming the [11-2] direction, the other crystallographic directions of the Au (111) surface can be confirmed. Two of the close-pack directions, [10-1] and [01-1], of the Au (111) surface are drawn on the image for the convenience of the following discussion. One of the close-pack directions of the C_{60} island A is also indicated by a green line. This green line has a 14º angle to the [10-1] direction, indicating that the close-pack direction of island A is 14º azimuthally rotated with respect to the close-pack direction of the Au (111) surface, which means it is a R14º C_{60} island. Island B has two parts, on the upper and lower terraces of the Au step, respectively. The two parts have the same close-pack directions, one of which is marked by the red line. This red line is 14º clockwise rotated from the [01-1] direction, therefore the island B is also a R14º C_{60} island. Moreover, island C is found to have the R0º structure, while island D has its close-pack direction the same as island A, which makes it again a R14º island. With the examples of islands A and B in Fig. 4.4, the R14º C_{60} monolayer is found to have its close-pack direction either clockwise or anticlockwise rotated from the close-pack directions of the Au (111) surface. Considering the Au (111) surface has three equivalent close-pack directions, there will be six possible orientations for the R14º C_{60} structure, which is consistent with the LEED pattern of the R14º C_{60} monolayer [5].

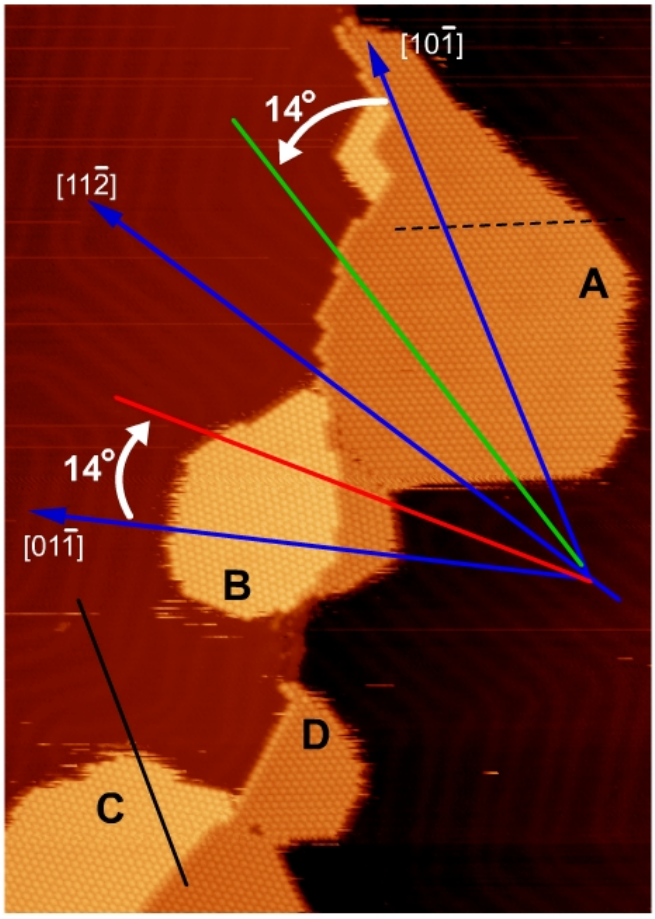

Fig. 4.4: 77 × 108 nm, V = -1.7 V, I = 0.03 nA. Four C_{60} islands grow from a monoatomic step edge on the Au (111) surface, marked A, B, C and D, respectively. Three crystallographic directions of the Au (111) surface, [10-1], [11-2] and [01-1]], are indicated by blue arrows, of which the [11-2] direction is parallel to the DLs while the [10-1] and [01-1] are two close-packed directions of the surface Au atoms. The close-packed directions of C_{60} island A, B and C are indicated by green, red and black lines, respectively. It is clear seen that the close-packed directions of islands A and B are 14º rotated from the [10-1] and [01-1] directions, anticlockwise and clockwise, respectively. Therefore islands A and B have the R14º structure. Island C is a R0º island and island D is R14º again. The dashed black line indicates the close-packed direction of the monolayer, along which the nearest C_{60}-C_{60} distance is measured to be 1.06 nm. Note the Au step edge running across the islands, which has been modified by the adsorption of the C_{60} molecules, thus consists of short segments that running along the close-packing directions of the C_{60} molecules.

A model for the R14º C_{60} monolayer is given by G. Schull and R. Berndt [7]. In their model, they suppose the C_{60} molecules in the R14º structure adopt the 1.002 nm bulk value of the nearest C_{60}-C_{60} distance. By fitting such a C_{60} monolayer onto an unreconstructed 1 × 1 Au (111) surface, the model results in such configuration: the close-packed direction of the R14º structure will be 14.5º rotated from the close-packed direction of the substrate, and every seventh molecule along the close-packed direction of the monolayer occupies identical adsorption site. This configuration leads to a (√589 × √589)R14.5º unit cell for the C_{60} monolayer, with each √589 × √589 unit cell consisting of 49 molecules in a 7 × 7 array. Such a 7 × 7 model of the R14º structure can be compared with the R0º structure, in which the molecules also periodically occupy identical adsorption sites, but the periodicity is 11 molecules instead of 7 and the unit cell is (38 × 38)R0º.

Here, we propose another model for the R14º structure, which is also based on an unreconstructed 1 × 1 Au (111) surface, as there is no evidence of remaining herringbone reconstruction underneath observed. As mentioned in the literature review, the R14º structure is found to be more stable than the R0º structure upon annealing, thus we propose that every C_{60} molecules in the R14º structure occupy identical a-top adsorption site, which is the same as the most stable R30º structure. By doing so, the nearest neighboring distance of the C_{60} molecules in my model is found to be 1.039 nm, which is larger than the 1.002 nm bulk value by around 4%. The azimuthal angle of the C_{60} monolayer is calculated to be 13.9º from the Au substrate, which is slightly smaller than the azimuthal angle of 14.5º in the 7 × 7 model. A

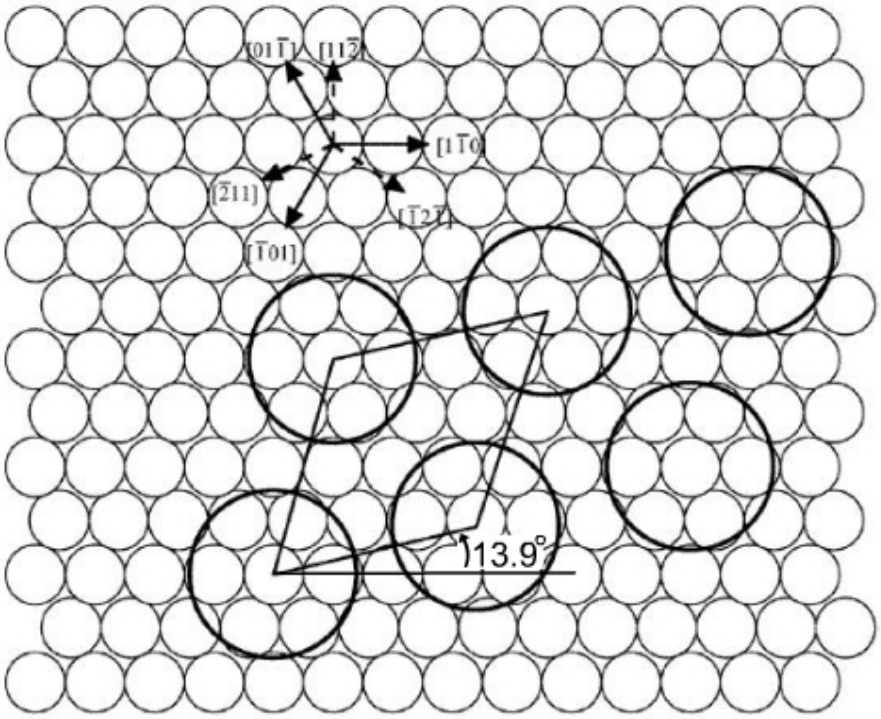

Fig. 4.5: The (√13 × √13)R13.9º model for the R14º structure. The small circles represent surface Au atoms, which form a bulk terminal 1 × 1 surface. The crystallographic directions for this surface are marked with arrows. The large circles represent the C_{60} molecules. In this model, every molecules in the R14º structure occupy identical a-top adsorption site, the nearest molecular distance is 1.039 nm and the C_{60} monolayer is rotated from the surface atomic lattice by 13.9º.

schematic diagram of my model can be seen in Fig. 4.5, it can be named the (√13 × √13)R13.9º. The two models are different in the nearest C_{60}-C_{60} distance, 1.002 and 1.039 nm, respectively, thus by measuring the realistic distance, the right model can be chosen. However, G. Schull *et al*. did not mention the nearest C_{60}-C_{60} distance in their STM experiment. In my study, the distance is variable along the three close-packed directions of the monolayer, averaging 1.06, 1.00 and 0.94 nm, respectively. This variation is due to a distortion of the STM image caused by the

thermal-drift. Nevertheless, the distance of 1.06 nm is measured along the close-packed direction (marked by the dashed line in Fig. 4.4) that has the smallest azimuthal angle (smaller than 3º) with the scanning direction, therefore this value should be very close to the realistic value, and it is close to the nearest C_{60}-C_{60} distance of 1.039 nm in my model.

There is another phenomenon should be noticed in the image shown in Fig. 4.4. The Au step covered by the C_{60} monolayer presents a saw-tooth-like feature. The step edge is divided into small segments, each segment is aligned with one of the three close-packing directions of the C_{60} molecules. Such feature indicates a modification of the step edge by the C_{60} molecules. This phenomenon will be discussed in detail in the Chapter 5.

4.3 The Dim Molecules in the C_{60} Monolayer

As mentioned above, the nearest neighbor molecular distance in my model of the R14º structure is 1.039 nm, while the energetically preferred distance should be equal to the bulk value of C_{60} solid, which is 1.002 nm. Therefore, the C_{60} monolayer adsorbed on the Au (111) surface with the R14º structure will suffer from a significant tensile stress, because its nearest C_{60}-C_{60} distance is stretched by ~4%. Such tensile stress could make the monolayer very unstable, however, the tensile stress seems to be relieved by a re-organization of the Au atoms at the C_{60}-Au interface, and this re-organization of substrate atoms leaves a fingerprint on the C_{60} monolayer. Fig. 4.6(a) and (b) show two R14º C_{60} islands, on which hexagonal superlattice formed by

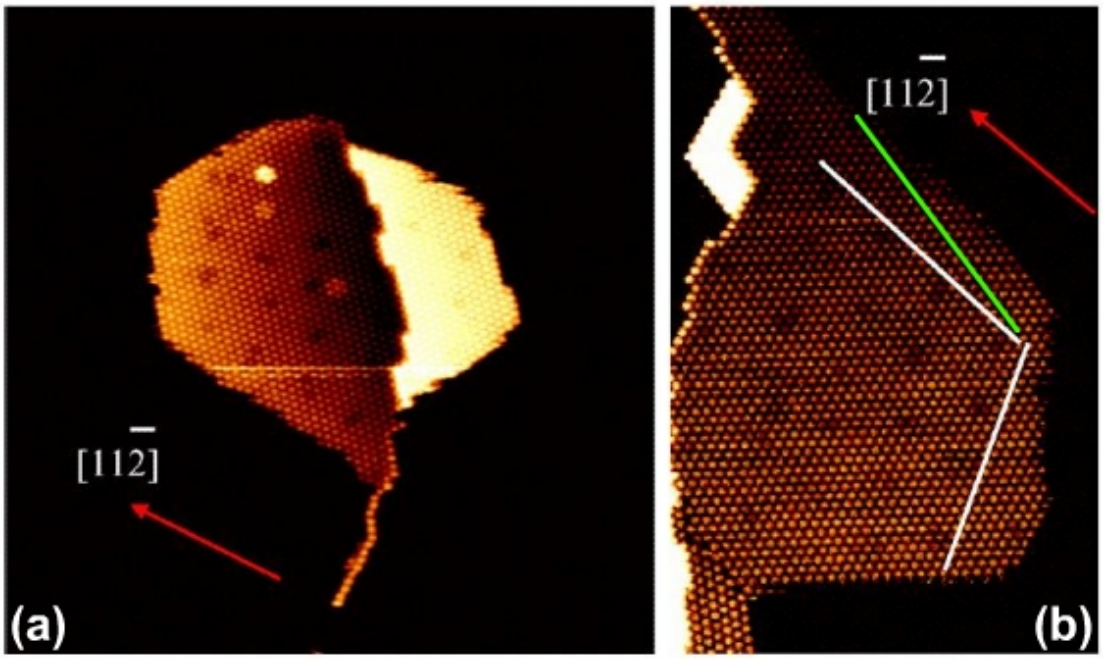

Fig. 4.6: Two R14º C_{60} islands with the hexagonal superlattice formed by dim spots. The alignment of the dim spots is indicated by the white lines. The close-packing direction of the molecules in the R14º island is indicated by the green line. The [11-2] direction of the Au (111) surface is indicated by the red arrows. It is clear seen that the superlattice vector is aligned with the [11-2] direction of the substrate, thus form a ~16º angle with the close-packed direction of the C_{60} monolayer. (a): 70.5 × 70.5 nm, V = -1.7 V, I = 0.03 nA. (b): 40 × 100 nm, V = -1.7 V, I = 0.03 nA.

dim spots can be seen. Each dim spots consists of 1-3 dim molecules, which are ~0.3 Å apparent lower than the surrounding molecules. The measured nearest neighbor distance of the dim spots distributes in a range from 6.0 nm to 7.5 nm over the whole monolayer. The variation of the nearest neighbor distance leads to a slight distortion of the hexagonal superlattice. As indicated in Fig. 4.6, the superlattice vectors are not aligned with the close-pack directions of the C_{60} monolayer, instead, they are aligned with the three equivalent [11-2] directions of the Au (111) surface, which are also the

directions of the DLs. Such an alignment with the substrate reconstruction ridge line (the DLs) is a strong evidence that the origin of these dim spots is related to an atomic re-organization of the substrate.

As introduced in section 2.5.3 of the literature review, both G. Schull and J. A. Gardener have observed the superlattice of dim spots on the R14º monolayer, and they attribute the cause of the lower apparent height of the dim molecules to the formation of nanopit underneath, which is consistent with our proposal of atomic re-organization at the interface. Moreover, J. A. Gardener *et al.* related the formation of the nanopit to the occupation of a specific adsorption site [3]. In the 7 × 7 model of the R14º structure, the periodicity for the C_{60} molecule to occupy identical adsorption site is ~7 nm. The separation of two nearest neighboring dim spots is also approximately 7 nm. It seems that among all the possible adsorption sites for C_{60} molecules in the R14º structure, there is one particular site that has the lowest energy barrier for the formation of the nanopit. Therefore, a nanopit will be formed and a dim spot will appear when this particular adsorption site is occupied. On the other hand, in my model, every molecule occupies identical adsorption site, thus it cannot offer a preferential location for the formation of the nanopit, if only the adsorption geometry (relative position of the molecule to the substrate atomic lattice) is considered. However, if the formation of nanopit requires a specific adsorption site, the dim molecules should appear periodically along a row of close-packing molecules, which will make the superlattice vector of the dim spot aligned with the close-pack direction of the monolayer. The realistic situation is as shown in Fig. 4.6, the superlattice vector

is actually aligned with the [11-2] direction of the substrate instead of the close-packing direction of the C_{60} molecules, which means that there should be no relation between the location of the nanopit and the specific adsorption site. Therefore, the 7 × 7 model shows no advantage in explaining the formation of nanopit over my model under this alignment. To determine which of the two models is true requires further investigation of the R14º structure. Furthermore, the alignment of the dim spots indicates a possible role of the original reconstruction ridge lines (the DLs) on the formation of the nanopit because the ridge lines run in the [11-2] direction. During the formation of the R14º C_{60} monolayer, the lifting of the reconstruction and the generation of the nanopit are achieved simultaneously by the atomic re-organization. It is a natural consequence that the original reconstruction pattern leaves some fingerprint on the arrangement of the nanopit.

Dim molecules are also observed on the R0º C_{60} monolayer, as can be seen in Fig. 4.7(a) and (b). However, in contrast to the superlattice formed by dim spots on the R14º monolayer, the distribution of dim molecules on the R0º monolayer is completely random. Furthermore, vacancies due to missing molecules are observed on the R0º monolayer. These vacancies are measured ~3 Å lower than the surrounding molecules. This ~3 Å height difference is comparable to the ~4.5 Å apparent height of the C_{60} monolayer, and it is larger than the ~0.3 Å height difference of the dim molecules on the R14º monolayer by an order of magnitude. Considering no protuberance feature can be observed within the dark spot, these dark spots are considered as vacancies. Besides the vacancies, dim molecules with two different

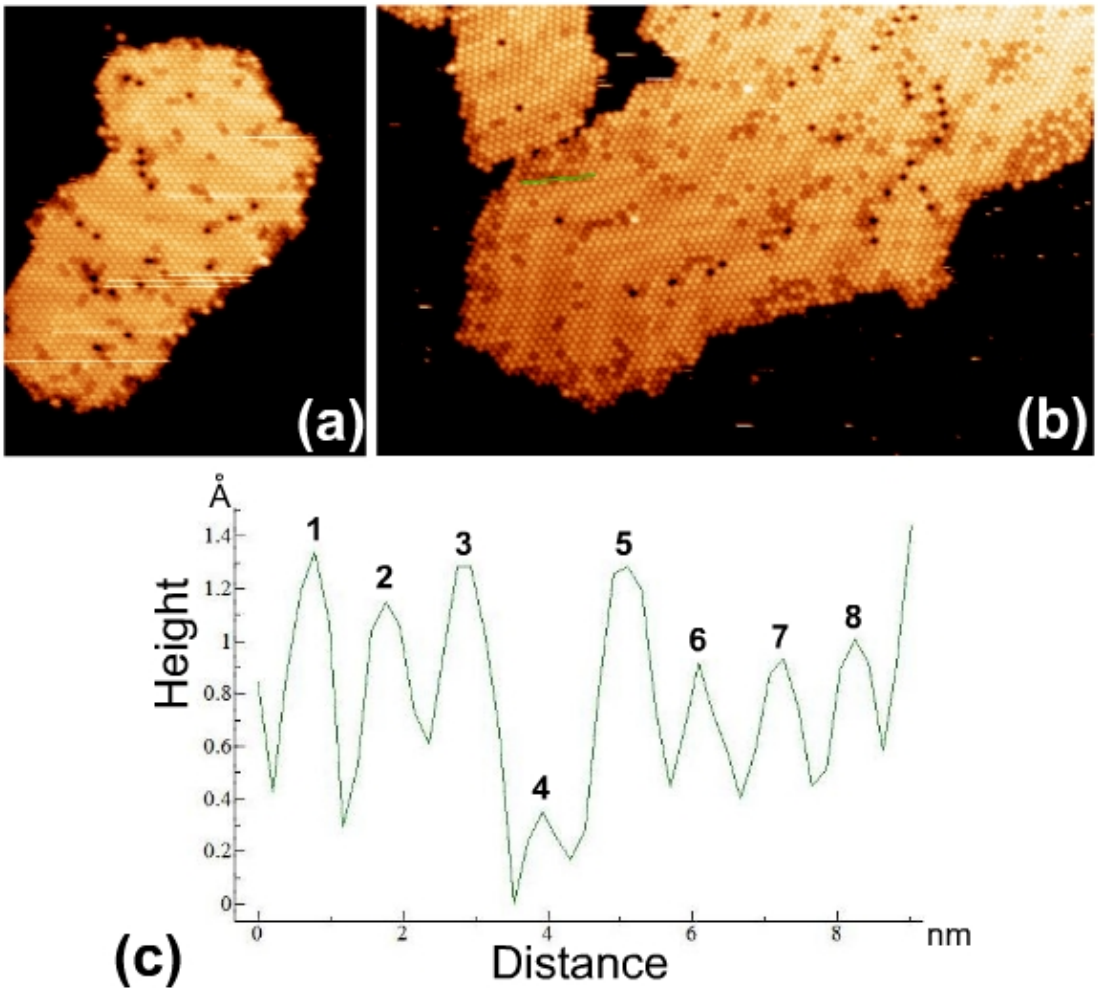

Fig. 4.7 (a): 48 × 59 nm, V = -1.7 V, I = 0.03 nA. A R0º C_{60} island with some vacancies is shown. Dim-A and dim-B molecules with different apparent heights can be identified. (b): The same image as the Fig. 4.1(b), a height profile is taken along the green line. (c): Height profile of eight molecules in a row. Molecule 1, 2, 3 and 5 have the average height of the molecules in the whole monolayer. Molecule 4 is a dim-A molecule which is ~0.9 Å lower than the average-height molecules. Molecules 6-8 are dim-B molecules which are ~0.3 Å lower than the average-height molecules.

apparent heights can be identified. Fig. 4.7(c) presents the height profile taken along a row of eight molecules (marked by green line) in the R0º island shown in Fig. 4.7(b). In the height profile, molecules marked 1, 2, 3 and 5 have the standard height for the

island. Molecule 4 is ~0.9 Å lower than the standard molecules, while molecules 6-8 are ~0.3 Å lower than the standard molecules. According to the different heights, molecules with a similar height as molecule 4 will be called dim-A molecules while molecules with similar height as molecules 6-8 will be called dim-B. The appearance of two kinds of dim molecules in the R0º monolayer is in contrast to the R14º monolayer, of which all the dim molecules have the same apparent height.

Regards to the origin of these dim molecules in the R0º monolayer, the possibility of nanopits formed underneath can be excluded at first because the monolayer reveals intact herringbone reconstruction pattern of the substrate. If a nanopit was formed on the Au (111) surface, the distribution of the surface strain would be disturbed, which would lead to a distortion in the reconstruction pattern. Normally, a DL of the reconstruction would form a closed U-shaped end with its neighboring DL in front of such defect on the Au (111) surface. However, the corrugation of the C_{60} islands shown in Fig. 4.7 reveals that the herringbone reconstruction of the substrate retains its original pattern. Furthermore, some dim molecules are sitting right on a DL of the substrate, which means that these dim molecules are adsorbed on an intact reconstructed Au (111) surface without any defects. Therefore, a different model is needed to explain the origin of the dim molecules in the R0º monolayer.

With a detailed examination of the distribution of the two kinds of dim molecules on the R0º island, we can find that there is a high density of dim-A molecules along the edge of the islands and around the vacancies. Compared with molecules in the

middle of the islands, the molecules at the island edges or next to a vacancies have reduced lateral coordination. The difference in lateral coordination may lead to different distribution of the density of states (DOS) on these molecules, thus result in different apparent heights in STM images. However, in the R14º islands introduced above, no dim molecules are found at the edge of the islands. A possible reason for this difference is that, for the R14º islands, the substrate reconstruction is lifted and nanopits are formed upon the adsorption of C_{60} molecules, both of which indicate a strong interaction between the substrate and the C_{60} molecules. (Moreover, besides the nanopits, all the C_{60} molecules in the R14º island sit on a flat 1 × 1 Au surface.) Therefore, the charge transfer from the Au substrate to the C_{60} monolayer may be large enough to submerge the electronic difference caused by reduced lateral coordination. On the other hand, for the island sitting on a reconstructed substrate, the interaction with the substrate should be relatively weak. The electronic difference caused by reduced lateral coordination thereby becomes determinative, resulting in the dim-A molecules concentrating in the neighborhood of the island edge and the vacancies. In addition, due to the herringbone reconstruction, the substrate is corrugated and anisotropically contracted. On such a substrate, the adsorption configuration and charge transfer to the C_{60} molecules should vary from point to point depending on the specific substrate topography. This variety may enhance the anisotropy of the electronic distribution over the monolayer thus lead to the lower appearance of some molecules. The dim molecules that are not directly adjacent to the island edges or the vacancies, which are primarily the dim-B molecules, are formed

by this reason. Furthermore, the variety in adsorption configuration may influence the intermolecular interaction between neighboring molecules and consequently influence the lateral coordination of the molecules, which can again lead to different apparent heights. Nevertheless, the influence of variable substrate topography is not as strong as the reduced lateral coordination caused by missing neighboring molecules, thus the height difference for the dim-B molecules is smaller than the dim-A molecules.

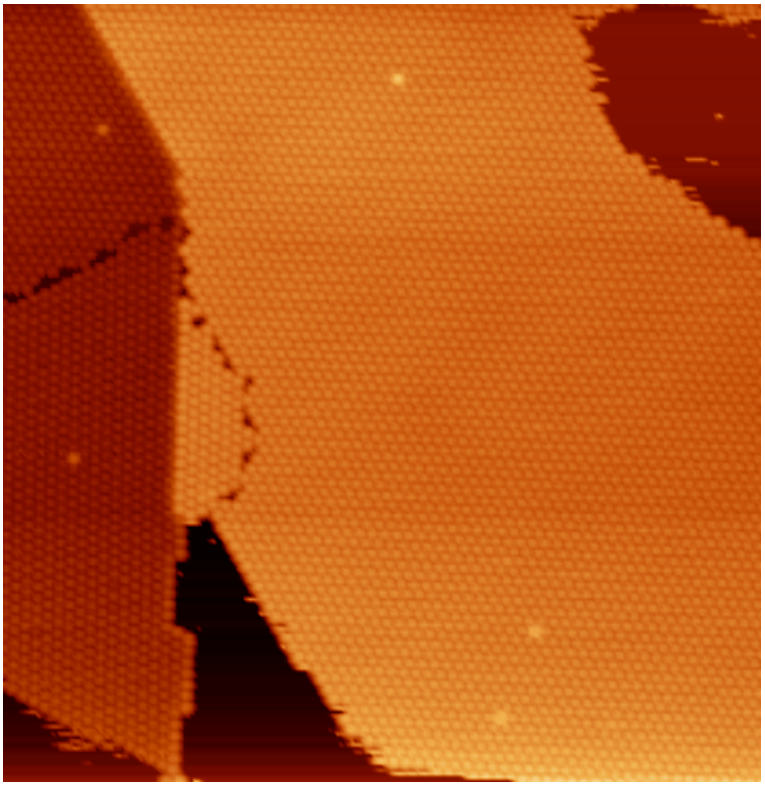

Fig. 4.8: 65.3 × 67.2 nm, V = -1.7 V, I = 0.04 nA. An Au (111) surface with nearly a complete monolayer of C_{60} molecules. An Au step runs from top to bottom on the left part of the image. Both the upper and lower terraces of the step are covered by C_{60} islands. R0º and R30º islands coexist in the image separated by domain boundaries. In these islands, five molecules, which are 1.1~1.3 Å higher than surrounding molecules, can be seen.

Besides the dim molecules found in the C_{60} islands, molecules brighter than the

surrounding molecules are occasionally found. As shown in Fig. 4.8, five bright molecules distribute on both R0º and R30º islands. These bright molecules are 1.1~1.3 Å higher than other molecules in the same layer. The bright appearance of these molecules may be caused by addition Au atoms trapped in the C_{60}/Au interface. These trapped Au atoms may come from the atoms that are released when the 4.4% contraction of a reconstructed Au surface is relieved by the adsorbed C_{60} molecules. The molecule sits on a trapped Au atom may appear brighter than the surrounding molecules. This phenomenon is right the opposite of the dim molecules, which sit on nanopits formed on the substrate. Later in Chapter 8, another phenomenon involving a C_{60} molecule sitting on a released Au atom will be introduced.

In this chapter, I have introduced the three C_{60} overlayer structures on the Au (111) surface, R0º, R14º and R30º at first. Later, some effects related to the diversity of the C_{60}/Au (111) interaction, such as the relief of the substrate reconstruction and the appearance of dim molecules on different overlayer structures. The above discussion will serve as a foundation when we further explore the C_{60}/Au (111) system in the following chapters.

References

[1] E. I. Altman and R. J. Colton, Surf. Sci. **279**, 49 (1992).

[2] J. K. Gimzewski, S. Modesti, Ch. Gerber, and R. R. Schlittler, Chem. Phys. Lett. **213**, 401 (1993).

[3] J. A. Gardener, G. A. D. Briggs, and M. R. Castell, Phys. Rev. B **80**, 235434 (2009).

[4] A. Fartash, Appl. Phys. Lett. **6**7, 3901 (1995).

[5] C. T. Tzeng, W. S. Lo, J. Y. Yuh, R. Y. Chu, and K. D. Tsuei, Phys. Rev. B **61**, 2263 (2000).

[6] X. Zhang, F. Yin, R. E. Palmer, and Q. M. Guo, Surf. Sci. **602**, 885 (2008).

[7] G. Schull and R. Berndt, Phys. Rev. Lett. **99**, 22105 (2007).

CHAPTER 5
C_{60} ADSORPTION ON STEPS AND GOLD-FINGERS

In Chapter 4, I discussed the interaction between the adsorbed C_{60} molecules and the Au (111) surface in terms of adsorbate induced surface structure changes. In this chapter, I am going to discuss the interaction between C_{60} molecules and the step edges on Au (111). A monoatomic step separating two terraces is a common feature on the Au (111) surface and is frequently observed in STM images. These steps are the preferred nucleation sites for the deposited C_{60} molecules at room temperature. Furthermore, the atomic structure of the steps is found to respond to the adsorption of C_{60} monolayer, by faceting for example. Therefore, a closer examination of the nucleation and growth processes of C_{60} monolayer from the step edge can lead to a better understanding of the C_{60}-Au (111) system. In addition, a 2-Dimensional nanostructure with a high density of parallel steps, so-called gold-fingers, was created in my experiment. The adsorption of C_{60} molecules on the gold-fingers reveals an interesting bi-functional property of this structure, which can be used to guide the assembly of molecules.

5.1 C_{60} Adsorption on the Step Edges

As mentioned before, the C_{60} molecules show high mobility on the Au (111) surface at room temperature. After landing on the surface, the molecules would diffuse across

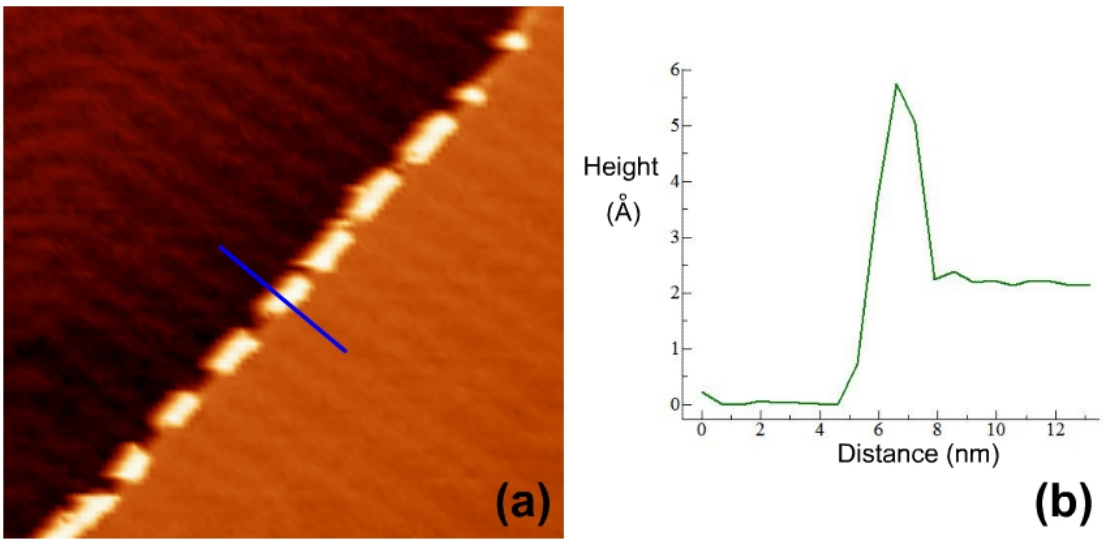

Fig. 5.1 (a): 48.5 × 46 nm, V = -1.7 V, I = 0.03 nA. Adsorbed C_{60} molecules form molecular chains along a monoatomic step edge on the Au (111) surface. (b): The height profile that is taken along the blue line in (a). The height of the molecule measured from the lower terrace is 0.6 nm, indicating that the C_{60} molecule is adsorbed on the lower terrace of the step.

the Au terrace until they are captured by a step edge. At extremely low coverage, all the C_{60} molecules are exclusively adsorbed on the FCC stacking segments of the Au step, forming short molecular chains along the step edge, as shown in Fig. 5.1(a). Each molecular chain consists of 3~4 C_{60} molecules. A height profile taken along the blue line is shown in Fig. 5.1(b), in which the molecules are measured 0.6 nm high from the lower terrace. Considering the normal apparent height of C_{60} molecules adsorbed on the Au (111) surface is ~0.6 nm, we can conclude that the first row of C_{60} molecules attached to the step are sitting on the lower terrace of the step. When more C_{60} molecules are deposited, the gaps between the molecular chains will be filled up. Further increase of the C_{60} coverage leads to the formation of 2-dimensional C_{60}

island on the lower terrace. The formed island is close-packed and expands from the step edge towards the terrace. The island formation on the upper terrace of the step will start at a latter stage, as shown in Fig. 5.2.

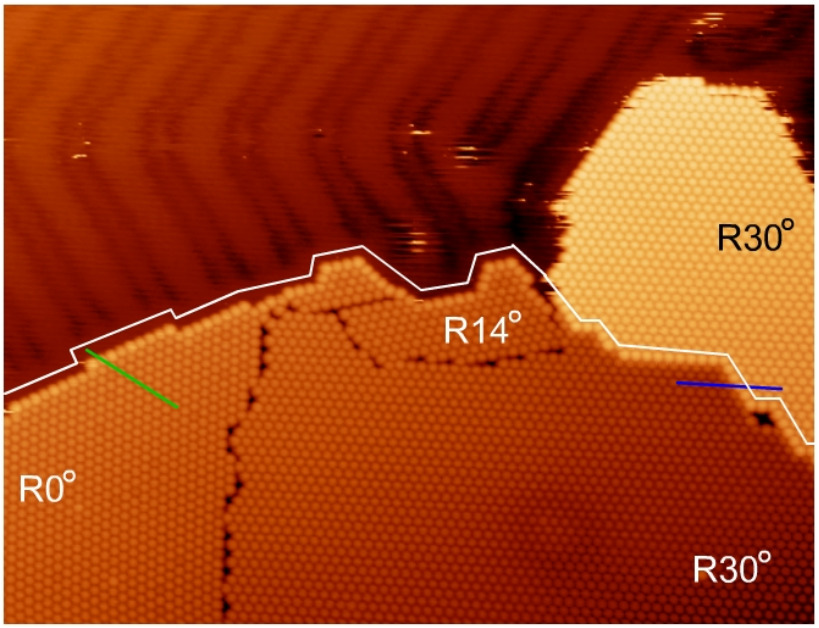

Fig. 5.2: 80 × 60 nm, V = -1.7 V, I = 0.04 nA. C_{60} monolayers with different orientations grew from a step edge, which runs from the left to the right of the image. The white line is drawn along the step. The specific orientation for each monolayer island is indicated. For the R30º island, it has two parts, one on the upper and the other on the lower terrace of the step. Despite the different monolayer structures, the step edge is faceted into short segments, which are aligned with the close-packed directions of the adjacent monolayer.

As shown previously in Fig. 4.4, the formation of a C_{60} monolayer leads to faceting of the step edge. The STM image in Fig. 5.2 also shows such faceting effect. A step runs across the imaged surface and a line is drawn next to this step to guide the eye. R0º, R14º and R30º C_{60} monolayers are all found in this image, as marked. All the three structures have the ability to facet the adjacent step edge. The R30º

monolayer in this image has a slightly different situation. It forms on both the upper and the lower terraces of the step. In this case, the step edge is again faceted. Faceting of step edges indicates a relatively strong C_{60}-C_{60} intermolecular interaction in the monolayer, because it can modify the atomic structure of the substrate in order to preserve the lateral ordering in the close-packed monolayer.

For the R0º and R14º monolayers in Fig. 5.2, the molecules attached to the step edge are slightly brighter than the molecules in the middle of the monolayer. This is a common phenomenon that is observed for all the C_{60} monolayers attached to a step edge. Fig. 5.3 presents two height profiles taken along the green line and the blue line in Fig. 5.2, respectively. In height profile (a), the edge C_{60} molecules appear ~0.57 Å higher than other molecules. At the same time, as shown in height profile (b), the molecules sitting on the upper terrace of the step is 2.3 Å higher than the ones on the lower terrace. This height difference is consistent with the physical height of a monoatomic step on the Au (111) surface. Furthermore, the brighter edge molecules can also be observed in this case, as indicated by an arrow. These bright edge molecules are not sitting on the upper terrace. Therefore, there are two possibilities that could lead to the measured height difference between edge molecules and those inside the island: the first is that these edge molecules are partially adsorbed on the step edge and are geometrically higher, as indicated in Fig. 5.3(c); the second possibility is associated with electronic effect. Because the edge molecules are attached to Au atoms at the step edge in addition to the substrate atoms underneath, the charge transfer to these molecules is expected to be enhanced. The first possibility

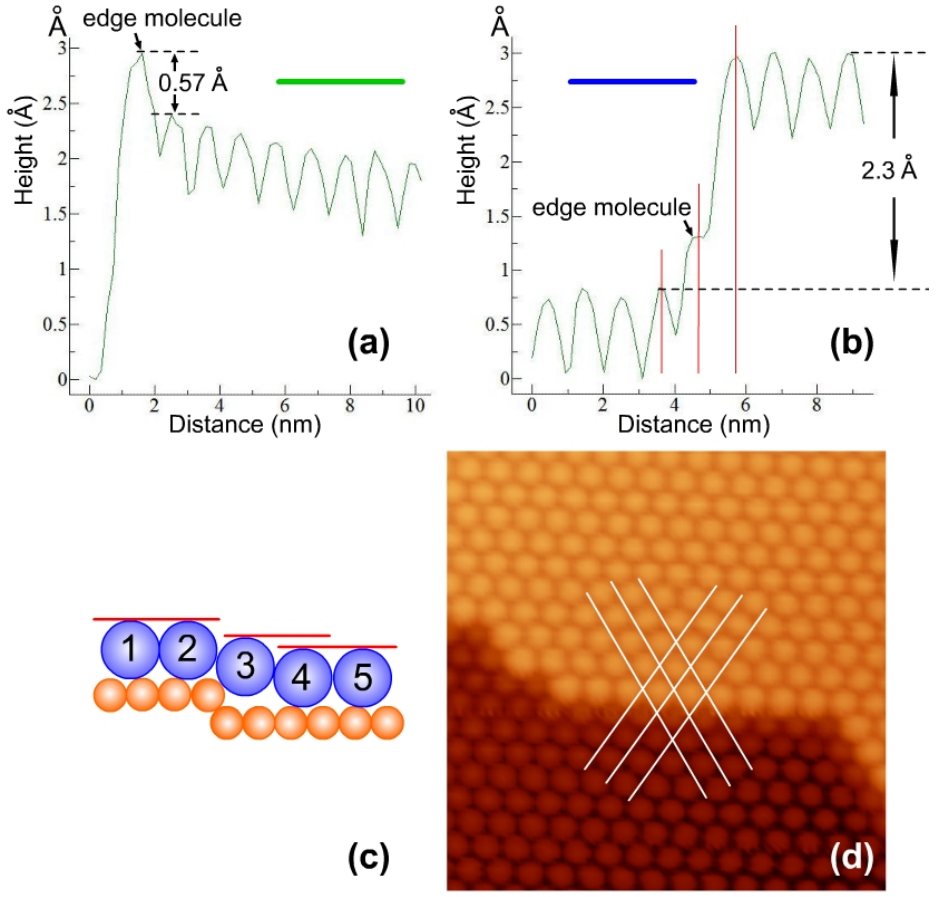

Fig. 5.3 (a): Height profile taken along the green line in Fig. 5.2. The height difference between the brighter edge molecule and its neighboring molecule is ~0.57 Å. (b): Height profile taken along the blue line in Fig. 5.2. The molecules on the upper terrace are ~2.3 Å higher than the molecules on the lower terrace. The edge molecule can still be identified, ~0.57 Å higher than the molecule on its left. With the help of the red lines drawn on the profile, we can find that the C_{60}-C_{60} distance remains constant across the step. No boundary gap due to Au atomic stacking offset is observed. (c): A possible model for the raised profile of the edge molecules. Yellow circles represent the substrate Au atoms. Large blue circles represent the C_{60} molecules. The edge molecule, number 3, is shown to be lifted above the lower terrace. The red lines indicate the height differences. However, as introduced in the text, this model is not realistic. The edge molecule is actually sitting on the lower terrace and its higher appearance is purely due to electronic effect. (d): 80 × 60 nm. A zoomed-in image shows the details of the step region of the R30º monolayer shown in Fig. 5.2, the white lines is drawn along the close-packed directions of the monolayer. We can find that besides the constant C_{60}-C_{60} distance across the step, the 2D ordering of the monolayer is also perfectly retained across an Au (111) step.

is less likely, because the configuration shown in Fig. 5.3(c) reduces the coordination between the edge molecules and the Au atoms, which is energetically unfavorable. Moreover, if a molecule adopts such an intermediate adsorption site on the step, its lateral intermolecular distances to the neighboring molecules would be shortened and revealed in STM images. However, as indicated by the red lines in Fig. 5.3(b), the distances between the edge molecule and its neighbors remain the same as that for the molecules in the middle of the monolayer. According to the above reasoning, the C_{60} molecules along the step edge should be adsorbed on the lower terrace and its higher apparent height is purely due to electronic effect.

As introduced above, the intermolecular distance between the molecules in the R30º monolayer remains unchanged over an Au (111) step. This is in conflict with conclusions drawn previously [1], because if all the molecules in the R30º monolayer adopt identical a-top adsorption site on both the upper and lower terraces, there would be a boundary gap dividing the monolayer along the step edge. The width of the boundary gap should be similar to the atomic lattice offset between the two gold layers. However, as seen in the height profile, no such gap is observed. Furthermore, as shown in Fig. 5.3(d), not only the intermolecular distance remains unchanged, but also the whole 2D ordering of the close-packed C_{60} monolayer is preserved over the step. The molecules on the upper terrace are perfectly matched into a single 2D lattice with the ones on the lower terrace. Such a molecular arrangement indicates that molecules on two sides of a step occupy different adsorption sites. A schematic diagram is shown in Fig. 5.4(a) to illustrate this situation, in which the molecules on

the lower terrace occupy identical a-top site and present the $(2\sqrt{3} \times 2\sqrt{3})R30^{o}$ structure. By expanding a C_{60} monolayer with perfect 2D ordering across the step, the molecules are found to occupy different, low symmetry adsorption sites on the upper terrace. For the R14º structure, the situation is similar. As shown in Fig. 5.4(b), on the lower terrace, the R14º monolayer adopts my model, which introduced in Chapter 4 that molecules occupy identical a-top sites. The molecules on the upper terrace thereby have to occupy different adsorption sites. In both cases, the step edges are faceted so that the first row of molecules attached to the step edge have identical adsorption configuration. For an R0º island, step faceting is not necessary because the close-packed directions of the R0º C_{60} monolayer are aligned with the close-packed

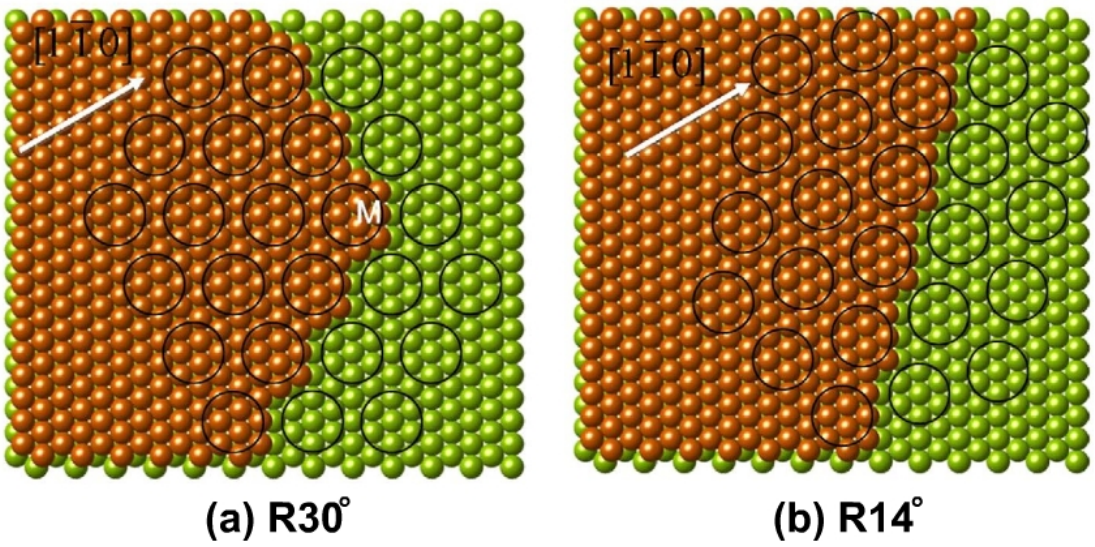

Fig. 5.4: Structural models for the R30º and R14º monolayers adsorbed over a step. The large open circles represent the C_{60} molecules. Green and yellow spheres represent the Au atoms on the lower and upper terraces, respectively. The [1-10] direction of the Au surface is indicated by the white arrow. In each model, the C_{60} molecules on the lower terrace occupy identical a-top sites while the molecules on the upper terrace have to adopt different adsorption sites. Moreover, the Au step is slightly faceted in order to allow the monolayer to remain its 2D ordering.

directions of substrate. The faceting illustrated in Fig. 5.4 should not be confused with the faceting observed in the STM images, which happens at a much large scale and has a different purpose that is to keep the step aligned with the close-packed directions of the monolayers. The white letter M in the Fig. 5.4(a) indicates a bending points due to the large scale faceting observed in STM imaging.

Based on the above discussion, the nucleation and growth of 2D C_{60} monolayer from a step edge of the Au (111) surface can be described as follows. When a C_{60} island is initially nucleated at a segment of a step, if this step segment consists of Au atoms aligned along the <110> direction, the C_{60} molecules are likely to form a R0º island. If the step segment is along the <112> direction, an R30º island is likely to formed. If the step segment is aligned with a direction about half way in between the above two directions, an R14º island is favored. However, once the azimuthal orientation of a C_{60} island is established, during subsequent growth this island will expand and meet other step edges. Under such a situation, the expanding C_{60} island will facet the step edge into short segments which are aligned with the close-packed direction of the existing C_{60} monolayer. As shown in the STM images in Fig. 5.2, the size of the islands formed on the two sides of a step is not equal. The C_{60} molecules prefer to grow on the lower terrace. However, when an R14º or R30º island expands across the step edge to the upper terrace, the Au atoms along the step edge will be slightly rearranged to allow the molecules on the two sides of the step to remain in a perfect 2D lattice. Even with the rearrangement of the step Au atoms, the C_{60} molecules still have to sacrifice their preferred a-top adsorption site to keep the

perfect 2D ordering of the close-packed monolayer over the step. The requirements for atomic rearrangement at the step and C_{60} occupying unfavored sites are the likely reasons why monolayer formation on the upper terrace lays behind that on the lower terrace.

To conclude this section, I'd like to discuss the relative strength of the C_{60}-C_{60} intermolecular interaction and the C_{60}-Au interaction. As introduced in the literature review, the C_{60}-Au interaction is thought to be very strong that it can lift the reconstruction of the Au (111) surface, and the desorption temperature of the first C_{60} layer is very high. The desorption temperature of the first C_{60} layer is ~130 K higher than the desorption temperature of the second and higher layers, which suggests that the C_{60}-Au surface interaction is stronger than the C_{60}-C_{60} interaction. This relative strength can be understood as the C_{60}-C_{60} interaction is mainly van der Waals interaction while the first C_{60} layer is chemical bonded to the substrate with charge transfer. However, phenomena contradictory to the above conclusion are observed, as introduced in both the previous and the present chapter. For example, the C_{60} molecules sacrifice the favored a-top adsorption sites to keep the lateral ordering of the monolayer, and the remaining herringbone reconstruction observed through the C_{60} monolayer. Furthermore, the C_{60} molecules can facet the Au step to make it aligned with the close-packed direction of the monolayer, as well as drive the step atoms to rearrange in order to keep the lattice constant of the C_{60} monolayer. All these phenomena indicate that the C_{60}-C_{60} interaction is stronger than the C_{60}-Au interaction. The answer for this contradiction is that, at room temperature, the C_{60}-C_{60} interaction

is actually stronger than the C_{60}-Au interaction, while the higher desorption temperature of the first C_{60} layer is due to a modification of the C_{60}-Au interface caused by the thermal annealing. As introduced in Section 2.5.3, annealing will lead to a disordered-phase of C_{60} monolayer with a high density of randomly distributed dim molecules [2]. Each dim molecule is associated with a nanopit formed underneath, the C_{60}-Au interaction involving a nanopit is much enhanced resulting in a high desorption temperature. Therefore, the higher desorption temperature of the first C_{60} layer does not mean that the C_{60}-Au interaction is stronger than the C_{60}-C_{60} interaction at room temperature. At room temperature, the C_{60}-C_{60} interaction is a more determinative factor for the structure of the C_{60} monolayer formed.

5.2 C_{60} Adsorption on the Gold-Fingers

As previously mentioned, a kind of zero-gradient stepped surface (ZGSS) is created in my experiment. A typical image of the ZGSS is shown in Fig. 5.5(a). To form a ZGSS, parallel gold stripes are drawn out from a monoatomic step pre-existing on the Au (111) surface by using high-field STM scanning. These monoatomic gold stripes are called gold-fingers according to their appearance. The detailed method of creating the gold-fingers was introduced in Section 3.2.5.

Properties of the ZGSS have already been studied in details by F. Yin and Q. Guo from our group [3~6]. The size of gold-fingers varies from case to case, of which the length can reach hundreds of nanometers and the width ranges from 3.5 nm to 34 nm. The distance between two neighboring gold-finger is on average ~13 nm. All the

gold-fingers grown from a common step have the same direction and they can only grow in one of the three equivalent <110> directions of the Au (111) surface, therefore, the two long steps for each finger consists of close-packed atoms. As introduced in Section 2.1.2, the two opposite steps of a close-packed monoatomic island on the Au (111) surface are different types, one forms a {111} microfacet with the substrate atoms and the other forms a {100} microfacet. In this case, the two parallel steps on a gold-finger will be one {111} type step and one {100} type step. Consequently, the whole ZGSS presents alternating {111} and {100} steps. For the Au (111) surface, the {111} step has lower step energy than the {100} step, thus is more stable. By annealing the ZGSS to 330 K or scanning it with a high electric field (~50 nA tunneling current and ~2 V bias voltage) in the direction perpendicular to the gold-fingers, the {100} steps will be faceted into a zigzag form, as shown in Fig. 5.5(b) [5]. This faceting is in fact a result of the {100} steps transforming into more energetically favored {111} steps. In STM images, the {111} step can be distinguished from the {100} step by the different reconstruction patterns associated with the two steps, as introduced in Section 2.1.2. An STM image showing the reconstruction pattern is presented in Fig. 5.5(c). The gold-fingers in this image grow along the [-110] direction, the discommensuration lines (DLs) thus run perpendicularly across these gold-fingers. The lower step of each gold-finger is identified as a {111} microfacet, because the DLs on the lower terrace propagate across the step linking with the DLs on the upper terrace. On the other hand, in front of the upper steps, the DLs bend to form U-shaped ends with neighboring DLs,

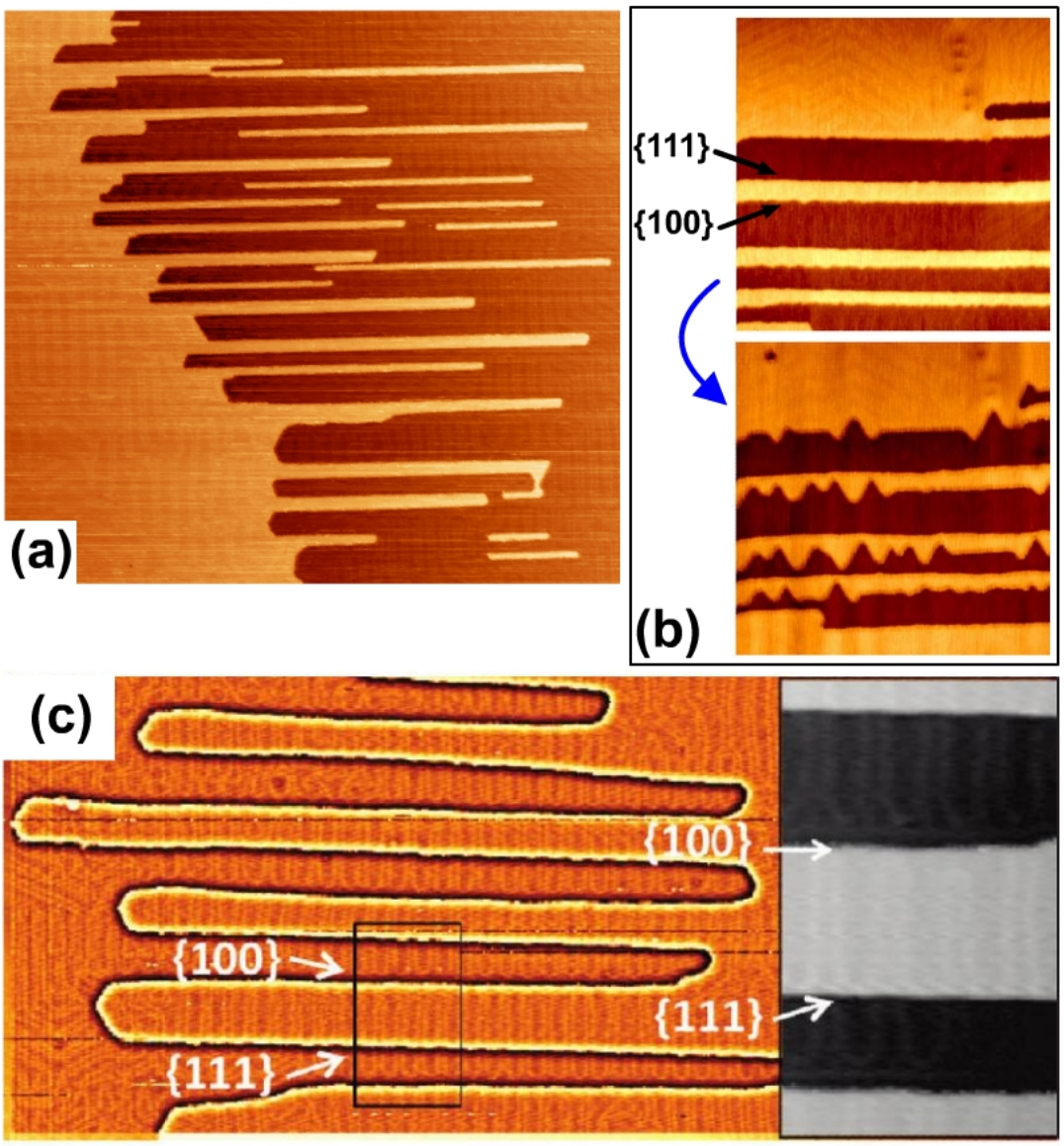

Fig. 5.5 (a): 80 × 60 nm, V = 0.6 V, I = 3.0 nA. A typical zero-gradient stepped surface, the gold-fingers run in the [-110] direction. (b) (from [5]): Both images are 145 × 145nm, showing the same region on a ZGSS before (upper image) and after (lower image) modification scans. Before scanning, the {111} and {100} steps are both straight. After five scan with 1.03 V and 50 nA (the scanning direction is perpendicular to the direction of the golf-fingers, thus vertically in the images), the {100} steps are faceted into a teeth-like structure, which consists of {111} microfaceted segments. Annealing has similar faceting effect on the {100} steps. (c): 300 × 177 nm, V = 2.0 V, I = 0.5 nA. An STM image shows the herringbone reconstruction pattern of the ZGSS. A zoom-in image of the region marked by the black rectangular can be seen in the inset. The different situations of the DLs at the {111} and {100} steps can be seen.

indicating that the upper steps belong to {100} microfacet. Furthermore, a single straight DL parallel to the step edge is found to separate an upper step from the U-shaped ends. As known, the wider regions between the DLs are FCC stacking and the narrow ones are HCP stacking, thus the U-shaped ends enclose the FCC regions. Therefore, the narrow region between the {100} steps and the single straight DL is also FCC stacking. Having outlined the different structures and characteristics of the two steps of the gold-finger, I would like to move on to discuss the nucleation and growth of C_{60} submonolayer on the ZGSS and we will see the two steps behavior differently as nucleation sites for the C_{60} molecules.

Fig. 5.6(a) shows the STM image of a ZGSS, of which the morphology after 0.1 ML C_{60} molecule deposition is shown in Fig. 5.6(b). C_{60} molecules are nucleated at both of the {111} and the {100} steps as well as the tip of the gold-fingers. However, the growth behavior of C_{60} on the two sides of a gold-finger is very different. On the {111} step, C_{60} molecules exclusively occupy the FCC stacking segments, resulting in a line of separated short molecular chains along the step edge. Some molecular chains have two rows of molecules. Similar adsorption structure has been observed on vicinal Au (111) surface, which consists of a series of parallel {111} steps [7]. On the opposite side of gold-finger, a close-packed C_{60} island is formed at the {100} step. By identifying the close-packing direction of the C_{60} molecules, it is found that this island has the R0º structure (marked as "α" in Fig. 5.6). This finding is consistent with the conclusion made in the previous section that if the Au step runs along the <110> direction, the C_{60} island nucleated on the step would adopt the R0º structure. Using

the same method, the island nucleated at the tip of the gold-finger is found to have the R30º structure (β). This island has a small part sitting on the upper terrace of the gold-finger, and the height different of the two parts is measured to be 2.3 Å, which is the same as the height of a monoatomic Au layer on the Au (111) surface. From the step edge connecting the bases of two neighboring gold-fingers, R14º (γ) and R0º islands are formed. The directions of the steps at the base of the fingers are not well-defined, thus C_{60} islands at such locations have different orientations. All the islands and molecular chains in this image are directly bonded with the lower terrace of the Au surface, except the small part of the R30º island sitting on the upper terrace of the gold-finger, at the fingertip. A height profile taken along the black line in Fig. 5.6(b) from point D to D' is shown in Fig. 5.6(c). All the C_{60} molecules in the height profile have the same height of 4.89 Å from the lower terrace, which is the standard height for the C_{60} molecules adsorbed on the Au (111) surface and measured by STM.

As shown above, even with the same set of deposition parameters, the local structure of C_{60} on the {111} and {100} steps of the gold-finger is different from each other. As introduced earlier, for the {111} step, the DLs on the lower terrace directly propagate to the upper terrace, thus the FCC regions of the gold-finger are directly connected to FCC regions of the lower terrace. The C_{60} molecules attached to the {111} step are exclusively nucleated in these FCC regions. However, there are a very small number of segments along the {111} step, where the nearby herringbone pattern is disturbed. At these segments, continue rows of C_{60} molecules are adsorbed and

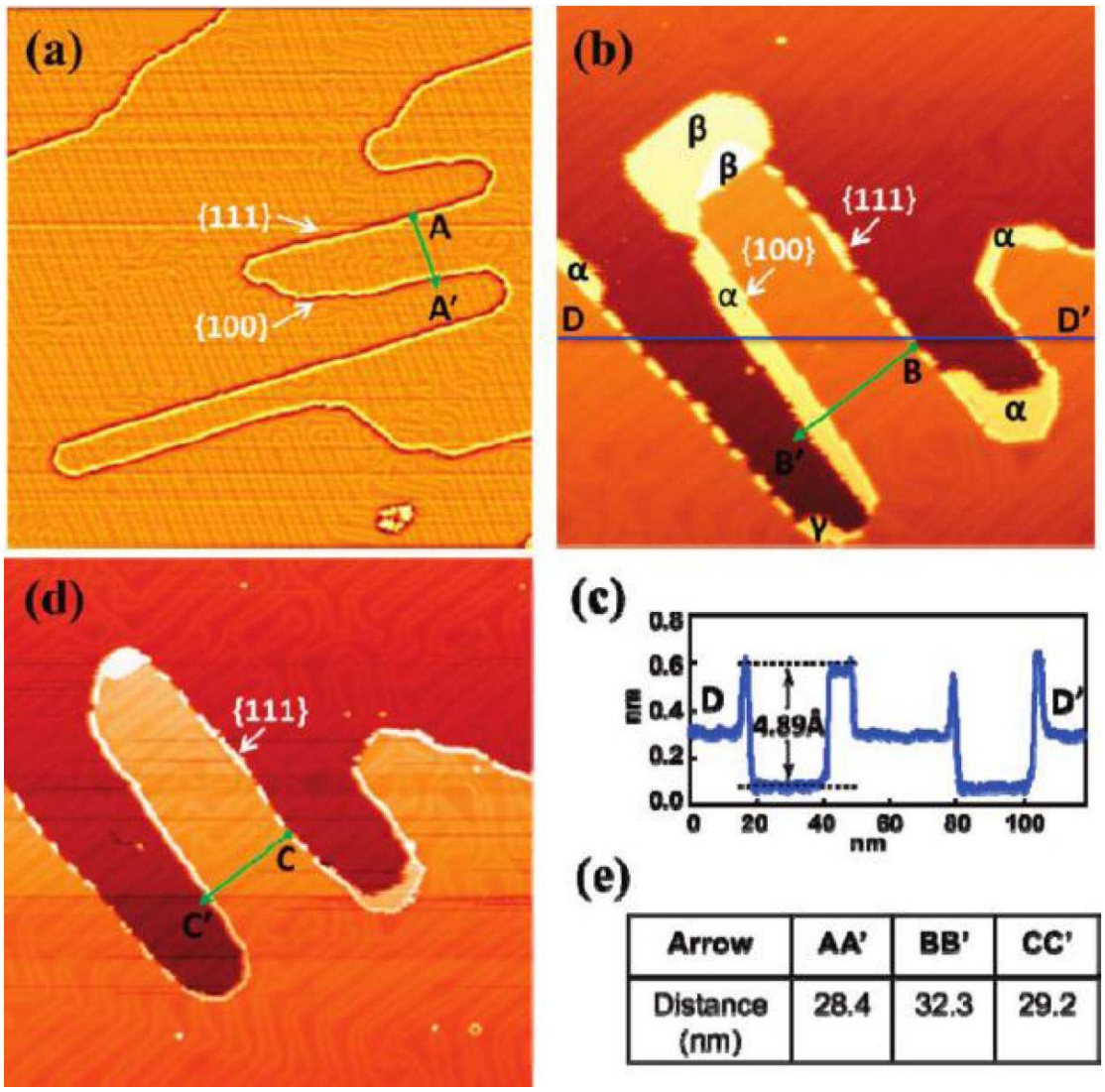

(e)

Arrow	AA'	BB'	CC'
Distance (nm)	28.4	32.3	29.2

Fig. 5.6 (a): 208 × 208 nm, V = -0.9 V, I = 0.03 nA. A ZGSS before C_{60} deposition. (b): 120 × 120 nm, V = -1.2 V, I = 0.03 nA. The same ZGSS with 0.1 ML of C_{60} molecules. Close-packed C_{60} islands grow from the {100} step of the gold-finger as well as from the fingertip and the step edges connecting the bases of two fingers. For the {111} steps, only the FCC regions are occupied by short molecular chains. Different C_{60} structures are marked by Greek letters, α for R0º, β for R30º and γ for R14º. (c): The height profile plot along the line DD' in (b). The height of the C_{60} molecules is 4.89 Å from the lower terrace, indicating that these molecules are directly adsorbed on the lower terrace. (d): 130 × 130 nm, V = -1.2 V, I = 0.03 nA. The same area imaged after 44 hours. Molecules in the close-packed island grown from the {100} step have diffused away, leaving behind a single row of molecules attached to the {100} step. The {111} step is still decorated with short molecular chains. (e): A table shows the distances measured between the points AA', BB' and CC' in image (a), (b) and (d), respectively.

have developed into small close-packed islands. In contrast to the situation at the {111} step, a large number of molecules are found to attach to the {100} step, giving rise to a close-packed island along the whole length of the {100} step. The long and narrow C_{60} island attached to the {100} step has the R0º structure with C_{60} molecules close-packed parallel to the step.

As shown in Fig. 5.5(c), there is a single DL in front of the {100} step on the lower terrace, which runs parallel with the step edge and separates the step from the U-shaped ends formed by paired DLs. The small region between the single DL and the {100} step has FCC stacking. Therefore, the full length of the {100} step is sitting on FCC region and is saturated by C_{60} molecules. In contrast, the {111} step is sitting on alternating FCC and HCP regions, of which only the FCC regions are occupied by C_{60} molecules. This is consistent with the truth that C_{60} molecules prefer to sit on the FCC regions of the Au (111) surface. When more molecules join the island grown from the {100} step, the single DL is "pushed out" from the step edge by the expanding molecular island, which means that the substrate can change its local structure to accommodate the molecules. Another aspect of the phenomenon is that the retreating DL indicates that the whole island is sitting on an FCC stacking surface. In other words, the reconstruction used to exist at this location has been lifted and the surface now has a 1 × 1-like lattice. As known, the reconstruction of the Au (111) surface is due to a 4.4% contraction of the first layer atoms. However, the lifting of the reconstruction does not necessarily mean the extra Au atoms have been released. The C_{60} island could be adsorbed on a compressed 1 × 1 surface which has the same

density of atoms as the reconstructed surface. If this is true, it indicates that the anisotropically compressed Au (111) surface can transform to a more isotropically compressed structure under the coordinating with the adsorbed C_{60} island.

During the nucleation and growth of C_{60} structures, the ZGSS serves as a bi-functional template. The two opposite steps of the gold-finger present different properties in facilitating the growth of C_{60} islands. The {111} step is easily passivated when all of its FCC regions have been occupied, while extended island can grow from the {100} step. When a C_{60} molecule moves into the space between two gold-fingers, it is more likely to join the island grown from the {100} step. There are two possible reasons behind the preferential growth of C_{60} island along the {100} step: the first is that C_{60} molecules prefer to adsorb on a 1 × 1 FCC stacked surface, which can be found at the foot of the {100} step. The second reason is that the {100} step has a higher surface energy than the {111} step, and C_{60} adsorption leads to a greater energy reduction at the {100} step. The phenomenon described in the first reason is common, of which the C_{60} islands are frequently observed to have lifted the substrate reconstruction and sit on a 1 × 1 FCC stacked surface. However, as introduced in the previous chapter, sometimes the reconstruction underneath the C_{60} islands is found to remain intact, which indicates the complexity of the Au (111) surface. The Au (111) surface consists of domains with parallel DLs and the size of the domains varies from place to place. At places where the domains are relatively small due to frequently bending of the DLs, there are a high density of defects associated with the elbow sites. The reconstruction of this kind of surface with a high density of elbow sites is less

likely to be lifted because large number of Au atoms need to be relocated. In front of the {100} step, there is a high density of DL bending site (the U-shaped ends), but the expansion of the C_{60} island successful lift this reconstruction and push the DLs backwards. The energy required to lift this reconstruction is probably compensated by the energy released from the {100} step due to the adsorption of C_{60} molecules. In conclusion, the close-packed C_{60} island prefer to form along the {100} step of the gold-finger.

The close-packed islands grown from the steps of the gold-fingers are found to be not stable at room temperature. The STM image in Fig. 5.6(d) is taken over the same surface as the image in Fig. 5.6(b), but 44 hours later. Between the collections of the two images, the sample was stored in the UHV chamber at room temperature and no thermal annealing was performed. Even so, in 44 hours time, nearly all 2D islands are disappeared. The only two remaining islands are the small R30º island sitting on the upper terrace at the fingertip and an R0º island in between the bases of two gold-fingers. Moreover, the R0º island is reduced in size in comparison to its original size. Another obvious change is that, as shown in Fig. 5.6(b), at the fingertip and the connecting regions between two gold-fingers, where the step edges have a high degree of curvature, some step edges are faceted by adsorbed C_{60} islands. After 44 hours, all these islands have disappeared thus there is no requirement for the Au atoms at the step edges to be aligned with the close-packed direction of the C_{60} islands. Therefore, these steps shift back to the original more rounded shape, as shown in Fig. 5.6(d), which seems to be more energetically favored in this case. With the C_{60}

molecules diffused away, there is only a single but continuous row of molecules attached to the {100} step. At the same time, the {111} step is still having all its FCC regions occupied by C_{60} molecular chains. The single DL in front of the {100} step, which used to be "pushed back" by the C_{60} island, has now moved back towards the step. However, it is still separated with the step edge by the single row of molecules. The distances from the edge of the {111} step to the mobile DL is measured: before C_{60} deposition, right after deposition and 44 hours later, these distances are marked by arrows linking AA', BB' and CC' in Fig. 5.6 (a), (b) and (d), respectively. The data is presented in the table in Fig. 5.6(e). The distance CC' is larger than the AA' by 0.8 nm, which is due to the addition of one row of molecules along the step. The disappearance of molecules in a 44 hour timescale from the imaged area indicates that the structures observed in the Fig. 5.6(b) are under dynamical equilibrium. C_{60} molecules keep on detaching from the edges of the islands at a very slow rate. These

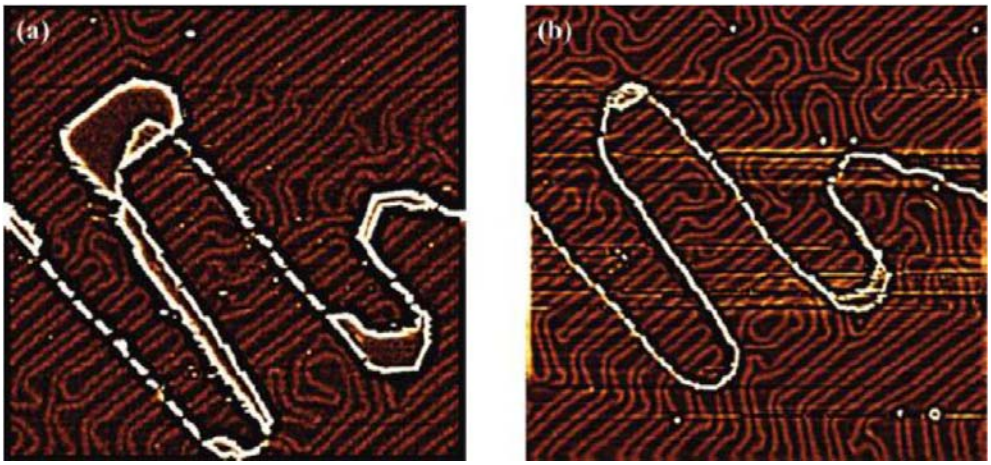

Fig. 5.7: The STM images before (a) and after (b) the diffusion of the C_{60} molecules. The contrast is adjusted to clearly show the herringbone pattern.

molecules will either move back to the island again or diffuse away and be captured by more stable structures outside of the imaged area.

Fig. 5.7 shows two STM images taken before and after the disappearance of the large number of C_{60} molecules, of which the contrast is adjusted to present the DL pattern clearly. The herringbone pattern in Fig. 5.7(b) has changed a lot form that in Fig. 5.7(a). This is a strong evidence that C_{60} molecules have diffused over these areas. It is likely that during the diffusion, the local surface strain is changed as individual molecules skip over and leading to a permanent change of the reconstruction pattern. However, we found that the reconstruction pattern reappeared in the region between two gold-fingers, where used to be covered by the C_{60} island, is very regular. The reformed pattern perfectly copies the pattern before the C_{60} deposition, which consists of an array of uniform U-shaped ends. Normally, the reformed reconstruction pattern is in-regular, as shown in the previous chapter with Fig. 4.3 and in Fig. 5.7(b) around the fingertip. The uniform pattern reformed between the gold-fingers probably indicates a very regular distribution of the surface strain in the ZGSS.

In this chapter, we discussed the interaction between the step edges on the Au (111) surface and the adsorbed C_{60} molecules. In Section 5.1, the close-packed C_{60} monolayer covering a step is found to retain its perfect lateral ordering over the step, indicating a relative strong intermolecular interaction. Furthermore, the C_{60} layer has the ability to facet the step edges. In Section 5.2, the adsorption of C_{60} molecules on ZGSS reveals the bi-functional characteristic of the gold-finger, of which the opposite steps behavior differently in facilitating 2D C_{60} island growth. This artificial surface

structure shows the potential to guide the self-assembly of molecular nanostructure.

References

[1] E. I. Altman and R. J. Cotton, Surf. Sci. **279**, 49 (1992).

[2] J. A. Gardener, G. A. D. Briggs, and M. R. Castell, Phys. Rev. B **80**, 235434 (2009).

[3] Q. Guo, F. Yin, and R. E. Palmer, Small **1**, 76 (2005).

[4] F. Yin, R. E. Palmer, and Q. Guo, Phys. Rev. B **73**, 073405 (2006).

[5] F. Yin, R. E. Palmer, and Q. Guo, Surf. Sci. **600**, 1504 (2006).

[6] F. Yin, R. E. Palmer, and Q. Guo, J. Phys.: Condens. Matter **21**, 445001 (2009).

[7] W. Xiao, P. Ruffieux, K. Ait-Mansour, O. Groning, K. Palotas, et al., J. Phys. Chem. B **110**, 21394 (2006).

CHAPTER 6
LOW TEMPERATURE GROWTH OF C_{60} STRUCTURES

In this chapter, I would like to introduce the nucleation and growth of C_{60} submonolayer structures on the Au (111) surface at cryogenic temperatures, 46 K and 180 K, respectively. The situation is quite different from that at room temperature. It provides another angle to look at the complex system between the C_{60} molecules and the Au (111) surface.

The $22 \times \sqrt{3}$ reconstructed Au (111) surface presents alternating FCC-stacking and HCP-stacking regions and the discommensuration lines (DLs) form a herringbone pattern. Due to the unique surface structure, it is quite frequently used as a template to guide the self-assembly of nanostructures. As introduced in Section 2.2.1 (Metal Deposition on the Au (111) Surface) and Section 2.2.2 (Organic Molecule Deposition on the Au (111) Surface), the elbow sites of the DLs are popular nucleation positions for atoms or molecules deposited on the Au (111) surface. For instance, metal atoms of Fe [1], Mo [2] and Ni [3] are found to nucleate at these elbow sites at room temperature, involving an atom exchange with the substrate. For organic molecules, nucleation of molecular islands is also found at the elbow sites, but at much lower temperatures [4-7]. In the case of C_{60} molecules, the present understanding is that the elbow site is unable to trap C_{60} molecules at room temperature. D. Fujita *et al*. [8] have reported the adsorption of individual C_{60} molecules at the elbow sites at 30 K,

but the subsequent nucleation and growth processes have not been reported. In my research, the adsorption, nucleation and growth processes are followed in detail by increasing the C_{60} coverage step by step at 46 K and 180 K, respectively. The nucleation and growth of C_{60} islands at these temperatures are influenced by many factors such as the local atomic structure around the elbow site and the difference of surface potential between the FCC and HCP regions.

The atomic structure of the Au (111) surface was introduced in detail in the literature review. However, for the convenience of the following discussion, I would like to go through some key features of this surface. Fig. 6.1(a) shows an STM image of the clean Au (111) surface with its typical herringbone reconstruction. The surface consists of alternating FCC (wider, ~3.5 nm) and HCP (narrower, ~2.4 nm) regions as indicated. The two regions are separated by the DLs, which bend systematically to form the herringbone pattern. There are two different kinds of DLs that can be distinguished by the ways they bend at the elbows: a type x DL has pointed elbows while the elbows of a type y DL are rounded. At an elbow site, if the type x DL points into the HCP region, it is called a pinched elbow, otherwise, if it points into an FCC region, it is called a bulged elbow. In this manner, the herringbone pattern presents alternating rows of pinched and bulged elbows, as marked in Fig. 6.1(a). The atomic structure around the elbow sites is important because we will use them later to discuss the different adsorption behaviours of C_{60} molecules at the two types of elbow sites. Fig. 6.1(b) is an atomic resolution image of two pinched elbows and two neighbouring bulged elbows. There are several rows of brighter atoms at each elbow

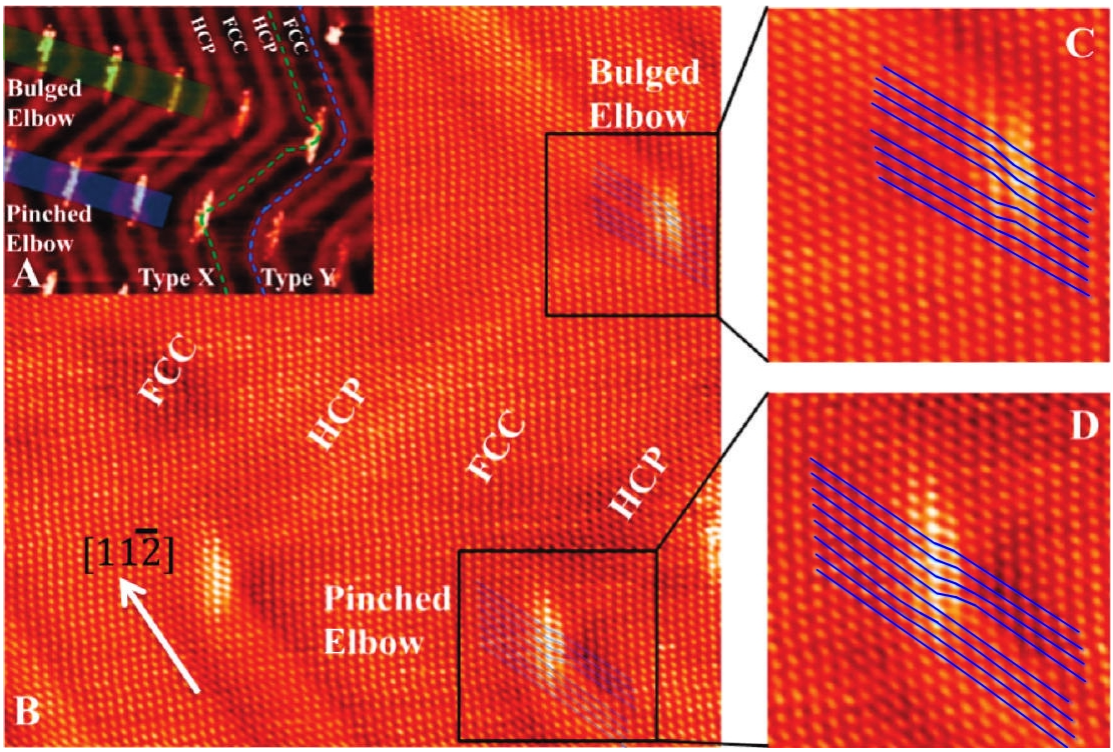

Fig. 6.1 (a): 45 × 20 nm. STM image of the reconstructed Au (111) surface shows the different features of this surface. Alternating FCC and HCP regions are separated by two kinds of DLs, type x (marked by green dashed line) DL has pointed elbows while type y (blue dashed line) DL has rounded elbows. For the different pointing directions of the elbows of the type x DL, bulged and pinched elbows can be distinguished. The rows of bulged and pinched elbows are marked by green band and blue band, respectively. (b): 19 × 20 nm, V = 4 mV, I = 12 nA. An atomic resolution STM image shows two bulged elbows and two pinched elbows. Au atoms in a same row are linked by blue lines, thus the extra row of atoms at each pointed elbow site can be seen clearly. As shown in the zoomed-in images of (c) and (d), for the bulged elbow, the extra row of atoms comes from HCP region while for the pinched elbow, the extra row of atoms comes from FCC region.

site of type x DL, indicating a higher surface charge density. The blue lines in Fig. 6.1(c) connect gold atoms in each rows and it can be clearly seen that there is an extra row of atoms terminating at each pointed elbow site. At the bulged elbow site, the extra atom row comes from the HCP region and terminates on the FCC side of the DL.

On the other hand, at the pinched elbow, the extra row comes from the FCC region and terminates on the HCP side of the DL, as shown in Fig. 6.1(c) (d). Because of the complex atomic structure and higher surface charge density, the elbow site is the preferential adsorption location for many metal atoms [1-3] and organic molecules [4-7], as well as the C_{60} molecules at 30 K [8]. A comprehensive study of the self-assembly of C_{60} molecules on the Au (111) surface at low temperatures is presented in this chapter.

6.1 Nucleation and Growth of C_{60} Structures at 46 K

Fig. 6.2 shows an STM image taken at 46 K on the Au (111) surface with 0.01 ML of C_{60} molecules, which were deposited at the same temperature. Individual C_{60} molecules and small C_{60} clusters form ordered arrays on the surface, indicating that they are all nucleated at the elbow sites of the DLs. The elbow site presents the ability of trapping C_{60} molecules, because the thermal energy of the molecules is low in comparison to the depth of the potential well presented by the elbow sites at this reduced temperature. This is in contrast to the situation at room temperature, where efficient diffusion leads to the accumulation of molecules predominantly at step sites. The trapping of individual C_{60} molecules by the elbows shown in Fig. 6.2 is similar to what was found previously at 30 K by D. Fujita *et al*. [8], but they did not observe any formation of small molecular clusters, probably due to the lower coverage in their case. The most noticeable feature in the image is that the nucleation of the molecular clusters is strongly dependent on the elbow types, which is revealed more clearly in

Fig. 6.3 and will be introduced later in detail. Before doing that, I am going to describe the various features in Fig. 6.2. With a careful examination of the image, it is found that 91.2% of all the elbow sites are occupied by either single molecules or small molecular clusters. Among the 56 occupied sites, 23 are occupied by individual molecules, 5 by C_{60} dimers, 5 by C_{60} trimers, 4 by C_{60} tetramers, and the rest sites by clusters with five molecules or more. The clusters with five or more C_{60} molecules do not have a uniform shape, because the edge diffusion of the molecules at this temperature is restricted. Therefore, the observed structures do not represent the thermodynamic equilibrium configuration. Due to the reduced diffusion length and the trapping of molecules at the elbow site, there is no C_{60} islands formed at step edges at this coverage. All the clusters are much smaller than the compact islands usually found at room temperature with similar coverage. However, even for these relatively small clusters, it is possible to identify their azimuthal orientations by comparing the direction of close-packing to the principal axes of the Au (111) substrate. By drawing lines linking close-packed C_{60} molecules, these clusters are found to exclusively adopt one of the three orientations that have been observed on large close-packed C_{60} islands at room temperature: R0º, R14º and R30º. This finding shows that specified molecular orientation occurs for molecular clusters as small as a dimer. The configuration of any overlayer structure is decided by the combined influences from intermolecular interaction and molecule-substrate interaction. In this case, the limited number of choices, three, of the axial orientation of C_{60} dimers reveals that the effect of molecule-substrate interaction still plays a significant role in

ordering of C_{60} molecules at this temperature. It is noted that the small molecular clusters are not stable and can switch their orientations between the three possible orientations.

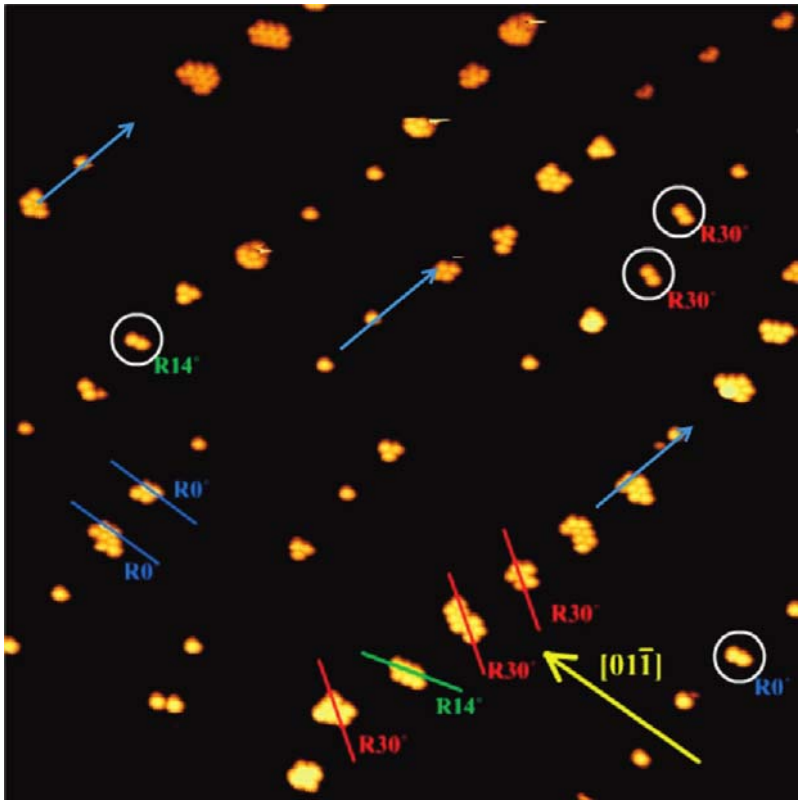

Fig. 6.2: 80 × 80 nm, V = -3.00 V, I = 0.03 nA, the C_{60} deposition and STM imaging were both preformed at 46 K. Individual C_{60} molecules and small clusters form ordered arrays by occupying the elbow sites of DLs. With the close-packing direction indicated by lines with different colours, C_{60} clusters with different orientations can be distinguished. R0º clusters are marked with blue words and the blue lines while green ones for the R14º clusters and red ones for the R30º. The [01-1] direction of the Au (111) surface is shown by the yellow arrow as a reference. White circles highlight four C_{60} dimers, the dimer axis takes three possible directions resembling the directions of close-packed C_{60} in R0º, R14º and R30º phases. Blue arrows indicate the rows of bulged elbows.

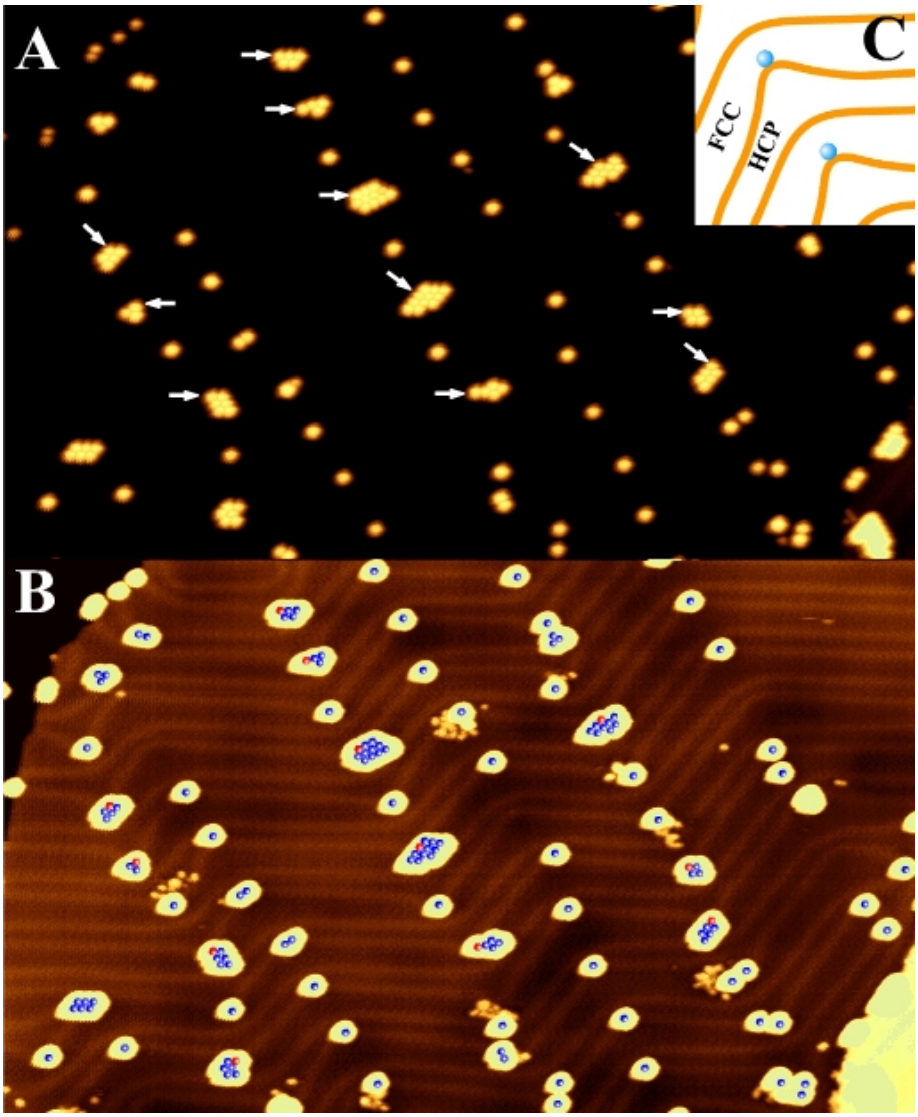

Fig. 6.3 (a): 60 × 100 nm, V = -3.00 V, I = 0.03 nA, deposition and imaging were both preformed at 46 K. Arrays of C_{60} molecules and clusters adsorbed on the Au (111) surface with 0.015 ML coverage. (b): The same image as shown in (a) with the contrast been adjusted to show the substrate herringbone pattern. Blue spheres are drawn to represent the true size and exact position of each C_{60} molecule. The red spheres in every cluster are the first molecules nucleated there. Two monoatomic Au steps can be seen at lower right corner and upper left corner. (c): A schematic image indicates the location of the first adsorbed molecule at each bulged elbow site. The red spheres in (b) are all located at this position. The C_{60} molecules represented by the red spheres are indicated by white arrows in (a). All these red spheres are found on the edge of the clusters and all the molecules in the clusters fall in FCC region.

As mentioned earlier, the bulged and pinched elbows are distinctly different in their ability to assist the nucleation of C_{60} clusters, in Fig. 6.2, the clusters preferentially nucleate at the bulged elbow sites. This difference has its root in the different local atomic structures of the two types of elbows, which are shown in Fig. 6.1(c) and (d). Fig. 6.3 shows another example of the different cluster density between the rows of bulged and pinched elbows. In Fig. 6.3(a), the C_{60} coverage has slightly increased to ~0.015 ML. It shows the same kind of adsorption feature where molecules are trapped at the elbow sites. A closer inspection reveals that nearly all the dimers, trimers and larger clusters appear in every other row, alternated by rows of exclusively single C_{60} molecules. Fig. 6.3(b) shows the same area as that in Fig. 6.3(a), but the image contrast is adjusted to reveal the herringbone pattern of the substrate. This allows us to identify that, the rows of individual molecules are on the pinched elbows and the molecular clusters are almost exclusively nucleated from the bulged elbow sites. Therefore, the nucleation of C_{60} cluster shows a site-specific characteristic at 46 K. The schematic image in Fig. 6.3(c) indicates the adsorption position for the individual C_{60} molecule at bulged elbow site. When a C_{60} molecule diffuses to an empty bulged elbow, it would like to adsorb at the terminating point of the extra row of Au atoms, which locates on the FCC side of the DL. In Fig. 6.3(b), the exact locations for each C_{60} molecules are indicated by blue spheres. In each cluster there is a special molecule that is highlighted by a red sphere. These red molecules locate at the pointed end of the bulged elbows, where the extra row of Au atoms terminates. Therefore, in the formation of C_{60} cluster at the bulged elbow, the

red molecules are probably the first molecules that adsorbed there, then, they will serve as nucleation cores for later coming molecules. When more molecules join these initial adsorbed molecules, clusters will be formed. As shown in Fig. 6.3(b), the later coming molecules did not surround the initial red molecule. Instead, they are exclusively adsorbed on the FCC side of the red molecule. Thus for all the clusters, the red molecules are on the edge, while the whole body of the clusters falls in FCC regions. By using a simple counting method, we find that 81% of the C_{60} molecules in the image, Fig. 6.3, are in the FCC region of the surface. The individual molecules adsorbed on the pinched elbow sites are the only molecules found in HCP regions.

Since the molecules land on the surface randomly, one expects the number of molecules falling into the FCC/HCP regions proportionate to their area ratio. In such a case we expect to see ~60% of molecules in the FCC region and 40% in the HCP region. However, as shown above, ~80% of all the molecules are found in FCC regions, indicating a preferential segregation of molecules occurs on the surface. This phenomenon is similar to the behaviours of many other organic molecules when deposited on the Au (111) surface as introduced in the Section 2.2.2 (Organic Molecule Deposition on the Au (111) Surface). Those organic molecules have a strong tendency to move from the HCP region to the FCC region over the DLs, which occurs very shortly after landing on the surface. Furthermore, this process is not reversible, once in the FCC region, the molecules are found to diffuse along the "channel" defined by the DLs, but unable to move back to the adjacent HCP region.

The same process seems also takes place for C_{60} molecules on the Au (111) surface at low temperature.

When the C_{60} molecules diffuse along the length of the FCC domain, if they meet an empty bulged elbow site, they will occupy the defect site introduced by the extra row of Au atoms and settle down there. Otherwise, if there is a single molecule already pinned at the bulged elbow site, the diffusing molecules are very likely to attach to the pinned molecule, cluster nucleation is thus facilitated. Subsequent growth of the molecular cluster is achieved by the addition of more molecules. For the pinched elbow site, the extra Au atom row terminates in the HCP region, therefore, the molecules pinned at the pinched elbows actually sit in the HCP region. Because the HCP region is starved of diffusing molecules, cluster nucleation is not favoured. Therefore, the different atomic structures of the bulged and pinched elbows result in a preferential nucleation of molecular cluster at the bulged elbows. However, if the deposition flux is high, there is an increased probability of finding molecules in the HCP domain, and nucleation around pinched elbows will become possible.

A further increase of the C_{60} coverage to 0.05 ML leads to an increase of the average size of the molecular clusters at the bulged elbows, as shown in Fig. 6.4. At the same time, molecular clusters including dimers, trimers and tetramers start to appear at pinched elbows. The growth of the clusters from the bulged elbow sites is clearly confined by the DLs. A number of clusters, such the ones marked with blue arrows, are just two molecules wide, but 7 to 8 molecules long. Because the growth follows the trend of the DLs, these clusters have developed a characteristic chevron

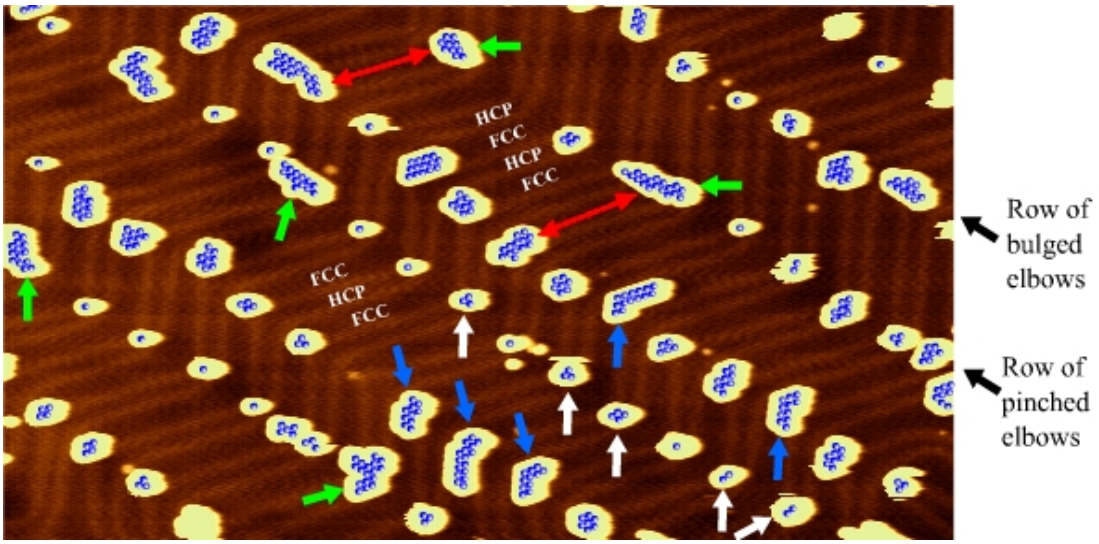

Fig. 6.4: 110 × 60 nm, V = -2.50 V, I = 0.03 nA, deposition and imaging are both performed at 46 K. The Au (111) surface has 0.05 ML C_{60} coverage. Rows of bulged elbows and rows of pinched elbows are marked. Compared to the situation in Fig. 6.3, Blue arrows indicate several C_{60} islands at the bulged elbow sites which become larger in size and have their shape confined by the DLs. C_{60} dimers, trimers and tetramers appear at pinched elbow sites at this coverage, most of which are confined in the HCP regions, as indicated by white arrows. At some pinched elbow sites, the C_{60} clusters extend to neighbouring FCC regions across the DL, as indicated by green arrows. Red arrows indicate a competition process: C_{60} molecules landing on the FCC region can either attach to a cluster nucleated at bulged elbow site or attach to cluster nucleated at pinched elbow site and extended to the FCC region.

shape. Several clusters are three molecules wide. Considering that the width of the FCC domain is about 3.5 nm, it can accommodate no more than three molecules in the direction perpendicular to the DLs.

On the other hand, the nucleation at the pinched elbow sites is less well defined. As stated earlier, at pinched elbow sites, the individually trapped C_{60} molecules actually locate in the narrow HCP region, of which the very limited domain width (~1.5 nm) is not favoured for the formation of C_{60} clusters without altering the DLs.

The clusters nucleated from the pinched elbows do not have a regular orientation. However, a number of clusters around the pinched elbows also have a large aspect ratio, as marked by the green arrows in Fig. 6.4, but the long direction of these clusters is not parallel to the local DLs. Instead, these clusters cover both the FCC and HCP regions. This unusual shape can be explained as follow: once a cluster is nucleated at the pinched elbow site, due to the small size of the HCP region next to the pinched elbow, the cluster can easily expand to the neighbouring FCC region. Then, it can capture the molecules diffusing in the FCC region and grow to a cluster covering both FCC and HCP regions. The red arrows in Fig. 6.4 indicate a competition process: two clusters sitting next to each other, one at bulged elbow and the other at pinched elbow. If a molecule lands on the FCC region between these two clusters, it can either diffuse to join the cluster at the bulged elbow or diffuse in the opposite direction to the pinched elbow. In this manner, though the nucleation of cluster at pinched elbow sites is delayed comparing to the bulged elbow sites due to the lack of molecules in the HCP regions, once the cluster has expanded over the DLs, its growth rate will be similar to those at bulged elbow sites.

In conclusion, for C_{60} deposition on the Au (111) surface at 46 K, both bulged and pinched elbow sites have the ability of trapping diffusing molecules. However, the nucleation of C_{60} clusters strongly favours the bulged elbow sites, due to the preferentially segregation of molecules into the FCC regions. The expansion of the cluster at bulged elbow sites is confined by the shape of the DLs. For the clusters at pinched elbow site, though their nucleation is delayed, they will expand to the

neighbouring FCC region at early stage, and then its growth will not be confined by the DLs.

6.2 Nucleation and Growth of C_{60} Structures at 180 K

In order to study the effect of temperature on the adsorption of C_{60} molecules on the Au (111) surface, the growth process of C_{60} clusters was repeated with the substrate being held at 180 K. Fig. 6.5 shows an STM image taken at 180 K over a surface with 0.006 ML of C_{60} molecules. Due to the low coverage, only individual molecules are observed. All these molecules are adsorbed at the DL elbow sites, indicating that the elbow site still has the ability of trapping diffusing molecules at this temperature. Furthermore, the preferential occupation of bulged elbow site is evident. In Fig. 6.5, there are 156 bulged elbow sites and 141 pinched elbow sites, by simply counting, it is found that 77.6% of the bulged elbow sites are occupied whereas only 48.9% of the pinched elbow sites are occupied. Two possibilities could lead to such site-specific adsorption. The first is that the binding energy at the pinched elbow site is lower than that at the bulged elbow site. At 46 K, the two types of elbow sites show no difference in their ability of trapping individual molecules, because the thermal energy of the C_{60} molecules is much lower than the depth of the potential well at the pinched elbow site. However, at 180 K, the increased thermal energy may lead to unstable adsorption at the pinched elbow site. The second possibility is the enhanced molecular transport from the HCP region to the FCC region. This process needs to overcome the barrier presented by the DLs, it is thus thermally activated. Therefore, at a higher temperature

of 180 K, the molecules land on the surface with relative high thermal energy, and hence they move from the HCP region to the FCC region so quick that they do not have chance to meet a pinched elbow sites. One or both of the above two possibilities lead to the preferential occupation of the bulged elbow sites.

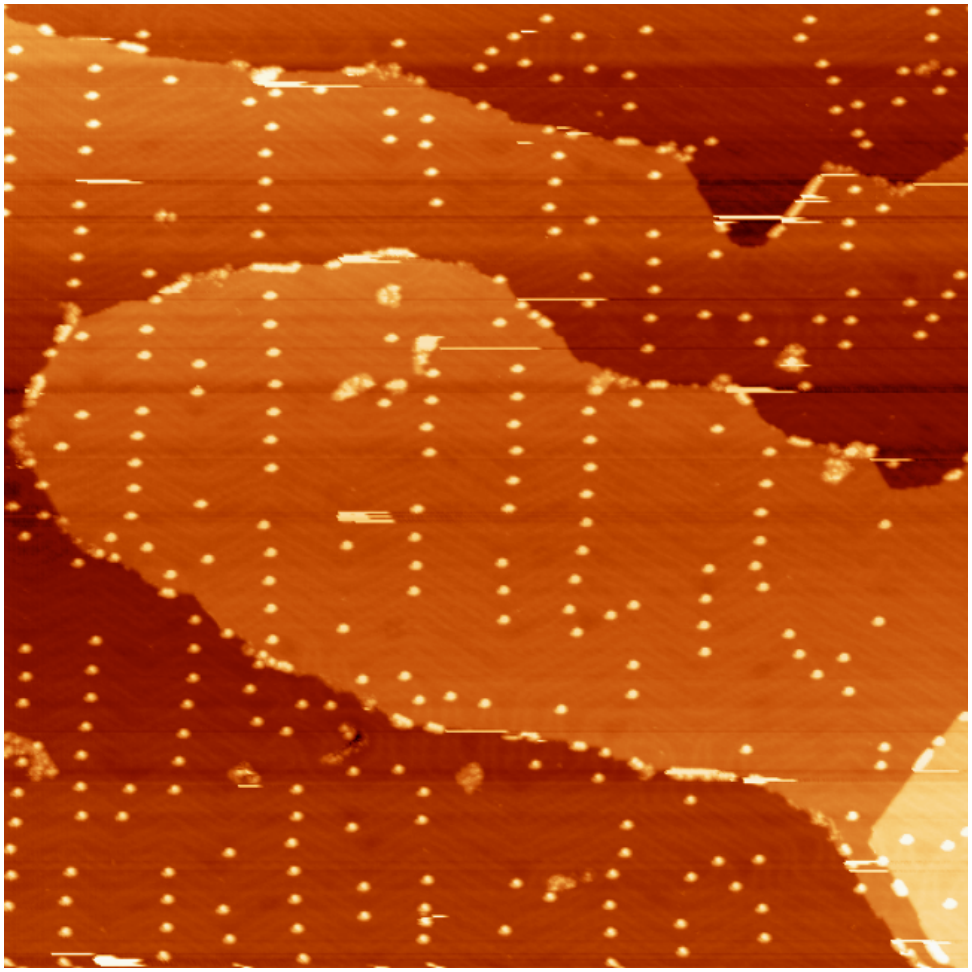

Fig. 6.5: 220 × 220 nm, V = -1.2 V, I = 0.01 nA, deposition and imaging are both performed at 180 K. STM image of 0.006 ML C_{60} molecules deposited on the Au (111) surface. Molecules are exclusively adsorbed on the elbow sites, with a preferential adsorption at the bulged elbow sites.

At 46 K, the bulged elbow site presents higher cluster nucleation rate than the pinched elbow site. At higher temperature, reduced molecule-trapping ability of the

pinched elbow sites amplifies the difference in nucleation rate between the two types of elbow sites. Fig. 6.6(a) shows an STM image over a surface with 0.15ML of C_{60} molecules, of which the deposition and imaging are both performed at 190 K. In this image, large C_{60} islands together with some individual molecules can be seen. Different from similar large islands observed at room temperature, which are nucleated from the step edges, the islands in Fig. 6.6(a) are evidently all nucleated from the elbow sites. Fig. 6.6(c) presents a similar C_{60} structure as that in Fig. 6.6(a). With the herringbone pattern of the substrate revealed, we find that all the individual C_{60} molecules in this image exclusively occupying bulged elbow sites. All the pinched elbow sites, except those are covered by the large islands, are free of adsorbed molecules. Two rows of empty pinched elbow site are highlighted by the black arrows in Fig. 6.6(c). Therefore, the site-specific characteristic of adsorption and the difference in nucleation rate for the two types of elbow sites are both enhanced at the temperature of 180~190 K, comparing to that at 46 K.

The large C_{60} islands shown in Fig. 6.6(a) and (c) have hexagonal appearance and well defined edges, indicating that they are formed by close-packing molecules and the island edges are aligned with those close-packed directions. This conclusion is confirmed by the image in Fig. 6.6(b), which reveals the packing of the molecules in the island. By finding the close-packed direction of the molecules, all the islands in Fig. 6.6(a) and (c) are found to have the R30^{o} structure. Furthermore, the herringbone pattern of the substrate is projected on to the C_{60} island, indicating that at this temperature, the C_{60}-Au interaction is not strong enough to lift the reconstruction. In

Fig. 6.6(c), we find that for a hexagonal island, four of its six edges are perfectly aligned with surrounding DLs, while the other two edges are aligned with the <112> direction of the substrate, which is the direction of the rows of elbow sites, as marked by the black arrows. There are some islands, of which the two edges along the <112> direction is very short, thus resulting in a parallelogram-like shape, for instance the one in the middle right of Fig. 6.6(c). The shapes of all these hexagonal and parallelogram islands are evidently defined by the pattern of the DLs, which is similar to the situation of the R30º island I introduced in Chapter 4 by Fig. 4.2(b). For that island, which grows at room temperature with the substrate reconstruction lifted, its two long edges are also defined by the DLs. However, the growth process suggested for the room temperature growth cannot be used to describe the island formation at 180 K. At room temperature, the transformation of HCP region and incommensurate region (which is the DL) into FCC region serves as a barrier for the expanding of C_{60} island, thus the island edge will stop in front of the DL. In comparison, at 180 K, the expanding of C_{60} islands does not need to lift the substrate reconstruction. Therefore, the role of the DLs is just guiding the diffusing molecules to approach the edges of the islands, and confines the shape of the islands by their corrugation height. This growth model can also explain why only R30º islands are formed at 180 K. Because the close-packed directions of the R30º structure are aligned with the directions of the DLs, if the edges of the islands are aligned with the DLs, they would consist of close-packing molecules, which is energetically favoured. If R0º and R14º phases are formed, the islands edges are expected to be faceted.

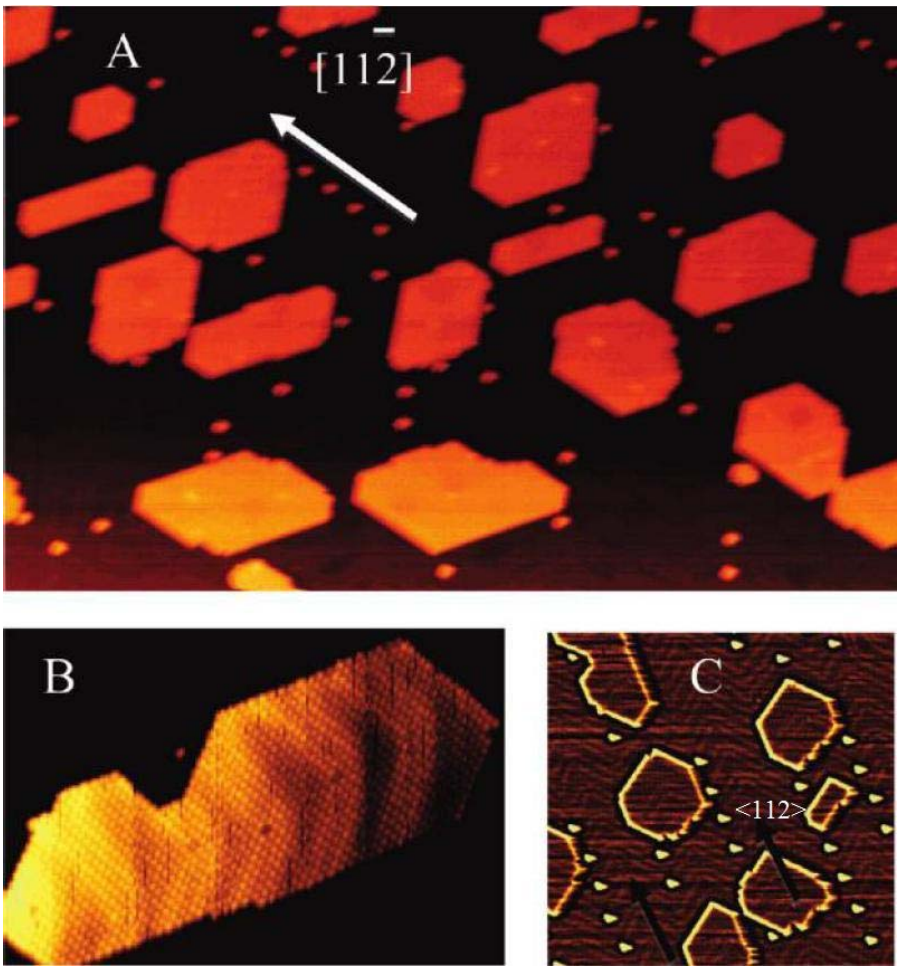

Fig. 6.6 (a): 180 × 113 nm, V = -1.1 V, I = 0.03 nA, deposition and imaging are both performed at 190 K. 0.15 ML of C_{60} molecules adsorbed on the Au (111) surface. Large hexagonal islands and some individual molecules can be seen. The image is slightly distorted due to the thermal drift. (b): 60 × 40 nm, V = -5.01 V, I = 0.03 nA. A close-packed C_{60} island reveals the herringbone pattern of the substrate. (c): 122 × 115 nm, V = -5.01 V, I = 0.03 nA. Molecules were deposited at 190 K and imaging was conducted at 170 K. The image is filtered to present the herringbone pattern. Two rows of empty pinched elbow sites are indicated by black arrows, which are aligned with the <112> direction of the substrate.

Since the islands in Fig. 6.6 are so large that each one covers several bulged and pinched elbow sites, it is not obvious that these islands are nucleated from the bulged elbow sites. Fig. 6.7 presents a surface with similar C_{60} coverage as that in Fig. 6.6.

The islands formed in the middle of the terrace are relatively small. Many of these islands do not touch any pinched elbow sites, as marked by the circles. Therefore, these islands must be nucleated from bulged elbow sites. Furthermore, the parallelogram shape of the islands indicates that the growth is guided by the DLs.

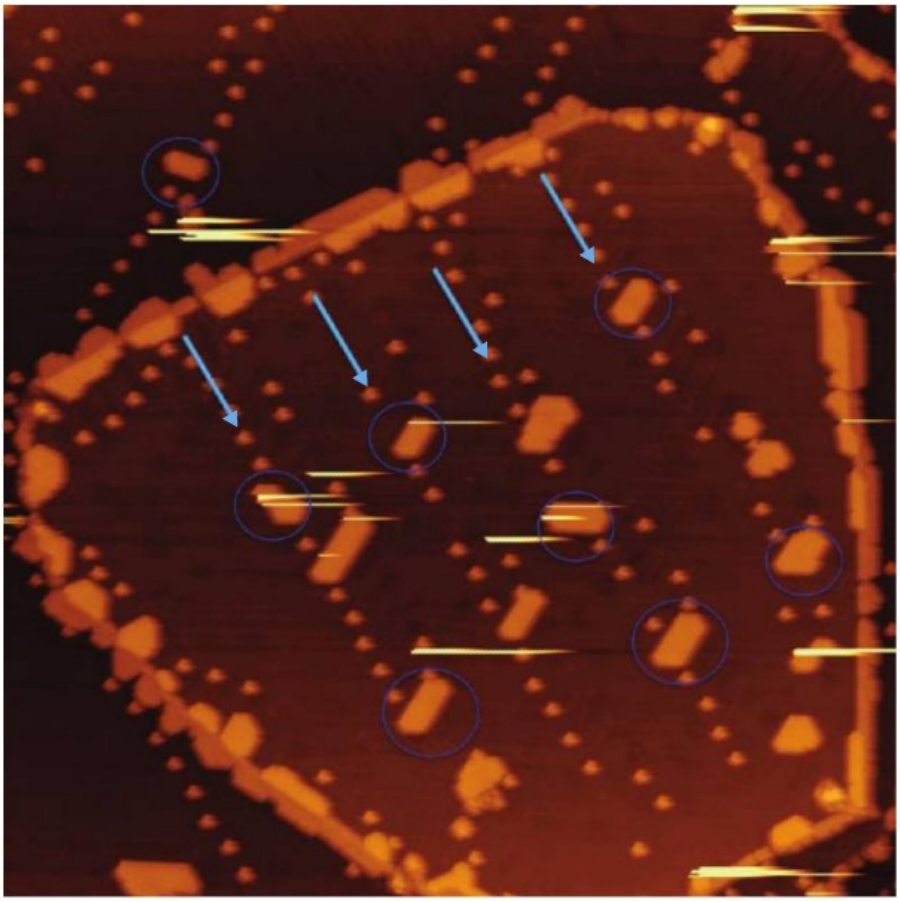

Fig. 6.7: 220 × 220 nm, V = -1.2 V, I = 0.03 nA, deposition and imaging are both performed at 180 K. 0.15 ML of C_{60} molecules adsorbed on the Au (111) surface. The blue arrows indicate four rows of bulged elbow sites with individual C_{60} molecules adsorbed on. The circles mark eight islands that are nucleated from bulged elbow sites and do not touch any pinched elbow sites.

Base on the data presented above, a picture of the nucleation and growth of C_{60} islands at ~180 K can be drawn. Due to site-specific adsorption, only bulged elbow

sites are populated with molecules at low coverage. When more molecules land on the surface, they prefer to join the molecules already pinned at the bulged elbow sites rather than occupy the empty pinched elbow sites. Similar to the situation shown in Fig. 6.4, the molecules in the clusters nucleated at the bulged elbow sites are aligned with the direction of the DLs, which means adopting the R30° structure. Once the clusters expand to a certain size, it becomes impossible for them to switch to other orientations as a whole, although orientation switch can happen for small clusters like dimers, trimers or tetramers. Therefore, the islands developed from these clusters will retain the R30° structure and have its edges defined by the DLs. As shown in Fig. 6.4, the clusters nucleated at pinched elbow sites have more random orientations and shapes, because they overcame the confining DLs at a very early stage. However, at 180 K, it is rare to find molecules adsorbed at pinched elbow site, thus no cluster or island will be nucleated from there.

Combining the discussions in the previous two chapters and that in this chapter, three different processes of the adsorption of C_{60} molecules on the Au (111) surface can be defined according to the different sample temperatures: (a) step controlled process at room temperature; (b) nucleation at both bulged and pinched elbow sites at 46 K; (c) single orientation growth due to site-specific nucleation at bulged elbow sites at 180-190 K. At room temperature, due to the high thermal energy of the C_{60} molecules, only the step edges can trap molecules, thus nucleation of island exclusively happens at the step edges. The orientation of the C_{60} island depends on the direction of the initial adsorbed step edge. Once an island is formed, it may show

various features like lifting of substrate reconstruction, formation of nanopit, appearance of dim molecules and faceting of the Au step edge. However, the appearance of these features depends on the equilibrium of the C_{60}-C_{60} interaction and the C_{60}-Au interaction. Furthermore, the local structures of the Au surface are found to influence this equilibrium. At 46 K, the situation is much more simple, both the bulged and pinched elbow sites can trap diffusing molecules. The density of molecules diffusing in the FCC regions is higher than that in the HCP regions, because the molecules landing on the HCP regions have certain probability to move to the adjacent FCC regions over the DL, but not vice versa. Therefore, the nucleation rate of clusters at bulged elbow sites is much higher than that at pinched elbow sites. The clusters formed at bulged elbow sites have their shape being defined by the DLs while the clusters at pinched elbow sites are much irregular in shape. At 180-190 K, the pinched elbow sites loss the ability of trapping molecules. Large close-packed R30º islands are nucleated from bulged elbow sites as the C_{60} coverage increases. The edges of these islands are aligned with the DLs.

A novel adsorption process different from above three has been observed in my research, and that will be presented in the next chapter.

References

[1] W. Lin, H. Chang, Y. Hu *et al*., Nanotechnology **21**, 015606 (2010).

[2] S. Helveg, J. V. Lauritsen, E. Lægsgaard *et al*., Phys. Rev. Lett. **84**, 951 (2000).

[3] D. D. Chambliss, R. J. Wilson and S. Chiang, Phys. Rev. Lett. **66**, 1721 (1991).

[4] M. Böhringer, K. Morgenstern, W. D. Schneider, *et al.*, Phys. Rev. Lett. **83**, 324 (1999).

[5] I. Fernandez-Torrente, S. Monturet, K. J. Franke, J. Fraxedas, N. Lorente, and J. I. Pascual, Phys. Rev. Lett. **99**, 176103 (2007).

[6] L. Gao, Q, Liu, Y. Y. Zhang, N. Jiang, *et al*., Phys. Rev. Lett. **101**, 197209 (2008).

[7] N. Jiang, Y. Y. Zhang, Q. Liu, Z. H. Cheng *et al*., Nano Lett. **10**, 1184 (2010).

[8] D. Fujita, T. Yakabe, H. Nejoh, T. Sato, and M. Iwatsuki, Surf. Sci. **366**, 93 (1996).

CHAPTER 7

TWO BONDING CONFIGURATIONS FOR C_{60} ON Au (111)

At the end of Chapter 6, three different adsorption processes of C_{60} molecules on the Au (111) surface have been concluded. At room temperature, the C_{60} molecules show high mobility on flat terraces and C_{60} islands are exclusively nucleated at step edges. With reduced sample temperature, the elbow site of type x discommensuration line (DL) can trap C_{60} molecules and facilitates island nucleation. At 46K, both the bulged and pinched elbow sites show this ability, while at 180 K, only the bulged elbow site can capture diffusing molecules. Contrary to general belief, the occupation of elbow sites by the C_{60} molecules at room temperature is observed from time to time. This appears in conflict with the high mobility of the C_{60} molecules at room temperature. Furthermore, with increasing coverage, C_{60} islands are found to nucleate in between two pre-existing elbow site molecules but keep a clear distance from them. This is unusual because C_{60} islands are usually formed along the Au step edges at room temperature or formed at the elbow site using a pre-existing molecule as nucleation core at low temperature. The adsorption process briefly described above will be introduced in detail in this chapter, and a possible explanation to the phenomenon will be given with the help of DFT simulation results from our collaborators Y. Wu, L. Wang and H. Cheng.

7.1 Stability of the C_{60} Islands Formed at Low Temperature

Before introducing the novel adsorption process at room temperature, I would like to talk about the stability of the individual C_{60} molecules and clusters adsorbed at the elbow sites at low temperature, from which we can see the influence of temperature on the behavior of C_{60} molecules.

At first, the Au sample is cooled to 46 K and 0.05 ML of C_{60} molecules are deposited onto the surface. From the STM image shown in Fig. 7.1, which was taken at 46 K, a similar adsorption structure as seen in the Fig. 6.4 in the previous chapter is presented. Individual C_{60} molecules are trapped by the elbow sites of type x DLs and some clusters or small islands are nucleated from these trapped molecules. The nucleation and growth process at this temperature was discussed in detail in Chapter 6. Now, in order to testify the stability of these structures, the sample temperature is raised step by step with no further C_{60} deposition. STM imaging is performed at each temperature to record the changes of the C_{60} structures as a function of temperature.

When temperature is raised to ~160 K, the single molecules adsorbed on the elbow sites start to move away. These molecules diffuse to either the step edges or join the pre-formed molecular clusters. For the molecular clusters, they can grow by capturing diffusing molecules, at the same time, molecules from the edges of a cluster can also detach from the cluster. Therefore, a ripening process is taking place, resulting in the enlargement of some C_{60} clusters at the expense of others. Fig. 7.2 shows an STM image taken at 180 K. From this image, one can see that many elbow sites are free of adsorbed molecules, though there are still several molecules that

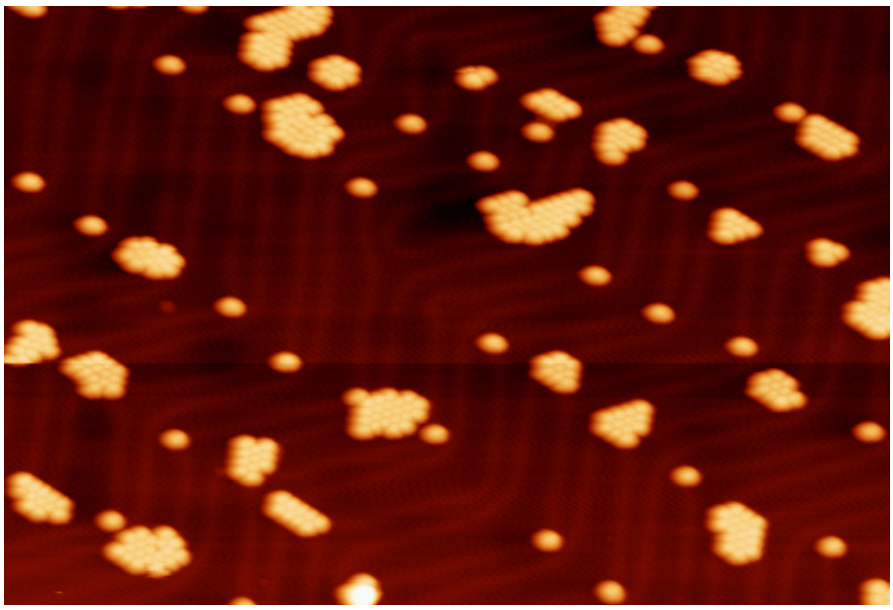

Fig. 7.1: 79.5 × 54 nm, V = -2.5 V, I = 0.03 nA. At 46 K, on an Au (111) surface with 0.05 ML of C_{60} molecules, the elbow sites of type x DLs are occupied by either single C_{60} molecules or molecular clusters. These clusters are evidently nucleated from the single molecules that trapped by the elbow sites.

remain at the elbow sites. Considering that almost every elbow sites are occupied at 46 K, as shown in Fig. 7.1, the elbow sites have lost their bonding with the C_{60} molecules due to the raised temperature. However, some elbow sites retain the single molecules adsorbed on them at 180 K, indicating that the temperature of 180 K is near the threshold of the elbow sites' trapping ability of the C_{60} molecules. At this temperature, the thermal energy of the C_{60} molecule is more or less comparable to the depth of the potential well presented by the elbow site, thus there is a certain probability that the diffusing molecule get trapped by the elbow site. This is consistent with the observation from Fig. 6.5, where the C_{60} molecules are directly deposited onto the Au surface held at 180 K. In that case, the small difference in the potential well depth between the bulged and the pinched elbow sites leads to a large difference

in the number of molecules trapped by the two kinds of elbow sites, where the bulged elbow site is a much more preferred adsorption site for the C_{60} molecules than the pinched elbow site.

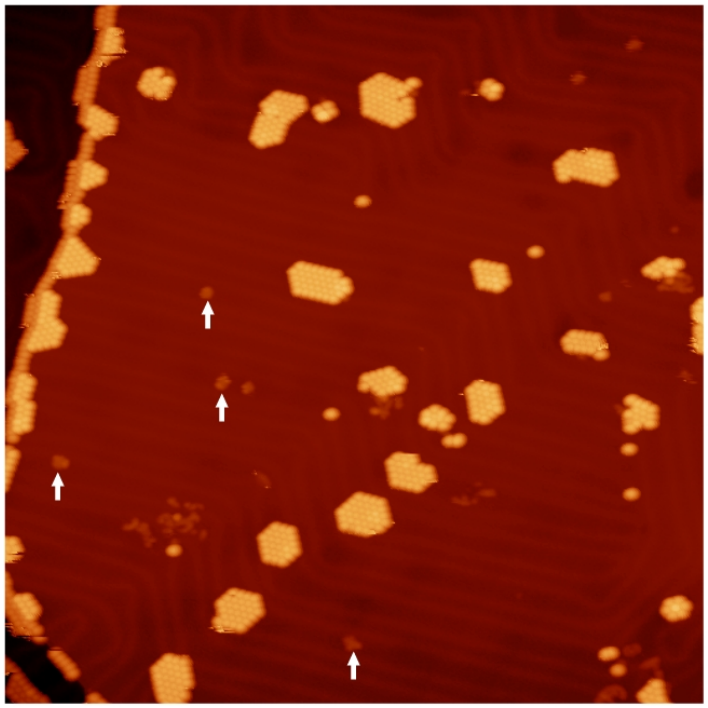

Fig. 7.2: 100 × 100 nm, V = -1.452 V, I = 0.03 nA. The same sample as shown in Fig. 7.1 with the temperature been raised to 180 K. Due to the increase thermal energy, many C_{60} molecules leave the elbow site and diffuse to the step edges or to join some large C_{60} clusters. A ripening process is taking place. However, some single C_{60} molecules remain on the elbow sites at this temperature.

In Fig. 7.2, there are some adsorbed structures randomly distributed on the surface, as marked by the white arrows in Fig. 7.2. They are about 1~1.5 Å high and shows no preferential adsorption on the elbow site of the DLs. Before cooling to 46 K, the Au (111) surface is imaged at room temperature, no such structure is observed. It appears in the image taken at 46 K and remains on the surface when the temperature is raised to 180 K. However, when the temperature reaches room temperature again,

this structure disappears automatically. Therefore, we conclude this structure to be some water molecules, which will adsorb on the surface when the sample temperature is low. These water molecules show no effect on the behaviors of the C_{60} molecules.

As the temperature increases further, the ripening process leads to the development of a few very large C_{60} islands. When the temperature reaches 284 K, which is close to room temperature, there are only a few large islands remaining on the terrace, as shown in Fig. 7.3(a). These islands consist of 150~450 C_{60} molecules. In comparison, there are no more than 30 molecules in the largest cluster at 46 K. At 180 K, the remaining clusters on the terrace normally consist of 25~45 molecules. The increasing of the average size of the clusters (large clusters are referred to as islands) as a function of the temperature can be used to describe the aggregation process of the C_{60} molecules. At 46 K, there is no aggregation of molecules on the Au step edge. A large number of single molecules and small clusters including dimers, trimers and tetramers distribute on the terrace. The density of clusters (and single molecules) is high. Almost every pointed elbow sites are occupied, which equal to ~6.35 clusters (and single molecules) per 1000 nm^2. When the temperature is raised to 180 K, as shown in Fig. 7.2, the density of clusters is evidently reduced as a result of ripening. Small clusters aggregate to form large clusters, leaving behind a large number of empty elbow sites. At this stage, besides some single molecules directly bonded with the defect point at each elbow site, only clusters consisting of more than 15 molecules can survive on the terrace. The density of clusters on the terrace is about ~2 clusters per 1000 nm^2. Many molecules have diffused to the step edges, small clusters

consisting of 7~24 molecules have grown from the step edge. Finally when the temperature reaches 284 K, the Au surface becomes very clean, most areas on the surface are free from C_{60} molecules. As shown in Fig. 7.3(b), the majority of the C_{60} molecules form large islands from the step edges, which is similar to the situation of room temperature deposition. The islands remaining on the terrace are large in size, consisting of hundreds of molecules. Consequently, the island density becomes very low, ~0.4 per 1000 nm^2.

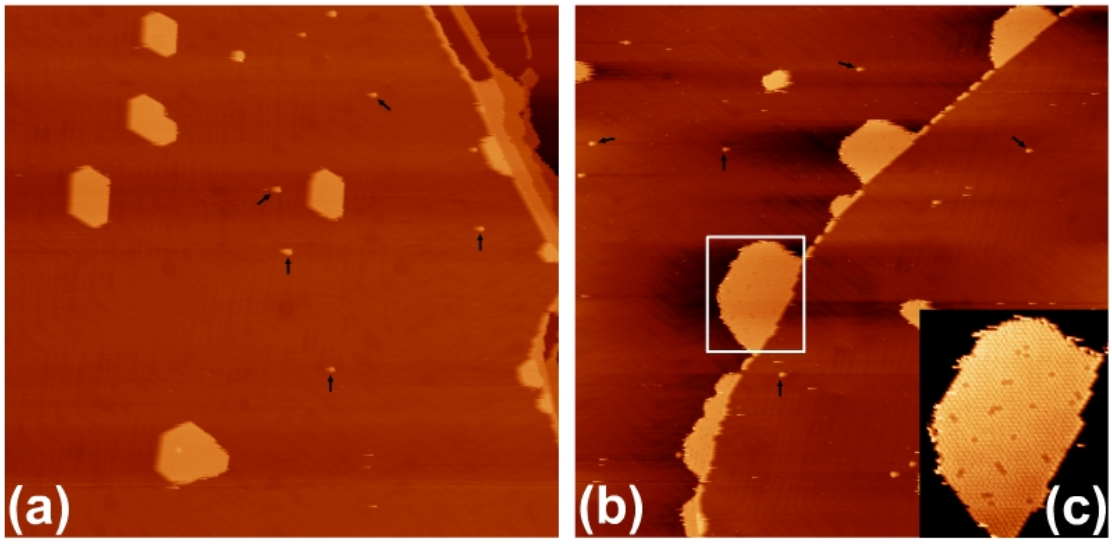

Fig. 7.3 (a): 198.8 × 191.4 nm, V = -1.40 V, I = 0.03 nA. (b): 200 × 200 nm, V = -1.40 V, I = 0.03 nA. The same sample as shown in Fig. 7.1 and Fig. 7.2 with the temperature been raised to 284 K. Most elbow sites are empty. The C_{60} molecules have diffused to Au step edges, and formed large islands there. Some large islands consisting of hundreds of molecules remain in the middle of the terrace. Surprisingly, at such a high temperature, some single molecules can still stay on the elbow site without diffusing away, as indicated by the black arrows. An R14º island formed on the step edge is highlighted by a white rectangle in (b). By adjusting contrast, as shown in (c), we can see the 7 × 7 superlattice formed by dim molecules on this island, indicating that nanopits are formed on the substrate and lead to the dim appearance of these molecules.

Nevertheless, even when the temperature has reached 284 K, we can still find some single C_{60} molecules bonded to the elbow sites and stay in the middle of the terrace, as indicated by the black arrows in Fig. 7.3(a) (b). These remaining single molecules have been found on both bulged and pinched elbow sites. This is a rather surprising observation. As introduced in the previous chapters, the C_{60} molecules show a high mobility on the Au (111) surface at room temperature, neither bulged nor pinched elbow site can trap them. Furthermore, when the C_{60} molecules are deposited onto an Au (111) surface held at 180 K, the pinched elbow site is already found to be not favoured by the adsorption of C_{60} molecules. Therefore, the single C_{60} molecules remaining on the elbow sites shown in Fig. 7.3 must have a different, but strong bonding with the elbow sites. This bonding is much stronger than the one formed between the C_{60} molecule and the elbow site at 46 K.

Besides the remaining single molecules, a 7 × 7 superlattice formed by dim molecules can be observed on one of the C_{60} islands in Fig. 7.3(b), which is highlighted by a white rectangle. A zoomed-in image of the island is shown in Fig. 7.3(c). As introduced in Chapter 4, the interaction between the adsorbed C_{60} molecule and the Au surface can lead to the formation of nanopits on the substrate. Molecules sitting in the nanopits have a dimmer appearance, thus the dim molecules seen in the island suggest that there are nanopits formed underneath. Pit formation is thermally activated, and it does not occur at 46 K. As temperature increases to 284 K, nanopits are formed. Pit formation also affects the individual molecules at the elbow sites. When the molecules are deposited at 46 K, they are pinned at the elbow sites purely

because the potential well presented by the elbow site is deeper than their thermal energy. When the temperature is raised, a nanopit is formed under some molecules before they diffuse away. Sitting on a nanopit will offer much better coordination with the substrate Au atoms for the C_{60} molecule, thus the bonding is strong enough to retain the molecule on the elbow site even at room temperature. However, the threshold temperature for the formation of nanopit seems to lie in the range between 160~190 K, which is also the temperature range that the C_{60} molecules start to diffuse away from the elbow sites. Diffusion and nanopit formation are a pair of competing processes taking place at 160~190 K. Each molecule has a certain probability to diffuse away or to remain on the elbow site by forming a nanopit.

Based on the above description, two kinds of bonding configurations formed between the C_{60} molecule and the elbow site of type x DL are distinctly identified. The first bonding configuration is formed when C_{60} molecules are deposited at 46 K. In this bonding configuration, the C_{60} molecule sits directly above the Au surface. The second bonding configuration is formed by creating a nanopit under the C_{60} molecule. For those single molecules observed in Fig. 7.3(a) (b), when they are originally deposited at 46 K, the first kind of bonding configuration is formed. During the rising of the temperature, they have transformed into the second kind of bonding configuration with a rearrangement of the underlying substrate atoms. In the next section, I am going to introduce a phenomenon, in which the C_{60} molecules can form the stronger bonding configuration directly on the elbow site when deposited at room temperature. A model for the stronger configuration will also be given.

7.2 Occupation of the Elbow Sites at Room Temperature

As a major finding of my research, for many times, single C_{60} molecules occupying the elbow sites of type x DLs has been observed at room temperature, an example is shown in Fig. 7.4(a). This image was taken from a surface with a very low coverage of C_{60} molecules, deposited onto Au (111) at room temperature. As a huge surprise, individual C_{60} molecules are adsorbed on the elbow sites of the DLs and stay in the middle of the terrace, instead of diffusing to the step edges. More than 70% of all the

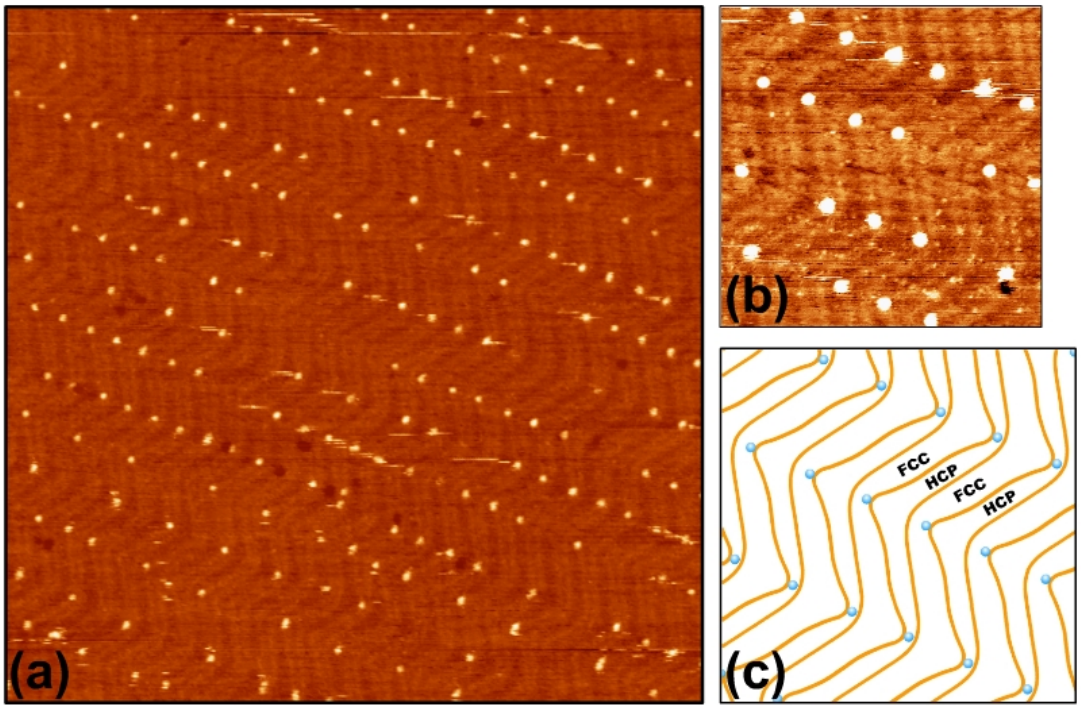

Fig. 7.4 (a): 200 × 200 nm, V = -0.80 V, I = 0.03 nA. STM image of 0.005 ML C_{60} molecules deposited on the Au (111) surface at room temperature. Individual molecules are adsorbed at the elbow site of type x DLs. (b): 9.6 × 9.6 nm, V = -0.80 V, I = 0.03 nA. A zoom-in STM image of (a). The precise adsorption positions of the C_{60} molecules on the bulged and pinched elbow sites are shown, respectively. (c): a schematic diagram of (b), from which it can be found that the adsorption position for the C_{60} molecules on elbow sites are exactly the same for the room temperature deposition and the low temperature deposition.

elbow sites are occupied by the single molecules. Furthermore, the C_{60} molecules show no preference for the bulged elbow sites. Equal percentages of all the bulged or pinched elbow sites are occupied. As a reference, C_{60} molecules show strong preference for the bulged elbow sites, when they are deposited onto a sample at 180 K. However, from Fig. 7.4(b) we can find that the adsorption locations for the single molecules on the elbow site are exactly the same as the ones found at 46 K. For a bulged elbow site, the C_{60} molecule is adsorbed on the FCC side of the bended DL, where the extra row of Au atoms terminates. For a pinched elbow, the termination point for the extra Au atom row is on the HCP side of the bended DL and the C_{60} molecule will be adsorbed at this point. These positions of C_{60} molecules are clearly shown in the schematic diagram of Fig. 7.4(c).

Based on the above observations, we can conclude that although the adsorption position at room temperature is the same as that at 46 K, the bonding configuration for C_{60} molecule at room temperature must be different from that at 46 K. The former is much stronger, as it can withhold the molecules in the middle of the terrace at room temperature while the later one starts to release molecules at 160 K and becomes empty at 284 K. Moreover, the stronger bonding configuration can be formed at both the bulged and pinched elbow sites, despite the two have different potential well depth, which leads to different affinities to C_{60} molecules at 180 K, as demonstrated in Fig. 6.5 of the previous chapter. We attribute the stronger bonding configuration to a nanopit formed in the Au surface lattice on the elbow site. Such a conclusion is based on two considerations. The first is that the elbow site has a very contracted and

disordered atomic lattice, of which the Au atom sometimes jump out of the elbow site upon the adsorption of metal atoms or organic molecules [1]. The second is the recently reported phenomena of nanopit formation on the Cu (111) [2], Ag (111) [3] and Au (111) [4, 5] surfaces, induced by the adsorbed C_{60} molecules. Therefore, the single C_{60} molecules adsorbed on the elbow sites at room temperature are either sitting in a large pit or above a small pit. Till now, two ways of forming the stronger bonding configuration are found. The first way is demonstrated in the previous section, in which the weaker bonding configuration can be transformed into the stronger bonding configuration via the nanopit formation during the rising of the temperature. The second way is shown in this section, when deposited onto a room temperature sample, sometimes the C_{60} molecules can directly induce the formation of nanopits and form the strong bonding configuration.

In order to verify the proposed strong bonding configuration, which involves the formation of the nanopit, DFT calculations are performed by our collaborators Y. Wu, L. Wang and H. Cheng from University of Florida, USA. The adsorption energies of C_{60} molecules on 1-, 3- and 7-atom pits are calculated. For the DFT calculation method, please refer to our paper "*Two bonding configurations for individually adsorbed C_{60} molecules on Au (111)*" [6]. Only the results will be introduced here.

The DFT simulation images for the 1-, 3- and 7-atom nanopit configurations are shown in Fig. 7.5. For all the three situations, the most stable configuration is achieved by having a hexagonal ring of the C_{60} molecules facing the substrate. The center of the hexagonal ring is aligned with the center of the nanopit in the *z* direction.

With such a configuration, very little geometrical distortion is found on the C_{60} cage in all the three cases. However, the positions of the Au atoms near the elbow site are changed corresponding to the adsorption of a C_{60} molecule and nanopit formation. This reconstruction is described in detail in Table 7.1. The average distance from a carbon atom in the bottom hexagonal ring to the first Au layer (d_z) is 1.80 Å, 1.68 Å and 0.15 Å for the 1-, 3- and 7-atom nanopit, respectively. The formation of nanopit also induces a local contraction of the Au layer, in which the inter-layer distance

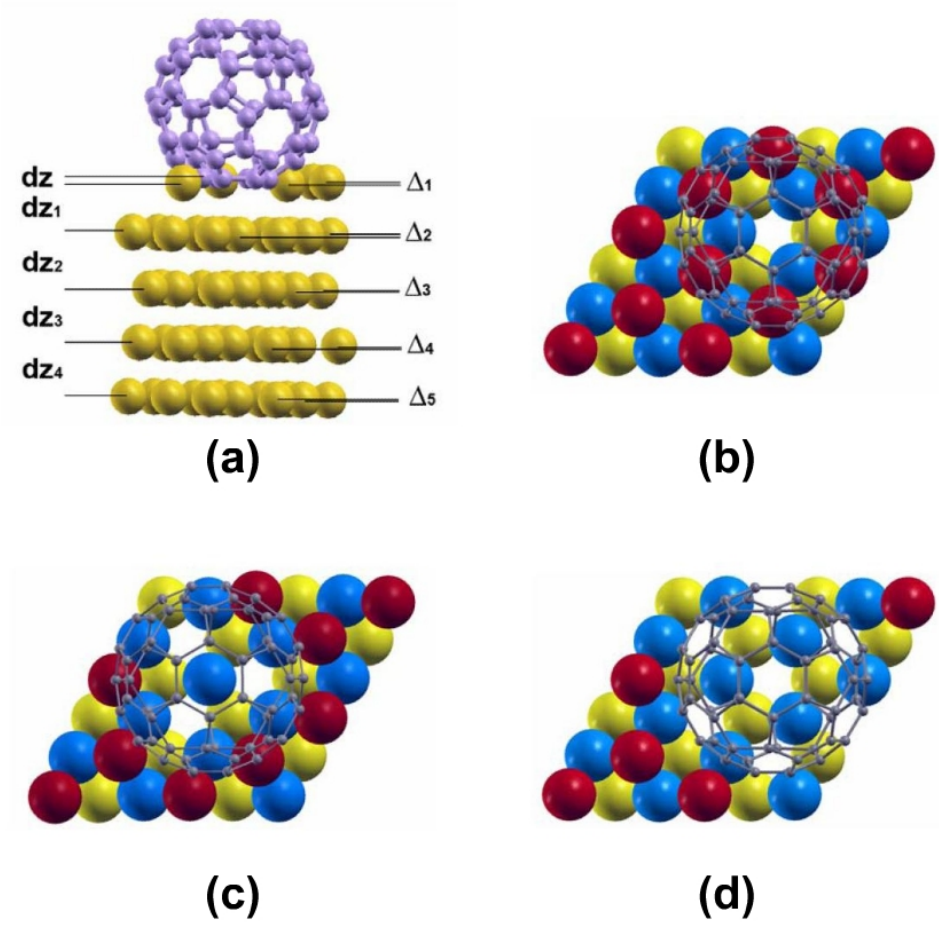

Fig. 7.5: C_{60} molecule adsorbed on the Au (111) surface with a nanopit formed underneath. The Au atoms of the first, second and third layer are represented by red, blue and yellow spheres, respectively. (a): The side view of a C_{60} molecule sitting on a 7-atom nanopit. (b), (c) and (d): The top views of C_{60} molecule sitting on 1-, 3- and 7-atom nanopit, respectively.

	1-atom nanopit	3-atom nanopit	7-atom nanopit
d_z (Å)	1.80	1.68	0.15
d_{z1} (Å)	2.32	2.27	2.25
d_{z2} (Å)	2.34	2.35	2.36
d_{z3} (Å)	2.35	2.35	2.35
d_{z4} (Å)	2.35	2.35	2.35
Δ_1 (Å)	0.04	0.05	0.10
Δ_2 (Å)	0.09	0.11	0.03
Δ_3 (Å)	0.01	0.01	0.03
Δ_4 (Å)	0.01	0.01	0.04
Δ_5 (Å)	0.01	0.01	0.01
Δ_{xy1} (Å)	0.04	0.18	0.02
Δ_{xy2} (Å)	-0.05	-0.06	0.03
Adsorption Energy (eV)	**2.07**	**2.33**	**2.56**

Table 7.1: Structural parameters and adsorption energies from DFT calculation: d_z is the average inter-layer distance, Δ is the average intra0layer buckling amplitude, and Δ_{xy} is the average lateral displacement of the Au atoms surrounding the nanopit.

between the first and second Au layer is reduced comparing to a perfect Au lattice. However, the third and fourth layer is barely influenced. The intra-layer buckling amplitude is also calculated. The results show enlarged buckling amplitudes of the second Au layer in the 1- and 3-atom nanopit structures. For the 7-atom nanopit

structure, the largest buckling amplitude is found in the first Au layer. Moreover, the formation of nanopit induces lateral displacements of the Au atoms near the nanopit. In the first Au layer, the atoms next to the nanopit are pushed away from the vacancy, while for the second layer, the atoms are attracted inward in the 1- and 3-atom nanopit structures and are slightly pushed outward in the 7-atom nanopit structure. The average lateral displacements of the Au atoms from their perfect lattice positions are listed in Table 7.1, of which the Δ_{xy1} and Δ_{xy2} represent the displacement in the first and second layer, respectively.

On a defect free Au (111) surface, the adsorption energy of C_{60} molecule is as low as 1.20 eV and the translational motion of the molecule is nearly barrier free at room temperature. In this case, it is difficult for elbow site to trap C_{60} molecule. With the formation of 1-, 3- and 7-atom nanopits, as shown in the DFT calculation results, the adsorption energies of the C_{60} molecule increase to 2.07 eV, 2.33 eV and 2.56 eV, respectively. The energy difference signals that the trapping of C_{60} molecule on the elbow site at room temperature is achieved by nanopit formation. Furthermore, the height of the single C_{60} molecule on elbow site is measured to be ~4 Å in STM image at room temperature. As a reference, this height is ~6.2 Å at 46 K. If the height difference is caused by the nanopit formed under the molecules at room temperature, its 2.2 Å value is in good agreement with the 7-atom nanopit model as shown in Fig. 7.5(a) and (d). The apparent height measured in STM image does not always reflect the real geometric height. However, the 2.2 Å height difference is too large for a pure electronic effect, at the same time, it is similar to the height difference measured

between the molecules respectively sitting on the upper terrace and lower terrace of an Au monoatomic step. Therefore, the DFT calculation supports our proposal that the C_{60} molecule stay on elbow sites at room temperature are trapped by a nanopit underneath, furthermore, it points out that the nanopit possibly consists of 7 missing Au atoms.

As introduced in the last part of the previous section, the nanopit formation is a thermally activated process, which requires certain temperature for it to take place. At 46 K, no nanopits are formed and the C_{60} molecules are all adsorbed on intact Au surface. When deposited at room temperature, the C_{60} molecules have a certain chance to occupy the elbow sites via nanopit formation, of which the possibility is related to the local topography of the Au surface and the deposition parameters. The trapping probability of the C_{60} molecule on elbow site is proportional to both the concentration of the elbow sites and the concentration of diffusing C_{60} molecules. The density of the elbow site on the Au (111) surface is not uniform but varies from place to place, depending on the bending frequency of the DLs. On surfaces consisting of relative narrow terraces, the density of elbow site is low due to partial relief of the surface strain by the step edges. Moreover, the step edge is a competing adsorption site of the C_{60} molecules. Therefore, at room temperature, the occupation of elbow sites by single C_{60} molecules preferentially happens on large terraces with a high density of elbow site. The sample used in my experiment meets this requirement. Single terraces as wide as ~μm are frequently observed, which is at least an order of magnitude larger than those used by others [4, 5 and 7]. On such a large terrace, the

C_{60} molecule will interact many times with the elbow sites before it meets a step edge. These interactions can reduce the kinetic energy of the C_{60} molecules, thus increase the trapping probability on the elbow sites. If the C_{60} molecule does not meet a step edge during its diffusing life-time, it will be adsorbed on an elbow site. On surface consists of narrow terraces, the C_{60} molecules are expected to diffuse to the step edges and be adsorbed there, like the situations introduced in Chapters 4.

In conclusion, the strong bonding configuration can be achieved at room temperature. It involves the formation of a nanopit under each single C_{60} molecule, which quite possibly consists of 7 missing Au atoms. However, there are certain conditions of forming the strong bonding configuration at room temperature, which require large terraces and high density of elbow site.

7.3 Cluster Nucleation between the Individual C_{60} Molecules

When all the elbow sites are occupied by single C_{60} molecules, further increase of the C_{60} coverage will lead to cluster nucleation. At room temperature, with pre-existing molecules on the elbow sites, the nucleation process of the C_{60} clusters is unusual, in which the clusters prefer to nucleate between two pinched elbow sites and be isolated with the single molecules on the neighboring elbow sites. In comparison, at 46 K, the clusters prefer to nucleate in the rows of bulged elbows and always use the single C_{60} molecule on the elbow site as the nucleation core.

After observing the C_{60} occupation of the elbow sites at room temperature, as shown in Fig. 7.4, more C_{60} molecules are deposited onto the surface with the sample

kept at room temperature. Fig. 7.6 shows an image corresponding to ~0.05 ML C_{60} coverage. The contrast of this image is adjusted to highlight the C_{60} structures. Single C_{60} molecules adsorbed on each elbow site form ordered arrays on the surface. Several domains can be distinguished, because the C_{60} rows on each domain have different directions. As introduced before, the rows of elbows are aligned with one of three equivalent <112> directions of the Au (111) surface. If we regard the direction of the rows of elbows as the orientation of the herringbone pattern, the image in Fig. 7.6 reveals that in an approximate 200 nm periodicity, the herringbone pattern changes its orientation systematically by 120º. As a result, C_{60} rows rotate their direction by 120º, moving from one of the three <112> directions to another. Besides the single C_{60} molecules adsorbed on each elbow site, small clusters are nucleated inside the C_{60} arrays. These clusters are quite uniform in size. In contrast, at 46 K, the cluster size distributes randomly from two molecules to twenty molecules under similar coverage (can compare the images of Fig. 6.4 and Fig. 7.6).

With a closer examination of the surface, the nucleation position for the C_{60} cluster is revealed. Many clusters are nucleated in between two pinched elbow sites and are isolated from the single molecules adsorbed on the neighboring pinched elbow sites, as shown more clearly in the STM image of Fig. 7.7(a), which is taken under the same C_{60} coverage as Fig. 7.6. In this image, alternating blue and green arrows indicate the rows of bulged and pinched elbow, respectively. The clusters along the rows of pinched elbow are exclusively nucleated in between two pre-existing elbow site molecules and do not show any physical connection with

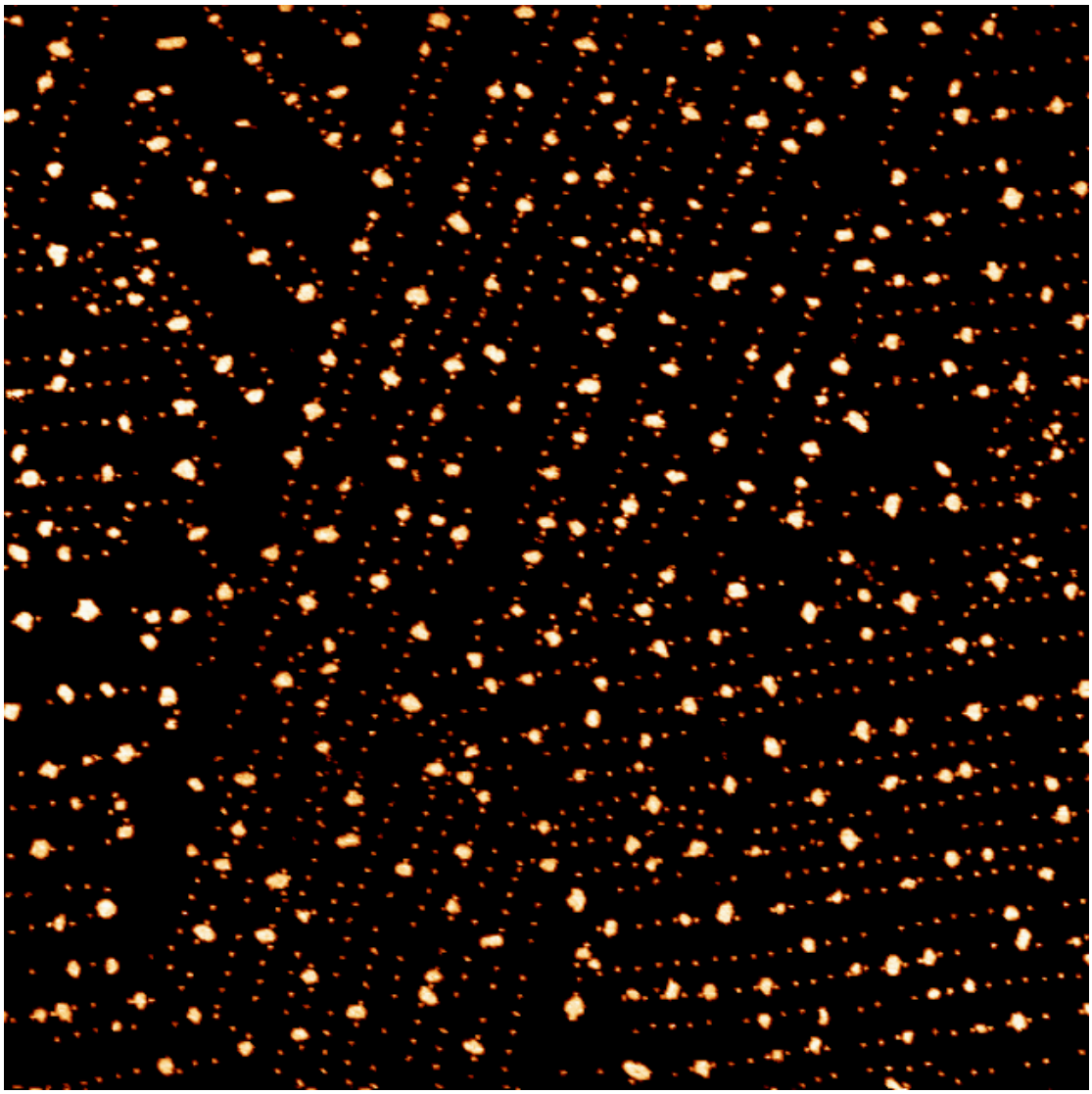

Fig. 7.6: 460 × 460 nm, V = -1.20 V, I = 0.05 nA. STM image of 0.05 ML C_{60} molecules deposited on the Au (111) surface at room temperature. C_{60} rows present three different orientations, which are 120º rotated from each other, and divide the surface to several domains. Along the C_{60} rows, clusters are nucleated. These clusters have uniform size, which is different from the situation at 46 K.

them. This kind of cluster is called α-cluster for clarity. At the same time, along the rows of bulged elbow, the single molecules on elbow sites are swallowed by the clusters, indicating that the clusters are nucleated from the existing elbow site molecules. We call this kind of cluster the β-cluster. In all the 53 clusters in Fig. 7.7(a),

there are 41 α-clusters, while only 8 are β-cluster. The remaining 4 clusters are not nucleated along the C_{60} arrays. Therefore, the nucleation of α-cluster is much preferred by the C_{60} molecules. The above nucleation process is distinctly different from the situation at low temperature. At 46 K, nucleation in the rows of bulged elbows are preferred at early growth stage, and in either bulged or pinched elbow rows, the single molecules pre-adsorbed on the elbow sites serve as nucleation cores for the clusters.

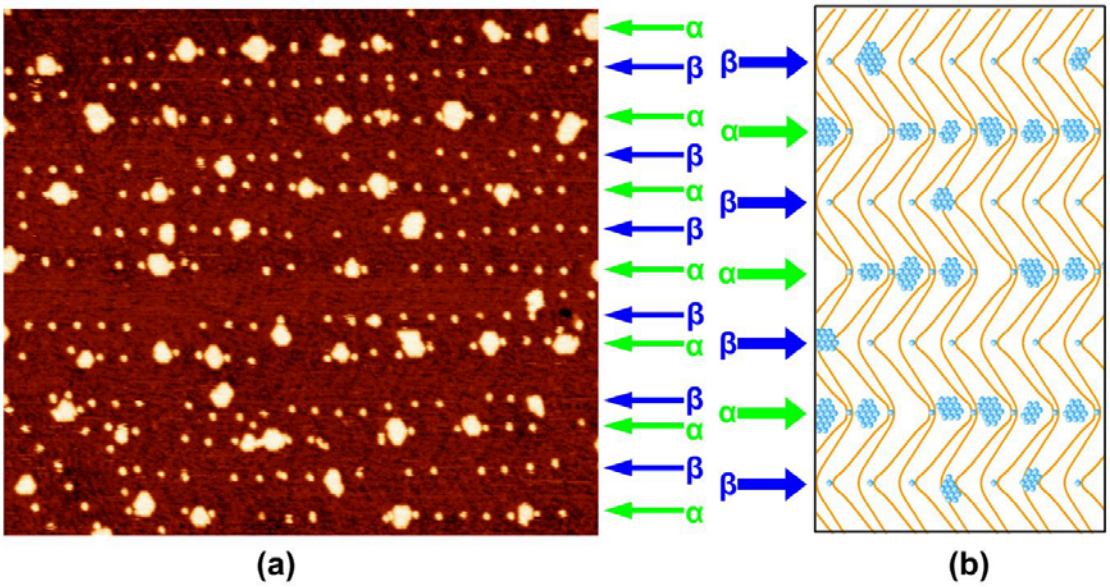

Fig. 7.7 (a): 198.8 × 176.4 nm, V = -1.20 V, I = 0.05 nA. STM image of 0.05 ML C_{60} molecules deposited on the Au (111) surface at room temperature. The rows of bulged elbow are marked by blue arrows, while the rows of pinched elbow are marked by green arrows. Along a row of pinched elbow, the C_{60} clusters are all nucleated in between two elbow site molecules, which are called α-clusters. On the other hand, the clusters in the row of bulged elbow are all nucleated from the elbow site molecules and are called β-clusters. (b): A schematic image indicates the different nucleation positions of the α-cluster and β-cluster. The α-clusters are nucleated in the wide FCC regions between two pinched elbow sites. The single molecules pre-adsorbed on the bulged elbow sites are already in the FCC region, and they serve as nucleation cores for the clusters.

A schematic diagram drawn according to the STM image is shown in Fig. 7.7(b), which shows the nucleation positions observed at room temperature. The α-clusters are actually nucleated in the wide FCC regions between the pinched elbow sites. The β-clusters are also nucleated in FCC regions and they use the single molecules adsorbed on the FCC side of the bulged elbow sites as their nucleation core. Therefore, both the α-clusters and the β-clusters are sitting in FCC regions. Before giving an explanation to the appearance of α-clusters, I would like to briefly recap the nucleation process at 46 K. In that case, all the elbow sites are occupied at first. The single C_{60} molecules adsorbed on the bulged elbow sites are on the FCC side of the DLs, therefore, they have a better opportunity to meet the diffusing molecules and thus serve as nucleation cores. On the other hand, the pinched elbow sites are not favored for the cluster nucleation because the single molecules on pinched elbow sites are in the HCP regions. For room temperature deposition, the diffusing life time of the C_{60} molecule is much longer than that at 46 K, therefore, at any given time, the density of diffusing molecule on the surface is much higher. These diffusing molecules have a higher probability to meet each other, because they are all diffusing along the FCC regions defined by the DLs. When two diffusing molecules meet, they will quite possibly form a dimer and diffuse together due to the strong intermolecular interaction mentioned in the Chapter 5. If more diffusing molecules are added to the dimer, a cluster can be formed without an elbow site molecule serving as a nucleation core. The most favored place on the Au (111) surface for such diffusing cluster to settle down is the FCC region between two pinched elbow sites, here the FCC region

is wide and hence can accommodate large stable clusters. In this manner, the rows of pinched elbows will be in line with a row of clusters, as indeed observed in STM images. Nevertheless, there is still a certain chance for these diffusing clusters to attach to the single molecules on bulged elbow sites. However, the FCC region next to the bulged elbow site is very narrow, because as its name indicated, the DLs at the bulged elbow sites bulge into the FCC region. Therefore, the narrow FCC region next to the bulged elbow site cannot contain diffusing clusters wider than three C_{60} molecules, and clusters narrower than three molecules are not stable at room temperature. Moreover, the above nucleation process can explain the appearance of the 4 clusters in Fig. 7.7(a), which are not aligned with any C_{60} array. They are the clusters diffusing along the FCC regions. In the next chapter, we will see another example of small groups of C_{60} molecules diffusing along the FCC regions in the form of clusters.

When the C_{60} coverage further increases to 0.3 ML, both the α-cluster and the β-cluster will grow larger. The STM image in Fig. 7.8 shows a typical surface of such situation. The α-clusters expand and swallow the neighboring single molecules on pinched elbow sites. Some narrow separated clusters meet each other during their expansion and merge into one large piece. Notably, although the C_{60} islands can be nucleated in the middle of the terrace in this case, the step edges still present strong affinity to the diffusing molecules. Large C_{60} islands can grow from the step edges and co-exist with the island nucleated in the middle of the terrace. Part of such a C_{60} island can be seen on the lower right corner of Fig. 7.8. The detailed behavior of the

C_{60} molecules, clusters and islands at this coverage level will be introduced and discussed in the next chapter.

Fig. 7.8: 768 × 768 nm, V = -1.20 V, I = 0.04 nA. STM image of 0.3 ML C_{60} molecules deposited on the Au (111) surface at room temperature. With higher C_{60} coverage, both the α-cluster and the β-cluster have grown larger. Some neighboring clusters have jointed and formed one large island. A huge C_{60} island grown from the step edge can be seen on the lower right corner of the image.

In conclusion, a strong bonding configuration for the C_{60} molecule adsorbed on the Au (111) surface is revealed in this chapter, in which the single C_{60} molecule sits

on a nanopit formed on the elbow site of the DLs. This bonding configuration has a high bonding strength and it can hold the molecule in the middle of the terrace at room temperature. In contrast, the bond formed between the C_{60} molecule and an intact Au surface at 46 K has low bonding strength and will release the molecule when the temperature is raised beyond ~160 K. The stronger bonding configuration can be obtained in two ways. The first, transferring of the weak bonding configurations formed at 46 K into the strong configuration by increasing the temperature. However, this transformation has a very low probability of success and only happens to a small percentage of all the elbow sites. The second way is that under certain conditions, for example with large Au terraces and a high density of elbow sites, nanopit formation can take place on every elbow site when the C_{60} molecules are deposited at room temperature. In this case, there will be one single C_{60} molecule adsorbed on each elbow site. Cluster nucleation on such a surface also shows unique characteristics. The majority of the C_{60} clusters are nucleated in between two pinched elbows and are isolated with the single molecules on the neighboring elbow sites. These clusters may be formed by the coalescence of diffusing molecules on the FCC regions and still can diffuse as a whole. The wide FCC region between the pinched elbows is the most favored location for these clusters to settle down. Such diffusion behaviors of C_{60} molecules, clusters and island will be discussed in detail in the next chapter.

References

[1] H. Bulou and J. P. Bucher, Phys. Rev. Lett. **96**, 076102 (2006).

[2] W. W. Pai, H. T. Jeng, C. M. Cheng, C. H. Lin, et al., Phys. Rev. Lett. 104, 036103 (2010).

[3] H. I. Li, K. Pussi, K. J. Hanna, L. L. Wang, *et al*., Phys. Rev. Lett. **103**, 056101 (2009).

[4] G. Schull and R. Berndt, Phys. Rev. Lett. **99**, 22105 (2007).

[5] J. A. Gardener, G. A. D. Briggs, and M. R. Castell, Phys. Rev. B **80**, 235434 (2009).

[6] L. Tang, X. Zhang, Q. Guo, Y. N. Wu, L. L. Wang, and H. P. Cheng, Phys. Rev. B **82**, 125414 (2010).

[7] E. I. Altman and R. J. Cotton, Surf. Sci. **279**, 49 (1992).

CHAPTER 8

DIFFUSION AND RIPENING OF C_{60} ON Au (111)

As introduced in Chapter 5, the C_{60} molecules which form the close-packed island along the {100} step of the gold-finger diffused away in 44 hours at room temperature. At low temperatures, the diffusing of C_{60} molecules is also observed. As shown in Chapter 7, when the temperature is raised from 46 K to 180 K and then to 284 K, ripening processes took place as a result of molecular diffusion. In my research, much attention has been paid to study the diffusion behavior of the C_{60} molecules on the Au (111) surface. The results from this study can help us to reach a more comprehensive understanding of the C_{60}/Au (111) system. Two experimental studies are completed in my research in order to examine the diffusion properties at both low temperature and room temperature. The first is the Au (111) surface with C_{60} molecules deposited at 46 K. By raising the sample temperature step by step, the diffusion is gradually activated and the diffusion behaviors at each temperature are revealed. The second is the surface introduced in the previous chapter, on which the single C_{60} molecules occupy each elbow sites of the discommensuration lines (DLs) at room temperature in an ordered array, as shown in Fig. 7.7. C_{60} clusters are nucleated in between the individual C_{60} arrays and stay in the middle of the terrace. These C_{60} structures evolve as a function of time, which reveals the diffusion and island ripening properties of the C_{60} molecules at room temperature. The findings from the above two studies will be introduced in detail in the following two sections, respectively.

8.1 Molecular Diffusion and Island Ripening at ~180 K

As introduced in Chapter 6, when deposited onto an Au (111) surface held at 46 K, single C_{60} molecules will occupy the elbow sites of the DLs and there is no aggregation of molecules at the Au step edges. These single molecules on elbow sites serve as the nucleation cores for subsequent C_{60} clusters. A typical example of such a surface is shown in the STM image in Fig. 8.1. This image is the same as the one shown in Fig. 6.4, of which the contrast is adjusted to show the herringbone pattern, the true size and locations for the C_{60} molecules are indicated by the blue spheres. From this image, we can see that there are more clusters nucleated along the rows of bulged elbows than along the rows of pinched elbows, which is caused by the different structures at the bulged and pinched elbow sites. At the bulged elbow site, the extra row of Au atoms terminates on the FCC side of the DL, therefore, the single molecules adsorbed on the bulged elbow site is on in FCC region. On the other hand, the single molecule is adsorbed on the HCP side on the pinched elbow site. Considering the preferential segregation of deposited C_{60} molecules to the FCC regions, there is higher probability for the single molecule on bulged elbow site to trap diffusing molecules to form a cluster. Furthermore, the shapes of C_{60} clusters in the rows of bulged elbows are defined by the trend of the DLs, as indicated by the blue arrows in Fig. 8.1. At the same time, the C_{60} clusters in the rows of pinched elbows overcome the confinement of the DLs at an early stage of its expansion, as indicated by the green arrows. Occasionally, The cluster nucleated from a bulged elbow site may also expand across the DLs at this C_{60} coverage, like the one marked

by white arrow. The features mentioned above are the key facts that will determine the outcomes of the following diffusion and ripening process.

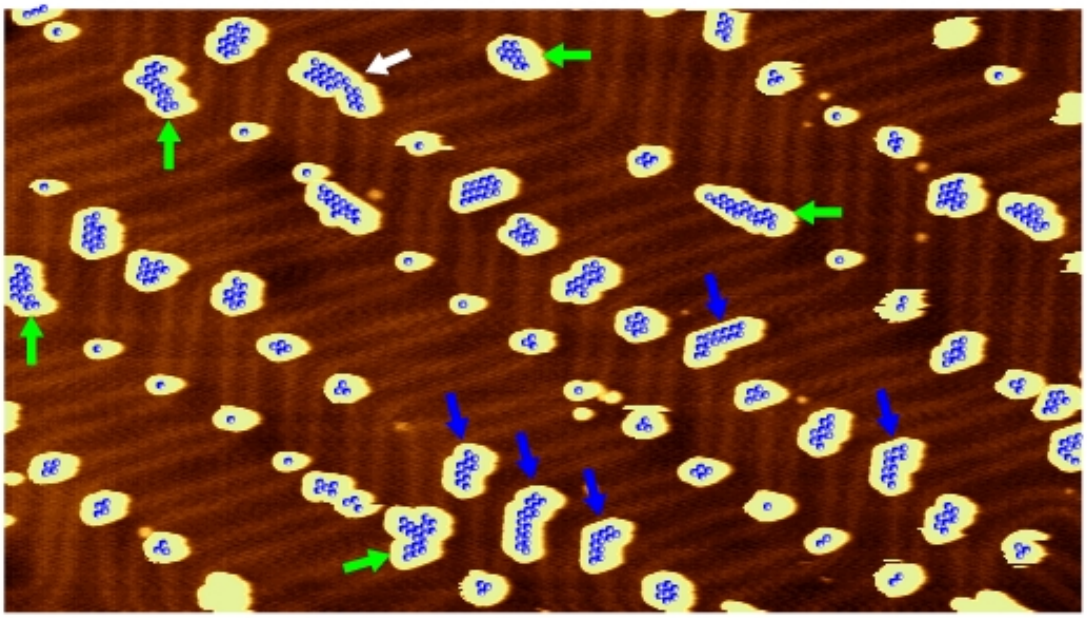

Fig. 8.1: The same image as shown in Fig. 6.4 in the previous chapter. 110 × 60 nm, V = -2.50 V, I = 0.03 nA. C_{60} clusters nucleated on the bulged elbow sites always have a long-narrow shape due to being confined by the DLs. Some examples are marked by blue arrows. Molecules adsorbed at the end of these clusters are easy to lose when temperature is raised. On the other hand, clusters nucleated on the pinched elbow sites expand to the neighboring FCC regions at early stage. The FCC region between two pinched elbow sites is relative wide, thus a large and stable C_{60} adsorption structure can be form there. Occasionally, cluster on the bulged elbow site can also overcome the DL's confine and present a irregular shape, as marked by white arrows.

As introduced in Chapter 7, for a surface with a similar C_{60} structure as shown in Fig. 8.1, if the sample temperature is raised step by step, a ripening process will take place. The single C_{60} molecules trapped on the elbow sites will start to leave at ~160 K. The STM image shown in Fig. 8.2 is taken at 180 K and it shows a number of

changes in comparison to the image shown in Fig. 8.1. I would like to describe the variety of structural changes one by one and discuss the diffusion and ripening properties of the C_{60} molecules revealed by each feature.

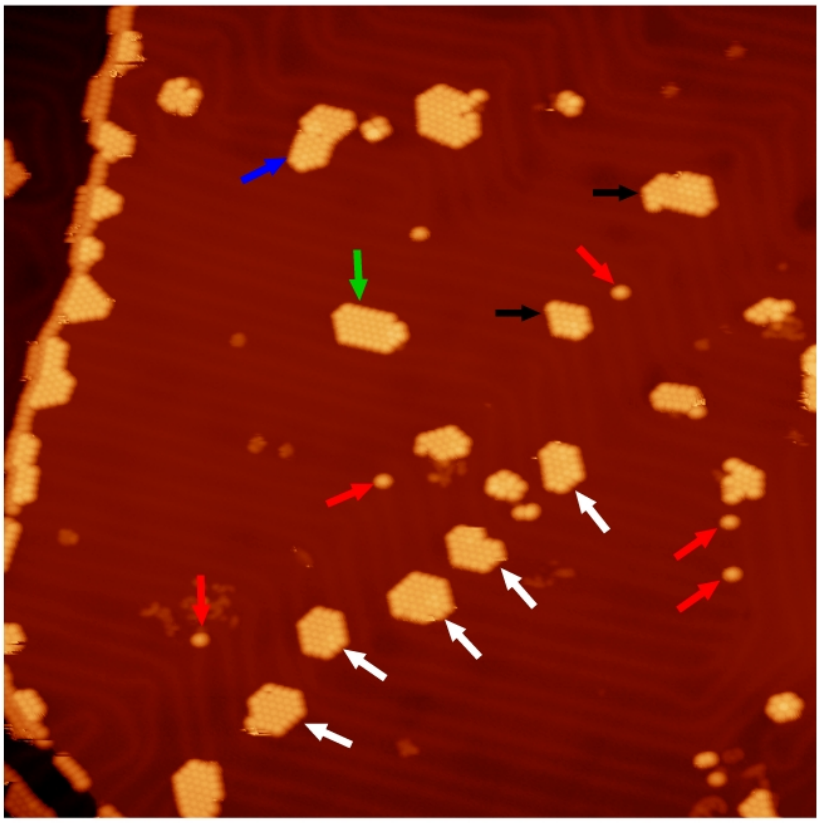

Fig. 8.2: 100 × 100 nm, V = -1.452 V, I = 0.03 nA. The same sample as shown in Fig. 8.1 with the temperature been raised to 180 K. At this temperature, many single C_{60} molecules have diffused away from the elbow sites. Red arrows mark several molecules remaining at the elbow sites. Some molecules diffuse to the step edges and are trapped there. Some molecular clusters used to occupy the elbow sites disappear while the others grow larger, which indicates that a ripening process is taking place. Most remaining clusters are found at pinched elbow sites, as marked by white arrows. The clusters retains at bulged elbow site are marked by black arrows. The green arrow marks a cluster that locates neither on a bulged elbow site nor on a pinched elbow site. The situation of two clusters with different orientations meet and coalescent is marked by the blue arrow.

First of all, the number of single molecules on the terrace is reduced, and there

are a significant number of molecules attached to the step edges. At first glance, we find that the molecules adsorbed on the upper terrace of the step form small close-packed clusters at each FCC regions, which are separated by empty HCP regions. At the same time, the molecules adsorbed on the lower terrace of the step form a continuous molecular line. This difference is caused by the different DL patterns on the upper and lower terraces, respectively. On the upper terrace, the DLs run perpendicularly to the step edge and divide the step edge into alternating FCC and HCP segments. Because of the preferential segregation of C_{60} molecules to the FCC regions of the surface, there are much more molecules diffusing in the FCC regions, C_{60} clusters thus prefer to be nucleated on the FCC segments of the step edge. On the other hand, the DLs on the lower terrace are nearly parallel to the step edge, thus the step edge has its whole length sitting on a uniform FCC stacking second layer. In this case, the formation of a continuous molecular line on the lower terrace of the step edge is preferred. This situation can be compared with the adsorption of C_{60} molecules on the zero-gradient stepped surface (ZGSS) as introduced in Chapter 5. For the gold-fingers of the ZGSS, though no molecules stay on the upper terrace, the different DL patterns associated with the {111} and {100} steps, respectively, lead to the formation of different C_{60} structures on the two kinds of step.

By closely examining the step edges in Fig. 8.2, we find that there are equally amount of C_{60} molecules adsorbed on the upper and lower terraces of the step. This phenomenon is unusual. From the experiment that the C_{60} molecules are deposited onto room temperature Au surface, the molecules are found to preferentially stay on

the lower terrace of the step. As shown in Fig. 5.1 in Chapter 5, the C_{60} island on the upper terrace of the step is nucleated much later than the one on the lower terrace and is much smaller in size, which indicates that the C_{60} molecules diffused to the step edge from the upper terrace prefer to jump across the step and to adsorb on the lower terrace. However, if there is already a C_{60} island formed on the lower terrace, the molecules on the upper terrace need to climb to the top of the island first, which is higher than the upper terrace, after that, they can diffuse to the island rim to settle down. This is a thermally activated process. At 180 K, the molecules do not have enough thermal energy to conquer this height. The diffusion of C_{60} molecules from the upper terrace to the lower terrace can be preserved by the presence of a single row of molecules along the step edge. Therefore, as shown in Fig. 8.2, even amounts of molecules are adsorbed on the two sides of the step.

Now, we turn our attention to the C_{60} clusters remaining on the terrace. As a result of ripening, the density of clusters on the surface in Fig. 8.2 is evidently lower than the density of clusters at 46 K. The straight boundaries of these clusters indicate that edge diffusion is activated at this temperature. Green arrows mark some clusters found in the straight segments of the DLs, which do not cover any elbow site. These clusters may be comprised locally by diffusing molecules, or they are formed somewhere else, most possible an elbow site, and diffused to the present location.

There is another interesting feature in the distribution of the C_{60} clusters in Fig. 8.2. The majority of the clusters on the surface are found on the pinched elbow sites, as marked by the white arrows. This is distinct from the situation observed in Fig.

6.6(c) in Chapter 6, in which the majority of the C_{60} clusters are nucleated on the bulged elbow sites. To explain the difference in the cluster's preferred nucleation locations in these two cases, we need to consider the different formation processes of the C_{60} structures. For the surface shown in Fig. 6.6(c), the C_{60} molecules are deposited onto an Au surface held at 180 K, on which the bulged elbows, compared with the pinched elbows, hold a much larger population of adsorbed single molecules which can serve as nucleation cores, therefore, the nucleation and growth of C_{60} cluster will occur mainly on the bulged elbows. On the other hand, for the situation described in this chapter, there are already clusters nucleated on both the bulged and the pinched elbow sites at a 46 K. When the temperature is raised from 46 K to 180 K, though the potential well associated with the pinched elbow sites is shallower than the one associated with the bulged elbow sites, the clusters nucleated on the pinched elbow sites present higher stability against the increasing thermal energy, which is revealed by the truth that there are much more C_{60} clusters on the pinched elbow sites than on the bulged elbow sites observed in Fig. 8.2.

The stability of a cluster in the ripening process does not solely depend on the bonding strength between the molecules and the substrate, but also depends on the shape of the cluster and the local atomic structure of the substrate. To explain the higher stability of the clusters on the pinched elbow sites, we can look back to Fig. 8.1. As mentioned earlier, at 46 K, the clusters on the bulged elbows sites have a long-narrow appearance, because they follow the trend of the DLs during their growth. Adopting such a shape, the molecules at the end of the cluster have low coordination

number and can easily break away from the cluster when the temperature is raised. Upon the leaving of the molecule at the end, the molecule next to it becomes the new end and thus has high possibility to leave. Lost of the molecules leads to a shrink in size for these clusters, thus the probability of capturing diffusing molecules subsequently gets smaller with the size. In the Ostwald ripening process, if a cluster loses more molecules than it captures, it will shrink and finally disappear. In this manner, the cluster on the bulged elbow site is not stable against the rising temperature. Once the Ostwald ripening process is activated by the leaving of the first molecule, the cluster on bulged elbow site can only get smaller and smaller. At last, the small cluster left on the elbow site will diffusing away as a whole, or the single molecule directly bonded with the defect point introduced by the extra row of Au atoms will be left alone.

On the other hand, there are two reasons for the clusters on pinched elbow sites to retain on the surface when the temperature reaches 180 K. The first reason is the local structure of the DLs around the pinched elbows. The first single C_{60} molecules adsorbed on the pinched elbow site sits on a narrow HCP region. This HCP region is so narrow that when a cluster is formed on the pre-adsorbed C_{60} molecule, the cluster will easily expand to the neighboring FCC region. The FCC region between two pinched elbow sites is the widest FCC region on the Au (111) surface. As introduced in Chapter 4, the C_{60} overlayer can form the most stable structure on an FCC stacking Au surface, because the lattice mismatch will be the smallest. Therefore, after expanding to the wide FCC region, the cluster on pinched elbow site will become

more stable than the one on bulged elbow site, which is adsorbed on a narrowed FCC region between two bulged elbows. The second reason is that the C_{60} clusters on pinched elbow site can obtain an energetically favored hexagonal shape more easily than the one on bulged elbow sites in the ripening process. When a molecule diffuse along the FCC region defined by two DLs and meet a cluster, if the cluster has already expanded across the DLs, the newly arriving molecule can thus overcome the barrier of DL via edge diffusion around the cluster to find the most energetically favoured position to settle down. This situation is more likely to happen to a cluster nucleated from pinched elbow sites, because it overcomes the confine of DLs at early stage of its growth. In comparison, when a diffusing molecule meets the cluster nucleated on bulged elbow site, of which the shape is confined by the two DLs, the only available adsorption position is the end of the cluster. This position is not stable and the molecule can break away easily. Therefore, it is easier for the clusters on pinched elbow sites to develop an energetically favoured hexagonal shape. Compared with a long-narrow shaped cluster on the bulged elbow site, the rim molecules of a hexagonal close-packed cluster on the pinched elbow site are hard to lose, which can help surviving from the ripening process. With all the above characteristics, the clusters nucleated from pinched elbow sites are more stable than the ones on bulged elbow sites against rising temperature.

However, in Fig. 8.2, there are still some clusters retaining on bulged elbow sites, as marked by the black arrows. These remaining clusters on bulged elbow sites could come from the clusters like the one in Fig. 8.1 marked by the white arrow.

Occasionally, the cluster adsorbed on bulged elbow site at 46 K can also overcome the confining DLs and expand to the neighboring HCP region. Therefore, this cluster can also develop a stable hexagonal shape during the ripening process for similar reasons as that for the clusters on pinched elbow site, thus surviving the temperature rise.

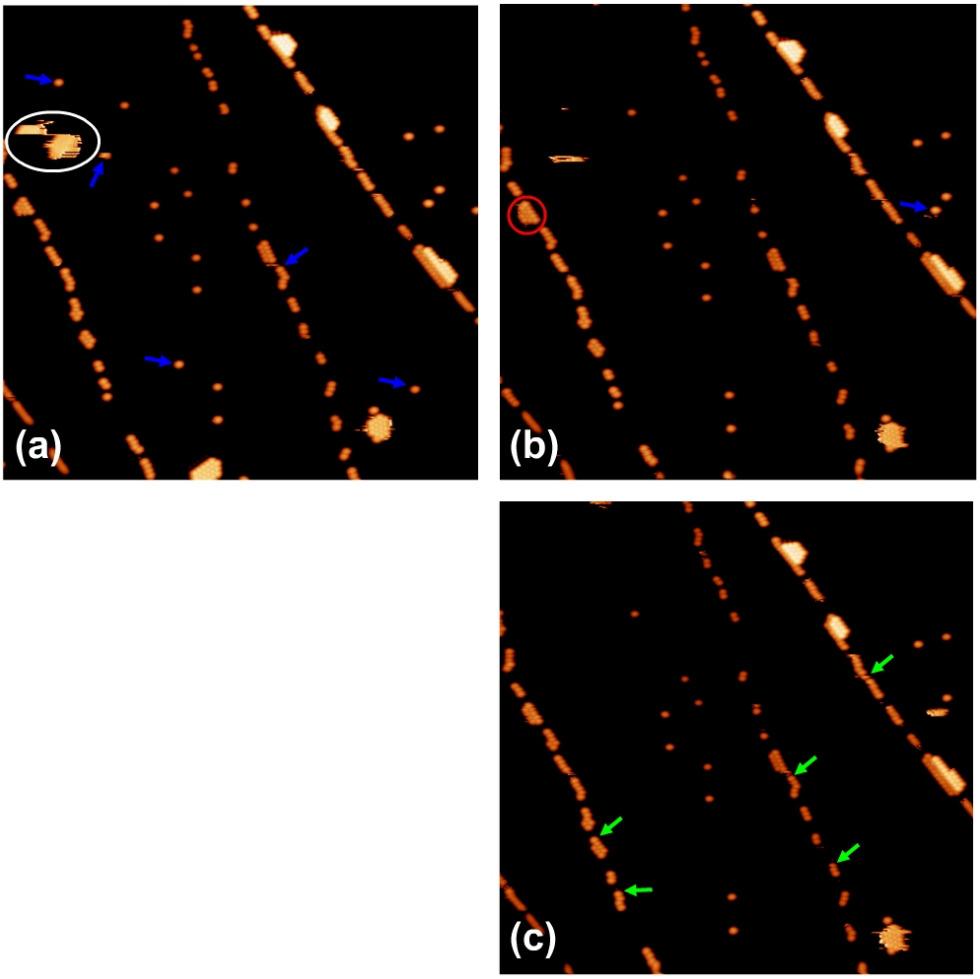

Fig. 8.3: 100 × 100 nm, V = -2.0 V, I = 0.03 nA. Three sequential STM images are taken over the same area at 168 K. The blue arrows indicate the C_{60} molecules that will disappear in the next image, while the molecules newly appear in an image are marked by green arrows. The white circle in (a) marks a C_{60} cluster that is diffusing during the STM scanning, which results in some bright lines along the scanning direction. The red circle in (b) marks a cluster attached to a step, which has firstly grown large by capturing a molecule but then lose two in the next image.

Fig. 8.3 offers us a direct description of the ripening process taking place at ~180

K. The three STM images shown in Fig. 8.3 were taken sequentially over the same area with a ~2 minute interval between each scan. The contrast of these images is adjusted to highlight the C_{60} structures. There are four Au step edges in each image, on which the attached C_{60} molecules form molecular segments. The single molecules and clusters found in the middle of the terraces are exclusively on the elbow sites of the DLs. The step on the farthest right is the only step which has C_{60} molecules adsorbed on its upper terrace and it has more C_{60} molecules attached than the other three, because it is on the edge of a large terrace while the other three steps are next to narrow terraces. From these three images, both the diffusion of individual molecules and the diffusion of a whole cluster can be identified. The blue arrows in Fig. 8.3 indicate the single molecules that will disappear in the next image, while the green arrows indicate the places where a molecule is newly attached in the current image. We can see that five out of six blue arrows are pointed to molecules on the elbow sites and all the five green arrows are pointed to step edge sites, which means that at this temperature, molecules are released from the DL's elbow sites and they will diffuse to the step edges or large clusters. This is consistent with the ripening process described above with Fig. 8.2.

Besides the diffusion of individual molecules, the Smoluchowski ripening, in which the clusters diffuse and coalescent as a whole unit, is also observed. The white circle in Fig. 8.3(a) marks a C_{60} cluster, which is diffusing during the STM scanning. The STM tip drives the cluster to move for some distance, which results in some bright lines in the image. These bright lines have the same apparent height in the STM

image as those immobile clusters. Such features in an STM image is a sign indicating that something is moving under the tip. Moreover, the top half of the cluster is offset with its lower half in the image, which means that the whole cluster has suddenly moved to a new location when the tip is scanning half way across the cluster. In the next image, Fig. 8.3(b), this cluster has diffused away. Only several bright lines are seen on the place where the cluster used to be, indicating that a C_{60} molecule is probably diffusing across there.

The red circle in Fig. 8.3(b) marks a C_{60} cluster attached to an Au step edge. Compared with the previous image, this cluster has captured an extra molecule thus grows bigger. However, in the next image, two molecules are found to have left this cluster. Such phenomenon indicates that during the Ostwald ripening process, the clusters are in dynamic equilibrium. C_{60} molecules can be either captured or released by the rim of the clusters. Therefore, the balance between capturing and releasing molecules determines whether the cluster would grow or shrink in the process. Normally, larger clusters, in which the rim molecules only take small proportion in the total number of the molecules in the cluster, will survive in an Ostwald ripening process.

8.2 Diffusion Behavior at 280 K

In the previous chapter, as shown in Fig. 7.7, on a surface with all the DL's elbow sites being occupied by single C_{60} molecules at room temperature, the following nucleation of C_{60} clusters does not use these single molecules as nucleation cores.

Instead, the clusters are predominantly found between two pinched elbow sites. In order to explain this phenomenon, I proposed that these clusters are formed by the aggregation of diffusing C_{60} molecules in the FCC regions defined by the DLs. In this cluster formation model, the C_{60} molecules will preferentially segregate to the FCC regions after landing on the surface, which leads to a high density of diffusing molecules in the FCC regions. Such preferential segregation of deposited molecules to the FCC region is a common phenomenon on the Au (111) surface [1-3]. When one diffusing C_{60} molecule meat another, a dimer will be formed. By adding more molecules, clusters can be formed in the FCC regions. Therefore, these clusters do not need the single C_{60} molecule adsorbed on the elbow site to serve as nucleation core, and they may still have the ability to diffuse. In this section, the diffusion behavior of the C_{60} molecules is carefully studied, which can provide evidence supporting the above cluster formation model.

For the surface shown in Fig. 8.2, if the sample temperature is further raised, as introduced in the previous chapter, the ripening process will lead to a clear Au surface with most of the C_{60} molecules attached to step edges and a small number of large C_{60} islands remaining on the terraces, as shown in Fig. 7.3. However, before achieving that state, an interesting feature is observed. The STM image in Fig. 8.4 is taken when the sample temperature is raised to 280 K. The landscape in this image is distinct from the one shown in Fig. 7.3, which is taken at a similar temperature, 284 K. As a reason for the difference, the images in Fig. 8.4 and Fig. 7.3 are taken over different areas of

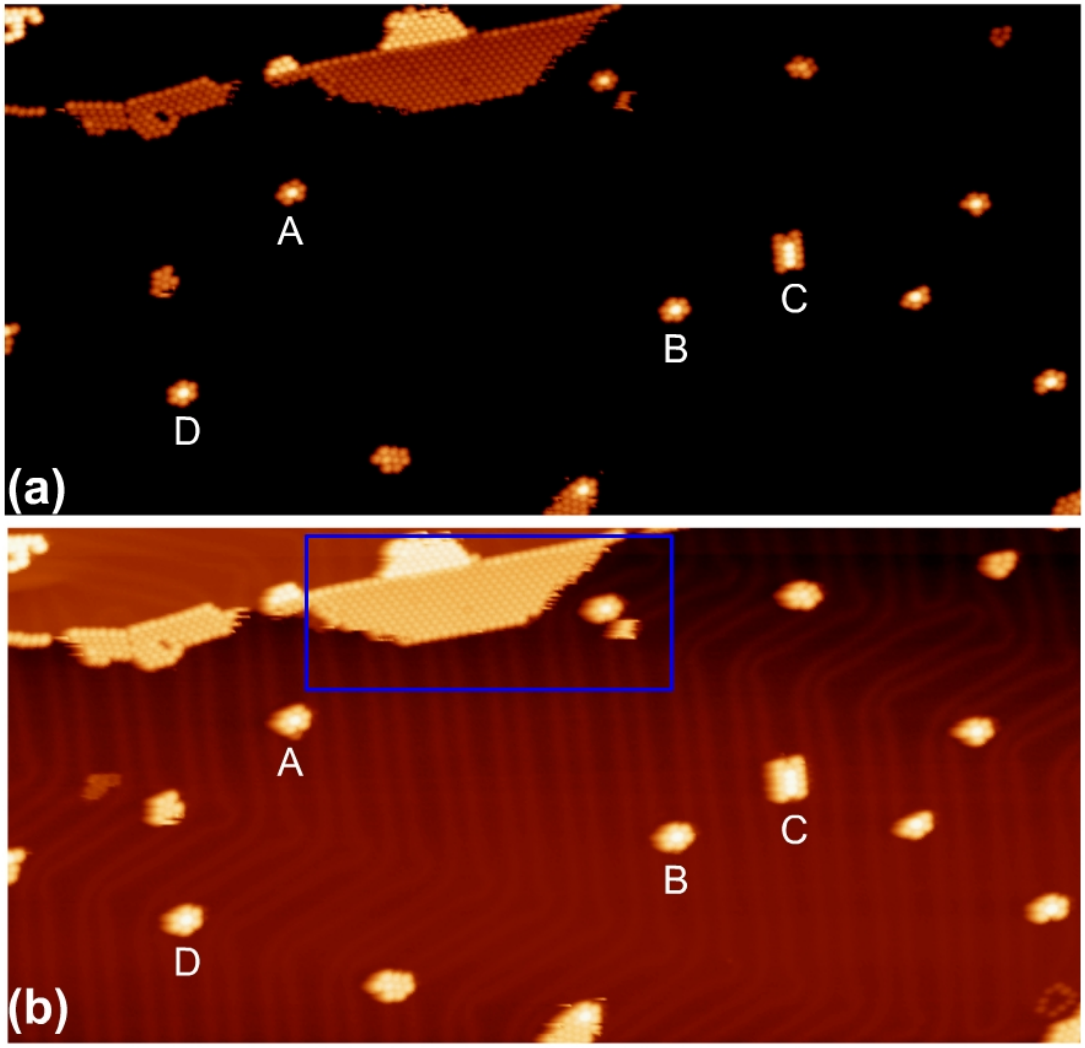

Fig. 8.4: 65.3 × 67.2 nm, V = -1.4 V, I = 0.03 nA. (a) and (b) are the same STM image, which is taken over the same sample (different areas) as the one shown in Fig. 8.2. The image is taken when the temperature reaches 280 K. The contrast of the image is adjusted to highlight the C_{60} intermolecular structure (a) and the substrate herringbone pattern (b), respectively. Three C_{60} clusters in the straight FCC regions are marked as "A", "B" and "C", while a cluster in between two pinched elbow sites are marked "D". These clusters will be discussed in derail and shown again in Fig. 8.5. The area marked by the blue rectangle will also be shown again in Fig. 8.6 for some detailed discussion.

the sample. The ripening process is at different stages on these two locations due to their different local environment. The surface shown in Fig. 8.4 is at an earlier

ripening stage than the surface shown in Fig. 7.3, though the temperatures at which they are imaged is differ by only 4 K.

As shown in Fig. 8.4, many C_{60} molecules are attached to the Au step edges and form relative large C_{60} islands there. On the largest island, three dim molecules, which indicate the formation of nanopit in the substrate atomic lattice, can be seen. Moreover, a small island on the upper terrace of the step is formed. These features are similar to what is shown at a latter ripening stage, as shown in Fig. 7.3. However, a great difference is found on the terrace. Neither single C_{60} molecules nor large islands are seen on the terrace in Fig. 8.4. Instead, many small clusters are distributed there. Different from the small clusters seen at 46 K, which have a wide distribution in size, the small clusters in Fig. 8.4 have a uniform size. In fact, there is a basic unit for these clusters, which consists of seven close-packed C_{60} molecules with the molecule in the centre appearing brighter. The majority of the clusters in Fig. 8.4 adopt this configuration, while some other clusters are formed by adding (or missing) one or two molecules to (or from) this basic unit. Most impressively, about half of all these clusters are not on the elbow sites of the DLs but in the middle of a straight segment of the DLs. On the other hand, most of the elbow sites are empty. The large clusters used to occupy the elbow sites at 180 K, as shown in Fig. 8.2, cannot be seen in this image. Base on the above observation, we can conclude that at this stage of ripening, due to the relative high temperature, large number of C_{60} molecules is released from the elbow sites or from the rim of C_{60} clusters. These released C_{60} molecules preferentially segregate to the FCC regions and diffuse along them. Such situation is

similar to the room temperature deposition, which will also result in a high density of diffusing molecules in each FCC region. The diffusing molecules will thereby aggregate to form clusters in the FCC regions and these clusters do not necessarily locate on an elbow site.

Compare the situation shown in Fig. 8.4 with the situation of room temperature deposition which is shown in Fig. 7.7, though the formation mechanism of the clusters is the same, the destinations of these diffusing clusters are different. In the former situation, the clusters will finally diffuse to Au step edges or join large C_{60} islands, in order to complete the ripening process. However, in the latter situation, the cluster will go to the elbow sites, becoming either a α-cluster between two pinched elbow sites or a β-cluster attached to a bulged elbow site. The reason behind this difference is the existence of single C_{60} molecules on each elbow site. In the former situation, the single molecules used to occupy the elbow sites have already diffused away during the temperature rise, while in the latter situation, all the elbow sites are occupied by single molecules. Therefore, the single C_{60} molecules pinned on each elbow site in the latter situation seems to play a key role in the determination of the destination of the diffusing clusters. As introduced in the previous chapter, these single C_{60} molecules on the elbow sites are adsorbed in nanopits formed underneath in the Au surface layer. The presence of the molecule and the induced rearrangement of substrate atoms can prevent the diffusion of the clusters. As a result, if all the elbow sites are occupied by single molecules, the clusters will be confined around the elbow sites, giving a landscape as shown in Fig. 7.7. On the other hand, without these single molecules on

the elbow sites, the clusters can diffuse and thus complete the ripening process. Besides retaining the clusters in the middle of terrace, the single C_{60} molecules pinned on elbow sites can also slow down the ripening process at room temperature, which will be introduced in next section.

Now, we can take a close look at the C_{60} clusters shown in Fig. 8.4(a). Obviously, these clusters have a magic number of seven. The seven C_{60} molecules form a close-packed configuration with one molecule in the centre and six molecules surrounding it. This structure is stable as all the six rim molecules have the same coordination number of three. Moreover, zoomed-in images of the three clusters marked as “A”, “B” and “C” in Fig. 8.4 are shown in Fig. 8.5(a) and (b). We can see that the size of seven-molecule cluster perfectly fits to the width of the FCC region defined by two parallel DLs. If measured between the bottoms of the DLs, the width of the FCC region is ~2.5 nm, which can contain cluster no more than three molecules wide. For the cluster C, which consists of 14 molecules, it adopts a rectangular shape with the long axis parallel to the DLs. In this way, its width will not exceed the width of the FCC region. Such a structure of the cluster C indicates that the construction of a cluster by diffusing C_{60} molecules is confined by the DLs. However, there is one place on the Au (111) surface that the C_{60} cluster can grow larger without overcoming the barrier of the DLs. That is the wide FCC region between two pinched elbow sites, which is ~4.2 nm wide. As shown in Fig. 8.5(c), this wide FCC region can contain a seven-molecule cluster (cluster D) with spare space for more molecules. Therefore, the wide FCC region between the pinched elbow sites is an ideal place for the clusters

to settle. Furthermore, if the cluster captures some diffusing molecules when stays in the wide FCC region, it will become too large to diffuse along the straight FCC region, and it will be retained there. This behavior is another reason for the majority of the clusters in Fig. 7.7 to be found in the wide FCC regions between two pinched elbow sites. On the surface as shown in Fig. 8.4, if a cluster becomes larger than seven molecules and be confined in the wide FCC region, it can release molecules one by one to complete the ripening process. However, as mentioned earlier, the ripening process is slowed down by the presence of single molecules on each elbow sites. Thus for the surface shown in Fig. 7.7, the clusters confined between the pinched elbow sites will stay there much longer.

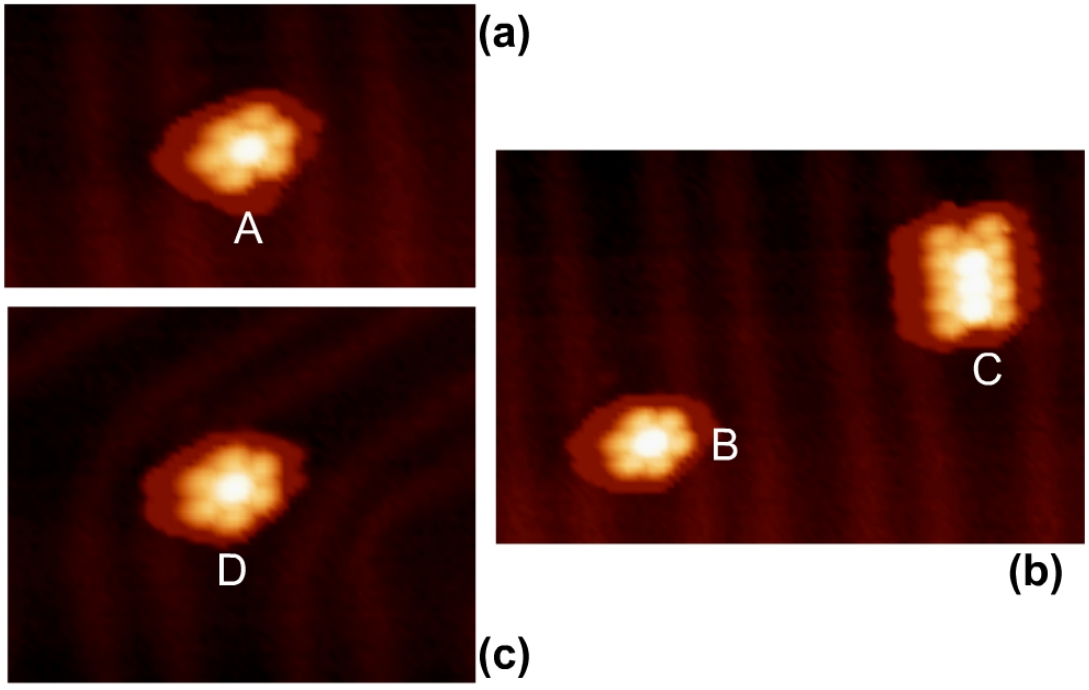

Fig. 8.5: Three zoomed-in images show the four C_{60} clusters marked by "A", "B", "C" and "D" in Fig. 8.4. (a): 16.4 × 9.8 nm. (b): 23.2 × 15.5 nm. (c): 16.4 × 13.1 nm. Cluster A, B and C are in the straight FCC regions. Their size is confined by the DLs. The wide FCC region between two pinched elbow sites can offer more space for the cluster to grow, as shown in (c).

The most prominent character of a seven-molecule C_{60} cluster in STM image is the brighter centre molecule. The area in Fig. 8.4 marked by the blue rectangle is shown in Fig. 8.6(a) with two height profiles taken along the blue line and the green line, respectively. The blue line runs across the C_{60} islands on both the upper and lower terraces of an Au step edge and a seven-molecule cluster. Its height profile is shown in Fig. 8.6(b). The C_{60} islands on the upper terrace is ~2.3 Å higher than the island on the lower terrace, the height difference is consistent with the height of a monoatomic step on the Au (111) surface. The C_{60} molecules in the island are ~6.6 Å high from the Au surface. In the C_{60} cluster, the centre molecule is 8.9 Å high from the Au surface, which is as high as the molecules adsorbed on the upper terrace of the step. The molecules surrounding the centre molecule appear as shoulders in the height profile, as shown in Fig. 8.6(c). The height of these surrounding molecules is ~7 Å, which is 1.9 Å lower than the centre molecule and roughly equal to the molecules in the island on the lower terrace. Due to the same height of the centre molecule in a cluster and the molecules on the upper terrace of a step, it is reasonable to reason that the higher appearance of the centre molecule is due to an Au atom trapped in the C_{60}/Au interface. There are many Au atoms diffusing on the surface, which is released from the area covered by the C_{60} islands. As introduced before, the C_{60} islands can lift the reconstruction of the substrate, the contracted Au surface thus becomes a 1×1 lattice, which will release the extra Au atoms. The diffusing Au atom may act as a nucleation core to collect diffusing C_{60} molecules. A molecule-atom dimer will be formed when the Au atom bond with the first C_{60} molecule, then, a cluster can be

formed by adding more diffusing C_{60} molecules to the molecule-atom dimer. The molecule-atom dimer seems to have a stronger affinity to the captured diffusing molecule than a normal member in the cluster, because the molecule-atom dimer is always found in the centre of a cluster. Due to the Au atom underneath, the centre molecule is ~1.9 Å higher than the other molecules in a cluster. As mentioned in Chapter 4 with the image in Fig. 4.8, in a C_{60} island formed on the Au (111) surface, there are occasionally a molecule appears ~1.2 Å higher than the surrounding molecules. These higher molecules may sit on Au atoms that did not diffuse out of the island-covered region. This situation is similar to what happened to the clusters seen here. Furthermore, the height differences between the brighter molecule and the surrounding molecules measured in Fig. 8.6 (1.9 Å) and in Fig. 4.8 (1.2 Å), respectively, is proportional to the island height measure in the two cases (6.6 Å to 4.4 Å). However, there is another possibility for the higher appearance of the centre molecules that is the electronic effect in STM imaging. The image shown in Fig. 8.4 is recorded with a sample negative bias of -1.4 V, which is close to the location of the HOMO in the C_{60}/Au (111) system [4, 5]. If the C_{60} cluster's HOMO has a high density of states on the centre molecules, the centre molecule will apparent brighter in the image. In this case, the centre molecule is not necessarily geometrical higher. However, there is an observation that does not support the electronic effect hypothesis. Not every centre molecule is brighter. The Most significant example is in the cluster C in Fig. 8.5. There are four centre molecules in the cluster, while only three of them are bright. The centre molecule on the top has the same apparent height as the

surrounding molecules. Base on above discuss, the brighter appearance of the centre molecule should be caused by an Au atom trapped at the C_{60}/Au interface.

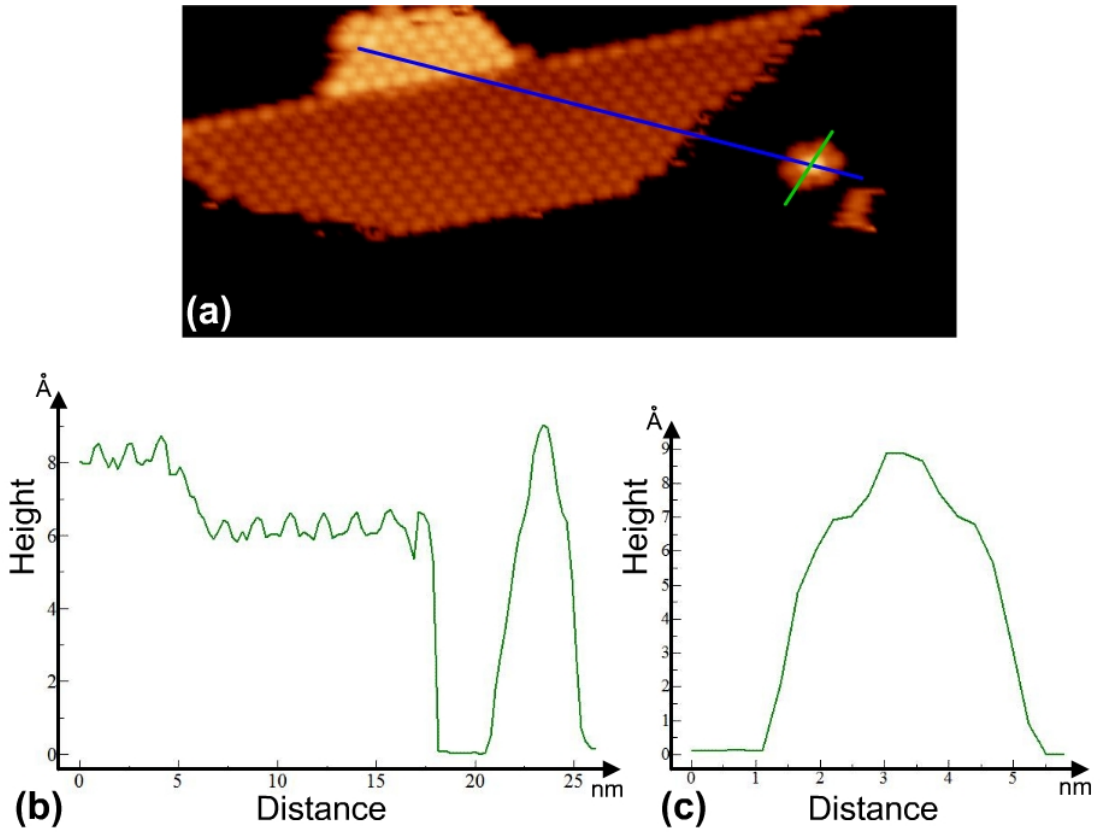

Fig. 8.6 (a): 39.4 × 9.8 nm. A zoomed-in image of the area marked by the blue rectangle in Fig. 8.4. Two height profiles are taken, along the blue line (b) and green line (c), respectively.

In this section, the diffusing phenomenon observed at 280 K is introduced. With a high density of diffusing C_{60} molecules in the FCC regions of the surface, clusters with a magic number of seven are formed by the aggregation of diffusing molecules. These clusters may either diffuse to attach to the Au step edges or diffuse to adsorb on the elbow sites, depending on whether there are single molecules pinned at each elbow site. Furthermore, Au atoms trapped at the molecule-substrate interface cause a bright appearance of the centre molecules of the clusters.

8.3 Diffusion and Ripening Processes at Room Temperature

For the surface with single C_{60} molecules and clusters adsorbed along the rows of elbows at room temperature, as shown in Fig. 7.7, ripening process is also observed. However, the speed of the ripening process is even slower than what is observed at low temperature. The single C_{60} molecules, which are strongly bonded on the elbow sites by nanopits, may act as decelerator for the diffusing of the molecules and clusters, thus slow down the ripening process. Therefore, noticeable change of the C_{60} structures usually happens in a day's time. Nevertheless, if more C_{60} molecules are deposited onto the surface to achieve a similar coverage as shown in Fig. 7.8, the ripening process will become more evident in relatively small timescale. The image in Fig. 8.7 presents a similar landscape as the one in Fig. 7.8. The C_{60} coverage in this image is ~0.3 ML. Similar to the situation observed at low temperature, both Ostwald ripening and Smoluchowski ripening occurs on the surface. The former is achieved by the exchange of molecules between the C_{60} clusters and island, while the later is achieved by the coalescence of clusters.

As shown in Fig. 8.7, most of the elbow sites of the DLs are occupied by either single C_{60} molecules or clusters. The C_{60} coverage on this surface is higher than that on the surface shown in Fig. 7.7, and the clusters seen here are larger and have overcome the DL's confinement. The DLs on the surface bend with higher frequency on the upper part of the image than on the lower part. As a result, the density of C_{60} molecule and cluster is higher on the upper part. On the lower part, there are long segments of straight DLs. Therefore, many clusters on these straight DLs do not cover

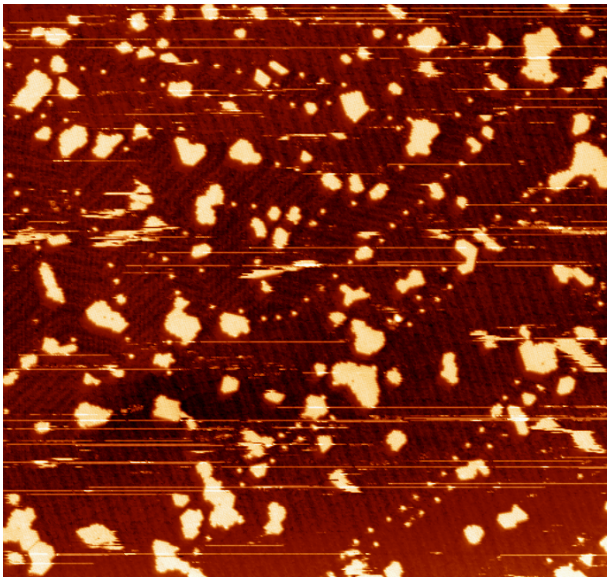

Fig. 8.7: 238.6 × 225.9 nm, V = -1.2 V, I = 0.03 nA. The Au (111) surface shown in this image has the similar C_{60} coverage as the surface shown in Fig. 7.8. Both Ostwald ripening and Smoluchowski ripening processes are observed on this surface.

any elbow site. However, all the single C_{60} molecules are exclusively found on the elbow sites. By comparing several images which are taken continuously on this surface, as shown in Fig. 8.8, an evolution of the C_{60} molecular structure can be identified. Single molecules are adding to (or losing from) the clusters between images. On the other hand, clusters themselves are appearing or disappearing between images. These phenomena could be a tip-sample effect that the molecules are drawn to migrate by the scanning tip. Also, there is another possibility that these molecular movements are the evidence of Ostwald ripening or Smoluchowski ripening processes, which are taking place on the surface.

The three images in the left column of Fig. 8.8 are recorded sequentially over the same area. The time separation between the captures of two succeeding images is ~2 minutes. Single C_{60} molecules are added to the clusters one by one, which is a symbol

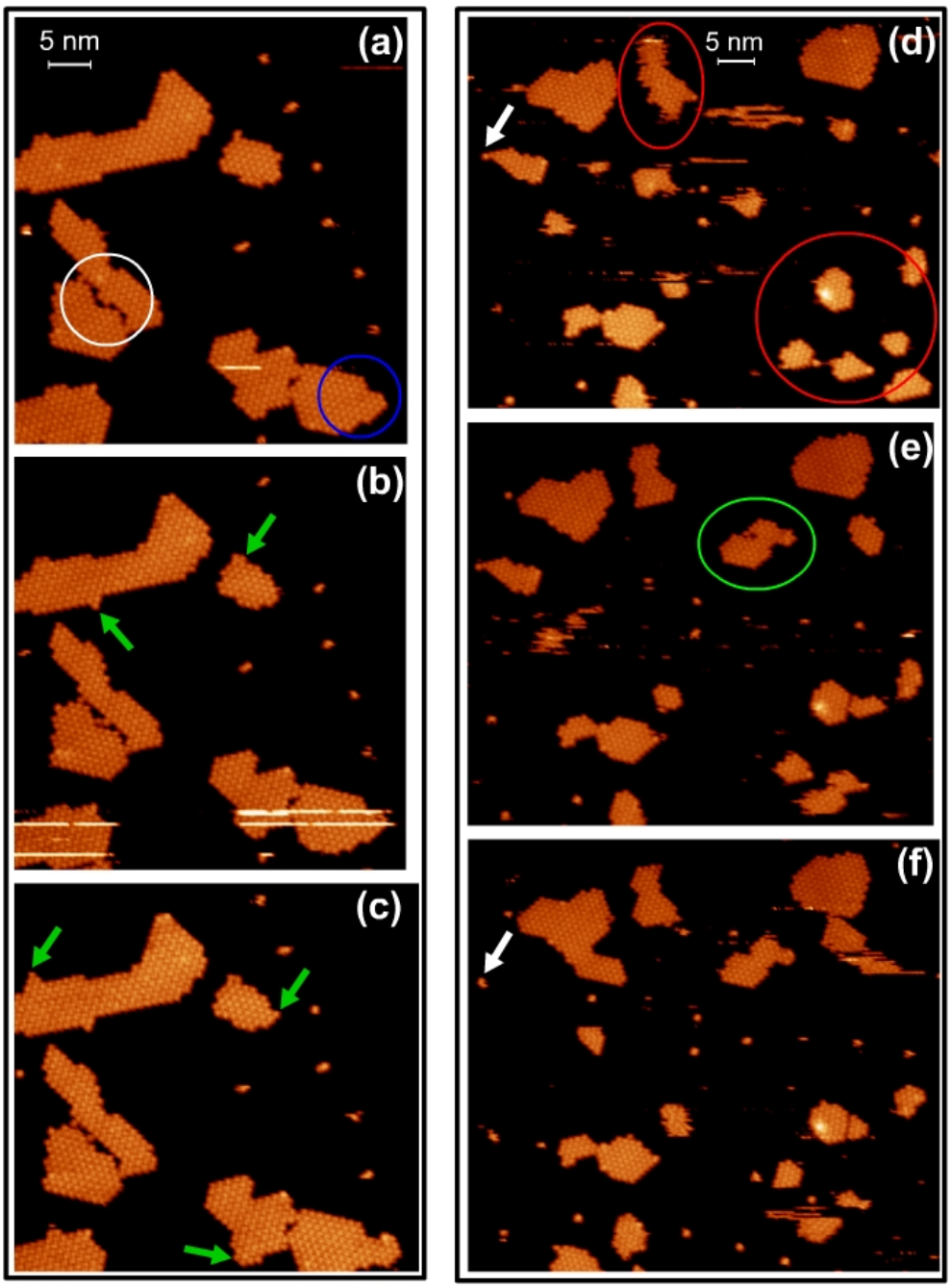

Fig. 8.8: Zoomed-in images of the surface shown in Fig. 8.7. All recorded with V = -1.2 V, I = 0.03 nA. The (a), (b) and (c) are three images recorded sequentially over the same area. The green arrows indicate the C_{60} molecules that newly join the cluster in the current image. The white circle marks a domain boundary between two clusters. The blue circle marks an edge of a cluster where large number of molecules is attached. The (d), (e) and (f) are three images recorded sequentially over another area. In this area, the C_{60} clusters diffuse and coalesce as whole units, as marked by the red and green circles. The white arrow indicates a cluster, which leaves a single molecule pinned on the elbow site when it diffuses away.

of the Ostwald ripening. The green arrows in these images indicate the molecules that are newly attached to the clusters in the current image. The blue circle marks an area where relatively a larger number of diffusing molecules are trapped. If a line is drawn linking the row of single molecules on the upper right part of the image, we can find that the blue circle will be crossed by the line, which means that the area marked by the blue circle is an elbow site. Therefore, the elbow sites are found to be the preferred location for the clusters to expand during the ripening process, probably because the elbow sites have strong affinity to the diffusing molecules. The white circle marks a domain boundary formed by two C_{60} clusters with different orientations. In the three sequential images, two molecules on the domain boundary keep on changing their positions, indicating that edge diffusion is activated under the current condition. The edge diffusion leads to a regular hexagonal shape of the clusters.

Besides the exchange of molecules one by one, the ripening is also taking place in a more efficient way, which is the diffusion and coalescence of the whole clusters. The three images in the right column of Fig. 8.8 are also sequentially recorded over the same area. The time separation between the captures of each two images is the same as above, which is ~2 minutes. However, the structural changes observed in the right column are much more dramatic than that in the left column. The two red circles in Fig. 8.8(d) mark two areas, where the diffusion and coalescence of clusters are evident. The green circle in (e) marks a cluster, while in (d), at the location of this cluster, there is a blurry structure. This structure looks like a cluster that is diffusing during the scanning. After the recording of the first image, it stops diffusing and

settles down. Therefore, in the next image, it presents as an adsorbed cluster. Such a diffusing cluster presents the same apparent height as a still C_{60} cluster in the same image, indicating that this kind of diffusing clusters does not desorb from the surface. However, they have lost the registration with the substrate surface, thus can move laterally across the terrace. Therefore, it is consistent with the description of the 2-dimensional gas phase C_{60} structure on the Au (111) surface in the Section 2.5.4 in the literature review. Also in that chapter, S. Guo *et al*. [6] reported that in ambient environment, on the surface with adsorbed C_{60} submonolayer, ~80% of all diffusing molecules diffuse in the form of clusters. This observation is also consistent with our finding under UHV condition.

There is a C_{60} cluster marked by a white arrow in (d), which diffuses away in the following images. However, as marked by the white arrow in (f), the cluster leaves a single molecule on the elbow site. Such behavior indicates that the molecule on the elbow site is stronger bonded to the substrate than the other molecules in the same cluster. To certain extent, these stronger bonded C_{60} molecules can retain the clusters during the ripening process, thus slow down the ripening speed. As mentioned earlier, the presence of elbow site molecules makes the ripening speed at room temperature even slower than what is observed at low temperature on a surface without elbow site molecules.

The ripening process always leads to fewer and larger islands on the surface. However, the C_{60} clusters adsorbed in the middle of a terrace on the Au (111) surface will not become very large, because during the ripening process, the C_{60} islands grow

from Au step edges present much stronger affinity to the diffusing molecules and clusters. Even at a very high C_{60} coverage, the size of the clusters on the terrace is confined under certain limit. At the same time, the islands nucleated from step edges can grow very large. On the surface shown in Fig. 8.9(a), the C_{60} coverage is as high as 0.5 ML. Two huge C_{60} islands grow from left and right respectively to the centre of the image, on which the second layer C_{60} structure are formed. The second layer C_{60} islands present an irregular dendritic shape, indicating that the edge diffusion is restricted on the top of the first C_{60} layer. On the Au terrace, the single C_{60} molecules and clusters can be still seen. Comparing with the surface shown in Fig. 8.7, the C_{60} clusters have grown larger, as a result of ripening. However, the enlargement is not evident, because the majority of the diffusing molecules and cluster are attracted by the huge islands grown from the step edges. As shown in Fig. 8.9(a), in a certain distance from the edge of the huge island, neither single molecules nor clusters can be seen. In other words, there is a blank region around these huge islands. All the molecules and cluster in the blank region or diffused into the blank region will be attracted and captured by the huge island. The width of the blank region seen in Fig. 8.9 is 30~60 nm.

As shown in Fig. 8.9, along the edge of the huge island, there are many C_{60} clusters attached. These clusters used to rest in the blank region or diffusing across the surface. As a result of the ripening process, they are captured by the huge island. However, instead of merging into the huge island, these clusters are separated with the huge island by a narrow boundary. Two reasons may explain the presence of the

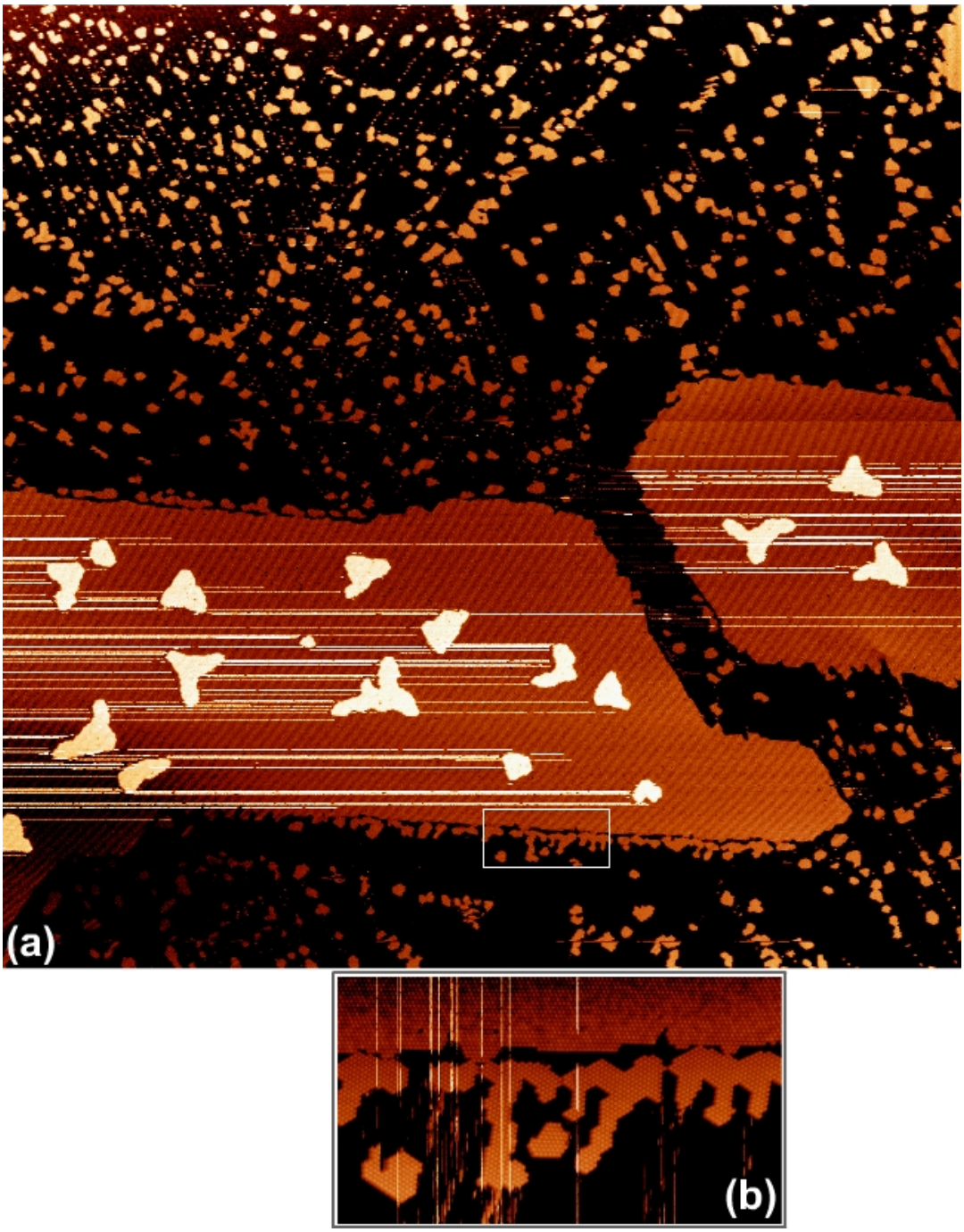

Fig. 8.9 (a): 768 × 768 nm, V = -1.3 V, I = 0.04 nA. A surface with ~0.5 ML C_{60} coverage. Two huge C_{60} islands can be seen, on which the second C_{60} layer is formed. On the Au terrace, the C_{60} single molecules and clusters are still there. However, the single molecules and clusters in a 30~60 nm distance from the edge of the huge islands are exclusively attracted and captured by the huge island, leaving a blank region around the islands. (b): 99.4 × 55.1 nm, V = -1.3 V, I = 0.04 nA. A zoomed-in image of the area marked by the white circle in (a). The clusters captured by the huge island are separated with the island by a narrow boundary.

boundary. The first is the reconstruction pattern of the Au (111) surface. As introduced in Section 2.5.3 in the literature review, in front of a C_{60} island, the DL deviates from its natural contour and forms a close loop to enclose the island. As shown in Fig. 8.10(a), a single DL runs parallel with the edge of the C_{60} island, while on the other side of the single DL, other DLs form U-shape ends. This herringbone structure is similar to the one in front of a {100} step of the gold-finger, which is introduced with Fig. 5.5 and Fig. 5.6 in Chapter 5. As demonstrated there, if C_{60} molecules want to join the growth front of the island, they must lift the substrate reconstruction and push the DLs backwards. For a whole C_{60} cluster to merge into the molecular lattice of the huge island shown in Fig. 8.9(a), it requires the rearrangement of a large number of Au atoms simultaneous, which is not energetically favored. Therefore, the DLs act as barriers that separate the clusters with the huge island. The second reason is the molecular mismatch between the cluster and the huge island. As shown in Fig. 8.10(b), the cluster may present different orientation with the huge island. If the cluster wants to merge into the huge island, a rotation is required, but such lateral movement is always restricted by the presence of other clusters.

Although there are barriers separate the C_{60} clusters with the huge island, if the time is long enough, we can still observe the coalescence of the clusters and the island. The images in Fig. 8.11 are recorded over the lower edge of the huge island shown in Fig. 8.9. Each of the image is comprised by four STM images, showing a continue contour of the island edge. From the three sequential images, which are taken with long interval, the evolution of the island edge can be seen. In each image, the contour

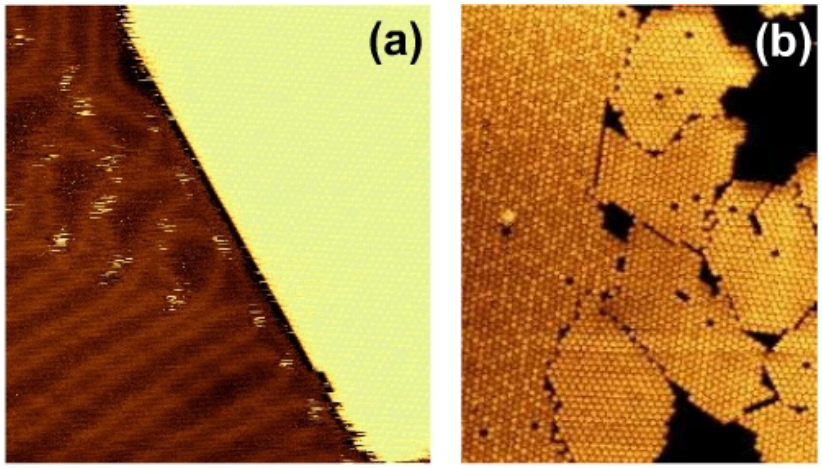

Fig. 8.10 (a): 60 × 60 nm, V = -1.5 V, I = 0.04 nA. The herringbone pattern in front of a C_{60} island. (b): 48 × 60 nm, V = -1.2 V, I = 0.028 nA. There is always a mismatch between the clusters and the huge island.

of the edge is different. Meanwhile, the distribution of individual clusters near the island is different. The above observations indicate that the clusters captured by the island will gradually merge into the island and new clusters keep on being captured, though the process progresses very slowly.

In order to reveal how the C_{60} molecules in the captured cluster overcome the barriers to merge into the huge island. The boundary between the cluster and the huge island is studied in derail. Two sequentially recorded images are shown in Fig. 8.12, which reveal the changes happened on the boundary. Some structural changes are highlighted by red circles in Fig. 8.12. The general trend of the structural change is that the molecules are moving from the clusters towards the huge island. These molecular movements could be driven by the scanning tip. However, because the trend of the structure change is consistent with the ripening process indicated by Fig. 8.11, in which the C_{60} clusters are gradually merging into the huge island, the

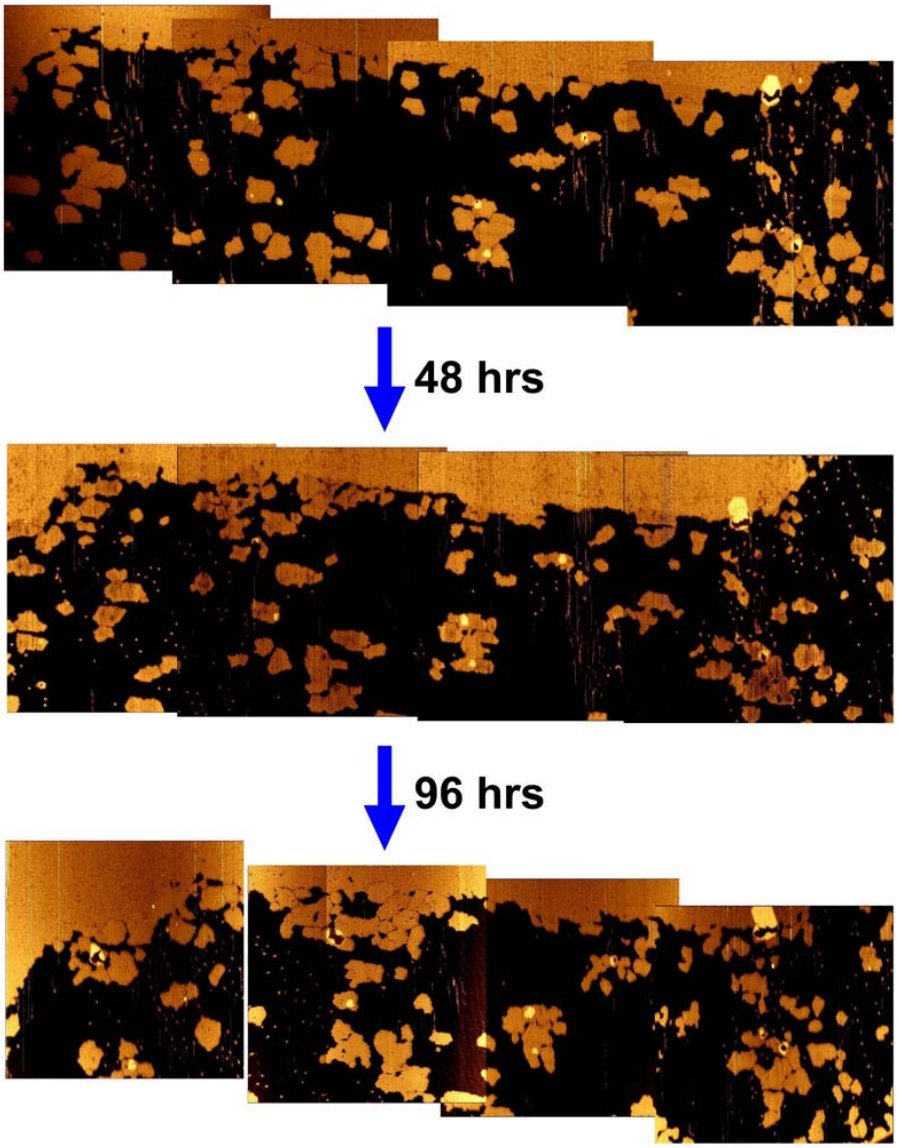

Fig. 8.11: Three images recorded with long intervals, showing the structural evolution of the island edge. The island edge shown here is the lower edge of the huge island on the left of Fig. 8.9. The C_{60} coverage is increased in these images compared with that in Fig. 8.9.

molecular movements observed in Fig. 8.12 are also quite possible a typical Ostwald ripening process helping the cluster to join the huge island. Exchanging a small number of molecules at a time, will cost less energy to overcome the two barriers mentioned above, thus the captured clusters can merge into the huge island piece by piece. Therefore, the ripening is actually completed in two steps. At first, the C_{60}

clusters diffuse as a whole unit to arrive the edge of the huge island, which is in the catalog of Smoluchowski ripening. Then, the clusters will merge into the island via Ostwald ripening, which occurs in the form of molecular exchange.

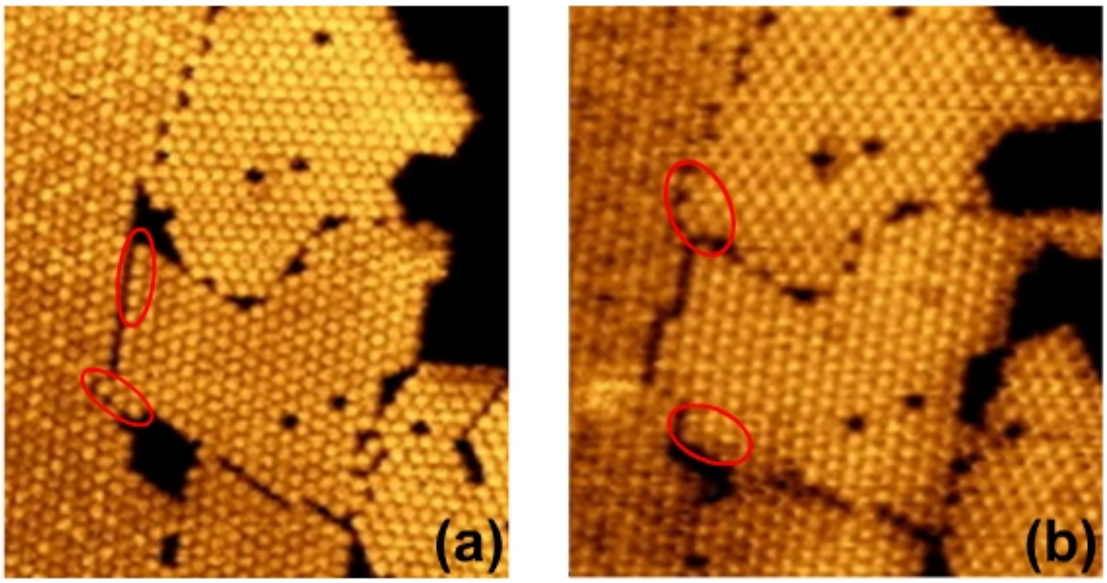

Fig. 8.12 (a): 24 × 32 nm, V = -1.1 V, I = 0.028 nA. (b): 28 × 32 nm, V = -1.1 V, I = 0.028 nA. Two sequentially recorded STM images show the detailed structure around the boundary area. The red circles highlight some structural changes happened at the boundaries. There is a trend that the molecules are merging into the huge island.

During the research of the molecular exchange between the clusters and the huge island, another interesting phenomenon is observed. As shown in Fig. 8.13(a), there is a large number of dim C_{60} molecules randomly distributed in the huge island. Meanwhile, the brightness of the molecules in the clusters is uniform. As mentioned many times, the dim appearance of molecules are associated with nanopits formed on the substrate surface. Therefore, the Au surface covered by the huge island has gone through a large atomic rearrangement, which is revealed by the presence of a large

number of dim molecules. On the other hand, the C_{60} molecules in the clusters present weaker interaction with the substrate, which can not modify the Au surface underneath. This can be easily understood because these clusters used to diffuse on the surface, which indicates a weak registration with the substrate. Naturally, people will wonder if the molecules transferred from the cluster to the island have the ability to create a nanopit. The answer can be found in Fig. 8.13(b). In this image, many clusters have merged into the island. However, there are some fingerprints of their former shapes. The dendritic structures along the edge of the island indicate that they are used to be some clusters, which were captured by the island and have merged into the island before the image is taken. On the island, a domain boundary parallel to the edge of the island can be seen, which is 6~11 nm deep from the island edge. On the inner side of this domain boundary, there are dim molecules randomly distributed. On the other side, between the boundary and the edge of the island, there is no dim molecule at all. The area without dim molecules is newly formed by the C_{60} molecules transferred from the clusters to the island. Therefore, we can conclude that the formation of nanopit requires a relatively long time to be spent. As introduced in Section 2.5.6 in the literature review, the herringbone pattern needs ~3 minutes to respond to an environment change, and the movement of atoms for relocating may last over 15 minutes [7]. The formation of nanopit is also a rearrangement of the surface atoms. Under a cluster which is newly captured, or under the newly formed area of the huge island, the rearrangement of the substrate atoms is not completed, thus no nanopits are formed and the C_{60} molecules present identical apparent height

on these areas, which gives a landscape as shown in Fig. 8.13. After long enough time, the nanopits will be formed under the C_{60} molecules transferred from clusters, thus the distribution of dim molecules will expand towards the island edge.

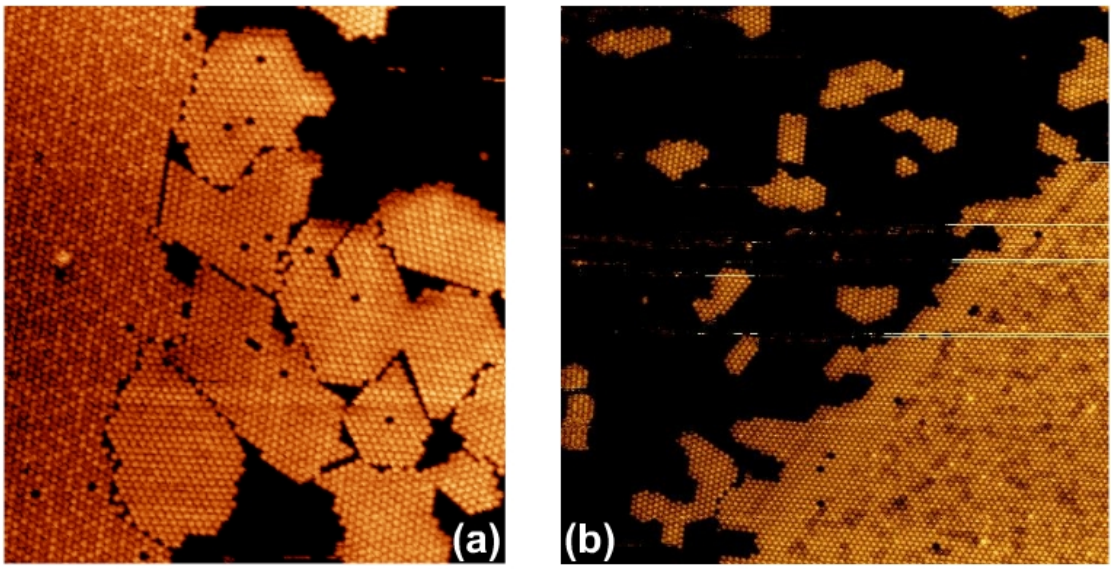

Fig. 8.13 (a): 61.4 × 68.42 nm, V = -1.1 V, I = 0.028 nA. On the left part of the image, there are dim C_{60} molecules distributed in the huge island. Meanwhile, the molecules in the clusters have uniform contrast. (b): 90 × 90 nm, V = -1.3 V, I = 0.04 nA. The dendritic structures along the edge of the huge C_{60} island are form by the clusters that have merged into the island. A domain boundary can be found running parallel to the island edge. All the dim molecules are distributed on the right side of this boundary while all the molecules have uniform apparent height on the left side.

In conclusion, I have introduced and discussed the diffusion and ripening behaviors of C_{60} molecules on the Au (111) surface, at both low temperature and room temperature. A combination of Ostwald ripening and Smoluchowski ripening is found in both cases. A diffusion model is suggested based on the observation: when there is high density of diffusing molecules in the FCC regions, they will aggregate to form

clusters with a magic number of seven. The trapping of these magic clusters by the elbow sites of the DLs leads to the landscape as shown in Fig. 7.7, in which the α-cluster between two pinched elbow sites are isolated from the single C_{60} molecules pre-adsorbed on the elbow sites.

References

[1] M. Böhringer, K. Morgenstern, W. D. Schneider, *et al.*, Phys. Rev. Lett. **83**, 324 (1999).

[2] I. Fernandez-Torrente, S. Monturet, K. J. Franke, J. Fraxedas, N. Lorente, and J. I. Pascual, Phys. Rev. Lett. **99**, 176103 (2007).

[3] N. Jiang, Y. Y. Zhang, Q. Liu, Z. H. Cheng *et al.*, Nano Lett. **10**, 1184 (2010).

[4] C. T. Tzeng, W. S. Lo, J. Y. Yuh, R. Y. Chu, and K. D. Tsuei, Phys. Rev. B **61**, 2263 (2000).

[5] X. Lu, M. Grobis, K. H. Khoo, S. G. Louie, and M. F. Crommie, Phys. Rev. B **70**, 115418 (2004).

[6] S. Guo, D. P. Fogarty, P. M. Nagel, and S. A. Kandel, J. Phys. Chem. B **108**, 14074 (2004).

[7] Y. Hasegawa and Ph. Avouris, Science **258**, 1763 (1992).

CHAPTER 9
CONCLUSION

In this thesis, the growth of C_{60} submonolayer structure on the Au (111) surface is systematically studied with variable temperature UHV STM. The research work can be summarized into three major parts: a) the assembly of C_{60} molecular structure on the Au (111) surface at room temperature; b) the assembly of C_{60} molecular structure on the Au (111) surface at reduced temperatures; c) the dynamical processes performed by the C_{60}/Au (111) system.

First, in the assembly of C_{60} molecular structures on the Au (111) surface at room temperature, the complicated interplay between the intermolecular interaction and the molecule-substrate interaction results in the rich features presented by the C_{60} molecular structure. The three kinds of close-packed C_{60} overlayer structures, R0º/in-phase, R14º and $(2\sqrt{3} \times \sqrt{3})$R30º, modify the C_{60}/Au (111) interface atomic structure differently, leading to different distributions of dim-apparent molecules in the C_{60} layer. The local density of the herringbone elbow site also influences the interface atomic structure, determining whether the reconstruction of the substrate can be lifted by the adsorbed C_{60} molecules. Furthermore, the rearrangement of the Au atoms under the adsorbed C_{60} molecules results in two different bonding configurations. If a nanopit is formed under the C_{60} molecule, it forms the strong bonding configurations, which is preferentially formed on the elbow sites of the DLs. It can retain the C_{60} molecule in the middle of the terrace at room temperature. The

decoration of the elbow sites at room temperature give a superlattice structure comprised by ordered arrays of individual molecules at each elbow site. Noticeable, the following island nucleation on this superlattice structure takes place at unexpected locations which is in-between of two elbow site molecules and the island is isolated from any elbow site (the α–island). The other bonding configuration involves intact Au surface and have lower strength.

There is another aspect of the room temperature study, which is the adsorption of C_{60} molecules on the zero-gradient stepped surface (ZGSS). This ZGSS consists of parallel gold-fingers. Each gold-finger has different atomic structure at its two opposite step edges. The two kinds of step edges are found to present different affinities to the C_{60} molecules or islands that attached to them, resulting in distinct adsorption structures on the two sides of each gold-finger. Such a bifunctional nanostructured surface has the potential to support the building of molecular devices.

Second, the study of the assembly of C_{60} molecular structure on the Au (111) surface at reduced temperatures reveals the effect of thermal activation on the behavior of the C_{60} molecule on the Au (111) surface and the different depths of the potential well presented by the different features on the reconstructed Au (111) surface. At 47 K and 180 K respectively, the nucleation and growth scenarios of the C_{60} structures are distinct from the situation of room temperature. No nanopit can be formed under the C_{60} molecule at either 47 K or 180 K. The C_{60} molecules are retained on the terrace due to reduced thermal activity. At 47 K, both pinched and bulged elbow sites can hold C_{60} molecules. The further growth of the C_{60} islands on

these two kinds of elbow site are in distinct ways because of the different local structures of the DLs. At 180 K, the C_{60} molecules preferentially occupy the bulged elbow sites, highlighting the difference between the pinched and the bulged elbows. Further deposition of C_{60} molecules at 180 K leads to the formation of close-packed islands. In contrast, at 47 K, the island growth follows the trend of the DLs. Such difference in the structure of the island indicates the different equilibriums of the intermolecular interaction and the molecule-substrate interaction presented at different temperatures.

Third, the dynamical processes of the C_{60}/Au (111) system are studied via two approaches. For the first, C_{60} molecules are deposited onto the Au (111) surface at 47 K and then the sample temperature is raised step-by-step until room temperature. The structural changes occurred in this process reveal the complex interplay of the intermolecular interaction, the molecule-substrate interaction and the thermal activities of the Au surface atoms and C_{60} molecules. When a large number of C_{60} molecules are released for free diffusion, C_{60} clusters with a magic number of seven will be formed. The molecules in the same cluster diffuse as a whole and the diffusion is confined within the FCC regions of the surface. Such diffusion scenario can also explain the unexpected nucleation site for the α–island mentioned above. When stored in UHV at room temperature, a ripening process occurs in the C_{60}/Au (111) system. Both Ostwald ripening and Smoluchowski ripening process are identified over a long timescale. The combination effect of the two ripening processes results in a slow structural change of the C_{60} overlayer, towards a uniform close-packed structure.

Numerous future works can be done based on the results listed above as further exploration towards the comprehensive understanding of the molecular assembly on metal surfaces. For the room temperature study of the C_{60} growth, my work mainly involves a relatively low C_{60} coverage (less than 0.5 ML), therefore, the situation of high coverage or even multilayer can be investigated. The rearrangement of the Au atoms at the C_{60}/Au (111) interface should be influenced by the number of adsorbed C_{60} molecules, therefore, the difference in the bonding configuration would result in different properties of the molecular system. Moreover, the formation of ordered arrays of individual C_{60} molecule by occupying each elbow site is a kind of pattern-guided growth of periodical molecular structures. Further nanoscale architectures performed on this template may lead to some interesting findings.

For the low temperature study of the C_{60}/Au (111) system, a promising future direction is using the scanning tunneling spectroscopy (STS) to examine the electronic property of the C_{60} molecular structures. This work has not been done in my research due to the limit of our equipment. The VT STM we used cannot offer the high stability that required by the STS experiment. Rich electronic characteristics are expected from the various topographic features presented by the C_{60} molecular structures on the Au (111) surface.

From the study of the dynamical processes happened to the molecular adsorbate on metal surfaces can reveal the basic rules that determine the behavior of the molecules. The understanding of these rules can help us to find the efficient method to construct molecular devices. Future research about the dynamical processes of the

C_{60}/Au (111) system can be carried out under various conditions or with other pre-deposited structures on the surface. Theoretical approaches to this problem may greatly help the understanding of the experimental results.

APPENDIX

The appendix contains five published papers based on the work in this thesis. Only the first page of each paper is presented.

1. The C_{60}/Au (111) interface at room temperature: A scanning tunneling microscopy study.

Surface Science 2008

2. Site-Specific Chemistry Directed by a Bifunctional Nanostructured Surface.

Langmuir 2010

3. Low-Temperature Growth of C_{60} Monolayers on Au (111): Island Orientation Control with Site-Selective Nucleation

Journal of Physical Chemistry C 2010

4. Organizing C_{60} Molecules on a Nanostructured Au (111) Surface

Surface Science 2010

5. Two Bonding Configurations for Individually Adsorbed C_{60} Molecules on Au (111)

Physical Review B 2010

Available online at www.sciencedirect.com
ScienceDirect
Surface Science 602 (2008) 885–892
SURFACE SCIENCE
www.elsevier.com/locate/susc

The C_{60}/Au(1 1 1) interface at room temperature: A scanning tunnelling microscopy study

X. Zhang, F. Yin, R.E. Palmer, Q. Guo *

Nanoscale Physics Research Laboratory, School of Physics and Astronomy, University of Birmingham, Edgbaston, Birmingham B15 2TT, UK

Received 22 October 2007; accepted for publication 13 December 2007
Available online 8 January 2008

Abstract

The interface between adsorbed C_{60} molecules and the (1 1 1) surface of gold at room temperature has been studied with the scanning tunnelling microscopy (STM). The first monolayer of C_{60} on Au(1 1 1) is known to exist in several phases: in phase, $2\sqrt{3} \times 2\sqrt{3}$R30°, and R14°, depending on the direction of the close-packed C_{60} molecules in relation to the close-packing direction of the gold atoms. For the in-phase C_{60} overlayer where the close-packing direction of the C_{60} molecules is aligned with that of the gold atoms, we find that the $22 \times \sqrt{3}$ reconstruction of the underlying Au(1 1 1) surface remains largely unchanged. For the $2\sqrt{3} \times 2\sqrt{3}$R30° phase, the surface reconstruction is also preserved to a great extent if the molecular layer sits on a region consisting of small $22 \times \sqrt{3}$ domains. On a larger domain, the $2\sqrt{3} \times 2\sqrt{3}$R30° structure is found to lift the surface reconstruction of Au(1 1 1). The R14° structure is observed for the first time in STM and a structural model consistent with findings from both STM and LEED is presented. A fairly regular pattern of atomic re-arrangement with a quasi-period of ~6 nm is found in regions of the Au(1 1 1) surface underneath the R14° C_{60} layer.

Keywords: Au(1 1 1); Gold; C_{60}; STM; Reconstruction; Interface; Adsorption; Fullerene

1. Introduction

The Au(1 1 1) surface has attracted much attention for a number of years because of its unique structure and properties. As the only face centred cubic (FCC) metal that exhibits a grossly reconstructed (1 1 1) surface, gold has been a model system for the study of surface reconstruction [1,2] and of the novel electronic and catalytic properties that arise from the reconstruction. The reactivity of Au(1 1 1) has been investigated by deposition of various atoms and molecules at a broad range of temperatures. In the case of metal deposition, nucleation of adsorbate islands usually occurs at the elbow sites of the herringbone pattern, giving rise to the formation of an ordered array of metal dots [3–5]. For molecular adsorption on Au(1 1 1), a most thoroughly investigated system is the binding of this surface to alkane thiols and the formation of self assembled monolayers [6–10]. The bonding between the sulphur atom in the thiol molecule and the surface gold atoms is strong enough to lift the surface reconstruction at room temperature. On the other hand, the adsorption of many other organic molecules including benzene has been found to leave the surface reconstruction unperturbed [11–14]. Among these molecules, most of them have a two-dimensional structure and the preferred adsorption orientation is such that the plane of the molecule lies parallel to the sample surface. In such a configuration, the herringbone pattern from the underlying reconstructed gold substrate is seen to superimpose on the structure of the molecular overlayer.

When three-dimensional molecules such as C_{60} are deposited onto Au(1 1 1), the much higher vertical corrugation from the molecular film itself makes it very difficult to identify any finger prints of the structure at the interface. Consequently there is, to date, a lack of experimental evidence wither the adsorption of C_{60} at room temperature

* Corresponding author. Tel.: +44 121 414 4657; fax: +44 121 414 7327.
E-mail address: Q.Guo@bham.ac.uk (Q. Guo).

0039-6028/$ - see front matter © 2008 Elsevier B.V. All rights reserved.
doi:10.1016/j.susc.2007.12.036

Langmuir Article

pubs.acs.org/Langmuir

Site-Specific Chemistry Directed by a Bifunctional Nanostructured Surface

Lin Tang, Xin Zhang, and Quanmin Guo*

School of Physics and Astronomy, University of Birmingham, Birmingham B15 2TT, United Kingdom

Received September 28, 2009. Revised Manuscript Received November 7, 2009

Using the scanning tunneling microscope (STM), we have created a bifunctional nanostructured surface which consists of parallel stripes of gold atoms on the Au(111) substrate. Each stripe has two parallel step-edges separated by a few nanometers in distance. The two step-edges have very different binding properties to molecules, and they are able to separate C_{60} molecules into two types of adsorbed structures, giving rise to a controlled formation of two-dimensional closely spaced multiple molecular nanostructures.

Introduction

Many important biological and chemical processes rely on specific binding between two or more molecules via molecular recognition.[1,2] The molecules involved in such binding process, e.g., antibody−antigen, have distinct binding sites with special functionalities. When molecules come into contact with a solid surface, such as that in heterogeneous catalysis, the molecules often end up in identical bonding sites due to the intrinsic long-range order and specific symmetry of the crystal surface. To direct molecules into different bonding configurations on the same surface, we need functional nanoscale structures,[3,4] analogous to the functionalities within molecules. By combining structured surfaces[5,6] and tailor-designed functional molecules,[7−9] it is possible to build a variety of nanoscale architectures potentially useful for a new generation of molecular electronic devices.[10,11]

A well-studied approach in surface organization of molecules is template directed growth, where a surface with a prefabricated pattern of structures is used to influence molecule−substrate and molecule−molecule interactions. For example, strain layers and dislocation networks have successfully been used for self-organized growth of metal islands[12,13] and molecular assemblies.[8,14−17] Surfaces with a regular array of steps, such as Au(111) vicinal surfaces,[18] have also been explored as interesting templates for the growth of metal and molecular nanostructures.[19−21]

In general, template directed growth relies on the existence of a regular and uniform structure on a patterned substrate. The regularity of the template, however, means that it is very difficult to grow two different structures at nanometer distances at the same time. Here, we report a new self-organized surface-growth phenomenon achieved by using a bifunctional, zero-gradient stepped surface (ZGSS)[22−24] and demonstrate the formation of two different types of close-spaced molecular nanostrucures on the same surface.

Experimental Section

The Au(111) surface was created with thermal deposition of gold onto highly oriented pyrolitic graphite. The graphite substrate was held at 650 K during deposition, and the final gold film was 300 nm thick. The gold film prepared in such way consists of interconnected (111)-oriented crystals. The sample was then transferred into an ultrahigh-vacuum chamber with a base pressure of 2×10^{-10} mbar and was cleaned by cycles of argon ion sputtering and thermal annealing. The bifunctional surface was created by extracting atoms from an existing step-edge on the Au(111) surface at room temperature, as reported previously.[22−24] A bias voltage in the range 1.0−2.0 V in conjunction with a high tunneling current of ∼40 nA was used for atom extraction. The extracted atoms self-organize into an array of parallel gold fingers. The process is very efficient, and it is capable of reorganizing several thousand atoms per minute. About 0.1 ML C_{60} molecules were deposited at a deposition rate of 0.05 ML/min from a homemade tantalum crucible onto the surface at room temperature (RT). Imaging was performed at RT using an Omicrometer variable temperature scanning tunneling microscope (VT-STM).

Results and Discussion

A typical example of the bifunctional ZGSS is shown in Figure 1a. It consists of parallel gold fingers of one atomic layer (2.4 Å) high, 15−26 nm wide, and several hundred nanometers

*Corresponding author: e-mail Q.Guo@bham.ac.uk, fax +44 121 4147327.

(1) He, Y.; Ye, T.; Su, M.; Zhang, C.; Ribbe, A. E.; Jiang, W.; Mao, C. D. *Nature* **2008**, *452*, 198.
(2) Fujita, M.; Oguro, D.; Miyazawa, M.; Oka, H.; Yamaguchi, K.; Ogura, K. *Nature* **1995**, *378*, 469.
(3) Ruffieux, P.; Ait-Mansour, K.; Bendounan, A.; Fasel, R.; Pattey, L.; Groning, P.; Groning, O. *Phys. Rev. Lett.* **2009**, *102*, 086807.
(4) Dil, H.; Lobo-Checa, J.; Laskowski, R.; Blaha, P.; Berner, S.; Osterwalder, J.; Greber, T. *Science* **2008**, *319*, 1824.
(5) Brune, H.; Giovannini, M.; Bromann, K.; Kern, K. *Nature* **1998**, *394*, 451.
(6) Chambliss, D. D.; Wilson, R. J.; Chiang, S. *Phys. Rev. Lett.* **1991**, *66*, 1721.
(7) Madueno, R.; Raisanen, M. T.; Silien, C.; Buck, M. *Nature* **2008**, *454*, 618.
(8) Theobald, J. A.; Oxtoby, N. S.; Phillips, M. A.; Champness, N. R.; Beton, P. H. *Nature* **2003**, *424*, 1029.
(9) Yokoyama, T.; Yokoyama, S.; Kamikado, T.; Okuno, Y.; Mashiko, S. *Nature* **2001**, *413*, 619.
(10) Dri, C.; Peters, M. V.; Schwarz, J.; Hecht, S.; Grill, L. *Nat. Nanotechnol.* **2008**, *3*, 649.
(11) Joachim, C.; Gimzewski, J. K.; Aviram, A. *Nature* **2000**, *408*, 541.
(12) Chambliss, D. D.; Wilson, R. J.; Chiang, S. *J. Vac. Sci. Technol. B* **1991**, *9*, 933.
(13) Helveg, S.; Lauritsen, J. V.; Laegsgaar, E.; Stensgaard, I.; Norskov, J. K.; Clausen, B. S.; Topsoe, H.; Besenbacher, F. *Phys. Rev. Lett.* **2000**, *84*, 5.
(14) Bohringer, M.; Morgenstem, K.; Schneider, W. D.; Berndt, R.; Maurie, F.; De Vita, A.; Car, R. *Phys. Rev. Lett.* **1999**, *83*, 324.
(15) Gao, L.; et al. *Phys. Rev. Lett.* **2008**, *101*, 197209.
(16) Ait-Mansour, K.; et al. *J. Phys. Chem. C* **2009**, *113*, 8407.
(17) Brune, H.; Giovannini, M.; Bromann, K.; Kern, K. *Nature* **1998**, *395*, 2997.
(18) Rousset, S.; Repain, V.; Baudot, G.; Garreau, G. Y.; Lecoeur, J. *J. Phys.: Condens. Matter* **2003**, *15*, S3363.
(19) Repain, V.; Baudot, G.; Ellmer, H.; Rousset, S. *Mater. Sci. Eng., B* **2002**, *96*, 178.
(20) Neel, N.; Kroger, J.; Berndt, R. *Appl. Phys. Lett.* **2006**, *88*, 163101.
(21) Treier, M.; Ruffieux, P.; Schillinger, R.; Greber, T.; Mullen, K.; Fasel, R. *Surf. Sci.* **2008**, *602*, L84.
(22) Guo, Q.; Yin, F.; Palmer, R. E. *Small* **2005**, *1*, 76.
(23) Yin, F.; Palmer, R. E.; Guo, Q. *Surf. Sci.* **2006**, *600*, 1504.
(24) Yin, F.; Palmer, R. E.; Guo, Q. *J. Phys: Condens. Matter* **2009**, *21*, 445001.

Low-Temperature Growth of C_{60} Monolayers on Au(111): Island Orientation Control with Site-Selective Nucleation

Xin Zhang, Lin Tang, and Quanmin Guo*

Nanoscale Physics Research Laboratory, School of Physics and Astronomy, University of Birmingham, Birmingham, B15 2TT, United Kingdom

Received: January 22, 2010; Revised Manuscript Received: March 17, 2010

We report a low-temperature scanning tunnelling microscopy (STM) study of the adsorption of C_{60} molecules on the (111) surface of gold. At 46 K, occupation of the elbow sites on Au(111) by individual C_{60} molecules as well as small molecular clusters is observed at a coverage of 0.01monolayer (ML). The molecular clusters are mostly found in the FCC regions adjacent to the bulged elbows while most of the pinched elbows remain decorated by single molecules. At a higher coverage of 0.05 ML, the islands nucleated at the bulged elbow sites increase in size, and at the same time, a delayed nucleation process starts around the pinched elbow sites. The C_{60} islands show different azimuthal orientations similar to that found for larger islands formed at room temperature. The islands in the FCC region near the bulged elbows grow with coverage, but are confined by the discommensuration lines. At 180−190 K, C_{60} molecules are found to preferentially attach to the bulged elbow site and island nucleation occurs exclusively on the bulged site. This single-site-nucleation phenomenon leads to the formation of C_{60} islands with a single orientation.

1. Introduction

Molecular self-assembly on surfaces has attracted a great deal of attention during the past decade, because of its potential in molecular electronic device fabrication.[1] Many surface assembly processes employ regularly patterned substrates as templates for guided growth of molecular structures.[2−4] Substrate patterning can be achieved by using lithography-based techniques, although there are plenty of naturally existing reconstructed surfaces with regular patterns that can be used to organize molecules at the nanometer scale.[5−8] One of such reconstructed surfaces that has been widely used in the research community is the unique $22 \times \sqrt{3}$-Au(111) surface, which has a herringbone-patterned dislocation network consisting of alternating FCC-stacking and HCP-stacking regions.[9−11] The reconstructed Au(111) surface has been used for template-directed growth of two-dimensional atomic and molecular structures. For instance, Ag atoms have been reported to diffuse to step edges to form finger-like structures,[12,13] while Fe,[14] Mo,[15] and Ni[16] atoms adsorb preferentially at the elbow sites of the herringbone pattern, involving an atom exchange process with the substrate. For organic molecules, the FCC and HCP regions exhibit different affinities to the molecules and the FCC region is usually found to be able to capture molecules more effectively due to its stronger interaction with the molecules.[17−19] Attachment of individual molecules by the elbow sites is mostly found at low temperatures, and at room temperature many molecules are free to diffuse on the surface.[3,7,8,20] In the case of the C_{60} monolayer on the Au(111) surface or similar (111) surfaces of other FCC metals, interesting morphology[21] and electronic structure[22] have been observed at low temperatures. A previous report by Fujita[23] shows the adsorption of individual C_{60} molecules at the herringbone elbow sites at 30 K. But as far as we know there is no detailed study on the nucleation and growth of C_{60} islands around the elbow sites. In this paper, we report a systematic investigation of the adsorption process of C_{60} molecules on the Au(111) surface and the subsequent growth of C_{60} clusters at 46 and 190 K. By increasing the surface coverage step by step, we found different nucleation behavior at the two types of elbow sites. The discommensuration lines are found to play an interesting role in confining the growth fronts. Moreover, for the small two-dimensional C_{60} clusters formed at 46 K, three different orientations have been observed and the orientation is clearly identified even for dimers. At 190 K, nucleation of C_{60} islands occurs exclusively at the bulged elbow site, and all the 2-dimensional molecular islands formed at this temperature adopt a single orientation.

2. Experimental Methods

The Au(111) sample was prepared by thermal evaporation of gold onto a highly oriented pyrolytic graphite (HOPG) substrate inside a high-vacuum chamber operating with a base pressure of 5×10^{-7} mbar. The substrate was preheated to 650 K with the shutter closed, and maintained at this temperature during deposition with the shutter open. The deposition rate as monitored with a quartz crystal oscillator was 2 nm/min, and the total thickness of the gold film is 250 nm. At the end of deposition, the shutter was closed while the sample was kept at 650 K for a further 30 min before cooling gradually to room temperature. The sample was then transferred to an ultrahigh-vacuum system (base pressure 1×10^{-10} mbar), which houses a variable-temperature scanning tunnelling microscope (VT-STM, Omicron), and treated with several cycles of Ar ion bombardment (1 keV energy, 10 μA/cm^2 ion current density) and thermal annealing (45 min at 1000 K). The sample surface prepared in such a way has large terraces with the (111) orientation, and shows the typical $22 \times \sqrt{3}$ surface reconstruction. STM imaging was carried out with the Omicron VT-STM, using chemically etched tungsten STM tips under constant current mode. The sample temperature can be reduced to 40 K on the STM stage with liquid helium, and with the help of a Lakeshore temperature controller, the sample temperature can

* To whom correspondence should be addressed. E-mail: q.guo@bham.ac.uk.

10.1021/jp1006318
Published on Web 03/24/2010

Surface Science 604 (2010) 1310–1314

Contents lists available at ScienceDirect

Surface Science

journal homepage: www.elsevier.com/ locate/susc

Organizing C_{60} molecules on a nanostructured Au(111) surface

Lin Tang, Xin Zhang, Quanmin Guo *

School of Physics and Astronomy, University of Birmingham, Birmingham B15 2TT, United Kingdom

ARTICLE INFO

Article history:
Received 3 March 2010
Accepted 21 April 2010
Available online 29 April 2010

Keywords:
C_{60}
Fullerenes
Au(111)
STM
Adsorption
Faceting
Surface diffusion

ABSTRACT

We have studied, using scanning tunneling microscopy, the adsorption of C_{60} molecules on a nanostructured Au(111) surface consisting of artificially created two-dimensional cavities. These cavities, one atomic layer deep, are found to be effective as molecular traps at room temperature. Gold atoms at step edges are found to respond to the adsorption of C_{60} molecules and gross faceting is observed for steps connected with $R30°$ oriented C_{60} molecular islands. Structural models are proposed to establish the step structures related to all three types of molecular islands.

1. Introduction

The adsorption of C_{60} molecules on the Au(111) surface was first studied using scanning tunneling microscopy (STM) in 1993 [1,2]. Two close-packed molecular monolayer structures, in-phase-$R0°/38\times38$ and $2\sqrt{3}\times2\sqrt{3}-R30°$, were observed to grow out of surface step edges. Since then, a number of investigations have been performed on this adsorption system using both STM [3–7] and spectroscopic techniques [8–10]. More recent STM studies [4,6] have observed an $R14°$ structure which was initially found with low energy electron diffraction [11], and also evidence for nano-pit formation on Au(111) [12] and Ag(111) [13] following thermal annealing of an adsorbed C_{60} layer. Since C_{60} islands are mostly nucleated at surface steps at room temperature, a number of studies have used surfaces with a high density of steps such as vicinal Au(111) [14,15] and artificially created stepped surfaces [16]. The use of stepped surfaces helps to identify the initial stages of nucleation and growth of C_{60} monolayers. Here we report findings of the adsorption and surface growth of C_{60} monolayer on a nanostructured Au(111) surface consisting of artificially created steps, atomic vacancies and adatoms of gold. Particular attention has been paid to observe how the structure of surface steps influences the nucleation and orientation of C_{60} islands. Structural models are proposed to clarify the locations of C_{60} molecules attached to different types of steps and C_{60} induced restructuring of steps.

2. Experimental

The Au(111) surface was created with thermal deposition of gold onto highly oriented pyrolitic graphite. The graphite substrate was held at 650 K during deposition and the final gold film was 300 nm thick. The gold film prepared in such way consists of interconnected (111)-oriented crystals. The sample was then transferred into an ultra high vacuum (UHV) chamber with a base pressure of 2×10^{-10} mbar, and was cleaned by cycles of argon ion sputtering and thermal annealing. Surface modification using the STM tip was performed at room temperature to extract atoms from naturally existing surface steps on Au(111). The extracted atoms self-organize into an array of parallel finger-like structures [17–19], some of which could be connected to form 2D nano-cavities [19] and semi-enclosed nano-cavities. This surface modification procedure also creates a number of atomic vacancies as well as adatom islands on the surface. C_{60} molecules were deposited at a deposition rate of 0.05 ML/min from a home-made tantalum crucible onto the nanostructured surface at room temperature (RT). Imaging was performed at RT using an Omicron variable temperature scanning tunneling microscope (VT-STM) with electrochemically-polished tungsten tips.

3. Results and discussion

Fig. 1 shows a typical STM topographic image of a nanostructured Au(111) surface used in our experiments. Detailed procedure for fabricating such a surface is given in previous publications [17,19]. In this STM image, one can see two closed 2D nano-cavities, each about ~12 nm wide, marked by black rectangles; and two open-ended nano-cavities marked by white rectangles. Also in the image, there are a

* Corresponding author. Tel.: +44 1214144657; fax: +44 1214147327.
E-mail address: Q.Guo@bham.ac.uk (Q. Guo).

0039-6028/$ – see front matter © 2010 Elsevier B.V. All rights reserved.
doi:10.1016/j.susc.2010.04.019

Two bonding configurations for individually adsorbed C_{60} molecules on Au(111)

Lin Tang,[1] Xin Zhang,[1] Quanmin Guo,[1] Yu-Ning Wu,[2] Lin-Lin Wang,[2] and Hai-Ping Cheng[2]
[1]*School of Physics and Astronomy, University of Birmingham, Edgbaston, Birmingham B15 2TT, United Kingdom*
[2]*Department of Physics and the Quantum Theory Project, University of Florida, Gainesville, Florida 32611, USA*
(Received 7 July 2010; published 9 September 2010)

Two distinct bonding configurations have been identified for individually adsorbed C_{60} molecules on the elbow site of Au(111) using scanning tunneling microscopy: a strong bonding configuration where the molecule sits in a single-atomic-layer-deep pit and a weak bonding configuration where the molecule sits directly above the dislocation of the elbow site. Density-functional theory calculations show that the most stable strong bonding configuration involves the molecule sitting inside a seven-atom pit with 2.56 eV adsorption energy.

DOI: 10.1103/PhysRevB.82.125414 PACS number(s): 68.47.De, 68.37.Ef, 68.43.Fg, 71.15.Mb

INTRODUCTION

Surfaces with a regular array of energetic sites are useful templates for growing nanoscale structures from site-specific nucleation. A classical example of such a template is the (111) surface of gold which has been extensively studied as a standard system for the growth of ordered two-dimensional arrays of metal islands.[1–5] The so-called herringbone reconstruction[6,7] of Au(111) gives rise to a surface dislocation network which is able to direct the incoming atoms toward the well-defined reactive "elbow sites"[1,8] where nucleation of metal islands takes place. For organic molecules, preferential decoration of the elbow sites has also been observed but mostly at low temperatures.[9,10] In the case of C_{60} adsorption on Au(111) at room temperature (RT), the formation of closed-packed molecular monolayers has long been identified as a consequence of nucleation at step edges without any preferential attachment of C_{60} molecules to the elbow sites.[11–14] Recent investigations have revealed an interesting phenomenon about C_{60} adsorption on noble-metal surfaces such as Ag(111) and Cu(111). It has been reported that the bonding of C_{60} molecules on Ag(111) involves a single-atom vacancy.[15] An even dramatic seven-atom vacancy pit has been proposed for the adsorption of C_{60} on Cu(111).[16] The seven-atom vacancy pit on Cu(111) induced by C_{60} adsorption[16] is particularly interesting since a C_{60} molecule inside such a pit is effectively bonded to single-atom high steps in all directions. Such a bonding configuration is consistent with the preferential attachment of C_{60} molecules to step edges as well as the observed significant enhancement of the bonding strength between the first molecular layer and the metal substrate. On gold surfaces, nanopit formation following the adsorption of C_{60} molecules on Au(110) (Ref. 17) has also been reported and more recently a similar phenomenon has been proposed for the Au(111) surface[18] based on a study of close-packed single layer C_{60} islands. There have been so far no reports on the bonding configuration for individually adsorbed C_{60} molecules on Au(111) at room temperature. We report here the observation with scanning tunnel microscopy (STM) of individually adsorbed C_{60} molecules on the elbow sites of Au(111) at room temperature. By comparing with the behavior of the same molecule adsorbed on Au(111) at low temperatures[19] and performing density-functional theory (DFT) calculations, we identified two distinct bonding configurations with marked difference in their bonding strength. DFT calculations show that the strong bonding configuration at room temperature can be explained by the introduction of a single-layer deep pit below the adsorbed C_{60} molecule.

EXPERIMENT

The gold sample was prepared by thermal evaporation of gold onto a highly oriented pyrolytic graphite substrate at 650 K. The sample was then transferred to an ultrahigh-vacuum system where it was treated with several cycles of Ar^+-ion bombardment and thermal annealing. The resulting surface shows predominantly (111) oriented gold with many atomically flat regions up to 1–2 μm in size. The flat terraces exhibit the typical herringbone pattern consisting of $22\times\sqrt{3}$ reconstructed domains. C_{60} molecules were deposited onto the gold surface from a homemade Knudsen cell with a deposition rate of ~0.05 monolayer (ML)/min. STM images were acquired using an Omicron variable temperature (VT)-STM.

RESULTS AND ANALYSIS

Following a 0.015 ML deposition of C_{60} molecules at 46 K, the molecules are found to attach exclusively to the elbow sites on the Au(111) surface, either as individual molecules or in the form of small molecular clusters, Fig. 1(a). Detailed analysis of nucleation and growth of C_{60} islands at 46 K can

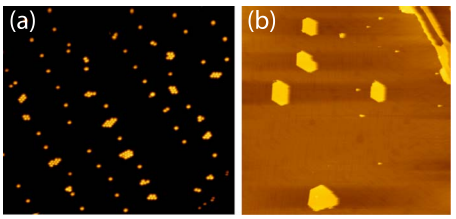

FIG. 1. (Color online) (a) Individual molecules and molecular clusters of C_{60} occupying the elbow sites at 46 K (74 nm $\times$82 nm, acquired with −3 V sample bias and 0.03 nA tunnel current). (b) STM image, 184 nm$\times$184 nm, showing step decoration (near the top right corner) and the formation of large molecular islands on the flat terrace upon thermal annealing to 284 K.

